Mechanical behaviour of thin film separators in rechargeable batteries

A thesis submitted to The University of Manchester for the degree of

Doctor of Philosophy

in the Faculty of Science and Engineering

2021

Yu Wang

Department of Mechanical, Aerospace and Civil Engineering, School of Engineering

Contents

Word count: 43314

List of Figures

List of Tables

List of Abbreviations

Abbreviations	Description
2D	Two-dimensional
3D	Three-dimensional
ASTM	American Society for Testing and Materials
AVESTD	Average of standard deviation
CGB	Critical geometric boundary
DIC	Digital image correlation
DLB	Design limit boundary
DMA	Dynamic mechanical analyser
EIS	Electrochemical Impedance Spectroscopy
EV	Electric vehicle
FE	Finite element
FEA	Finite element analysis
FEM	Finite element method
F-K	Föppl–von Kármán
GRG	Generalised reduced gradient
HVE	Hyper-viscoelastic
ISS	Inverse stress solution
LIB	Lithium-ion battery
MD	Machine direction (material direction)
MIP	Mercury intrusion porosimetry
MR	Mooney-Rivlin
NH	Neo-Hookean
PE	Polythene/polyethylene

PP	Polypropylene
S4R	4-node quadrilateral shell element with reduced integration
SEM	Scanning electron microscope
SS	Stress solution
TD	Transverse direction (material direction)
TTD	Through-thickness-direction
TTSP	Time–temperature superposition principle
TS	Two-step
VSG	Virtual strain gauge

List of Notations

Notation	Description
α	Non-dimensional geometrical parameters, i.e. W/R
β	Non-dimensional geometrical parameters, i.e. D/W
C_{10}, C_{01}	Material parameters in hyperelastic model
D	The length of the extended parts of dogbone geometry
δ_c	Assumed defect parameter caused by sample cutting
δ_m	Assumed defect parameter caused by manufacturing
E	Young's modulus or elastic modulus
ε	Uniaxial nominal (engineering) strain
$\dot{\varepsilon}$	Nominal (engineering) strain-rate
ε_{cr}	Critical buckling strain
ε_l	Measured nominal (engineering) strain in longitudinal direction
ε_m	The upper limit strain of elastic regime
ε_R	Constant nominal (engineering) strain given in stress-relaxation stage
ε_t	Measured nominal (engineering) strain in transverse direction
η	Scale factor
η_i	Viscosity for the ith Maxwell branch
$\mathbf{F}$	Deformation gradient
$\mathbf{F}_t(t-s)$	Relative deformation gradient
G	Shear modulus
$G(t)$	Time-dependent shear modulus
G_0	Instantaneous shear modulus
G_i	Shear modulus for the ith Maxwell branch
G_∞	Long-term shear modulus

$g(t)$	Normalised relaxation modulus
g_0	Normalised instantaneous relaxation modulus
g_∞	Normalised long-term relaxation modulus
g_i	The dimensionless relaxation parameter for the ith Maxwell branch
γ	Non-dimensional geometrical parameters, i.e. W/h
h	Thickness
I_1, I_2	First and second invariants of strain tensor, respectively
k	Ionic conductivity
L	The length of the gauge area of the specimen
λ	Uniaxial stretch ratio
$\lambda(t)$	Stretch ratio history
λ_e	The lowest positive eigenvalue
$\lambda_j^{Meas}(t)$	Experimentally-measured stretch ratio at the jth data point
M	The number of data points used in SS method
M_1	The number of data points of λ for each data set at the ramp-loading stage used in ISS method
M_2	The number of the data sets used for calibration used in ISS method
M_3	The number of data points of λ for each data set at the stress-relaxation stage used in ISS method
N_M	MacMullin number
P	Uniaxial nominal (engineering) stress
$P^R(t^R)$	Nominal (engineering) stress with time in the stress-relaxation stage
P_0	Uniaxial instantaneous nominal (engineering) stress
P_0^R	Nominal (engineering) stress at the beginning of the stress-relaxation
P_∞	Long-term nominal (engineering) stress
$P_j^{Meas}(t)$	Experimentally-measured nominal (engineering) stresses at the jth data point associated with $\lambda_j^{Meas}(t)$

$P_j^{Cal}(t)$	Calculated nominal (engineering) stresses at the jth data point associated with $\lambda_j^{Meas}(t)$ in SS method
Φ	Porosity
R	The radius of the extended parts of dogbone geometry
R^2	The coefficient of determination or R-squared value
RMSD	Root-mean-square deviation
σ	Cauchy stress (or true stress)
$\boldsymbol{\sigma}$	Cauchy stress tensor
σ_0	Instantaneous Cauchy stress
$\boldsymbol{\sigma}^D$	Deviatoric part of Cauchy stress tensor
$\boldsymbol{\sigma}^{\boldsymbol{H}}$	Hydrostatic part of Cauchy stress tensor
$\boldsymbol{\sigma}_0$	Instantaneous Cauchy stress tensor
$\boldsymbol{\sigma}_0^D$	Deviatoric part of instantaneous Cauchy stress tensor
$\boldsymbol{\sigma}_0^H$	Hydrostatic part of instantaneous Cauchy stress tensor
σ_y	Yield stress
t	Time
t^R	Relaxation time
t_0^R	The time when relaxation begins
τ	Tortuosity
τ_i^R	The retardation/relaxation times for the ith Maxwell branch
u_{pre}	Pre-stretched displacement
u_{cr}	Critical displacement for onset of buckling
$V(\varepsilon_l)$	Current volume of the gauge area at longitudinal strain ε_l
V_0	Initial volume of the gauge area
$v(\varepsilon_l)$	Effective Poisson's ratio with longitudinal strain
W	The width of specimen
W_e	Strain energy potential

w	Out-of-plane displacement
$\lvert w\rvert_{max}$	Maximum out-of-plane displacement in the gauge area
w^0	Initial geometric imperfections

Abstract

In the past decade, increasing fire accidents have been reported for electric vehicles (EVs) after the EV rechargeable batteries suffered from mechanical abuses. Separator is the most important component in a rechargeable battery in terms of safety. Its mechanical behaviours play a crucial role for the overall safety of the battery, and therefore, should be thoroughly investigated. The aim of this PhD programme is to develop mechanical models under uniaxial tensile stress state and the associated testing techniques for thin film separators commonly used in lithium-ion batteries. The main objectives are to improve the mechanical test method, explore the mechanical characteristics, and establish a time-dependent constitutive model for the separator under tensile stress state. The thesis introduces the background of the research and gives a thorough literature review, based on which the important outstanding issues are outlined. A comprehensive study is carried out by a combination of FEM simulations, experiments, and analytical methods.

Firstly, it is demonstrated that wrinkling phenomena, which commonly occurred in standard uniaxial tensile tests because of the ultra-thin thickness characteristics, can adversely influence the test measurement. A numerical study is conducted to improve its measurement accuracy, and a novel critical geometric boundary (CGB) is proposed for the design of samples to meet the uniaxial tensile test standards.

Secondly, uniaxial tensile tests are conducted under the quasi-static condition for typical types of separators, including both dry and wet process separators, using 3D digital image correlation (DIC) technique. It shows that the CGB method successfully diminishes the measuring errors for separators whose anisotropy are not high. Typical mechanical properties and 1D strain-dependent porosity variation are discussed and concluded. Inhomogeneous strain distribution is found in dry process separators, but not in wet process separators. It implies that the longitudinal engineering strain can be accurately measured by a virtual extensometer for wet process separators. The valid conditions for the uniaxial tensile tests of dry process separators are determined.

Thirdly, viscoelastic behaviour of separators subjected to cyclic loading is an essential characteristic that should be considered for the long-term application of rechargeable batteries. A tension-relaxation test is designed and conducted in a range of low loading strain-rates using a virtual live extensometer. The hyperelastic constitutive and finite-strain viscoelastic models are combined theoretically to establish an analytical hyper-viscoelastic (HVE) model. To determine the HVE model, a novel parametrical calibration method is proposed and compared with other two traditional methods. By comparing with the experimental results, the proposed HVE model can simultaneously describe viscoelastic effects, and large deformation.

Finally, several topics, including the change of the electrochemical behaviour with the deformation of separators in unit cell and the relationship between tortuosity/porosity and strain under mechanical abuses, which were planned but not performed due to the impact of Covid-19, are briefly outlined, together with the discussion of future works.

Declaration

The author hereby declares that no portion of the work referred to in this thesis has been submitted in support of an application for another degree or qualification of this or any other university or other institute of learning.

Copyright statements

i. The author of this thesis (including any appendices and/or schedules to this thesis) owns certain copyright or related rights in it (the “Copyright”) and he has given The University of Manchester certain rights to use such Copyright, including for administrative purposes.

ii. Copies of this thesis, either in full or in extracts and whether in hard or electronic copy, may be made only in accordance with the Copyright, Designs and Patents Act 1988 (as amended) and regulations issued under it or, where appropriate, in accordance with licensing agreements which the University has from time to time. This page must form part of any such copies made.

iii. The ownership of certain Copyright, patents, designs, trademarks and other intellectual property (the “Intellectual Property”) and any reproductions of copyright works in the thesis, for example graphs and tables (“Reproductions”), which may be described in this thesis, may not be owned by the author and may be owned by third parties. Such Intellectual Property and Reproductions cannot and must not be made available for use without the prior written permission of the owner(s) of the relevant Intellectual Property and/or Reproductions.

iv. Further information on the conditions under which disclosure, publication and commercialisation of this thesis, the Copyright and any Intellectual Property and/or Reproductions described in it may take place is available in the University IP Policy (see http://documents.manchester.ac.uk/DocuInfo.aspx?DocID=24420), in any relevant Thesis restriction declarations deposited in the University Library, The University Library’s regulations (see http://www.library.manchester.ac.uk/about/regulations/) and in The University’s policy on Presentation of Theses.

Acknowledgements

I would like to express my sincere gratitude to my supervisor, Professor Qingming Li, for his encouragement, patience, support and guidance to me in my PhD student life. Professor Li's meticulous attitude to research deeply influenced me and let me know what a real scholar should be like. Without his guidance and persistent support, this thesis will not be possible to complete.

I am grateful to my examiners, Dr P.J. Tan from University College London and Professor Lee Margetts from The University of Manchester, for their reviews and suggestions, as well as their time spent on my thesis. The Viva is an experience of great value for me, and I will never forget it.

My thanks to my colleagues, Dr Yongle Sun, Dr Yinzhong Yan, Dr Andrea Codolini, Dr Chengxing Yang, Dr Chuanguo Chai, Dr Kangpei Meng, Shunfeng Li, Wei Sun, Xianglin Huang and Yuyang Xing, who are members of Professor Li's research group, as well as Dr Zhe Sun, Dr Yihe Huang, Dr Chengguang Liu and Dongxu Cheng, who were working in the same office, for their various helpful advice during this research.

Furthermore, I would like to thank Mr Stuart Morse, Mr Christopher Cowan and Mr Andrij Zadoroshnyj, who work in the James Lighthill Building, Dr Mark Quinn, Dr Andrea Codolini, Dr Marc Schmidt, Dr Stephen Burley and Yuyang Xing in the Department of MACE, for their help in my experiment. Without your supports, it is impossible to complete the experiment in this research successfully.

Last but not least, I would like to acknowledge with gratitude, the support and endless love from my parents, Mr Nianxing Wang and Mrs Xuemei Zhong, who are the most solid backings to me. Without their financial and spiritual support, I would not be able to complete my PhD study. Also, I would like to thank my girlfriend, Dr Shuang Hu, who was also studied and graduated from the UoM, for her companion and support over the past three years.

Contributions

I. Publications contributing to the thesis

1. **Wang, Y.**, Li, Q. M., Xing, Y. (2020) Porosity variation of lithium-ion battery separators under uniaxial tension. International Journal of Mechanical Sciences, 174, pp. 105496.
2. **Wang, Y.**, Li, Q. M. (2021) Critical geometric boundary for the design of wrinkling-free thin film samples in the elastic regime of a uniaxial tensile test. International Journal of Mechanical Sciences, 204, pp. 106485.
3. **Wang, Y.**, Xing, Y., Li, Q. M. (2021) A hyper-viscoelastic model for battery separators based on inverse-stress-solution parametrical calibration method (in writing)

II. Other publications

4. Yang, C., Li, Q. M., **Wang, Y.** (2021) Compressive properties of cuttlebone-like lattice (CLL) materials with functionally graded density. European Journal of Mechanics - A/Solids, 87, pp. 104215.

1 Introduction

1.1 Separators used in liquid electrolyte batteries

Separator, as a critical component used in liquid electrolyte batteries, is a kind of porous thin film (or membrane) that is usually made from insulation materials (e.g. polymer, nonwoven fibres, and ceramic). Separator is placed between two electrodes (i.e. anode and cathode inside the battery) to prevent their physical contact, which could lead to a short circuit. Meanwhile, it allows the transport of ionic charge carriers, as shown in Figure 1-1.

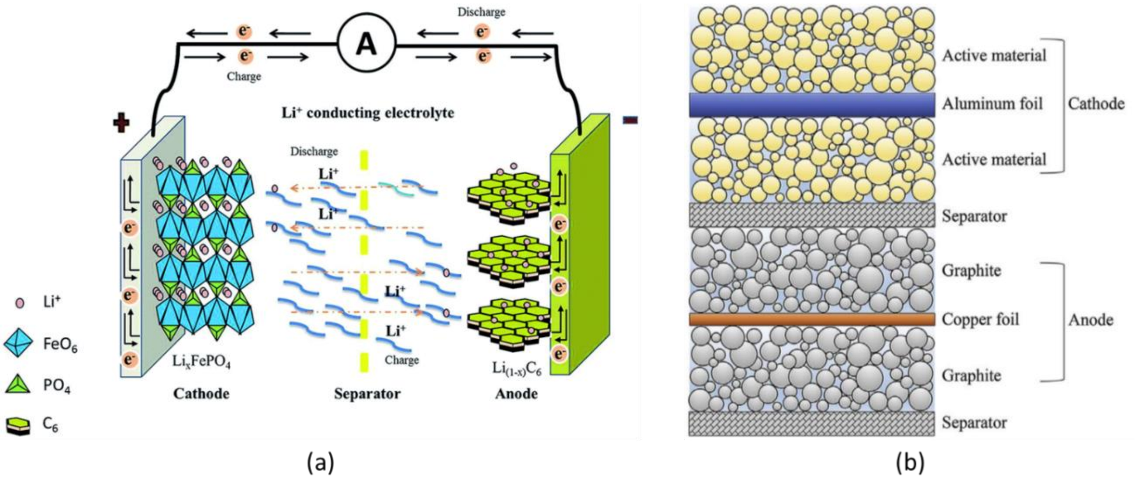

Figure 1-1 The schematic illustration of (a) the working principle (adapted from Lee et al. 2014), and (b) representative internal structure (adapted from Zhu et al. 2018a) of a typical lithium-ion battery.

Separators that are most commonly used in batteries can be divided into three types in terms of physical conditions: (1) microporous polymer membranes, (2) nonwoven fabric mats, and (3) inorganic composite membranes (Zhang 2007). Among them, microporous membranes made of polypropylene (PP) or polythene/polyethene (PE) are the most frequently used separators in commercial lithium-ion batteries (LIBs), and their mechanical properties have been widely investigated. According to the manufacturing/fabrication process, the microporous separators can be primarily divided into dry-processed and wet-processed. The fabrication of both dry- and wet-processed separators can be described by four main steps (Johnson and Wilkes 2001, 2002a, b, Lee et al. 2014): (1) heating, (2) extruding, (3) annealing (dry-processed) or solvent extraction (wet-processed), and (4) stretching, as shown in Figure 1-2 in details.

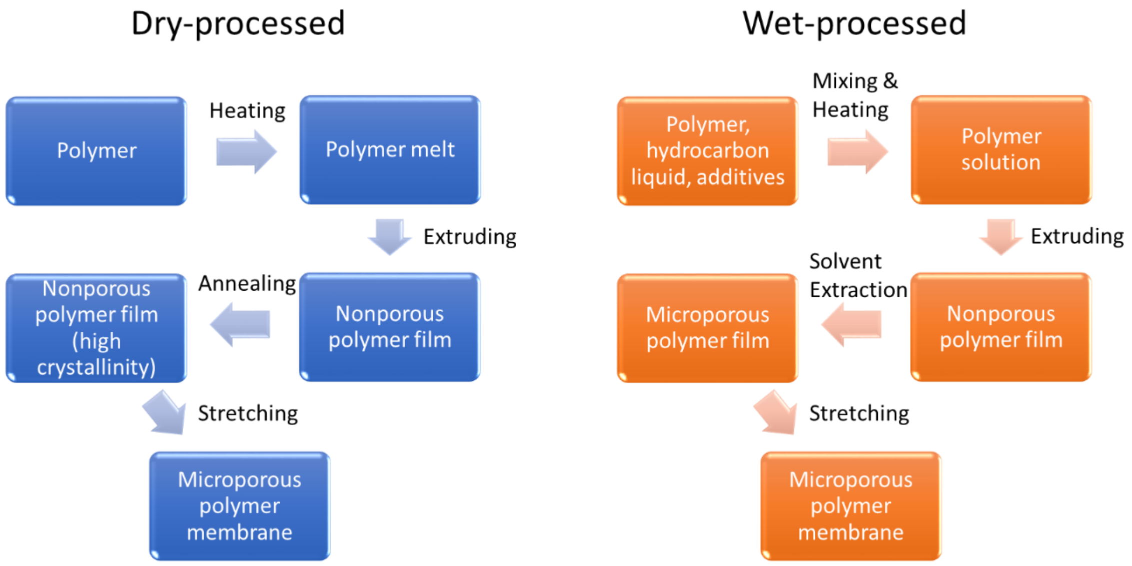

Figure 1-2 The manufacturing/fabrication process of dry- and wet-processed microporous separators (adapted from Lee et al. 2014).

According to previous studies (Ihm et al. 2002, Arora and Zhang 2004, Deimede and Elmasides 2015), the cost of dry-processed separators is usually lower than the cost of wet-processed separators due to the maturity of the manufacturing technique and the simplicity of raw materials for dry-processed separators. Compared to the dry-processed separators, wet-processed separators can have relatively evenly distributed pores, high puncture resistance, good mechanical behaviours, and can be more easily produced at smaller thickness, and therefore, wet-processed separators are suitable for high-capacity batteries (DeMeuse 2021, Luo et al. 2021). However, wet-processed separators traditionally occupied only a small amount of the separator market due to the complexity of the raw material preparation (Arora and Zhang 2004) and the high cost of the solvent extraction operation (Weighall 1991, Deimede and Elmasides 2015). In recent years, with the continuous improvement of the wet-processed separator technique, the market share of wet-processed separators has been increased significantly (CCM 2017) and is becoming as popular as the dry-processed separators (Markets 2018, Pulidindi and Pandey 2021). Due to the different manufacturing methods, their microstructures are also different. Figure 1-3 displays the microscopic images of both dry- and wet-processed separators, captured by a scanning electron microscope (SEM). To avoid confusion in the following text, MD and TD are used to describe the material directions in this thesis, where MD represents the machine direction (or the rolling direction) of the separator, and TD represents the transverse direction (perpendicular to the MD) of the separator.

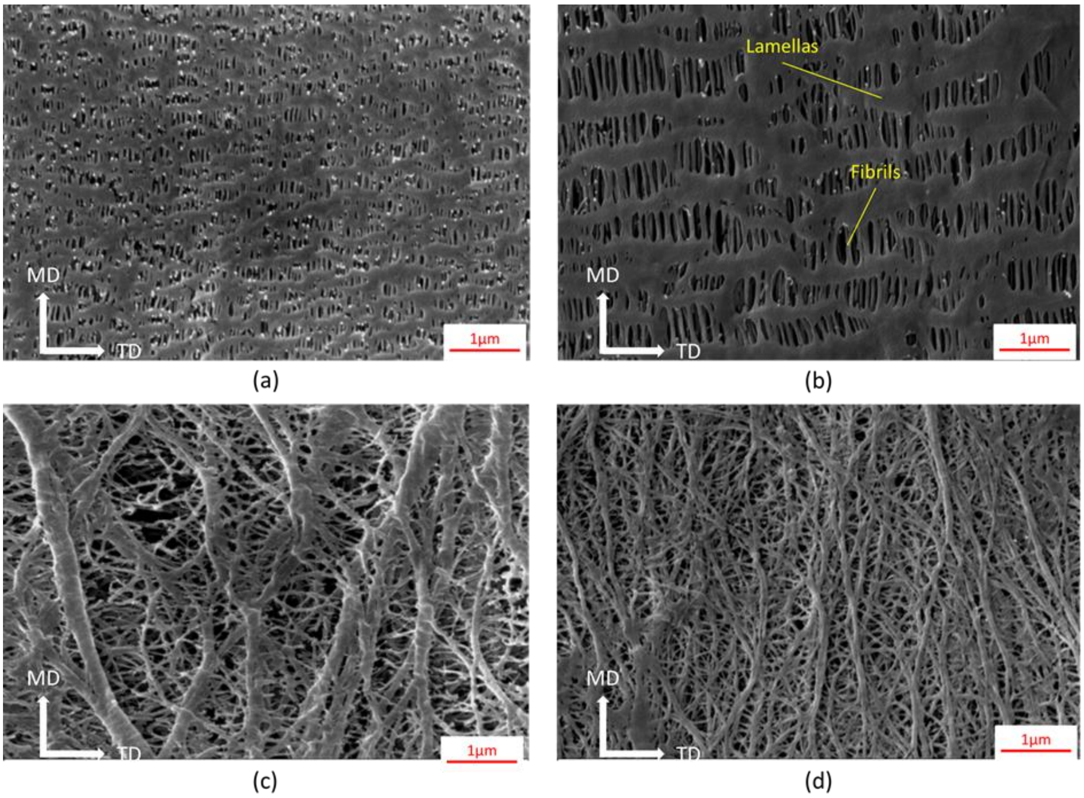

Figure 1-3 SEM images of (a) Celgard 2325 (a representative tri-layer dry-processed separator), (b) Celgard 2500 (single layer dry-processed separator), and Asahi Kasei Hipore (wet-processed separator) with (c) 16 µm thickness and (d) 25 µm thickness.

1.2 Motivation and scope

1.2.1 Motivation

In most previous studies on batteries, separators were considered to be undamaged (Doyle et al. 1993, Fuller et al. 1994, Nunes-Pereira et al. 2013). In recent years, batteries have been commonly used in electric vehicles (EVs), which implies that batteries can be easily exposed to abuse scenarios (Spotnitz and Franklin 2003, Santhanagopalan et al. 2009). The abuse scenarios can be mainly divided into mechanical abuse (e.g. mechanical shock, crush, penetration), electrical abuse (e.g. overcharge/overdischarge, external/internal short circuit,), environmental abuse (e.g. extreme temperature, fire), and chemical abuse (e.g. emissions, flammability) (SAE 2009, Ruiz et al. 2018).

In the case of mechanical abuse, the internal components of a battery are inevitably subjected to mechanical loading and deformation, and the separators can be easily penetrated and damaged by the broken particles from the electrodes (Sahraei et al. 2012, Sahraei et al. 2015, Xiong et al. 2020a, Yuan et al. 2020). As the most critical component, the damage of the separator can trigger internal short circuit (Cai et al. 2011, Sahraei et al. 2014, Wang et al. 2016) and even lead to significant safety issues, e.g. thermal runaway (Santhanagopalan et al. 2009, Wang et al. 2017). Besides the damage introduced to the separator, it was found that the deformation of the separators can also indirectly affect battery’s functions, e.g. the deformed pore-structure can change the tortuosity (Cannarella and Arnold 2013), which is a key factor that influences the internal resistance and mass transport (Arora and Zhang 2004, Tjaden et al. 2016), or even causes the lithium plating that can penetrate the separators (Cannarella and Arnold 2015).

In this context, researchers have conducted comprehensive research on the mechanical properties of separators for more than a decade. As a result, several constitutive models and numerical modelling methods (including macroscopic and microscopic models) have been developed, which will be introduced in detail in Chapter 2. These constitutive models are crucial for the safety design and assessment of the batteries using numerical simulations. However, some important gaps still need to be addressed, e.g. material behaviour under finite-strain deformation, the relationship between micro- or meso-scale characteristics and macroscopic deformation, etc.

1.2.2 Scope of this thesis

The aim of this PhD programme is to develop a material characterisation method with an associated experimental procedure to describe the mechanical behaviour of separators at low strain-rates. Since the safety issue in batteries is a complex problem (including mechanical, thermal, electrical and chemical aspects), it is better to investigate it using a multiphysics simulation software or platform, e.g. COMSOL Multiphysics, LS-DYNA. The material characterisation method proposed in this thesis can help build a more accurate material mechanical model, which can be offered to the multiphysics simulation software for designing batteries or predicting the safety-related response (not only mechanical) in batteries. Hence, it should be noted that the work in this thesis is not to directly guide the improvement of the battery design or predict the damage of the separators, but to focus on improving the accuracy of the mechanical model of the separator.

The detailed objectives can be divided into three major parts

1) To propose a research method to optimise the uniaxial tensile experiment to improve the accuracy of the mechanical property measurements for thin film samples.
2) To correlate macro-scale deformation to the meso-scale phenomenon (e.g. porosity).
3) To develop a reliable constitutive material model and material parameter calibration method, which can cover finite-strain viscoelastic behaviour for separators.

The scope, methodology and inter-relationships among various parts of the thesis are shown in Figure 1-4 to cover the aim and objectives.

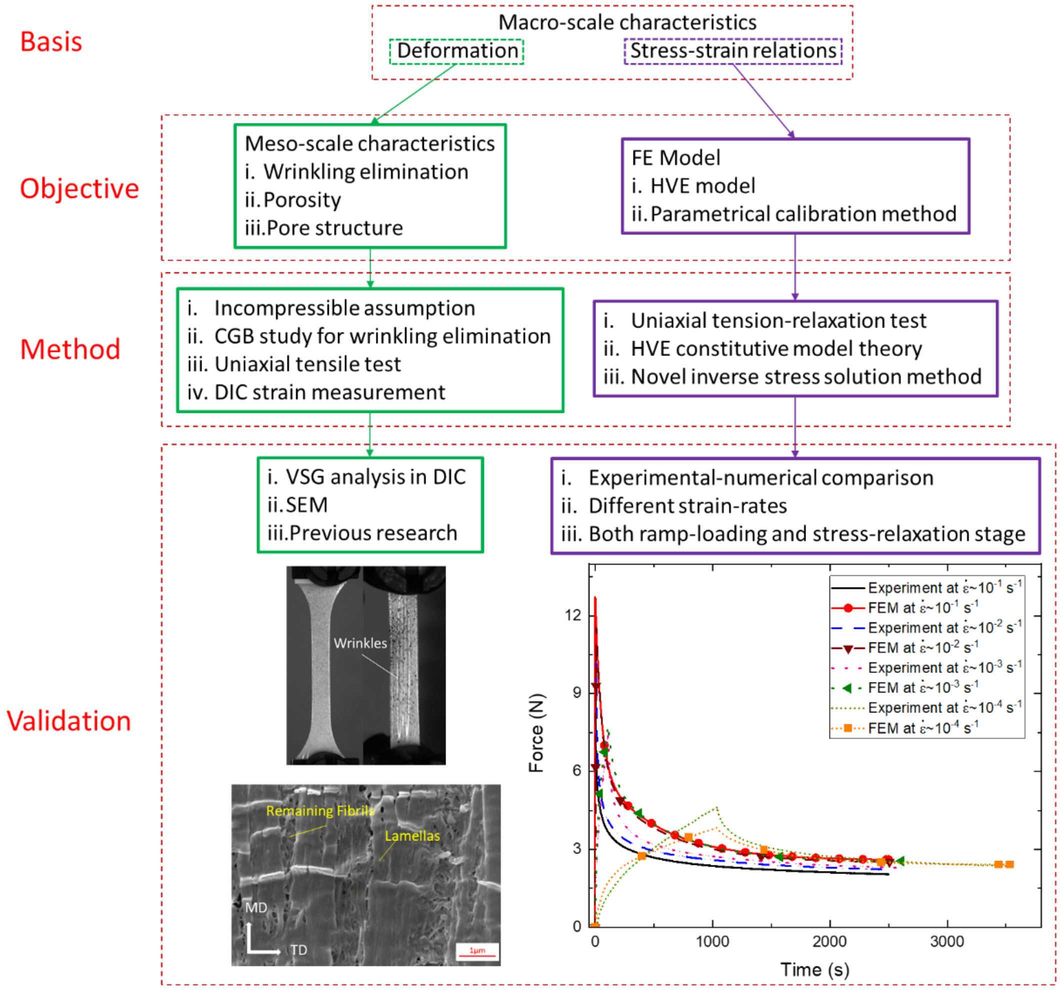

Figure 1-4 The scope of the thesis. ‘CGB’ represents critical geometric boundary; ‘DIC’ represents digital image correlation; ‘VSG’ represent virtual strain gauge; ‘HVE’ represents hyper-viscoelastic; ‘FE’ represents finite element.

1.3 Outline of the thesis

This thesis is divided into seven chapters, which are organised according to the scope introduced in Figure 1-4. This research is featured by connecting the meso-scale characteristics of separators to their macro-scale characteristics (e.g. porosity-strain relation). Then, the research focuses on the description of the mechanical behaviours of separators at the macro-scale level by developing a material characterisation method, including a viscoelastic finite-strain constitutive model and parametrical calibration method.

Chapter 1 presents an introduction of the background, motivation, aim, objectives and the scope of the thesis.

In Chapter 2, a thorough literature review, which includes the mechanical properties of the separators and the experimental, theoretical and modelling methods that are relevant to this research, is presented. The review firstly introduces the previous studies that focus on the mechanical properties of the separators under different conditions, from both time-independent and time-dependent perspectives, respectively. Then, by identifying the limitations of the outcomes from previous studies, the methodologies, which could help address these limitations but are currently used for other materials, are also reviewed.

In Chapter 3, as the wrinkling can adversely affect the measurement in the uniaxial tensile test, a dogbone geometry and a numerical method via finite element (FE) modelling are proposed for thin film structure samples (e.g. separators). A geometry-related formula is concluded and used for the subsequent mechanical experiment of the separators.

In Chapter 4, a uniaxial tensile test is designed, based on the research outcome from Chapter 3, and conducted for four different types of commercial separators. With the help of the 3D digital image correlation (DIC) technique, the proposed method for eliminating the wrinkling in Chapter 3 is also validated here. From the experimental results measured by 3D DIC, various mechanical properties (e.g. stress-strain relations, Poisson’s ratio) can be determined. In addition, the dependence of the meso-scale parameter (porosity) on the deformation of separators is also determined by theoretical and characterisation methods.

In Chapter 5, according to the phenomenon of nonlinear elasticity in finite-strain deformation observed in the experiment in Chapter 4, a finite-strain viscoelastic model, termed hyper-viscoelastic (HVE) model, is proposed, which is suitable for the large deformation of isotropic separators. The parametrical calibration methods for the HVE model used in past studies and newly proposed in this research are presented. Then, the HVE models are calibrated with experimental results based on three parametrical calibration methods. Lastly, the validation of the HVE model is demonstrated using experimental results within a finite-strain at various nominal strain-rates.

In Chapter 6, the intrinsic connections among various parts of the work presented in Chapter 3 to Chapter 5, as well as their limitations, are discussed. The potential applications of this PhD research to the study of the safety issues of liquid electrolyte batteries are also discussed.

In Chapter 7, an overall summary and main conclusions are drawn based on this research work. The future research outlooks are also commented on and suggested.

2 Literature Review

2.1 Introduction

As introduced in Chapter 1, the separator is a permeable porous membrane made of insulation materials, which is placed between anode and cathode to prevent short circuit while allowing the transport of ionic charge carriers. Once the temperature goes too high, the pores will shut down to prevent further electrochemical activity and thermal runaway (Chung et al. 2009), which can lead to a harmful consequence. In order to meet the safety requirements of separators used in batteries, a number of factors need to be considered, as shown in Table 2-1.

Table 2-1 Key factors and requirements for separators used in commercial batteries (Arora and Zhang 2004, Zhang 2007, Lee et al. 2014, Deimede and Elmasides 2015).

Key Factors		General requirements
Geometric factors	Thickness	<25 μm
	Porosity	40%~60%
	Pore size	<1 μm
Permeability	Gurley value	<0.025 s/μm
	Macmullin number	<8
Wettability	Electrolyte absorption ability	Wet out rapidly and completely
Mechanical strength	Tensile strength	>98 MPa
(for 25 μm thick separators)	Puncture strength	>300 g/mil
Stability	Chemical stability	Long-term stable in batteries
	Thermal stability	<5% shrinkage after 60 min at 90 °C environment in both MD (machine direction) and TD (transverse direction)
	High-temperature stability	Can prevent electrodes from contacting each other even under high-temperature condition
	Dimensional stability	Can lay flat and not curl at the edge, even exposed to the electrolyte
Shutdown performance		Effectively stops ionic transport between the electrodes once the temperature goes too high (~130 °C)

[a] The puncture strength (g/mil) means a gram-force per 0.025 mm thickness, which means 300 g/mil ≈ 117 N/mm (Baldwin et al. 2010).

Previously, researchers or the industry only considered the ultimate tensile strength as the key mechanical property of separators. Therefore, in the early battery studies, the electrochemical behaviours (e.g. charge-discharge performance (Djian et al. 2007), ionic conductivity (Landesfeind et al. 2016)) of various electrode materials (Wu et al. 2003, Howard and Spotnitz 2007) were the most concerned, whereas the mechanical behaviours of separator were usually less considered. However, since the LIB fire accidents in EVs caused by unknown thermal runaway were increasing in recent years (Wang et al. 2012, Eisensteine 2017) and the damage of separator is most suspected as the reason for such accidents, its mechanical properties have received great attention and require more in-depth research (Orendorff 2012).

This chapter focuses on the review of the key knowledge and the research development of the mechanical properties of separators. As most separators studied in previous studies are dry-processed and wet-processed separators, the mechanical properties of these two separator types will be the focus of this review. Firstly, the consequence caused by the deformation and damage of separators will be reviewed. Then, the time-independent and time-dependent (i.e. viscoelasticity) mechanical properties are reviewed, respectively. Furthermore, the review will also include two relevant issues, i.e. a constitutive model in large deformation and viscoelasticity, and the numerical method for wrinkling phenomenon. Finally, the problems and outstanding issues in the available literature will be outlined to justify the necessity of this research.

2.2 Influence of deformed separators in batteries

In previous studies, the influence of the separator, which has been subjected to mechanical abuse, on batteries can be mainly divided into two types, i.e. the deformed separator and the damaged separator. For the latter, the damaged separator usually suffers from severe mechanical abuse, and a crack or visible fracture can be observed (Yuan et al. 2020, Zhu et al. 2020). The damaged area of the separator will no longer prevent the physical contact between electrodes, which will cause internal short circuit and even thermal runaway (Roth et al. 2007, Santhanagopalan et al. 2009, Ramadass et al. 2014). For example, Santhanagopalan et al. (2009) inserted a nickel particle between electrodes to simulate the electrode contact due to the separator damage, and found that temperature increased due to short circuit.

For the deformed separators, since the separator does not have a direct electrochemical reaction with other components in the battery, the deformed separator that has not been damaged will only affect the ionic transport (Cannarella and Arnold 2013). This influence of the deformed separators on batteries has been studied on two different scales, i.e. microscale and macroscale.

At the microscale level, the geometric characterisation method, e.g. X-ray-microscopy-based microstructure reconstruction (Finegan et al. 2016, Xu et al. 2020) or SEM-based microstructure reconstruction (Lagadec et al. 2016, Lagadec et al. 2018c, Zhu et al. 2018b), can be used to understand the ionic movement through the pores, as shown in Figure 2-1. Here, ‘TTD’ represents the through-thickness direction.

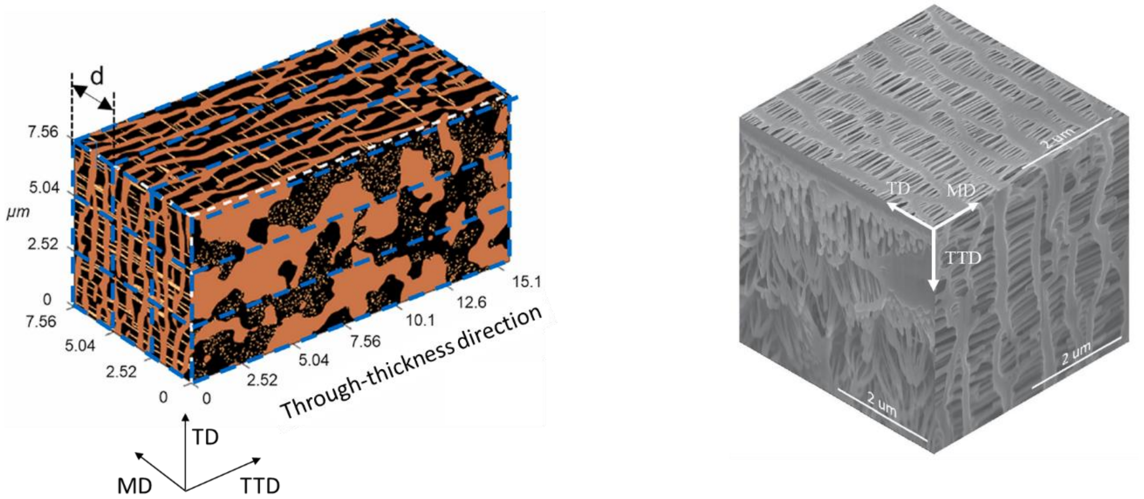

(a) (b)

Figure 2-1 The illustration of the microstructure of separator reconstructed by (a) X-ray microscopy (adapted from Xu et al. 2020) and the focused ion beam (FIB) SEM (adapted from Zhu et al. 2018b).

This ionic movement can be expressed using the tortuosity of the separator τ (Tye 1983), which is theoretically defined by the ratio of the length of a pore to the thickness of the separator, i.e.

$$\tau = l_{pore}/h_{sep} \tag{2.1}$$

where l_{pore} is the path length of the ion through the pore between two surfaces and h_{sep} is the thickness of the separator, which is illustrated in Figure 2-2. Therefore, from the microstructure of the separator, the average tortuosity of the separator can be calculated using the average of the path length and the thickness (Matyka et al. 2008, Wiedenmann et al. 2013, Lagadec et al. 2018a). It should be noted that in the previous studies and the following context, the tortuosity of the separator is actually an average tortuosity.

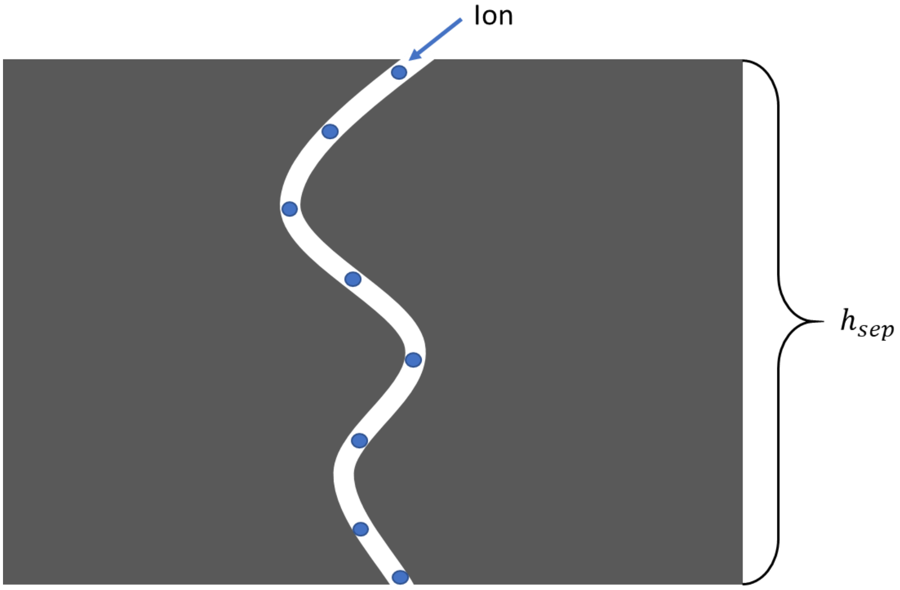

Figure 2-2 The illustration of the concept of the geometrical tortuosity.

However, it is impossible to conduct an in-situ mechanical test for the separator to observe how the microstructure is affected, as the sample used for X-ray microscopy is too small (Finegan et al. 2016), and the new fibrils created during the loading process is too vulnerable to the electric beam from the SEM (Zhu et al. 2018b). To overcome these difficulties, Xu et al. (2017) firstly developed a 2D microstructure FE model for Celgard 2400 separator by processing the 2D SEM images, and then developed a new 3D microstructure reconstruction approach using X-ray computed tomographic data and 2D microstructure model (Xu et al. 2020). The correlated 3D microstructure model can be used to simulate the microstructure variation and predict the tortuosity of the separator under mechanical abuse.

At the macroscale level, the MacMullin number or the tortuosity of the separators (Patel et al. 2003) is the most commonly used property to describe the influence of deformed separators on the function of battery. The MacMullin number N_M can be expressed as

$$N_M = k_{el}/k_{sep} \tag{2.2}$$

where k_{el} is the ionic conductivity of the electrolyte solution and k_{sep} is the effective ionic conductivity of the electrolyte immersed separator. The SI-based unit (i.e. the International System of Units) of conductivity is Siemens per meter (S/m). For the tortuosity, it is impossible to measure the geometric change of the microstructure at a macroscale level. Therefore, the tortuosity is usually combined with porosity into a 'diffusibility' or 'effective relative diffusivity' value, which can be given by (Kramer et al. 2008, Tjaden et al. 2016)

$$\frac{\Phi}{\tau} = \frac{D_{eff}}{D_{bulk}} \tag{2.3}$$

where Φ is the porosity, D_{eff} and D_{bulk} denote the effective and bulk diffusion coefficients, respectively. In the field of battery research, the term on the right side in Eq. (2.3) can be expressed as $D_{eff}/D_{bulk} = k_{sep}/k_{el} = 1/N_M$ (Djian et al. 2007). Therefore, the relationship between MacMullin number and tortuosity of the separator is given by

$$N_M = \frac{k_{el}}{k_{sep}} = \frac{\tau}{\Phi} \tag{2.4}$$

Based on this relationship, the tortuosity or MacMullin number of the separators can be obtained by assembling a simple capacitor (i.e. single or multi-layer separators sandwiched by two same metal electrodes), then measuring its ionic conductivity or ionic resistivity (i.e. the inverse of conductivity) by Electrochemical Impedance Spectroscopy (EIS) (Landesfeind et al. 2016). For instance, Cannarella and Arnold (2013) conducted an in-situ compression test by assembling a pouch capacitor with 32 electrolyte-immersed separator layers sandwiched by two foil electrodes and established a Bruggeman power-law function to describe the relationship between porosity and tortuosity of the deformed separators.

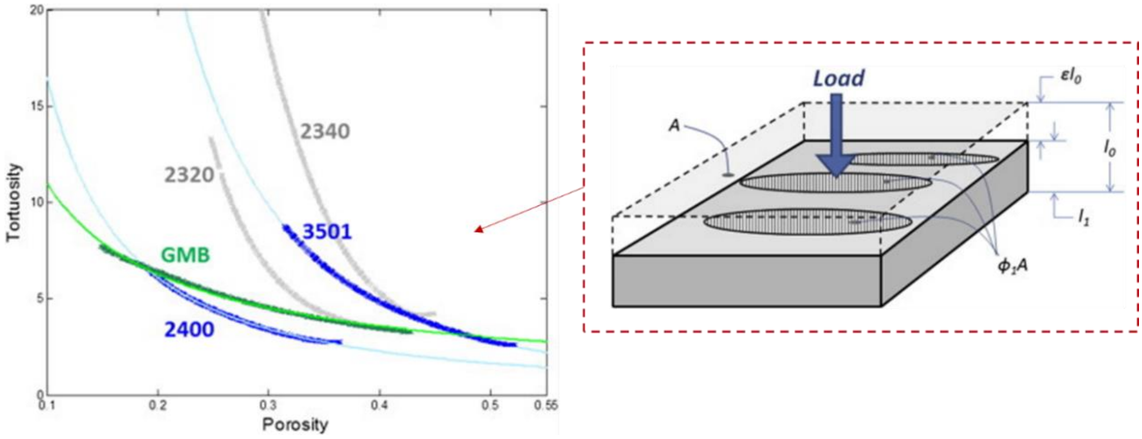

Figure 2-3 The relationship between the tortuosity and the porosity caused by out of plane compression for different types of separators (adapted from Cannarella and Arnold 2013).

Besides tortuosity, in the case of out-of-plane compression, the deformed separators may also suffer a pore closure (Li et al. 2014, Zinth et al. 2014). The local pore closure area can lead to lithium plating and lithium dendrite (Lee et al. 2014, Cannarella and Arnold 2015, Zhao et al. 2019). Lithium plating is a phenomenon that the metallic lithium forming on the graphite anode, caused by the amount of lithium ions arriving at the negative electrode surface exceeds the amount of lithium ions that can be intercalated (Zinth et al. 2014). Then, the metallic lithium can be deposited in the form of dendrites, which are sharp and can easily pierce or penetrate the separator (Li et al. 2014). Therefore, these localised lithium plating and lithium dendrite can deteriorate the reliability and durability of batteries (Liu et al. 2016b), or even worse, penetrate/damage the separator and connect positive and negative electrodes, leading to short circuit and thermal runaway (Xiong et al. 2020b, Lai et al. 2021).

2.3 Time-independent mechanical properties of separators

2.3.1 Tensile mechanical property

Usually, researchers investigated the tensile mechanical property of the common commercial separators by dividing them into two types, i.e. dry-processed separator and wet-processed separator. For either dry- or wet-processed separators, the isotropic or anisotropic mechanical behaviours are primarily determined by the stretching method used in manufacturing, which was introduced in Chapter 1. For the dry-processed separators, even though there are both uniaxial (Johnson and Wilkes 2001, 2002a, b) and biaxial stretching methods (Zhang et al. 2017b, Ding et al. 2019a) in the industry, the former has been more successful to date, and has attracted more attentions in the study of its mechanical properties. For the wet-processed separators, a relatively isotropic behaviour can be found (Arora and Zhang 2004, Zhang et al. 2016a, Lagadec et al. 2018c) as the biaxial stretching techniques are commonly adopted in the manufacturing process (Arora and Zhang 2004, Lagadec et al. 2018b). As a result, the dry-processed separators manufactured by uniaxial stretching method have a slit-like pore structure, which is mainly formed by the TD (transverse direction) oriented lamellas and the MD (machine direction) oriented fibrils between lamellas, as shown in Figure 1-3(a) and (b). On the other hand, pores in wet-processed separators are formed by unoriented fibrils of different sizes, as shown in Figure 1-3(c) and (d).

By reviewing the previous studies, the tensile mechanical properties of commonly used dry-processed separators are summarised in Table 2-2. The data source and the measurement method are also presented in a footnote.

Table 2-2 Mechanical properties of commonly used commercial dry-processed separators.

Separator	Composition	Thickness (μm)	Porosity (%)	Orientation	Young’s modulus (MPa)	Ultimate strength (MPa)
Celgard 2400	PP[a]	25[a]	41[a]; 32 (Djian et al. 2007)	MD	873[b] (Chen et al. 2014); 659[b] (Xu et al. 2016); 843[c] (Sheidaei et al. 2011); 955[cd] (Yan et al. 2018a)	139[a]; 146.5 (Chen et al. 2014)
				TD	502[b] (Chen et al. 2014); 253[b] (Xu et al. 2016); 430[c] (Sheidaei et al. 2011); 485[cd] (Yan et al. 2018a)	13.7[a]; 13.4 (Chen et al. 2014)
Celgard PP2075	PP[a]	20[a]	48[a]	MD	1279.1[bd] (Kalnaus et al. 2017)	195.2[a]
				TD	224.4[bd] (Kalnaus et al. 2017)	14.7[a]
Celgard 2340	PP/PE/PP[a]	38[a]	45[a]	MD	528[b] (Xu et al. 2016)	160[a]; 164 (Xu et al. 2016)
				TD	167[b] (Xu et al. 2016)	16.2[a]; 17.7 (Xu et al. 2016)
Celgard 2325	PP/PE/PP[a]	25[a]	39[a]; 41 (39-PP layers, 44-PE layer) (Finegan et al. 2016)	MD	935[b] (Chen et al. 2014); 887.6[bd] (Kalnaus et al. 2017); 460.66[b] (Hao et al. 2020)	166.7[a]; 175.2 (Chen et al. 2014)
				TD	510[b] (Chen et al. 2014); 344.4[bd] (Kalnaus et al. 2017); 165.21[b] (Hao et al. 2020)	14.7[a]; 14.7 (Chen et al. 2014)
Celgard H1612	PP/PE/PP[a]	16[a]	44[a]	MD	505.47[b] (Hao et al. 2020)	196.1[a]
				TD	205.18[b] (Hao et al. 2020)	15.7[a]

[a] Data taken from the manufacturers' product brochures.

[b] Young’s modulus obtained from uniaxial tensile tests.

[c] Young’s modulus obtained from DMA tests.

[d] DIC method used in strain measurement.

In Table 2-2, it shows that some data obtained in different studies may vary. For the ultimate tensile strength, the data obtained from various studies are close to the ones taken from the manufacturers' product brochures. However, significant differences can be found in Young’s modulus among previous studies, where either uniaxial tensile test or dynamic mechanical analysis (DMA) were used. By comparing the experimental methods and results in those studies, three potential reasons can be discussed to explain these differences, i.e.

(i) There are measuring errors on strain due to possible slippery in the clamps, leading to the over-calculated strain in the gauge area when the crosshead displacement is used to calculate the strain (Xu et al. 2016). To increase the accuracy of strain measurement, Kalnaus et al. (2017) and Yan et al. (2018a) used the digital image correlation (DIC) method to improve the measurement accuracy, as shown in Figure 2-4.

(ii) The separators are highly sensitive to the loading speed and the environmental temperatures due to their intrinsic viscoelastic characteristics (Yan et al. 2020), which will be elaborated in Section 2.4.

(iii) The methods used to determine Young’s modulus are different, e.g. Chen et al. (2014) used a strain range of 0-0.5% while Kalnaus et al. (2017) defined the elastic regime up to a strain of 1.5%.

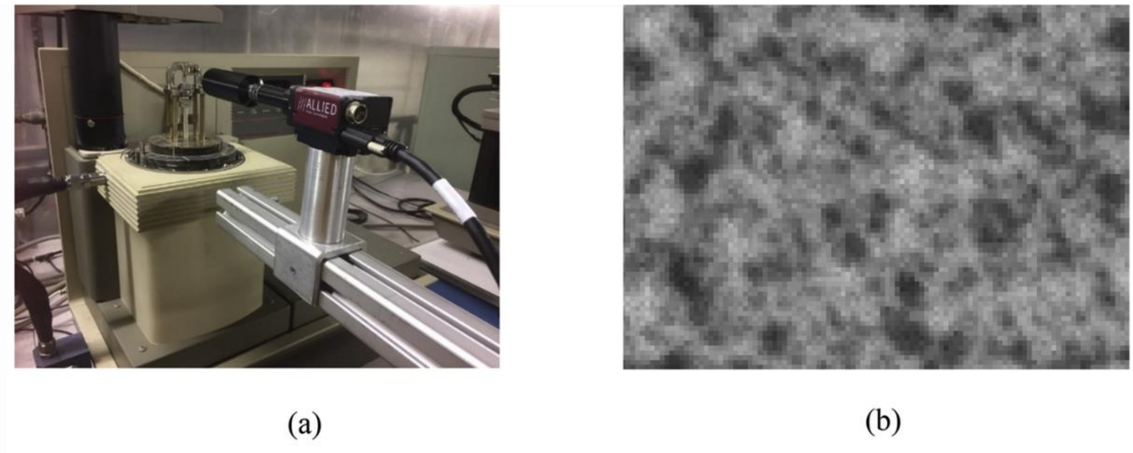

Figure 2-4 (a) The typical 2D DIC set-up; (b) A typical speckle pattern on the sample surface for DIC tracking (Yan et al. 2018a).

It is evident that, among these commercial dry-processed separators, apparent anisotropy is observed, which is reflected by the differences of both Young’s modulus and ultimate tensile strength in MD and TD. To characterise the anisotropy, several constitutive models and numerical models have been proposed. Liu et al. (2016a) firstly proposed the use of Hill 48 yield criterion to define the anisotropic yield surface, which can be expressed as

$$\sigma_y = \sqrt{F_H(\sigma_{22}-\sigma_{33})^2+G_H(\sigma_{33}-\sigma_{11})^2+H_H(\sigma_{11}-\sigma_{22})^2+2L_H{\tau_{23}}^2+2M_H{\tau_{31}}^2+2N_H{\tau_{12}}^2} \tag{2.5}$$

where F_H - N_H are six coefficients that can be determined experimentally. For the anisotropic elasticity, Yan et al. (2018a) defined the anisotropic plane-stress conditions for a typical dry-processed separator (i.e. Celgard 2400) via establishing an in-plane compliance matrix as following

$$\begin{bmatrix} 1/E_{11} & -v_{21}/E_{22} & 0 \\ -v_{12}/E_{11} & 1/E_{22} & 0 \\ 0 & 0 & 1/G_{12} \end{bmatrix} \tag{2.6}$$

where E_{11} and E_{22} are the Young's moduli in the MD and TD, and v_{ij} is the Poisson's ratio that corresponds to the contraction in direction j while the extension is applied in direction i. G_{12} is the shear modulus.

In the finite element (FE) software LS-DYNA, material cards MAT-126 and MAT-36 are the most commonly used models for anisotropic materials. MAT-126 is usually used in simulating aluminium honeycombs and crushable foam materials with anisotropic behaviour, and Zhang et al. (2016a) tried to use this material model to simulate the dry-processed separators, which was successfully validated by the experimental results (including load-displacement relationship and the deformation images). MAT-36, which is used for modelling sheets made from anisotropic material under plane-stress conditions, was investigated with the help of the 3D DIC technique (Kalnaus et al. 2018a). It is found that MAT-36 can not only match the load-displacement results but also predict the oval deformation pattern under out-of-plane indentation. Both material cards need the data input of the tensile experimental results (engineering stress-strain relations) of the sample in 0°, 45° and 90° directions.

On the other hand, there is less research on wet-processed separators. Chen et al. (2014) and Zhang et al. (2016a) reported the tensile mechanical properties of wet-processed separators, which are summarised in Table 2-3.

Table 2-3 Mechanical properties of several commercial wet-processed separators.

Separator	Composition	Thickness (um)	Porosity (%)	Orientation	Young's modulus (MPa)	Ultimate strength (MPa)
Toray-V20CFD (Chen et al. 2014)	Unknown polyolefin	20	42	MD	675	65.3
				TD	781	72.6
Toray-V20EHD (Chen et al. 2014)	Unknown polyolefin	20	43	MD	696	102.7
				TD	823	127.8
Teijin-Lielsort (Chen et al. 2014)	PE substrate coated with fluorine-based compound	15	-	MD	733	120.6
				TD	622	90.1
Unknown ceramic-coated separator (Zhang et al. 2016a)	Al/PE/Al	16(2/12/2)	37	MD	-	~180[e]
				TD	-	~150[e]

[e] Estimated from literature.

From their research, it can be noted that wet-processed separators have similar Young's modulus and tensile strength in both orientations due to the biaxial stretching process during manufacturing. On the other hand, the manufacturers usually adjust the manufacturing process of the wet-processed separator to achieve the targeted material parameters, e.g. porosity, thickness, ultimate strength. This means that even for the same type of wet-processed separators, their mechanical performances may be different due to different manufacturers or specific requirements. Besides microporous polymer membranes, the tensile mechanical properties of other types of separators (e.g. non-woven separators (Zhang et al. 2016a, Kalnaus et al. 2017), cellulose separators (Xie et al. 2019)) have also been investigated, but they are outside the scope of this research and will not be further illustrated.

2.3.2 Compressive mechanical property

As the thickness of the separator is too thin to be tested in conventional out-of-plane compressive tests, multiple separator layers (≥32) were usually stacked together to address the difficulties (Cannarella et al. 2014, Gilaki and Avdeev 2016, Zhang et al. 2016a). In order to guarantee the measurement accuracy of such thin samples, it is better to use a linear variable differential transformer (Cannarella et al. 2014, Basu and Debnath 2019) or a virtual live extensometer (Pan and Tian 2016) to track the displacement of the loading crosshead. For the dry-processed separators, it is noted that the effective compressive modulus in through-thickness direction (TTD) is similar to the one under tension in TD. Cannarella et al. (2014) believed that it is because dry-processed separators have experienced strain hardening in MD during the manufacturing but not in the other two directions. Thus, the mechanical properties of separators were assumed to be the same in TDD and TD by researchers in numerical simulations (Liu et al. 2016a, Zhang et al. 2016a). However, the stacked separator samples may easily trap air between the layers and the boundary conditions, which is different from those in real batteries and may cause a measuring error. To address this challenge, Yan et al. (2018b) developed a capacitance-based displacement measurement system, which is sufficiently sensitive to measure the deformation of two layers of separator in TTD under compression. A similarity in the mechanical properties between the TTD and TD was also observed in their experiment (Yan et al. 2018b), which shows consistency with previous studies using the multiple layers stacked samples method (Cannarella et al. 2014, Gilaki and Avdeev 2016, Zhang et al. 2016a).

As a porous membrane material, it is clearly seen that the monolayer dry-processed separator under out-of-plane compression undergoes three stages, namely the linear elastic stage, the plateau stage and the densification stage (Cannarella et al. 2014, Zhang et al. 2016a, b, Yan et al. 2018b, Sarkar et al. 2019, Lee and Kim 2020), showing similar characteristics to foams/cellular solids (Li et al. 2006, Sun and Li 2015), as shown in Figure 2-5(a) and (b). Interestingly, other types of separators (e.g. dry-processed tri-layer separator) show less characteristics that are similar to cellular/foams solids under compression. Ding et al. (2020a) later found out that these distinctive compression responses were determined by the difference in the cross-section microstructure of the separators. They pointed out that due to the uniaxial stretching process in the manufacturing, parallel lamellae align along the TTD (Figure 2-5(d)), similar to the microstructure in the TD of the surface. These lamellae, acting like a columnar structure, have good resistance to the compression load in TTD, resembled as the cell wall structure in cellular materials (Flores-Johnson et al. 2008). This phenomenon also reveals the underlying reason for the similarity of mechanical properties in the initial stage (before yield points) between the TTD and the TD. For the separators manufactured by the biaxial stretching process, no matter it is dry- or wet-processed, no apparent yield phenomenon can be detected (Figure 2-5(c)) due to the absence of the cell-wall-like lamellae (Figure 2-5(d)).

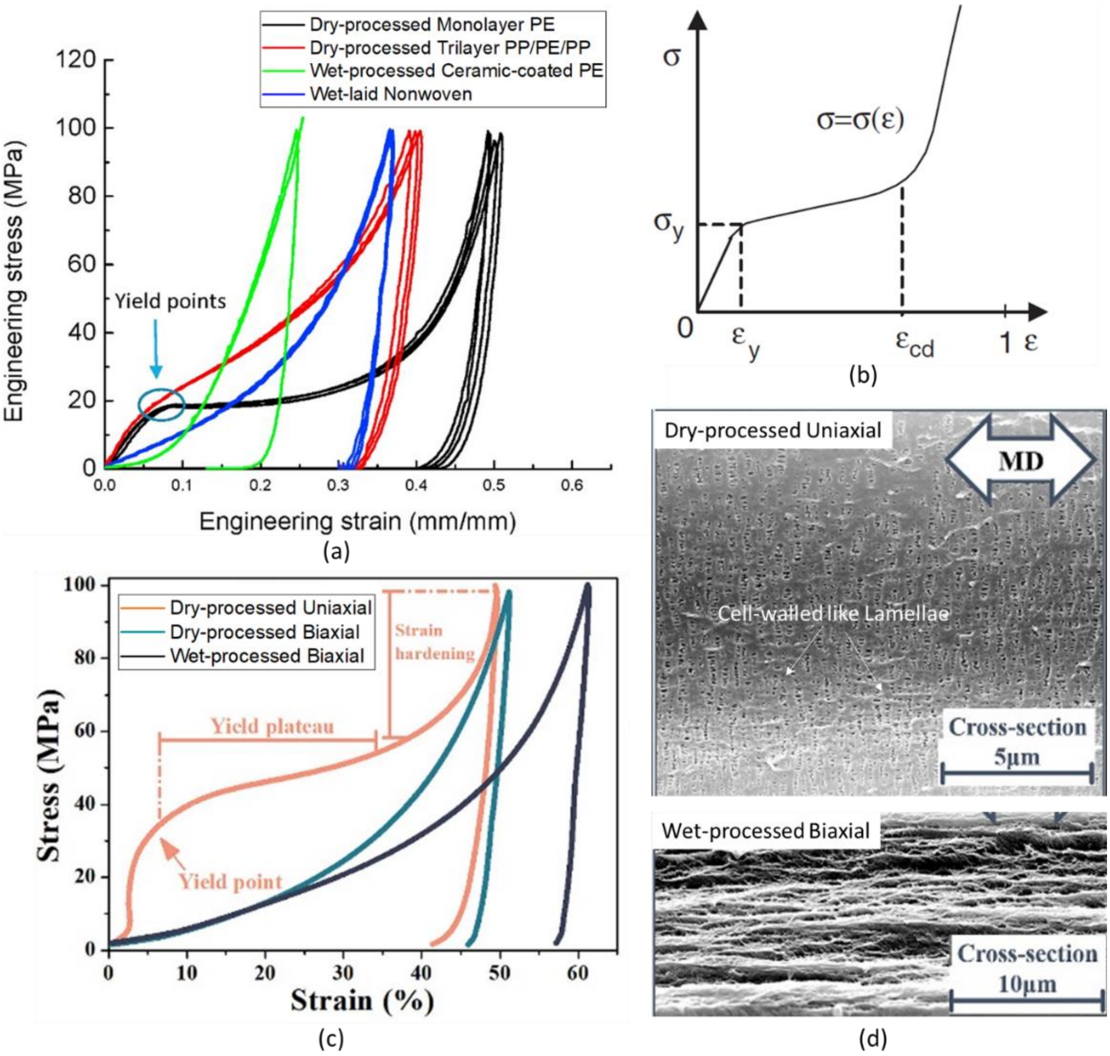

Figure 2-5 Compression stress-strain curves in TTD of (a) various types of commercial separators (adapted from Zhang et al. 2016a), (b) a typical cellular material (adapted from Li et al. 2006), (c) separators manufactured by different stretching methods (adapted from Ding et al. 2020a), and (d) the SEM images of the cross-section of separators (adapted from Ding et al. 2020a).

2.3.3 Strain-rate, temperature and fluid-immersed dependence

Due to the particularity of the porous microstructure, the strain-rate, temperature and solvent-immersed dependent behaviours of separators that are easily affected by each other, were usually studied together.

The strain-rate is usually defined as the derivative of the strain with respect to time, i.e. $\dot{\varepsilon} = d\varepsilon/dt$. Generally, different strain-rates would not change Young's modulus of materials but only affects the flow stress (or yield stress) (Hu et al. 2015). For a separator in dry condition, however, it is found that both the modulus and flow stress increase linearly with the logarithm of strain-rate under either tension or compression. In the study done by Gor et al. (2014), they found that this phenomenon is actually attributed to the viscoelastic properties of materials, but in order to establish a time-independent constitutive model, they used effective Young's modulus to represent the viscoelastic properties. Therefore, according to (Gor et al. 2014, Kalnaus et al. 2018b), the strain-rate dependence of effective Young's modulus and flow stress can be expressed as

$$E(\dot{\varepsilon}) = E_0 + C_E \lg(\dot{\varepsilon}/\dot{\varepsilon}_0) \tag{2.7}$$

$$\sigma^{flow}(\dot{\varepsilon}) = \sigma_0^{flow} + C_\sigma \lg(\dot{\varepsilon}/\dot{\varepsilon}_0) \tag{2.8}$$

where E_0 and σ_0^{flow} correspond to the reference strain-rate $\dot{\varepsilon}_0$; and C_E and C_σ are rate strengthening coefficients.

On the other hand, the mechanical properties of separators were also found to be weakened by the increasing temperature (Avdeev et al. 2013). Kalnaus et al. (2018b) extended the existing strain-rate model with considering temperature factors, and Eqs. (2.7) and (2.8) can be extended to

$$E(\dot{\varepsilon}, T) = (E_0 + C_E(T) \lg(\dot{\varepsilon}/\dot{\varepsilon}_0))e^{-\gamma_E(T-T_0)} \tag{2.9}$$

$$\sigma^{flow}(\dot{\varepsilon}, T) = \left(\sigma_0^{flow} + C_\sigma(T) \lg(\dot{\varepsilon}/\dot{\varepsilon}_0)\right)e^{-\gamma_\sigma(T-T_0)} \tag{2.10}$$

where rate strengthening coefficients $C_E(T)$ and $C_\sigma(T)$ become a linear temperature-related function $k_0 + k_1 T$ ($k_{0,1}$ should be determined separately for C_E and C_σ), while constants γ_E and γ_σ are temperature softening coefficients.

In practical applications of liquid electrolyte batteries (e.g. LIBs), separators are not in a dry condition and are always immersed in a solution containing electrolyte salt in an organic solvent (Arora and Zhang 2004). Based on this, researchers tried to test separators immersed into different kinds of fluid, e.g. water, DMC (Dimethyl carbonate) and LIB electrolyte (e.g. 1.1M LiPF6 in EC/DMC where EC is Ethylene carbonate) (Avdeev et al. 2013, Cannarella et al. 2014, Gor et al. 2014, Xu et al. 2016, Yan et al. 2018b), and distinct differences have been found in tension and compression. For tension properties, the water could slightly strengthen the separators (Xu et al. 2016) while the other two solutions weaken the separators (Cannarella et al. 2014). Similar to separators in dry condition, the effective Young's modulus and flow stress increase linearly with the logarithm of strain-rate. In the case of compression, however, this similar phenomenon only appears in quasi-static condition, while sudden increases of effective Young's modulus and flow stress have been found in fluid-immersed separators when $\dot{\varepsilon} \gtrsim 10^{-3}$ (Cannarella et al. 2014). Gor et al. (2014) attributed this unusual phenomenon to the combination of 'poroelasticity' and viscoelasticity (i.e. the compression response of a porous elastic material filled with viscous fluid), and then developed a constitutive model for separators in such conditions in a small strain range.

2.4 Viscoelastic behaviour of separators

As a membrane totally or mainly composed of polymeric materials, viscoelasticity is critical and should inevitably be considered. The separator may experience viscoelastic creep under membrane stress caused by the volume expansion of active materials (Lagadec et al. 2018b), resulting in increased internal electrical resistance and significant reduction of electrical capacity (Peabody and Arnold 2011). For the viscoelasticity of these polymeric materials, there are two commonly used research methods, namely stress relaxation test and creep test (Bosnjak et al. 2020). The classic linear viscoelastic constitutive models used to investigate the respective tests above-mentioned are the generalised Maxwell model (Yan et al. 2020) and the Kelvin–Voigt model (Sheidaei et al. 2011). The schematic diagrams of the two viscoelastic models can be seen in Figure 2-6, where the springs and dashpots represent the elastic and viscous parts of the material, respectively. The stress-strain relationships of the two models can be expressed as

$$\text{Generalised Maxwell Model:} \quad \sigma(t) = \int_0^t G(t-s)\frac{d\varepsilon(t)}{dt}ds \tag{2.11}$$

$$\text{Kelvin–Voigt Model:} \quad \varepsilon(t) = J(t)\sigma_0 + \int_0^t J(t-s)\frac{d\sigma(t)}{dt}ds \tag{2.12}$$

where s is a time variable, σ_0 is the initial stress (i.e. stress at time zero); $G(t)$ and $J(t)$ are stress relaxation shear modulus and creep compliance, respectively, which have a relationship of $G(s)J(s) = 1/s^2$ (this can be interconverted by Laplace transform) (Sheidaei et al. 2011). Both $G(t)$ and $J(t)$ are usually expressed in a Prony series form that

$$G(t) = G_\infty + \sum_{i=1}^{N} G_i e^{-t/\tau_i^R} \tag{2.13}$$

$$J(t) = J_0 + \sum_{i=1}^{N} J_i \left(1 - e^{-t/\tau_i^R}\right) \tag{2.14}$$

where G_∞ and J_0 are respectively the long-term relaxed (shear) modulus and the instantaneous compliance; G_i and J_i are the fitted relaxation constant and the creep constant, respectively; $\tau_i^R = \eta_i/G_i$ and η_i are respectively the retardation times and the coefficient of viscosity for the ith term; N is the number of viscoelastic branches (i.e. Prony terms).

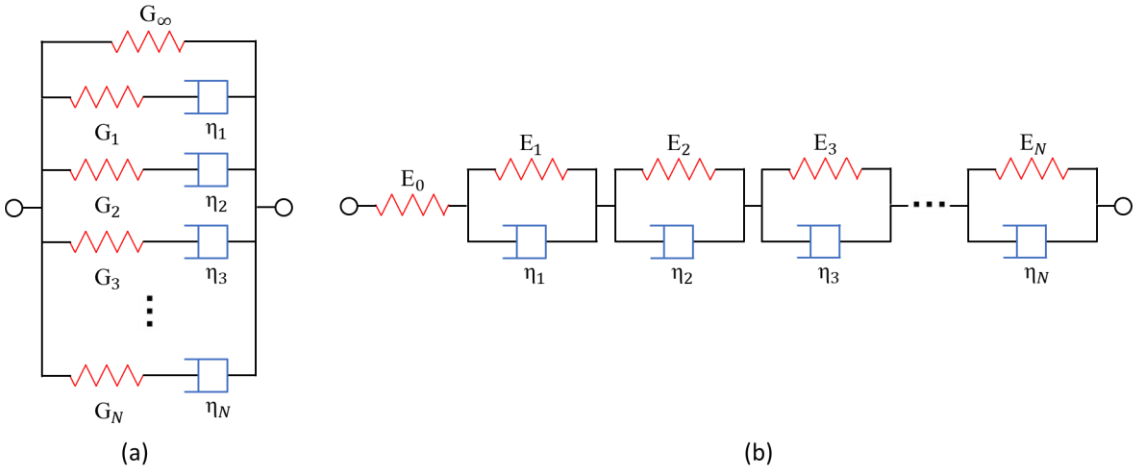

Figure 2-6 Schematic diagrams of (a) generalised Maxwell model, and (b) Kelvin–Voigt model.

To explore the viscoelasticity, separators were usually measured by DMA in a tensile creep mode (Sheidaei et al. 2011, Xu et al. 2016, Yan et al. 2018a). By applying each stress level in the creep test, the creep compliance can be determined by $J(t) = \varepsilon(t)/\sigma$ (Yan et al. 2018a), and the creep constant J_i can be fitted using experimental results $J(t)$. By far, orthotropic viscoelastic models have been well developed for separators, but only for uniaxial stretched dry-processed separators in a small strain limit, i.e. less than a strain of 0.01 (Yan et al. 2018a, Yan et al. 2020).

Besides, the viscoelastic behaviours of separators are sensitive to temperatures (Yan et al. 2020). According to the time-temperature superposition principle (TTSP) (Ferry 1980, Ward and Sweeney 2004), Wu et al. (2014) extended the viscoelastic model by considering temperature factors, and Eq. (2.13) can be extended to

$$G(t,T) = G_\infty + \sum_{i=1}^{n} G_i\, e^{-t/\left(a_T(T)\tau_i^R\right)} \tag{2.15}$$

where $a_T(T)$ is obtained through constructing a master curve at a reference temperature from a set of curves measured under an isothermal condition over a range of temperatures (i.e. 25–60 °C in their investigation). Although the G_∞ and G_i in Eq. (2.15) were considered as a constant in (Wu et al. 2014), it is still possible that G_∞ and G_i can be changed by the temperature outside this range.

2.5 Hyper-viscoelastic model for solids under large deformation

As mentioned above in Section 2.4, even though the viscoelastic behaviour was investigated in previous studies, the viscoelastic model is only applicable to small strain deformation. However, in the case of mechanical abuse (e.g. crush, drop or other mechanical loading) in actual battery application, the maximum principal nominal strain of the separator can reach around 0.3 before the occurrence of short circuit (Yuan et al. 2020), which means a constitutive model with large strain capability would be beneficial to the research on the safety issue of batteries or separators.

To address the limitation of the viscoelastic model under finite-strain condition, a hyper-viscoelastic (HVE) model that combines hyperelastic model with viscoelastic model (i.e. generalised Maxwell model) was developed (Johnson et al. 1994) and has been widely used in FEM software such as Abaqus (Sunderland et al. 2001, Grujicic et al. 2009, Briody et al. 2012, Wei and Olatunbosun 2016, Abaqus 2019). The HVE model is able to describe the mechanical behaviours of materials such as rubber (Ghoreishy 2012, Wei and Olatunbosun 2016, Fazekas and Goda 2019) and polymer (Grujicic et al. 2009, Briody et al. 2012, Shojaeiarani et al. 2019) under various strain-rates within the range of viscoelasticity (Fazekas and Goda 2019, Shojaeiarani et al. 2019). For the hyperelastic model, a number of empirical and semi-empirical hyperelastic models have been developed (Nicholson and Nelson 1990), e.g. Neo-Hookean model, Mooney–Rivlin model (Mooney 1940, Rivlin 1948), Ogden model (Ogden 1986), Yeoh model (Yeoh 1993) and Marlow model (Marlow 2003). Unlike traditional elastic constitutive models, the hyperelastic models are described in terms of a 'strain energy potential' $W_e(\varepsilon)$, which defines the strain energy stored in the material per unit of reference volume as a function of the strain (Abaqus 2019). For the viscoelastic model, the generalised Maxwell model is often used (see Figure 2-6(a)) to describe the time-dependent stress response influenced by viscoelasticity.

When the framework of the HVE model is established, three commonly used methods were usually adopted to determine the HVE parameters.

The first method is the so-called two-step method (Grujicic et al. 2009, Briody et al. 2012, Wei and Olatunbosun 2016), where the hyperelastic parameters and the viscoelastic parameters are determined separately. This method is popular as it is easy to determine the parameters by a tension-relaxation test, as shown in Figure 2-7. For the hyperelastic part of the HVE model, the corresponding parameters can be determined by the short-term ramp-loading data (e.g. uniaxial tensile loading, biaxial tensile loading, etc.), as the ascending region shown in Figure 2-7(b). For the viscoelastic part of the HVE model, the Prony series parameters can be determined by the normalised relaxation stress-time curve $\sigma(t^R)/\sigma(t_0^R)$ where $t^R = t - t_0^R$ represents the relaxation time, t_0^R is the time when the relaxation begins and $\sigma(t_0^R) = \sigma_0$.

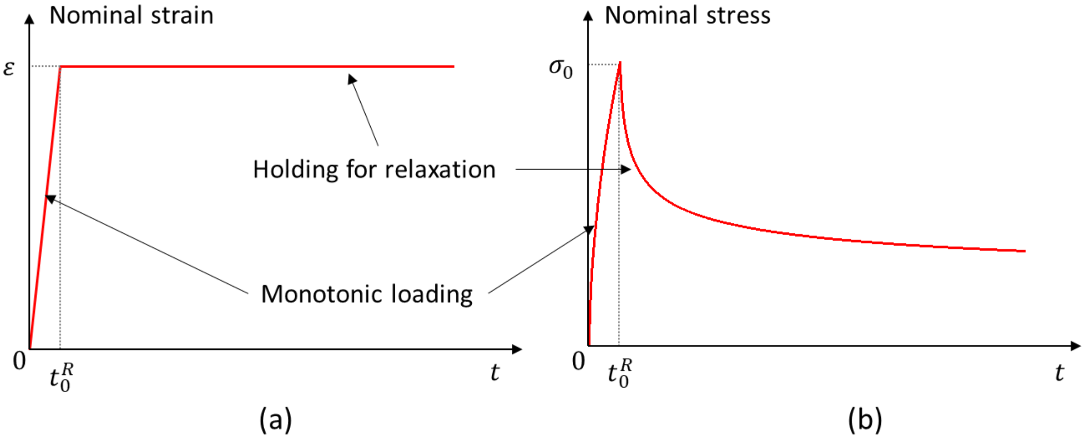

Figure 2-7 The schematic of (a) the representative curves of nominal strain vs. time, and (b) nominal stress vs. time in the tension-relaxation experiment.

However, it should be noted that the hyperelastic model is a time-independent model. When the hyperelastic model is used in the HVE model, the stress-strain relations should be the ‘instantaneous’ stress-strain relations. It is noted that the term ‘instantaneous’ stress can be understood as the stress without relaxation (or viscoelastic effect), which can be obtained from the summation of the overall stress increment from all elastic springs in a generalised Maxwell model in responding to a finite strain increment within an infinitesimal time. Meanwhile, the viscoelastic model is used to describe the time-dependent variation of the initial ‘instantaneous’ stress, which can be understood as the collective stress responses of all Maxwell cells in a generalised Maxwell model. Therefore, the application of the two-step method may cause significant errors as the hyperelastic model determined directly from the experimental ramp-loading data includes the viscoelastic effects, and the initial relaxation stress at the beginning of the relaxation stage is not the ‘instantaneous’ stress response generated instantly (Kossa and Berezvai 2016), as shown in Figure 2-8 (Fazekas and Goda 2018).

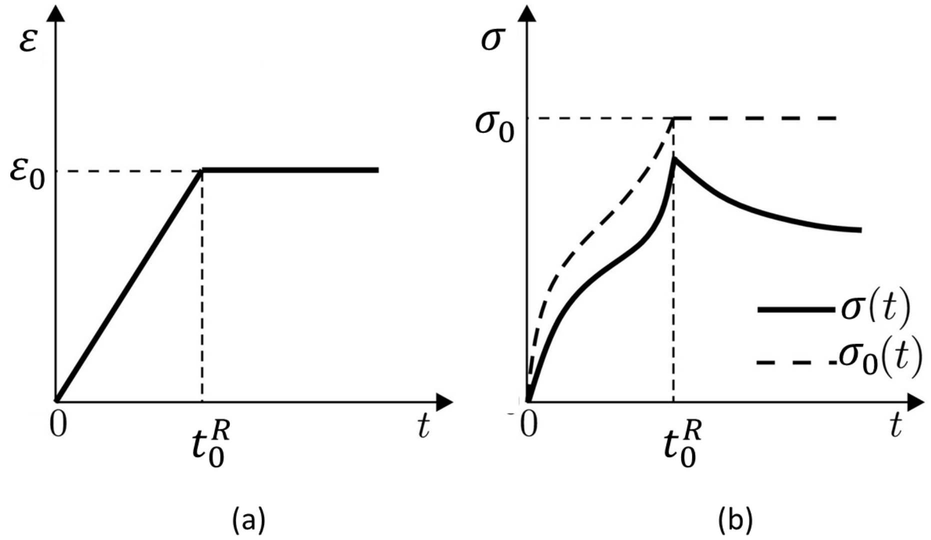

(a) (b)

Figure 2-8 (a) The strain (stretch) history, and (b) the instantaneous/total Cauchy stress response ($\sigma_0(t)$) in case of uniaxial tension-relaxation test with realistic ramp loading where $\sigma(t)$ is the measured uniaxial stress (adapted from Fazekas and Goda 2018).

The second method, which is a FEM-aided calibration method, was proposed. Ghoreishy (2012) proposed to use the ramp-loading tensile data (i.e. there is no relaxation stage) under a high strain-rate of $\sim 0.08 s^{-1}$ to establish the instantaneous time-independent hyperelastic model. Then, an inverse optimisation program is performed for the calibration of the Prony series parameters using HVE-based FE modelling results until the numerical results have good agreement with the ramp-loading test results of samples in other geometrical shapes. Then Shojaeiarani et al. (2019) used this method to test the sample with the same geometry at various strain-rates rather than changing the geometry of the sample shape. They first determined the initial hyperelastic parameters using the two-step method by conducting a short-term monotonic uniaxial loading test (i.e. ramp-loading test at a loading rate of 10 mm/min), and then optimised both hyperelastic parameters and viscoelastic parameters synchronously by minimising the error between the measured and computed force in both ramp-loading and stress-relaxation stages. It has been shown that this method enables the HVE model to capture the experimental stress-strain relations at the ramp-loading stage under various strain-rates, as shown in Figure 2-9 (Shojaeiarani et al. 2019). However, no stress-relaxation prediction at different loading strain-rates via FE simulation was shown by this method in their investigation.

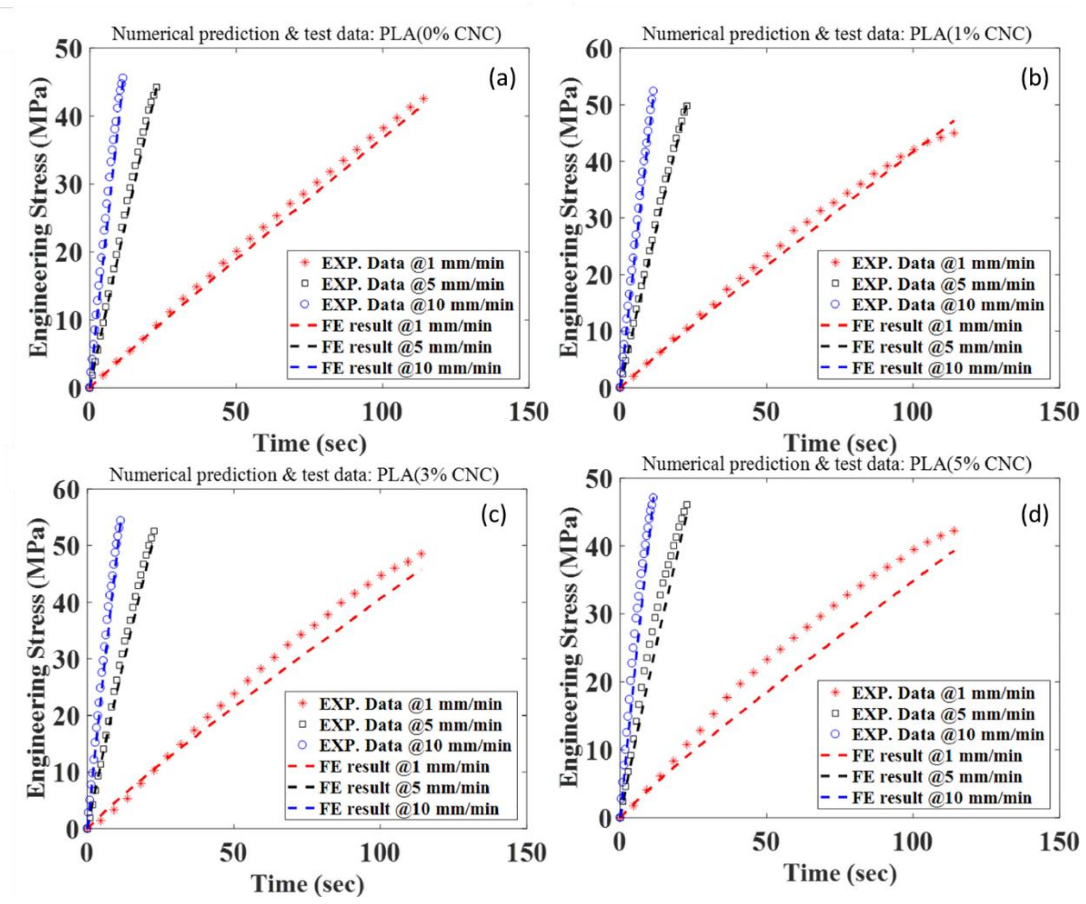

Figure 2-9 The comparison of experimental data and HVE model predictions of the tensile stress at three different loading speeds of 1, 5, and 10 mm/min for (a) pure Poly(lactic acid), and for pure Poly(lactic acid) containing b) 1%, c) 3%, and d) 5% of cellulose nanocrystals reinforcements (Shojaeiarani et al. 2019).

However, the FEM-aided calibration method requires large scale computations by continuously optimising the HVE parameters, lacks physics explanation, and cannot describe the relaxation process (Nayyar 2013) due to the time of the experimental data at high loading strain-rates is far less than the time required in the relaxation stage.

To address the limitation of both above-mentioned methods, the stress solution calibration method was proposed. Goh et al. (2004) proposed a finite time-increment formulation in the numerical implementation algorithm to calibrate the incompressible HVE parameters based on the known experimental values of stress, strain, and time obtained from the tension-relaxation tests at various strain-rates. In this method, the instantaneous stress-strain relationship can be described by a selected hyperelastic model, whereas the time-dependent stress variation with strain can be calculated by deducting the viscoelastic effects determined by the Prony series parameters. By using an optimisation algorithm (e.g. generalised reduced gradient (GRG) nonlinear algorithm) to minimise the errors between the calculated and the experimentally-measured time-dependent stress in both ramp-loading and stress-relaxation stages, all the parameters (including hyperelastic and viscoelastic parameters) can be calibrated and determined. Later, based on the calibration method proposed by Goh et al. (2004), Fazekas and Goda (2018, 2019) extended the method to cover both the incompressible and highly compressible HVE material model and different experimental loading modes (i.e. uniaxial/biaxial tension or compression, simple shear, pure shear, etc.). It should be noted that in (Fazekas and Goda 2018), experimental data in both ramp-loading and stress-relaxation stage under a constant loading strain-rate were used in calibration and validation, while in (Fazekas and Goda 2019), only ramp-loading data under various loading strain-rates were used to be calibrated and validated. This method (i.e. stress solution method) has two limitations, i.e. (1) relaxation performance can only be predicted accurately for ramp loading with constant strain-rate, even though the parameters were calibrated using both ramp-loading and stress-relaxation stages; (2) there are too many parameters to be optimised, i.e. both hyperelastic and viscoelastic parameters.

2.6 Wrinkling phenomenon of separator

Thin films, or membrane structures, commonly exist in both nature and engineering, and the occurrence of wrinkling, caused by nearly ‘zero bending stiffness’ (Wong and Pellegrino 2006b) due to its very thin thickness, is undesirable in some specific circumstances. Battery components, especially the separator, are easily wrinkled in mechanical tests or even inside the battery. Moreover, the literature of studies related to this kind of stretch-induced wrinkling will also be included in the review.

2.6.1 Stretch-induced wrinkling in uniaxial tensile test

Typically, in order to obtain a material's mechanical properties (e.g. Young's modulus, Poisson's ratio, yield stress, etc.), the most common test method is the uniaxial tensile test (Boresi 2003). However, for the mechanical tensile test of separators, which is a typical thin film structure material, the wrinkling phenomenon occurs frequently in previous studies (Zhang et al. 2016a, Zhu et al. 2018c, Hao et al. 2020). Even though the wrinkling pattern and the out-of-plane displacement can be measured by 3D Digital Image Correlation (DIC) (Nayyar et al. 2014, Dai et al. 2020), Zhu et al. (2018c) pointed out that the strain on the transverse direction measured by the virtual extensometer (i.e. a function in commercial DIC software) will be significantly affected due to the wrinkling. In addition, the calculated Poisson's ratio will be greater than what it should be, as shown in Figure 2-10. Therefore, the transverse strain obtained under this wrinkling circumstance may not be qualified to be determined as the intrinsic material property.

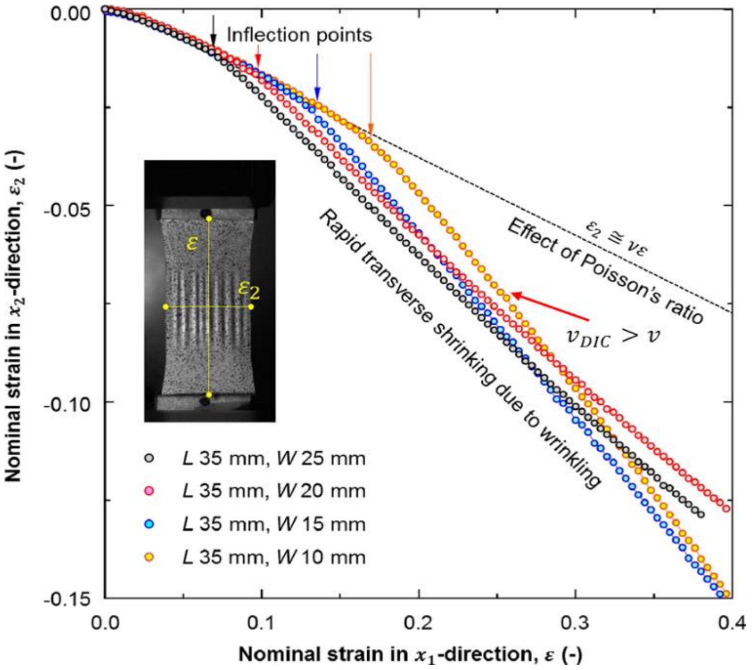

Figure 2-10 Transverse strain vs. longitudinal strain curves for uniaxial tensile tests of a single layer PP dry-processed separator in TD by testing samples with four aspect ratios. The yellow arrow lines denote the virtual extensometer in DIC software. The figure is adapted from (Zhu et al. 2018c).

2.6.2 Potential wrinkling inside the battery

In most studies, the causes of the wrinkling phenomenon inside the battery can be divided into the thermal stability aspect (Arora and Zhang 2004, Lee et al. 2014) and the mechanical stability aspect (Hirayama and Takahashi 2016, Nomura and Kataoka 2018).

In the thermal stability aspect, the separator should satisfy the requirement that it must not shrink significantly and must not wrinkle during the high-temperature drying process (Arora and Zhang 2004, Lee et al. 2014). It means that commercial separators that are allowed to be sold on the market hardly experience wrinkles due to temperature rise in daily use. For example, Love (2011) performed thermomechanical tests and analyses for several types of commercial separators, only separators under certain conditions showed significant shrinkage, but no obvious wrinkling was observed.

Practically, wrinkling could happen either in the process of assembling the separator into the battery or when the separator is deformed inside the battery. It should be noted that the main difference between these two cases is that the separator inside the battery is subjected to constraints in out-of-plane direction, i.e. other battery components, e.g. electrodes and the shell case, to prevent the wrinkling. However, no relevant study can be found.

2.6.3 Development of wrinkling research for thin film structure

Among previous wrinkling studies, the stretching of a rectangular sample by two fully-clamped ends (i.e. uniaxial tensile test using rectangular shape samples) is one of the most concerned wrinkling cases for 2D membranes, as shown in Figure 2-11. Theoretically, buckling is a state of unstable equilibrium usually caused by a compressive load over the critical value. However, in the uniaxial tensile test, the loading object should be in a uniaxial tension state. Therefore, it is necessary to find why buckling occurs in such a loading condition.

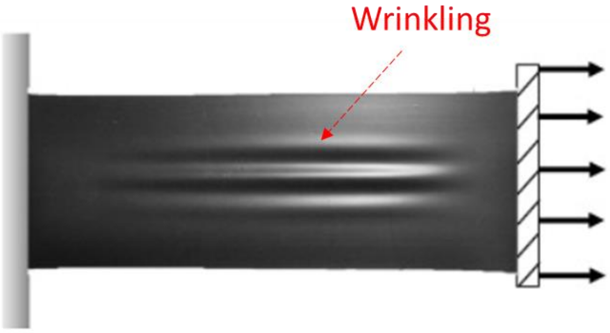

Figure 2-11 An optical image of a wrinkled polyethene sheet under uniaxial tension boundary condition (adapted from Nayyar et al. 2011).

To figure out this, Tension Field Theory was firstly proposed based on zero bending stiffness by Wagner (1931) nearly a century ago, which has been further developed into analytical (Mansfield 1969, 1970, 1981, Lin and Mote Jr 1996, Coman 2007, Iwasa 2017) and experimental (Iwasa 2018) methods to understand the wrinkling phenomenon. For the simple case that a rectangular thin plate uniaxially stretched by two fully-clamped ends, the critical load (or the critical longitudinal stress) for the occurrence of wrinkling in the such thin plate is usually obtained by the modifications of Euler buckling analysis (Wong and Pellegrino 2006b, Timoshenko and Gere 2009).

With the help of FE numerical simulation, Friedl et al. (2000) revealed that some local areas of the rectangular thin film are in a transverse compressive state during the uniaxial tensile test (see in Figure 2-12), even though the compressive stress value is very small. This transverse compressive stress is actually caused by the combination of Poisson’s ratio effect and the constraints of the transverse movement near the clamping ends. Moreover, as the thickness of the thin film is too small to withstand the compressive load, the bending stiffness can be regarded as approximately zero. Therefore, Friedl et al. (2000) proposed a buckling coefficient to simplify the solution of the critical longitudinal stress for the onset of wrinkling, which is suitable for all isotropic linear-elastic materials.

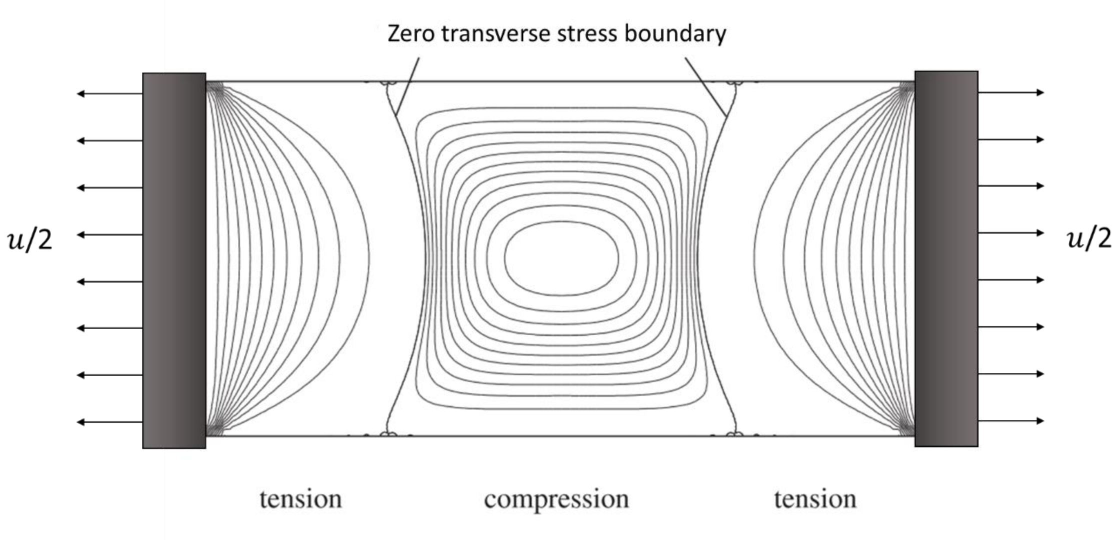

Figure 2-12 The isolines of the transverse stresses of a rectangular thin film with aspect ratio of 2, under uniaxial tension boundary condition (adapted from Friedl et al. 2000).

Besides analytical methods, the eigenvalue analysis using the numerical method can also be used to predict the critical load (Nayyar 2010, Huang et al. 2020) and critical wrinkling mode (Martins et al. 2020). However, the eigenvalue analysis is limited to a linear system (Abaqus 2019). Therefore, the bifurcation analysis (or the post-buckling analysis) is important when nonlinearity (e.g. material nonlinearity, geometric nonlinearity, boundary nonlinearity, etc.) occurs.

For the bifurcation analysis of simple geometries (i.e. rectangular thin film), analytical methods have been proposed to obtain the approximate solutions (Jacques and Potier-Ferry 2005, Wong and Pellegrino 2006b, Steigmann 2008). However, for more complex geometries or constitutive models, nonlinear finite element analysis (FEA) is generally needed (Jacques and Potier-Ferry 2005, Wong and Pellegrino 2006c, Lecieux and Bouzidi 2010, Nayyar et al. 2011, Yan et al. 2014, Sipos and Fehér 2016, Ding et al. 2019b, Liu et al. 2019, Wang et al. 2019b, Wang et al. 2019c, Huang et al. 2020), and its effectiveness has been demonstrated experimentally (Cerda et al. 2002, Cerda and Mahadevan 2003, Lecieux and Bouzidi 2010, Dai et al. 2020). The bifurcation point can be obtained by a wrinkling evolution curve from a post-buckling FE simulation, as shown in Figure 2-13.

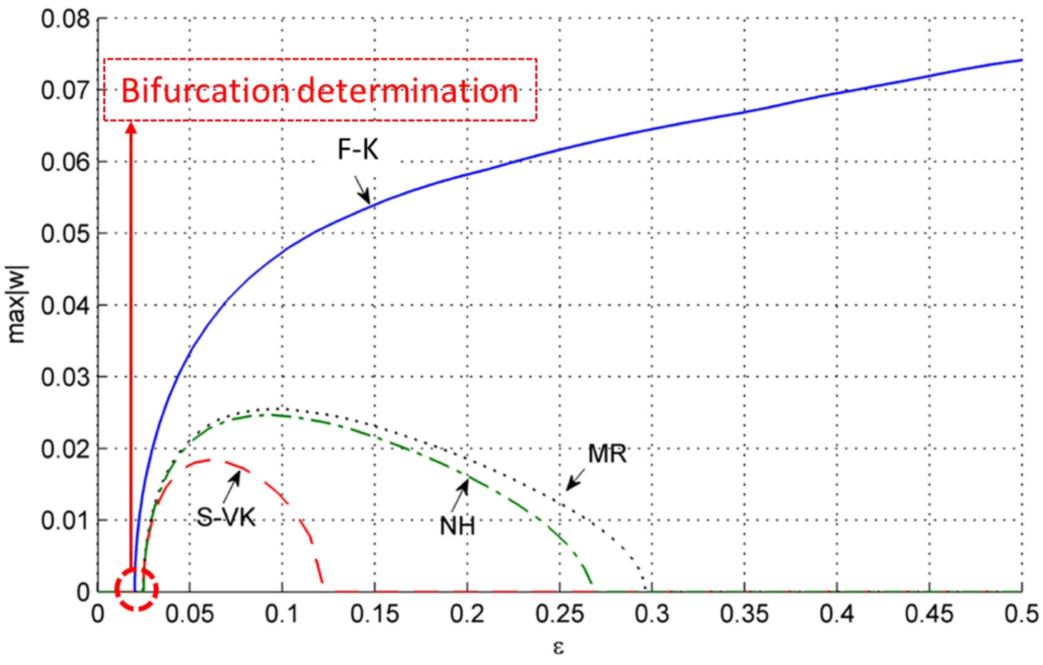

Figure 2-13 The bifurcation diagram determined by maximum out-of-plane displacement vs. strain ε (i.e. wrinkling evolution) of a case from (Li and Healey 2016). 'F-K', 'S-VK', 'NH' and 'MR' are four different constitutive models.

Cerda et al. (2002) quantitatively determined the relationship between the wrinkle wavelength and the uniaxial strain by experiment. Later, they took the amplitude of the wrinkle into consideration and realised that the occurrence of the wrinkling phenomenon is essentially dependent on the geometry (Cerda and Mahadevan 2003). Based on this observation, Puntel et al. (2011) found that, besides the geometry factors, Poisson's ratio is another factor that should be involved in estimating the wrinkle behaviours. Apart from the studies mentioned above, other numerical and experimental studies support such point of view, i.e. geometry and the Poisson's ratio are the two most important factors that determine the wrinkling behaviours of the isotropic thin film (Friedl et al. 2000, Kim et al. 2012b, Kudrolli and Chopin 2018, Fu et al. 2019, Khalil et al. 2019, Panaitescu et al. 2019, Wang et al. 2019b).

On the other hand, the classical Föppl–von Kármán (F–K) model was firstly proposed to predict the wrinkling behaviours (e.g. wavelength and amplitude) for rectangular thin film (Von Kármán 1967). However, it was found that the F-K model is applicable only to the initial post-buckling behaviour whereas the subsequent disappearance of wrinkling cannot be predicted correctly (Zheng 2009, Healey et al. 2013). To solve this problem, Healey et al. (2013) corrected and extended the classical F-K model to large deformation using a geometrically-correct-membrane model in numerical bifurcation analysis. Based on a hyperelastic material model, Nayyar et al. (2011) investigated the stress state and the bifurcation for the large deformation of rectangular thin film samples with different aspect ratios and thicknesses. They concluded that the critical condition for the occurrence of wrinkling should be evaluated numerically by post-buckling analysis instead of eigenvalue analysis due to the nonlinearity of the system. Meanwhile, they validated the scaling relationship between wrinkle behaviour and the geometry-deformation-related term observed by Cerda and Mahadevan (2003). Later, Nayyar et al. (2014) further studied the wrinkling of viscoelastic thin films using a hyper-viscoelastic model and demonstrated improved wrinkling predictions in comparison with experimental results. Li and Healey (2016) investigated the stability boundary separating the parametric space into wrinkling and non-wrinkling spaces for thin film structures with different material models. It was found that the wrinkling evolution based on the F-K model is more sensitive than that based on the hyperelastic models, but they have similar critical strain for the onset of the wrinkling. Wang et al. (2019b) recently proposed the use of the second variation of potential energy to determine its post-buckling evolution, in which it was showed that wrinkling magnitude decreases with the decrease of the Poisson's ratio and disappears completely when the Poisson's ratio is reduced to less than 0.35. Moreover, the wrinkling phenomenon in orthotropic membrane materials was successfully explained using the energy decomposition method (Zhu et al. 2018c), which was further developed mathematically into an extended F-K nonlinear orthotropic plate model (Liu et al. 2019, Yang et al. 2020). Besides the wrinkling behaviour of a rectangular thin film stretched by two fully-clamped ends, wrinkling behaviours under other boundary or loading conditions have also been investigated comprehensively by numerical and experimental methods (Tessler et al. 2005, Wong and Pellegrino 2006a, b, c, Wang et al. 2009, Lecieux and Bouzidi 2010, Huang et al. 2015, Kudrolli and Chopin 2018, Wang et al. 2018, Faghfouri and Rammerstorfer 2020, Huang et al. 2020, Li et al. 2021).

2.7 Concluding remarks

In this chapter, the mechanical properties of separators and their influence on the liquid electrolyte batteries are reviewed first. Both the fundamental knowledge and state-of-the-art research have been presented and discussed. It was found that previous studies have led to a good and comprehensive understanding of the mechanical behaviours of separators, and several constitutive models have been developed. However, there are still some limitations in the previous studies for both analytical methods and experimental methods, which need to be addressed, as shown in the following summary.

1) Poisson’s ratio, another critical mechanical property in the constitutive model, was simply regarded as 0.3 or other constants in most literature. However, due to the characteristics of porous microstructure, the Poisson’s ratio of a separator may not remain constant, like a normal material, under deformation.
2) Most studies focused on separators manufactured by uniaxially stretched dry-processed, e.g. Celgard series separators, while the wet-processed separators market grew dramatically in recent years (CCM 2017, Markets 2018). According to literature (Ding et al. 2020a), the various manufacturing methods may cause the difference not only in mechanical behaviours of wet-processed separator under compression, but also in other properties such as Poisson’s ratio, viscoelasticity, strain-rate dependence, etc.
3) Even though the comprehensive constitutive models were well developed, which can include various behaviours, e.g. orthotropic characteristics, viscoelasticity, most of them are considering elastic regime only in small-strain conditions. However, large deformation of separators under tension has been observed, and the finite nonlinear elastic regime can also be seen for most separators (Zhang et al. 2016b, a, Zhu et al. 2018b, Ding et al. 2020b), which indicates that the classical elastic-plastic model and the traditional viscoelastic model used in small strain deformation may not be suitable for the polymeric separators in this case.
4) The traditional experimental method for thin film samples (i.e. separators in this research) based on ASTM D882 may cause significant measurement errors in the TD even though the DIC technique is used.

Therefore, in addition to the literature on separators themselves, other relevant studies, which have potential to solve the limitations, are also reviewed in this chapter, i.e. hyper-viscoelastic model, and wrinkling mechanism of thin film structure. To address the limitations presented above, a comprehensive numerical-experimental-analytical study is conducted in this study and will be presented in the following chapters of this thesis.

3 Wrinkle-Free Design for Thin Film Samples in Uniaxial Tensile Tests

3.1 Introduction

As introduced in Section 2.6.1, the wrinkling that occurs during the uniaxial tensile test can adversely affect the measurement accuracy (Zhu et al. 2018c), and therefore, a method that can eliminate this influence should be studied.

In previous research, researchers commonly applied three methods, i.e. changing the boundary conditions (Iwasa 2018, Huang et al. 2020), changing the geometric parameters (e.g. increasing the length-to-width aspect ratio or reducing the width-to-thickness ratio (Nayyar et al. 2011)), or redesigning the sample geometry using topology optimisation method (Luo et al. 2017a, b), to reduce or eliminate the occurrence of wrinkling in thin film structures. Since the present research aims to reduce the adverse influence of the wrinkling on the uniaxial tensile tests of thin film materials, the proposed method should not compromise the accuracy of the tensile test measurements, which excludes the possible use of the methods proposed in (Iwasa 2018, Huang et al. 2020) for uniaxial tensile tests. Moreover, no matter how large the aspect ratio is used for the rectangular thin film sheet, wrinkling is unavoidable when the ratio of width to thickness is over around 1100 or the Poisson’s ratio is greater than or equal to 0.35 (Wang et al. 2019b). For some specific samples with very tiny thickness, their thickness may not be changed practically. Therefore, it is impossible to make the test specimens meet the requirement of the width-to-thickness ratio for wrinkling elimination (i.e. less than 1100) and the requirement of uniaxial tensile test (i.e. the specimen size is sufficiently large for uniaxial tensile test) at the same time. For the last method, Luo et al. (2017b) investigated a stress-based topology optimisation method by changing the geometry of the thin film to enable the minimum principal stress to keep positive in all membrane regions, which, however, is not suitable for uniaxial tensile test because the proposed geometrical shape cannot guarantee the uniaxial stress state.

In summary, a method proposed in this research should not only reduce the wrinkling but also enable the stress state of the sample to keep uniaxial tension. In the pilot study, the author tried to design a dogbone geometry for the sample and accidentally found that the wrinkling had been reduced, which indicated that the wrinkling phenomenon might be avoided by changing the sheet geometry from rectangular to dogbone shapes. Moreover, according to ISO 527-3:2018, the dogbone design based on this standard will not reduce the measurement accuracy, which implies that the dogbone geometry may be potentially used for the design of thin film samples that can be used for uniaxial tensile test without wrinkling. Hence, in this chapter, a critical geometric boundary (CGB) is proposed to guide the design of thin film samples and help ensure accurate measurements in uniaxial tensile tests.

In this chapter, the overall geometries and material properties of rectangular and modified dogbone-shaped thin film are described in Section 3.2, where the dogbone thin film sample is defined by three geometry-related non-dimensional numbers as independent design parameters. Numerical method is used in Section 3.3 to propose the concept of critical geometric boundary. In Section 3.4, the global bifurcation phenomenon is studied based on the parametric analyses of the three non-dimensional numbers, based on which the critical geometric boundary is determined to guide the design of wrinkle-free dogbone thin film samples in a uniaxial tensile test. In addition, the underlying mechanism of the wrinkling delay and the influences of geometric defects on the results will also be evaluated and discussed. Lastly, Section 3.5 gives the summary of this chapter.

3.2 Problem description

The schematic diagrams of both rectangular and dogbone geometries are shown in Figure 3-1. The longitudinal direction is the loading direction, i.e. x_1 direction, while the transverse direction is the direction perpendicular to longitudinal direction, i.e. x_2 direction. To distinguish the spatial direction and the material direction (i.e. MD and TD defined in Chapter 1), the terms ‘longitudinal direction’ and ‘transverse direction’ represent the spatial direction in the rest of thesis. The rectangular geometry was determined according to ASTM D882, and the dogbone geometry was designed according to ISO 527-3:2018. These two standards were proposed for the determination of the tensile properties of thin sheets and films with thickness less than 1.0 mm. The length-to-width aspect ratio L/W of the rectangular region is fixed to 5 in this study, which is recommended in the testing standard to obtain accurate stress and strain measurements. To find out how a dogbone geometry can help to reduce the wrinkling in uniaxial tensile test, two parameters, i.e. the radius R and the length D of the extended parts at two sides of the dogbone sample (the overall dogbone length is $L_t = 5W + 2D$), will be considered, and two more non-dimensional numbers $\alpha = W/R$ and $\beta = D/W$ will be introduced. The influence of the thickness h is also considered using a non-dimensional number $\gamma = W/h$. The material model used in this study is a typical incompressible linear elastic material model with $E = 18MPa$ and $v = 0.5$ (which is actually set as 0.495 in Abaqus), which will be explained later in Section 3.4.3. The boundary condition considered in Figure 3-1 is referred to the standard uniaxial tensile experiment where two individual grips are used to fully clamp the short edges of the sample and move one end in x_1 direction (the moving edge displacement is denoted by u), which has also been used in previous studies (Nayyar et al. 2011, Healey et al. 2013, Fu et al. 2019, Wang et al. 2019b, Luo et al. 2020). When the geometry of the sample is changed into dogbone geometry, the stress analysis becomes more complex. Hence, a finite element (FE) modelling using the commercial software Abaqus 2019 will be adopted to study the wrinkling phenomenon in the linear elastic regime in a uniaxial tensile test. It should be noted that all parameters investigated in this research will be discussed in non-dimensional forms.

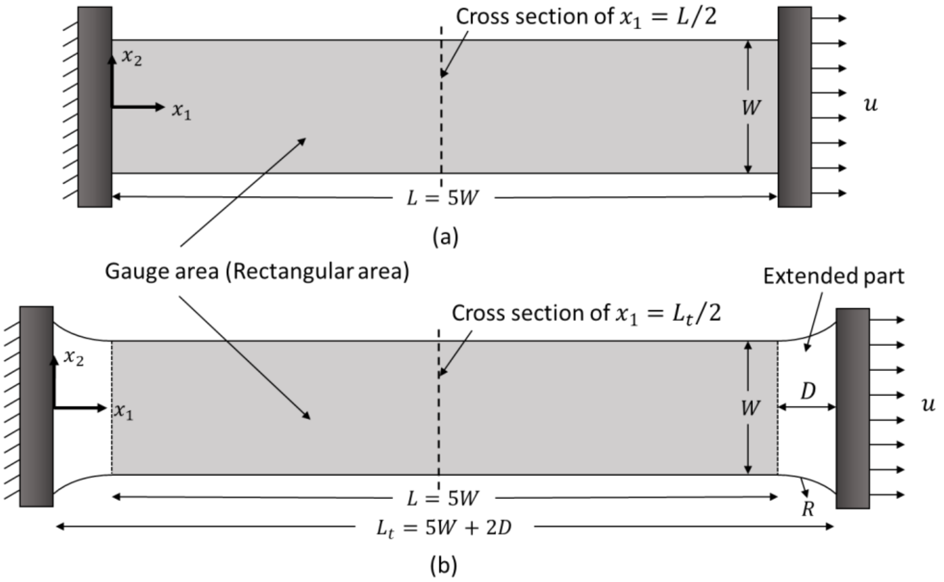

Figure 3-1 Geometry of stretched thin film samples in (a) rectangular shape, and (b) designed dogbone shape. The shadow areas of the samples are the gauge areas, and the areas outside the gauge area for the dogbone shape are the extended parts determined by R and D described by non-dimensional numbers $\alpha = W/R$ and $\beta = D/W$.

3.3 Numerical simulation

In this study, an eigenvalue buckling analysis with applying a pre-load (displacement will be given as the load here) will be carried out first, followed by a nonlinear post-buckling analysis, which has been used and validated successfully in wrinkling numerical studies for thin film structures (including various geometry and boundary conditions) (Jacques and Potier-Ferry 2005, Nayyar et al. 2011, Li and Healey 2016, Fu et al. 2019, Liu et al. 2019, Wang et al. 2019b, Huang et al. 2020). To obtain good computational accuracy, a fine mesh size of $W/100$ is used, which means that there are 100 elements along the width of the rectangular region, and the aspect ratio of each element is approximately unity (Nayyar et al. 2011, Huang et al. 2020). As a finite strain will be achieved in this study, the thin shell element S4R (4-node quadrilateral shell element with reduced integration) is used.

3.3.1 Eigenvalue buckling analysis

The eigenvalue buckling analysis is used to determine the critical buckling load of a structure when the stiffness matrix of the model becomes singular. In this study, an initially pre-stretched small displacement u_{pre} is applied to generate a perturbation, which changes the stiffness matrix from its base state before the buckling analysis (i.e. the pre-buckling stage). Unless stated otherwise, the magnitude of u_{pre} is determined to be $0.01L$, which will be further discussed in Section 3.3.2. To ensure the occurrence of the buckling mode under stretched conditions, the Lanczos method is selected here to guarantee that only positive eigenvalues can be extracted. In ‘Eigenvalue Buckling Prediction’ in Abaqus (2019), the critical displacement for the onset of buckling is obtained by

$$u_{cr} \approx u_{pre} + \lambda_e \Delta u \tag{3.1}$$

where Δu is an arbitrarily pre-set incremental displacement ($\Delta u = 0.0025L$ is used in this study); λ_e is the lowest positive eigenvalue obtained from the eigenvalue analysis, which depends on the given values of u_{pre} and Δu. Since the critical displacement u_{cr} is uniquely determined by the original buckling problem, the second term in Eq. (3.1) (i.e. $\lambda_e \Delta u$) is a constant for the given u_{pre}. Due to the potential geometric nonlinearity caused by the non-negligible geometry change, which could happen before the buckling of structure, the critical displacement may not be predicted accurately by Eq. (3.1) because Eq. (3.1) is only valid for a linear system (Abaqus 2019), as shown later in Section 3.3.4. In the eigenvalue buckling analysis, it is found that all the rectangular and dogbone models have two same lowest eigenvalues, i.e. a symmetric eigenmode and an antisymmetric eigenmode, as shown in Figure 3-2 and Figure 3-3, which was also observed in the previous study (Martins et al. 2020). It should be known that notation U3 in the figures is the normalised out-of-plane displacement of the mode shapes. Therefore, in the following study, these two modes will be used to introduce the initial imperfection.

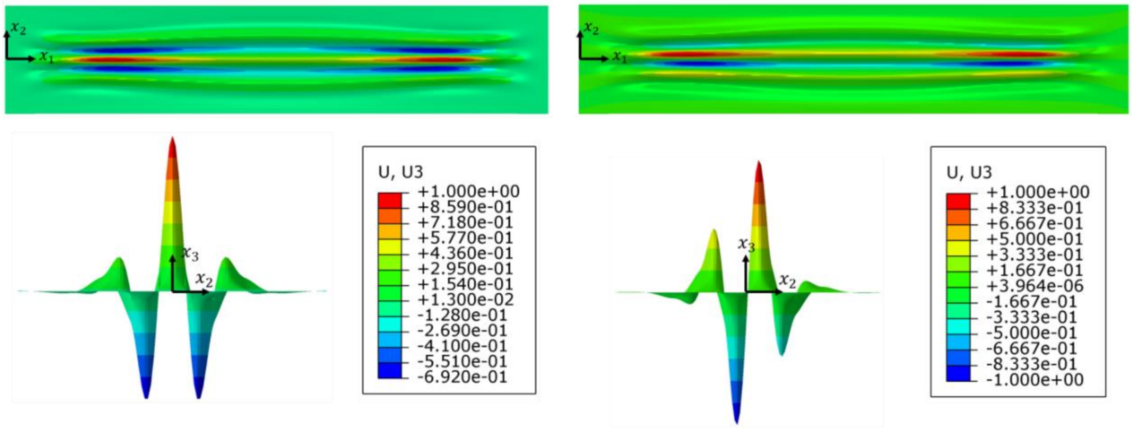

(a) (b)

Figure 3-2 (a) Symmetric eigenmode, and (b) antisymmetric eigenmode corresponding to the same lowest eigenvalues of the rectangular geometry with $\gamma = 1500$.

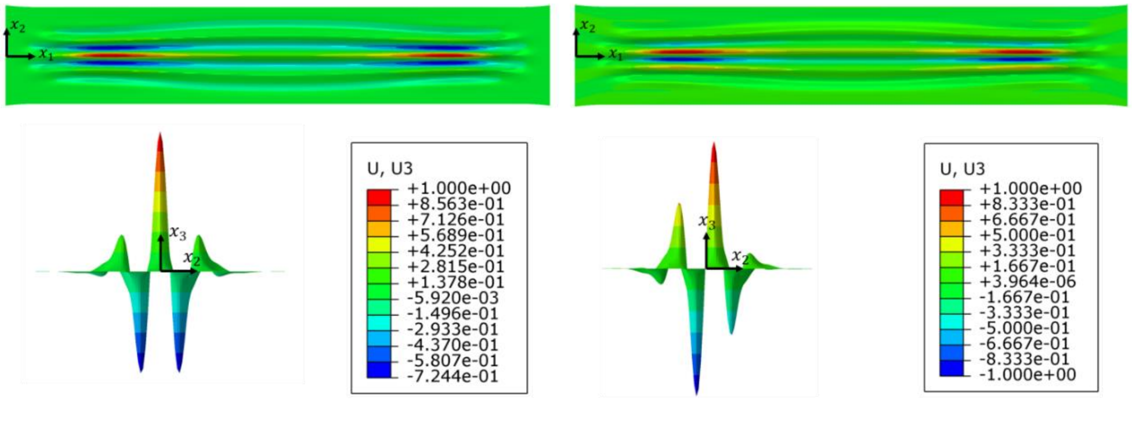

(a) (b)

Figure 3-3 (a) Symmetric eigenmode, and (b) antisymmetric eigenmode corresponding to the same lowest eigenvalues of the dogbone geometry with $\alpha = 0.4,\ \beta = 0.3,\ \gamma = 1500$.

3.3.2 Post-buckling analysis

Because the wrinkling occurs during stretching, which may cause unstable and discontinuous response at the point of buckling (i.e. the bifurcation point), the modified Riks method with considering initial geometric imperfections is also used in this study to find the static equilibrium states during the nonlinear post-buckling bifurcation. By introducing initial geometric imperfections w^0, a linear superposition of eigenmodes is added to the perfect geometry to create the perturbed geometry before the start of a post-buckling analysis, which has a form of

$$w^0 = \sum_{s=1}^{N} \eta_s \mu_s \tag{3.2}$$

where N is the number of eigenmodes, μ_s is the sth eigenmode and η_s is the associated imperfection scale factor. In this study, $N = 2$ is taken, i.e. the first two eigenmodes will be used as stated at the end of Section 3.3.1. In the post-buckling evolution, strain ε is the nominal longitudinal strain defined by the gauge elongation (i.e. $\Delta L/L_0$), which is usually used in a uniaxial tensile test. To trace the bifurcation path, a maximum arc length increment of 1% of the estimated total arc length is used in the simulation. Non-dimensional term $|w|_{max}/h$ is used to describe the evolution of the wrinkle amplitudes where $|w|_{max}$ is the maximum out-of-plane displacement in the rectangular area. The critical buckling strain ε_{cr} in the post-buckling analysis is determined by the bifurcation point where $|w|_{max}/h$ starts a sudden increase. To unify the standard of the determination of the critical buckling strain, the strain of $|w|_{max}/h = 0.1$ is ε_{cr}.

Since the small geometric perturbation may change the initial stiffness matrix of the model, it is necessary to investigate the influence of imperfection sensitivity on post-buckling evolution (Cao and Hutchinson 2012). In this study, following factors are considered, i.e. the scale factor η, the eigenmode Φ obtained from various pre-stretched displacements and the parallel execution in Abaqus/Standard.

Same scale factors $\eta = \eta_1 = \eta_2$ are set as $0.0001h$, $0.001h$ and $0.01h$ for both rectangular and dogbone geometry. The first two eigenmodes used here are taken from eigenvalue analyses with $u_{pre} = 0.01L$. The results of the examined cases are shown in Figure 3-4, in which $|w|_{max}/h = 0.1$ represents the start of bifurcation and the corresponding strain is the critical buckling strain ε_{cr}.

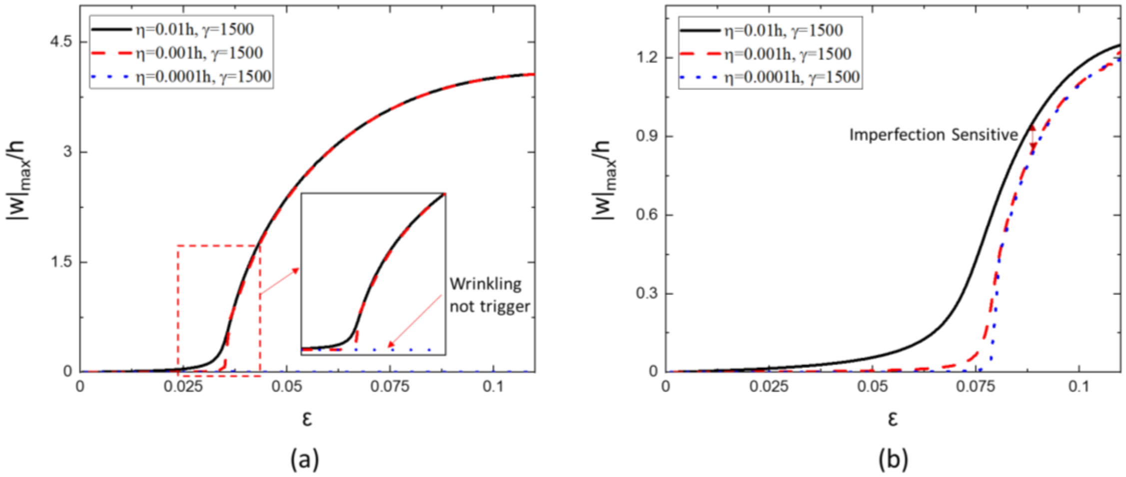

Figure 3-4 Bifurcation diagrams in terms of $|w|_{max}/h$ vs. strain ε for (a) rectangular geometry (with $\gamma = 1500, u_{pre} = 0.01L$), and (b) dogbone geometry (with $\alpha = 0.4$, $\beta = 0.3, \gamma = 1500, u_{pre} = 0.01L$) with various imperfection scale factors η.

It can be seen that $|w|_{max}/h$ starts to increase rapidly at the bifurcation point defined by the critical buckling strain ε_{cr}. With the reduction of the imperfection scale factor η, the bifurcation happens more suddenly, leading to better definitions of the bifurcation point and the critical buckling strain whereas the global bifurcation phenomena remain the same. Similar observations were reported for hyperelastic materials in the study by Wang et al. (2019b). However, bifurcation may not be successfully triggered in numerical simulation if the initial imperfection is too small, as shown in Figure 3-4(a). On the other hand, larger initial imperfection can make the bifurcation diagram smoother but would also make it difficult to determine the critical buckling strain, and sometimes even affect the bifurcation behaviour (e.g. larger magnitude caused by a larger imperfection in Figure 3-4(b)). Therefore, the scale factor $\eta = \eta_1 = \eta_2 = 0.001h$ is determined to be used in the following study.

In addition, it is also important to understand if the eigenmodes, determined under different base states described by various pre-stretched displacement u_{pre}, would influence the post-buckling evolution (Nayyar 2010). Hence, eigenmodes determined under various u_{pre} are introduced for $\eta = 0.001h$, and the results are illustrated in Figure 3-5.

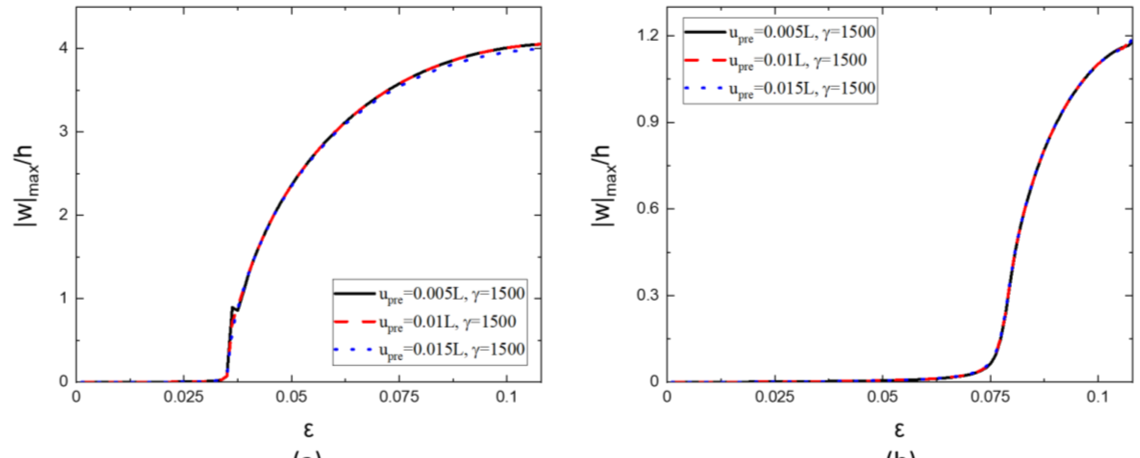

(a) (b)

Figure 3-5 Bifurcation diagram of (a) rectangular geometry (with $\gamma = 1500, \eta = 0.001h$) and (b) dogbone geometry (with $\alpha = 0.4$, $\beta = 0.3, \gamma = 1500, \eta = 0.001h$), with eigenmodes for various pre-stretched displacements u_{pre}.

As shown in Figure 3-5, for both the rectangular and dogbone geometries, the post-buckling evolution is not affected by eigenmodes extracted from different pre-stretched states. However, if the pre-stretched displacement is not large enough (e.g. for dogbone film model with large R and D and $u_{pre} = 0.005L$) or exceeds the critical value, the eigenvalue solution cannot be calculated. Therefore, $u_{pre} = 0.01L$ is selected, which ensures the existence of eigenvalue solutions, and the associated eigenmodes can be obtained for all models in this study.

In this research, all simulations are running on a High Performance Computing (HPC) cluster CSF-3 with ~9,500 cores supported by The University of Manchester. In order to reduce the computation time of the simulation, parallel execution can be run by submitting a parallel batch job. However, according to Manual from Abaqus (2019), some physical systems may be highly sensitive to the small perturbation (e.g. initial imperfection), which can cause small numerical differences when running jobs on different CPUs due to the finite precision effects. Hence, it is necessary to understand the influence of the parallel execution. Similar to the above studies on two factors, post-buckling analysis has been done for both rectangular geometry and dogbone geometry models (with $\gamma = 1500, \eta = 0.001h, u_{pre} = 0.01L$) using both single CPUs and multiple CPUs, and the global bifurcation diagram and the computational time are summarised in Figure 3-6 and Table 3-1.

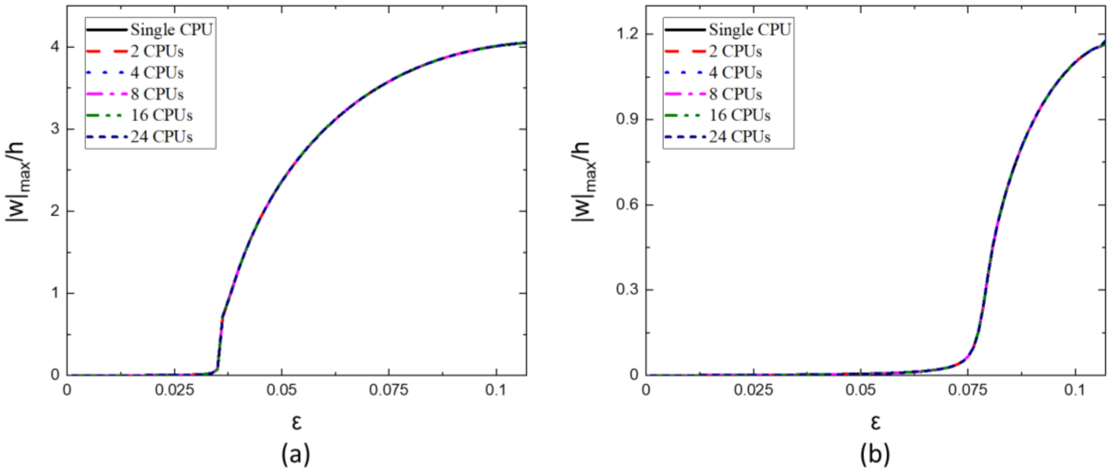

(a)

(b)

Figure 3-6 Bifurcation diagrams of (a) rectangular geometry (with $\gamma = 1500, \eta = 0.001h, u_{pre} = 0.01L$), and (b) dogbone geometry (with $\alpha = 0.4$, $\beta = 0.3, \gamma = 1500, \eta = 0.001h, u_{pre} = 0.01L$), using single and parallel executions in post-buckling analysis.

Table 3-1 Summary of post-buckling analysis for single and parallel executions.

Model Geometry	Geometric Parameters	Element Number	CPUs	Computational Time (s)
Rectangular	$\gamma = 1500$	50000	Single	2911
			2	1767
			4	796
			8	614
			16	606
			24	578
Dogbone	$\alpha = 0.4, \beta = 0.3, \gamma = 1500$	57120	Single	3323
			2	1883
			4	964
			8	728
			16	615
			24	635

It is evident that computational efficiency increases with the increase of CPUs (except for the dogbone when the processor number increases from 16 to 24), while no difference in the simulation results can be found. When the number of processors exceeds 4, the reduction of computational time with the increase of CPU number becomes less noticeable.

In conclusion, to balance the precision of the numerical results and the computation efficiency, four parallel CPUs with $\eta = 0.001h$ and $u_{pre} = 0.01L$ are used in the rest of this study.

3.3.3 Mesh sensitivity

Even though the mesh was usually set up with element size of $W/100$ (Nayyar et al. 2011, Huang et al. 2020), it is still necessary to investigate the effect of elements size on the numerical results. Similar to the parametric study in Section 3.3.2, the rectangular geometry model (with $\gamma = 1500$) and the dogbone geometry model (with $\alpha = 0.4,\ \beta = 0.3, \gamma = 1500$) are analysed here. The elements sizes to be investigated are $W/50$, $W/100$ and $W/150$. The bifurcation diagrams of models with different mesh sizes are shown in Figure 3-7, and the computational details are summarised in Table 3-2.

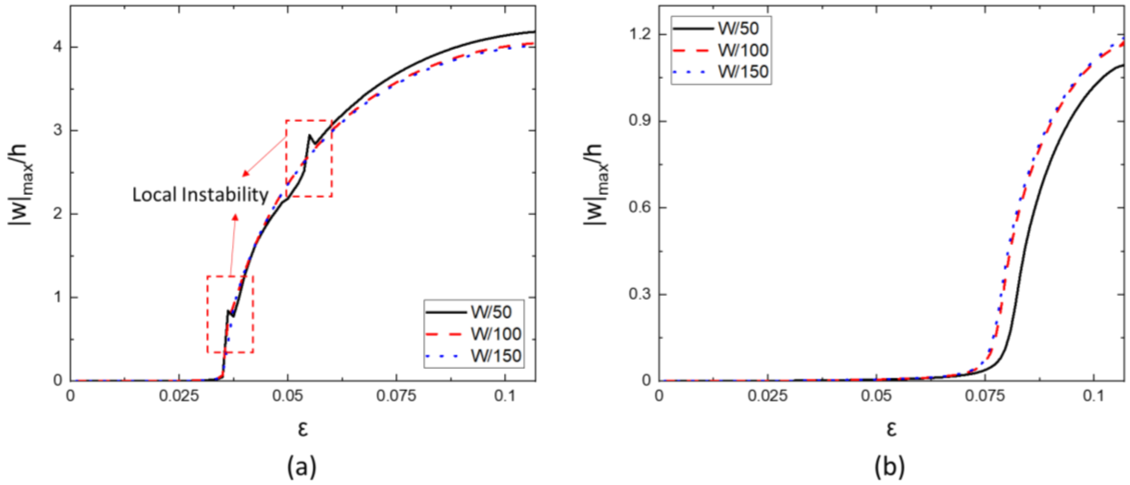

Figure 3-7 Bifurcation diagrams of (a) rectangular geometry (with $\gamma = 1500$), and (b) dogbone geometry (with $\alpha = 0.4,\ \beta = 0.3, \gamma = 1500$), using three elements sizes.

Table 3-2 Summary of computational details in the mesh sensitivity study.

Model Geometry	Geometric Parameters	Element Sizes	Element Number	Computational Time (s)
Rectangular	$\gamma = 1500$	$W/50$	12500	250
		$W/100$	50000	796
		$W/150$	112500	2384
Dogbone	$\alpha = 0.4, \beta = 0.3, \gamma = 1500$	$W/50$	14000	259
		$W/100$	57120	964
		$W/150$	126000	2548

As shown in Figure 3-7, when using the mesh with elements size of $W/50$, the curve for rectangular geometry shows local instability and the curves for both geometries show noticeable differences from those for the other two smaller element sizes. In addition, when applying finer mesh (i.e. elements size equals to $W/150$), it will take more computational time while the accuracy improvement is negligible. Therefore, the mesh with elements size of $W/100$ is a suitable choice to balance accuracy and efficiency.

3.3.4 Determination of the critical buckling load

In this case, it should be noted that as the loading condition is displacement controlled, the critical buckling load indicated from eigenvalue buckling analysis is the critical displacement of the moving edge when the buckling occurs, which can be predicted by Eq. (3.1). For better comparison with post-buckling analysis, displacement of the moving edge at the bifurcation point in the post-buckling analysis is defined as the critical buckling load $u_{cr,post}$ here. In previous studies (Nayyar 2010, Huang et al. 2020), researchers assumed that the structure is stiff and elastic, and therefore, the problem is linear. However, it is found that the critical buckling load varies with the pre-stretched state (u_{pre}), as shown in Table 3-3, due to the involvement of geometric nonlinearity, which happens for both rectangular and dogbone thin film samples. The geometric nonlinearity is caused by the non-negligible geometry change, which happens before the buckling of the structure (i.e. pre-buckling stage). Therefore, the linear-perturbation-load-based eigenvalue buckling analysis is unable to give an accurate critical buckling load, but can still provide useful estimates of buckling mode shapes (Abaqus 2019). On the other hand, the critical buckling load predicted by post-buckling analysis is independent of the pre-stretched state (u_{pre}), as the Riks method can perform a geometrically nonlinear load-displacement analysis, which means that the critical buckling load can be determined more precisely and consistently.

Table 3-3 Critical buckling load u_{cr} computed by eigenvalue analysis and post-buckling analysis.

Model Geometry	u_{pre}	λ_e	$u_{cr,eigenvalue}$	$u_{cr,post}$
Rectangular ($\gamma = 1500$)	$0.0025L$	10.21	$0.0280L$	$\sim 0.035L$
	$0.005L$	9.70	$0.0292L$	$\sim 0.035L$
	$0.01L$	8.58	$0.0315L$	$\sim 0.035L$
	$0.02L$	5.93	$0.0348L$	$\sim 0.035L$
	$0.03L$	2.52	$0.0363L$	$\sim 0.035L$
Dogbone	$0.0025L$	17.44	$0.0461L$	$\sim 0.075L$
($\alpha = 0.4, \beta = 0.3, \gamma = 1500$)	$0.005L$	17.24	$0.0481L$	$\sim 0.075L$
	$0.01L$	16.81	$0.0520L$	$\sim 0.075L$
	$0.02L$	15.84	$0.0596L$	$\sim 0.075L$
	$0.03L$	14.68	$0.0667L$	$\sim 0.075L$

Note: $u_{cr,eigenvalue}$ is the estimated critical buckling displacement obtained by Eq. (1), $u_{cr,post}$ is the critical buckling displacement obtained from post-buckling analysis.

3.4 Critical geometric boundary (CGB)

This study focuses on the linear elastic response of a thin film sample under uniaxial tensile test, and therefore, the concerned strain has an upper limit (ε_m). Without losing generality, a limit nominal strain of $\varepsilon_m = 0.08$ is used in the determination of CGB because it covers possible elastic regimes for various engineering materials.

Firstly, the bifurcation process of rectangular samples with various γ is investigated to determine the range of γ, in which the wrinkling can be eliminated. Generally, the critical buckling strain increases with the decrease of the width-to-thickness ratio γ (i.e. increasing thickness h with a given 2D geometry), which will be further explained later in Section 3.4.4. It should be noted that, in many practical applications, thin film materials are used directly for the uniaxial tensile tests, i.e. their thicknesses cannot be changed, and therefore, the only option is to design their geometric shapes to avoid the wrinkling occurrence. It can be known from Figure 3-8 that when $\gamma > 1200$, the critical buckling strain $\varepsilon_{cr} < 0.08$. Therefore, the dogbone samples thinner than $h = W/1200$ should be considered for wrinkling. Besides, it should be noted that even though the buckling mode for $\gamma = 1100$ can be obtained from eigenvalue analysis, no distinct bifurcation can be found in post-buckling analyses.

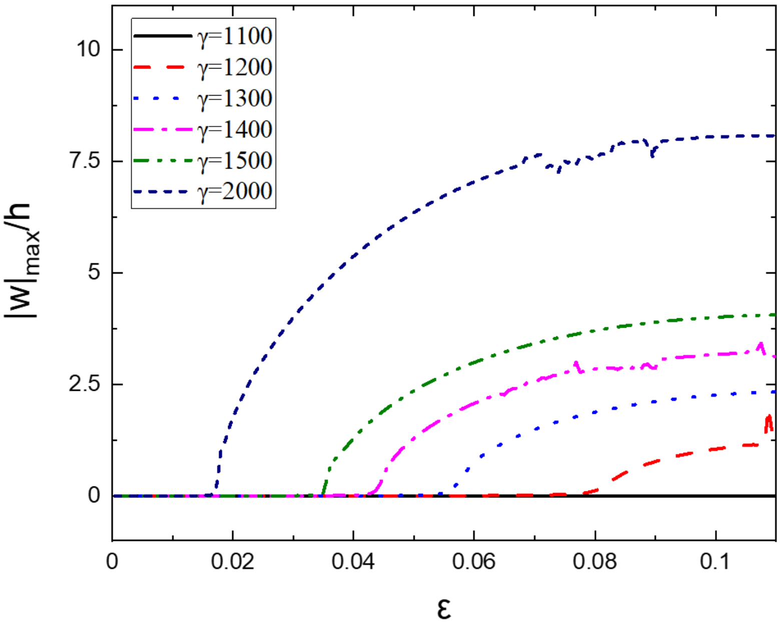

Figure 3-8 Bifurcation diagrams for rectangular geometries with various γ.

Within the scope of this research, two cases are identified, i.e. (i) Case-I: wrinkling delay when $\varepsilon_{cr} > \varepsilon_m$. In this case, wrinkling will not happen during the elastic deformation stage when $\varepsilon \leq \varepsilon_m$, but may still happen when the strain enters the plastic regime, which is outside the scope of this study.

(ii) Case-II: wrinkling elimination when there is no distinct bifurcation (only negligible out-of-plane displacement introduced by the initial imperfection) for any given strain before or even after ε_m.

When either $\varepsilon_{cr} = \varepsilon_m$ or ‘wrinkling elimination’ happens, the associated non-dimensional numbers (α, β, γ) will define a critical geometric boundary (CGB) to divide the parametric space into wrinkling and non-wrinkling regimes. It should be noted that although $\varepsilon_m = 0.08$ is used in this research to cover the majority of materials, other values of ε_m may be used for a particular material to obtain a more accurate CGB by following the same methodology proposed here.

3.4.1 Critical geometric boundary for wrinkling delay

In this section, the wrinkling delay case will be demonstrated and discussed for various α and β values and a given $\gamma = 1500$.

When $\gamma = 1500$ and $\alpha = 0.4$, the critical buckling strain ε_{cr} increases with the increase of parameter β, as shown in Figure 3-9. Compared to the rectangular geometry with the same width to thickness ratio (γ), the dogbone geometries not only delay the occurrence of wrinkling, but also reduce its growth. When β approaches to zero, the bifurcation diagram approaches to that for rectangular geometry, as shown in Figure 3-9. Nested Intervals Method is used to calculate the critical parameter β on the CGB. The threshold of the precision of the critical parameter β is set as 0.05 here. The critical parameter β is determined as the smallest β when $\varepsilon_{cr} \geq 0.08$, which, together with the given α and γ, are used as a critical point on CGB (or CGB point). In Figure 3-9, for instance, $\beta = 0.305$ (i.e. the green curve) is the smallest value for $\varepsilon_{cr} \geq 0.08$ (ε_{cr} is determined by $|w|_{max}/h = 0.1$), and therefore, $\alpha = 0.4$, $\beta = 0.305$, $\gamma = 1500$ is a CGB point.

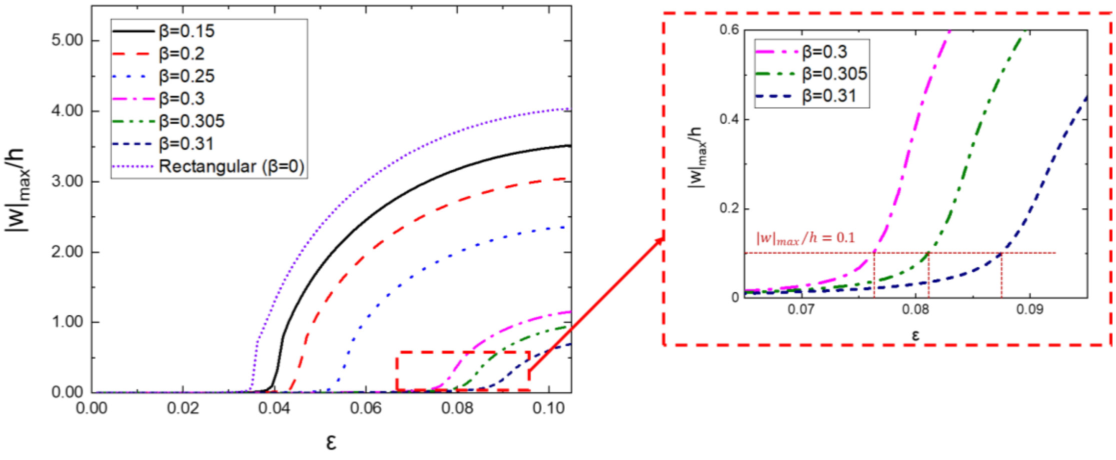

Figure 3-9 The bifurcation diagrams of dogbone geometry with $\alpha = 0.4$, $\beta = 0.305$ and varying parameters β, and their local curves near strain of 0.08.

By using the same method presented above, critical parameters β in the range of $0.04 < \alpha < 3.2$ are determined by observing the bifurcation point via the post-buckling analysis using FEA modelling, as shown in Figure 3-10(a). The CGB curve expressed by

β vs. α under $\gamma = 1500$ is presented in Figure 3-10(b). According to the CGB curve, the relationship between α and β can be described by

$$\beta = A\alpha^{-B} \tag{3.3}$$

where amplitude A and exponent B are constants fitted to the numerical results. For the dogbone geometry with $\gamma = 1500$, A and B are fitted as 0.2326 and 0.3036 with an R-squared of 100%, respectively. Moreover, Regime I, i.e. the area that $\beta < A\alpha^{-B}$, is the region where wrinkling will occur when strain ε is less than 0.08, while Regime II is the region where there is no wrinkling occurrence during the uniaxial tensile test when ε is less than 0.08.

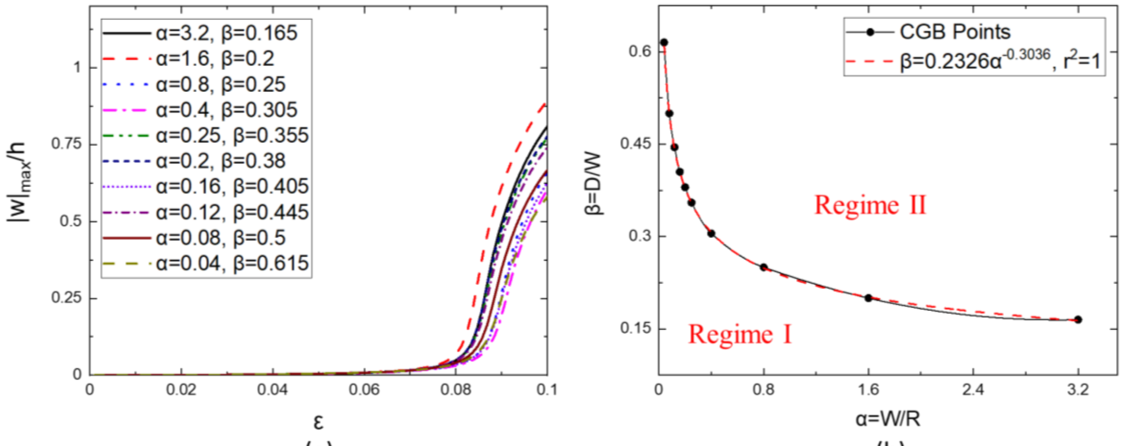

(a) (b)

Figure 3-10 (a) The bifurcation diagrams of the points on CGBs for varying α, and (b) the CGB points and fitted curve between α and β for $\gamma = 1500$.

3.4.2 Critical geometric boundary for wrinkling elimination

For the thinner dogbone geometries with $\gamma = 2000$, the CGB curve of β vs. α is determined by both wrinkling delay and wrinkling elimination phenomena as introduced at the beginning of Section 3.4 (before the start of Section 3.4.1), as shown in Figure 3-11(a). For the case of $\alpha > 0.16$ and $\gamma = 2000$, the CGB points are determined by wrinkling delay as presented in Section 3.4.1. However, for the case of $\alpha \leq 0.16$ and $\gamma = 2000$, the critical strains ε_{cr} are not able to be postponed beyond 0.08. Figure 3-11(b) shows an example for the dogbone geometry with $\alpha = 0.16$ and $\gamma = 2000$ where the critical buckling strain is initially delayed by the increase of β. However, with the further increase of β, the bifurcation phenomenon disappears before $\varepsilon_{cr} = 0.08$. Therefore, in spite of determining the CGB points by taking the smallest points of (α, β, γ) when $\varepsilon_{cr} \geq 0.08$, the CGB points in the case of $\alpha \leq 0.16$ and $\gamma = 2000$ are determined by the disappearance of the bifurcation phenomenon before $\varepsilon_{cr} = 0.08$, as shown in Figure 3-11(a).

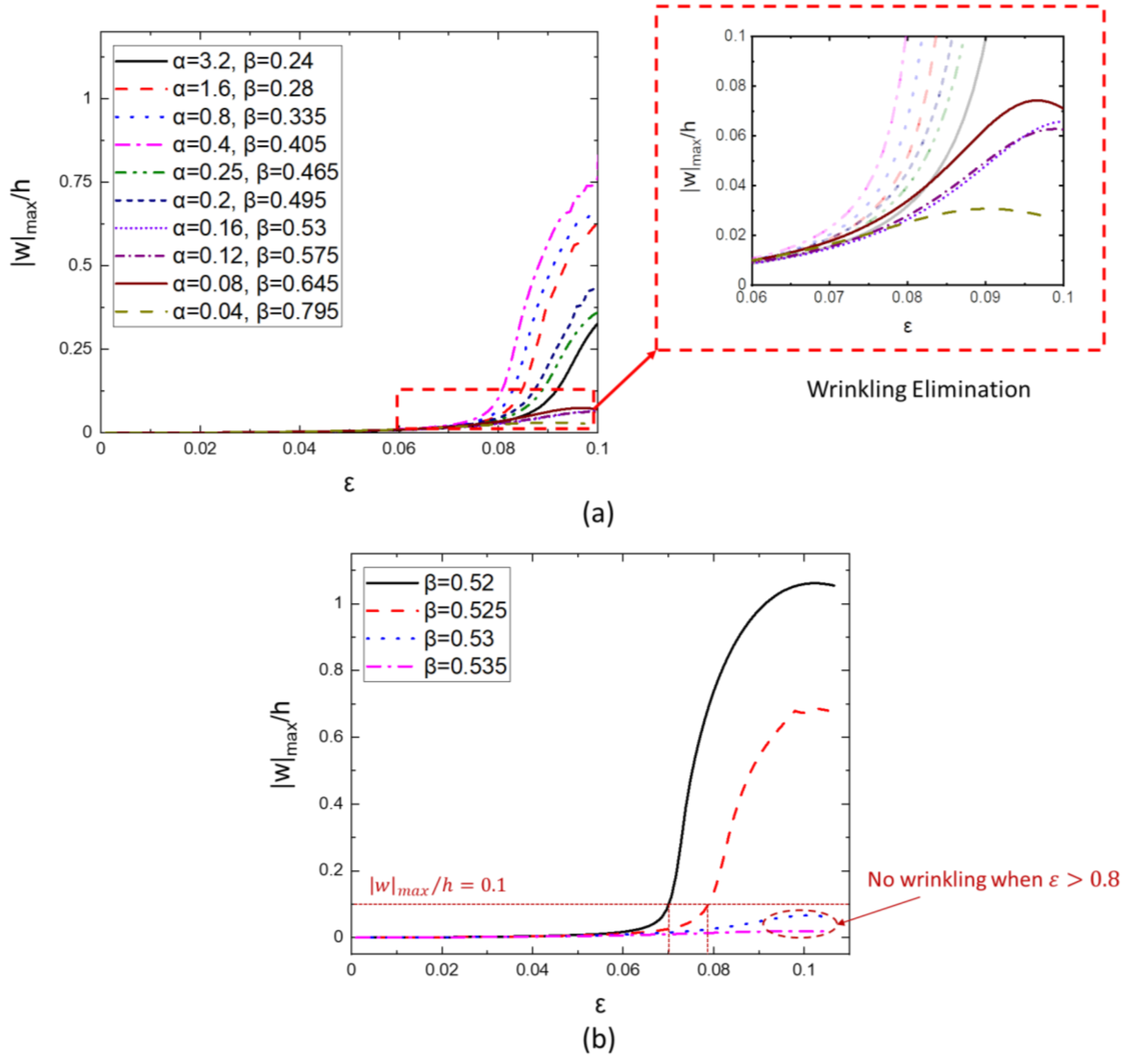

Figure 3-11 (a) The bifurcation diagrams for the CGB points with various α and β where wrinkling elimination happens for the dogbone geometries with $\alpha \leq 0.16$, $\gamma = 2000$; (b) The bifurcation diagrams of dogbone geometry with $\alpha = 0.16$, $\gamma = 2000$ and various β.

Similarly, the CGB points expressed by β vs. α for $\gamma = 2000$ and its fitted curve are presented in Figure 3-12, where the CGB points associated with 'wrinkling delay' are represented by solid marks whereas the CGB points associated with 'wrinkling elimination' are represented by open marks. Even though the CGB points are determined by a different mechanism, it can be seen that the trend of the relationship between β and

α is similar to that (Figure 3-10(b)) determined by 'wrinkling delay' in Section 3.4.1. Hence, the relationship between β and α can also be described by Eq. (3.3), and A and B are fitted as 0.3188 and 0.2752 with an R-squared of 99.998%, respectively.

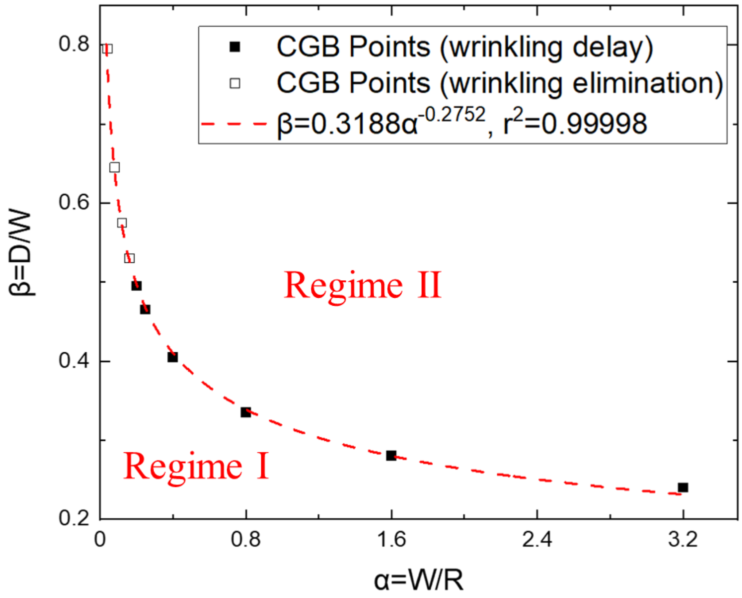

Figure 3-12 The CGB points and fitted curves between β and α for $\gamma = 2000$. The solid marks represent CGB of 'wrinkling delay', and the open marks represent CGB of 'wrinkling elimination'.

In addition, it should be noted that the existence of two CGB modes can only be observed in the case of $\gamma = 2000$, while for γ with other values, only 'wrinkling delay' (i.e. $\gamma = 1250, 1500$) or 'wrinkling elimination' (i.e. $\gamma = 2500, 4000$) can be found (see Section 3.4.3 and Figure 3-14). Therefore, Regime II in Figure 3-12 actually contains two modes of wrinkle-free design, i.e. wrinkle still exists when $\varepsilon > 0.08$ and wrinkle disappears completely, as shown in Figure 3-13. Another interesting phenomenon is that in this case, the boundary between 'wrinkling delay' and 'wrinkling elimination' is almost the boundary between Regime I and Regime II, indicating that $\gamma = 2000$ can be regarded as the boundary to distinguish whether Regime II is caused by 'wrinkling delay' or 'wrinkling elimination' (i.e. Regime II represents 'wrinkling delay' for $\gamma < 2000$ and 'wrinkling elimination' for $\gamma > 2000$).

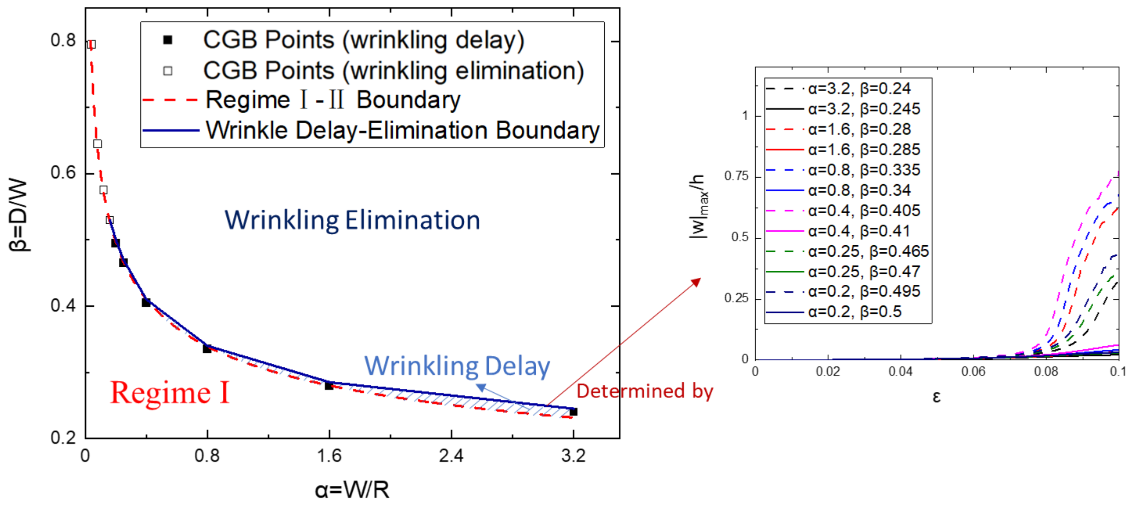

Figure 3-13 The special Regime II that consists of ‘wrinkling elimination’ and ‘wrinkling delay’ in the case of $\gamma = 2000$.

3.4.3 CGB surface and formula

As shown in Figure 3-8 and mentioned at the beginning of Section 3.4, the CGBs are required to be determined for $\gamma > 1200$. Therefore, the CGBs related to all three non-dimensional numbers α, β and γ can be determined by the method presented above, as illustrated in Figure 3-14. Similar to Figure 3-12, the CGB points of ‘wrinkling delay’ are represented by solid marks and the CGB points of ‘wrinkling elimination’ are represented by open marks. It should be noted that the CGB points for thicker geometries (e.g. $\gamma = 1250, 1500$) are all associated with ‘wrinkling delay’, and the CGB points for thinner geometries (e.g. $\gamma = 2500, 4000$) are associated with ‘wrinkling elimination’. The bifurcation diagrams associated with the CGB points for other γ values can be seen in Figure 3-14.

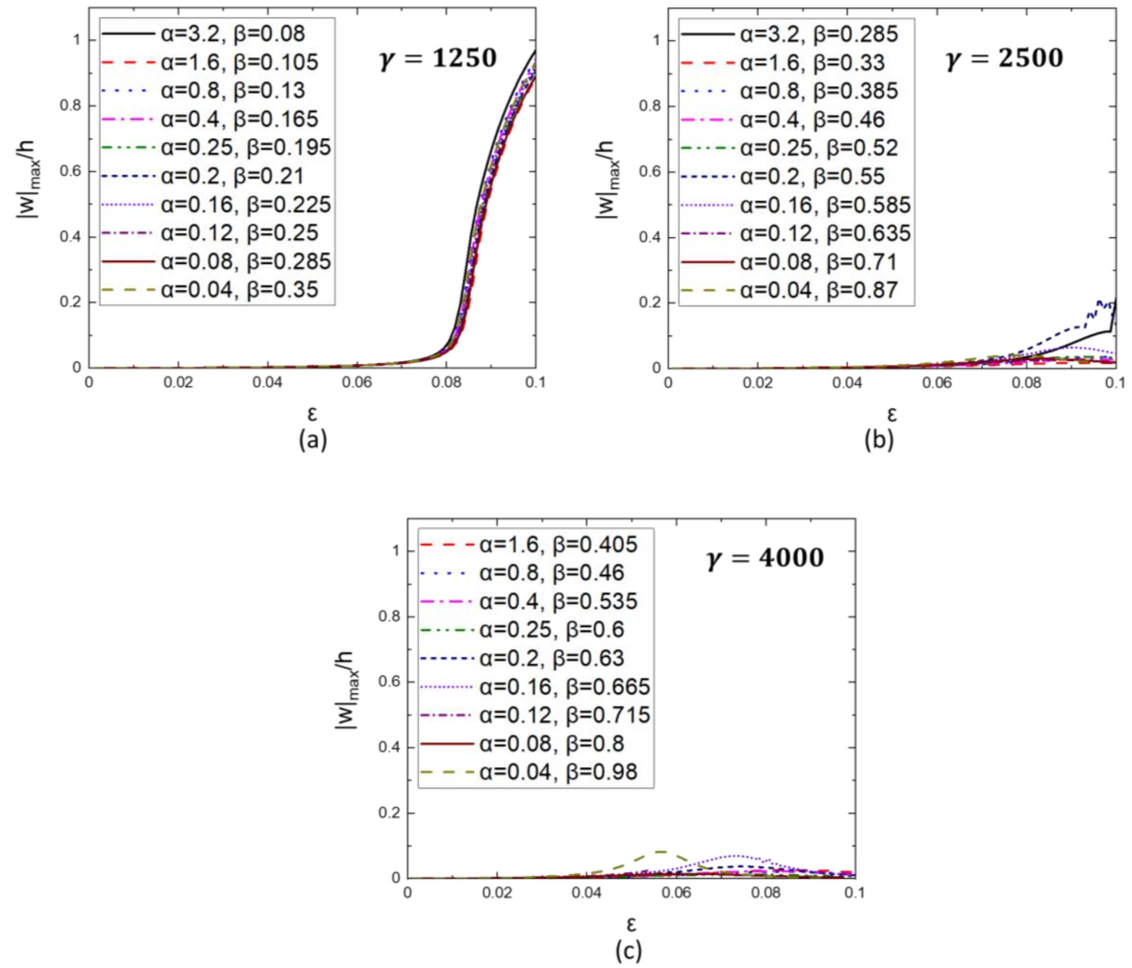

Figure 3-14 The bifurcation diagrams of the CGBs for (a) $\gamma = 1200$, (b) $\gamma = 2500$, and (c) $\gamma = 4000$.

Due to the design limit that the width D of the extended parts of the dogbone geometry cannot be greater than the radius R, the analysis of CGB should remain in the regime of $\alpha\beta \leq 1$, as the red dashed line shown in Figure 3-14. Hence, Regime III, i.e. the area where $\alpha\beta > 1$, is outside the design region. It is interesting to note that no CGB exists for $\alpha = 3.2$ when $\gamma = 4000$, which is clearly shown in Figure 3-14 and Figure 3-15.

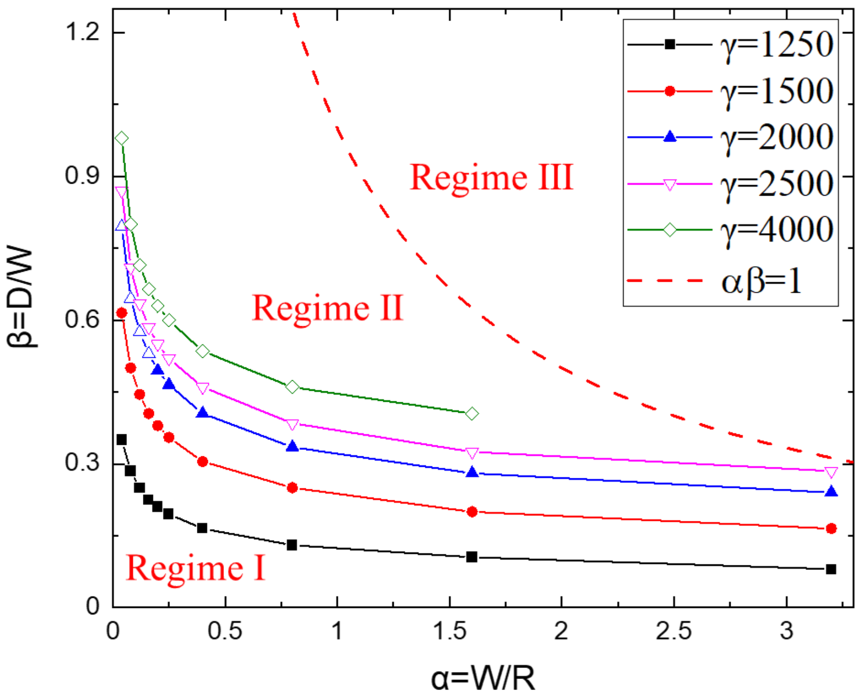

Figure 3-15 The CGB relationships between α and β with different thickness ratio γ. The solid marks represent CGB of ‘wrinkling delay’, and the open marks represent CGB of ‘wrinkling elimination’.

According to Figure 3-15, the CGB relationships between β and α are similar for various γ values, which implies that Eq. (3.3) is suitable to predict all CGB points for $\gamma > 1200$. The fitted values of A and B are summarised in Table 3-4 for various γ values.

Table 3-4 Fitted value of constants A and B for various γ values.

γ	A	B
1250	0.1215	0.3370
1500	0.2326	0.3036
2000	0.3188	0.2752
2500	0.3679	0.2534
4000	0.4392	0.2284

According to Table 3-4, A and B are functions of γ. Therefore, Eq. (3.3) can be modified as

$$\beta(\alpha,\gamma) = f(\gamma)\cdot\alpha^{-g(\gamma)} \tag{3.4}$$

As shown in Figure 3-8, the critical buckling strain $\varepsilon_{cr} = 0.08$ for the rectangular geometry with $\gamma = 1200$, which gives a lower boundary of CGB, i.e. $\beta(\alpha, 1200) = 0$ in Eq. (3.4). Hence, two functions in Eq. (3.4) are proposed as

$$\begin{cases} f(\gamma) = a_1(\gamma - 1200)^{a_2} \\ g(\gamma) = a_3\cdot\gamma^{-a_4} \end{cases} \tag{3.5}$$

where parameters $a_1 = 0.043, a_2 = 0.30, a_3 = 3.769, a_4 = 0.3421$ are used to fit numerical results for various γ values. Figure 3-16 shows that the functions proposed above can give good fitting results.

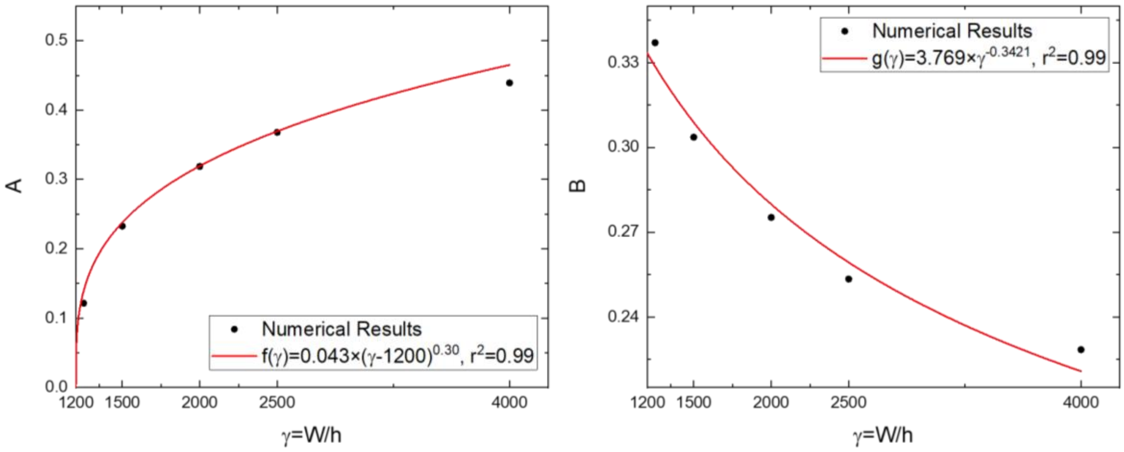

(a) (b)

Figure 3-16 Parameters (a) A, and (b) B for various γ values and the corresponding fitting function curves.

By substituting Eqs. (3.4) to (3.5), the CGB for all possible shapes of dogbone thin film samples with $\gamma > 1200$ can be defined by

$$F(\alpha,\beta,\gamma) = \beta - 0.043\cdot(\gamma - 1200)^{0.30}\cdot\alpha^{-(3.769\cdot\gamma^{-0.3421})} = 0 \tag{3.6}$$

The surface $F(\alpha,\beta,\gamma) = 0$ is presented in Figure 3-17, which transforms the curves in Figure 3-15 into a 3D surface (i.e. both violet and pale green unmeshed parts). The red dashed line is the estimated boundary to distinguish the CGB mechanisms (i.e. CGB of 'wrinkling delay' represented by the violet part and CGB of 'wrinkling elimination' represented by the pale green part). The meshed orange surface is the design limit boundary (DLB) similar to the red dashed line illustrated in Figure 3-15. The black dotted line in Figure 3-17 is the intersection line of the CGB and DLB surfaces, and the CGB surface should not be beyond this line. As presented above, Regime I, which is located beneath the CGB surface, is the region that wrinkling will occur before ε reaches 0.08; Regime II, where the location is above the CGB surface and below the DLB surface, is the region where no wrinkling happens prior to strain ε of 0.08; Regime III, which is located above the DLB surface, is the region where the design of dogbone sample is not feasible. Hence, DLB $> F(\alpha, \beta, \gamma) > 0$ should be considered when designing a thin film dogbone sample for a uniaxial tensile test.

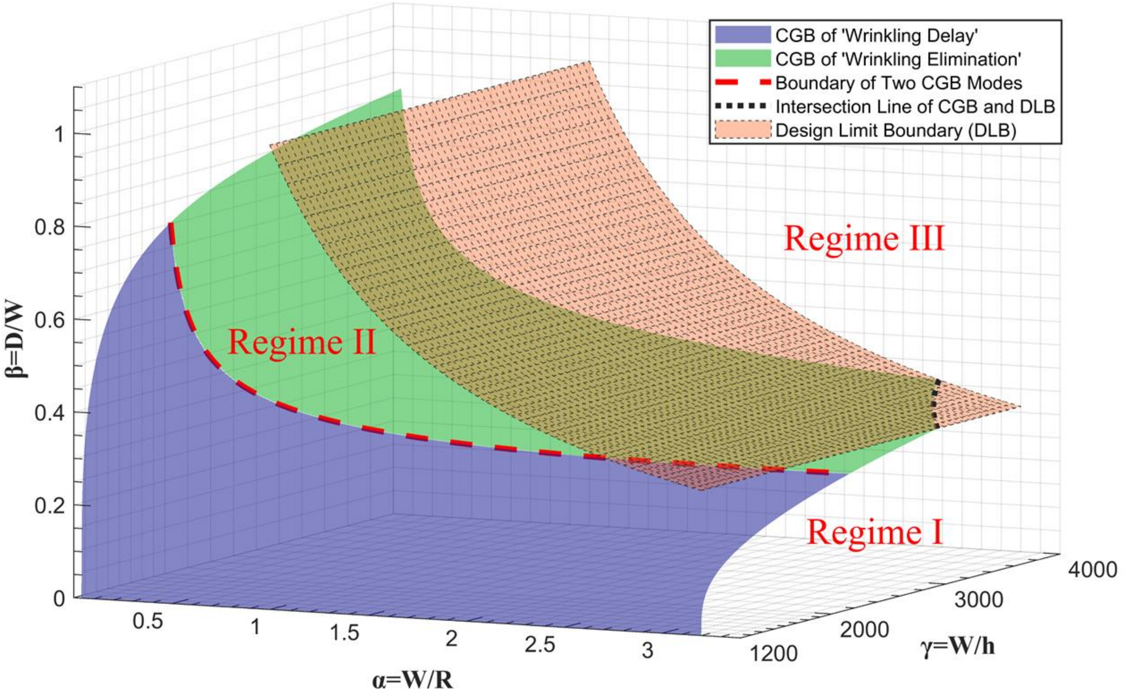

Figure 3-17 A 3D regime diagram of the CGB for parameters with $\gamma > 1200$.

In practical uniaxial tensile tests, the materials' elastic properties (e.g. Young's modulus and Poisson's ratio) may be different, which could influence the wrinkling behaviours during the experiment. According to previous studies, the value of Young's modulus only affects the magnitude of the stress in the thin film sheet, but not the wrinkling behaviour (Wong and Pellegrino 2006b, Nayyar et al. 2011); the wrinkling phenomenon will become less significant by decreasing the Poisson's ratio (Wang et al. 2019b, Martins et al. 2020). In this study, the CGB formula (i.e. Eq. (3.6)) and the corresponding CGB surface in Figure 3-17 are determined based on an incompressible elastic material model, which is the upper limit of materials' Poisson's ratios. It should be noted that CGB surface becomes lower for the thin film materials with smaller

Poisson's ratios, which implies that the present CGB is more conservative, i.e. the design of thin film sample based on Eq. (3.6) or Figure 3-17 is conservative for the prevention of wrinkling. Hence, the proposed CGB can be regarded as an upper boundary of the CGB for all elastic thin films and can be used as general guidance for the design of thin film dogbone samples in uniaxial tensile tests. At the same time, the proposed design can also guarantee that the gauge area of the sample remains in uniaxial stress state, which will be discussed in the following section.

3.4.4 Stress analysis and mechanism of wrinkle delay

In this section, a 2D FE model with quadrilateral plane-stress elements (CPS4R) (Nayyar et al. 2011) is developed for the stress analysis and wrinkling prediction of dogbone thin film samples in a uniaxial tensile test. In previous studies (Friedl et al. 2000, Nayyar et al. 2011, Huang et al. 2020), it was found that wrinkling is actually an in-plane buckling caused by the lateral compression. The critical wrinkling (or buckling) tensile stress then can be analysed by the stress ratio $C = \sigma_{22_{min}}/\sigma_{11_{avg}} < 0$ (Huang et al. 2020), which was firstly proposed in (Friedl et al. 2000). $\sigma_{22_{min}}$ is the maximum compressive stress (as the value is negative for compressive stress, the minimum stress value represents the maximum compressive stress) in transverse direction (x_2 direction here) and $\sigma_{11_{avg}}$ is the average tensile stress along the transverse centre cross-section of $x_1 = L_t/2$ (or $x_1 = L/2$ for rectangular geometry), as shown in Figure 3-1. In a simply-supported rectangular thin-plate model, the critical buckling tensile stress $\sigma_{11,cr}$ increases with the decrease of $|C|$ (Friedl et al. 2000). The relationships between $|C|$ and strain ε for both rectangular and dogbone geometries are shown in Figure 3-18(a). The curves of maximum compressive stress vs. strain ε and the curves of average tensile stress vs. strain ε for rectangular and dogbone geometries are illustrated in Figure 3-18(b) and (c), respectively. It should be noted that both maximum compressive stress and average tensile stress are expressed in non-dimensional forms, i.e. $\sigma_{22_{min}}/E$ and $\sigma_{11_{avg}}/E$, to maintain the generality of the results.

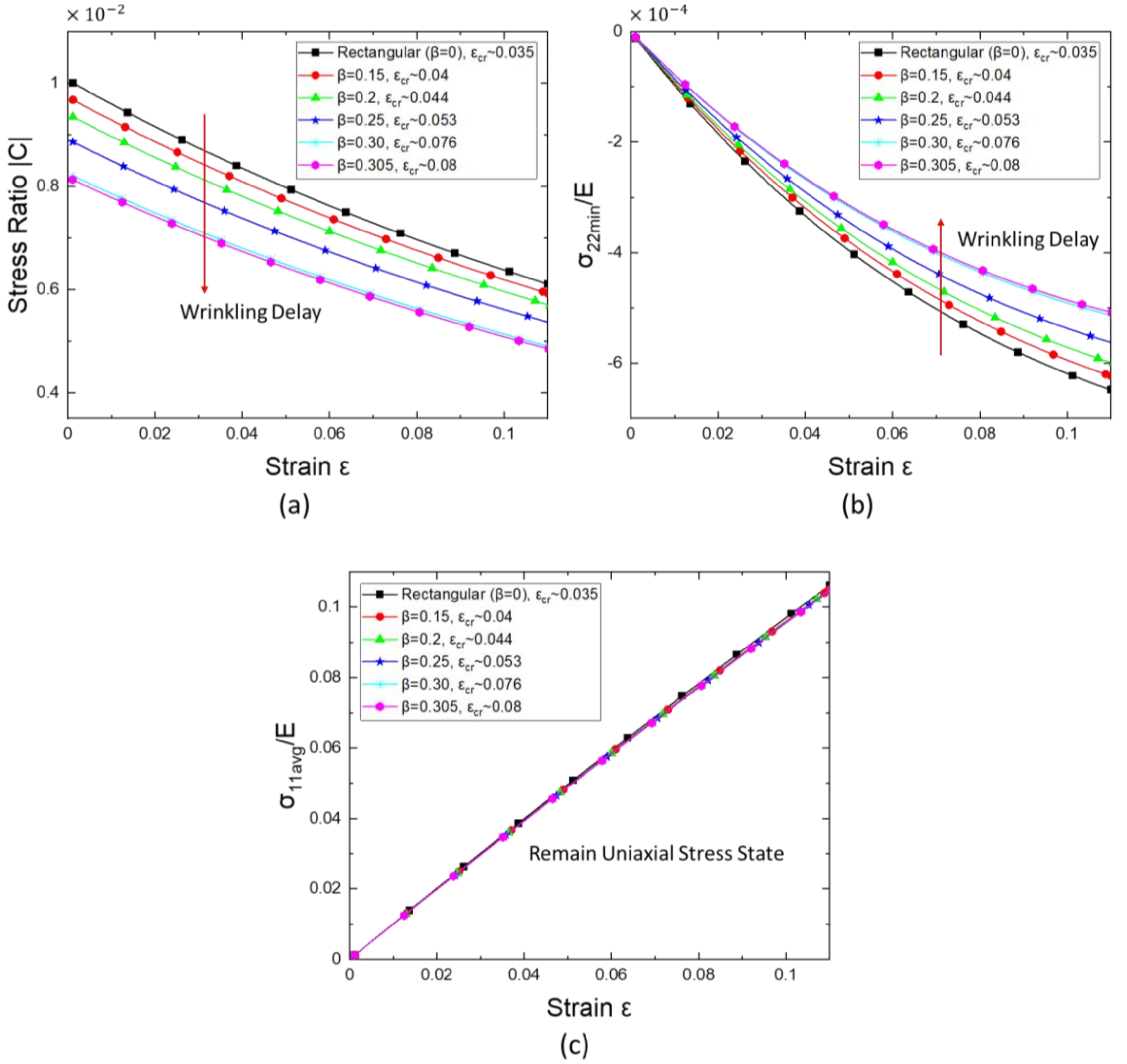

Figure 3-18 The variations of (a) stress ratio $|C|$, (b) the maximum compressive stress, and (c) the average tensile stress, with strain ε for both rectangular geometry (with $\gamma = 1500$, $\beta = 0$) and dogbone geometry (with $\alpha = 0.4$, $\gamma = 1500$, various β).

As the compressive stress and buckling area occur in the gauge area in both rectangular and dogbone geometries, the problem can be equivalent to a simply supported rectangular plate. According to (Friedl et al. 2000, Timoshenko and Gere 2009), the critical buckling tensile stress $\sigma_{11,cr}$ for a simply supported plate can be assumed as

$$\sigma_{11,cr} = \frac{\pi^2 E}{12(1-v^2)}\left(\frac{h}{W}\right)^2 \left[\frac{\left(n\cdot\frac{W}{L}\right)^4 + 2\left(mn\cdot\frac{W}{L}\right)^2 + m^4}{-Cm^2 - \left(n\cdot\frac{W}{L}\right)^2}\right] \tag{3.7}$$

where n and m are the half wave numbers in the x_1 and x_2 directions (defined as same as in Figure 3-1), respectively. As can be seen from Figure 3-2 and Figure 3-3, the eigenmodes in rectangular and dogbone geometries are similar, which indicates that the half wave numbers n and m are the same in all geometries in this study. It should be noted that Eq. (3.7) is just used to qualitatively determine the onset of stretch-induced wrinkling of a sheet, and the geometric parameters W and L in Eq. (3.7) should be taken approximately for the part of the sheet where the transverse stress is compressive (Nayyar et al. 2011) (i.e. the geometric parameters W and L are not the same as those introduced in Section 3.2). Even so, it can be seen from Eq. (3.7) that if all parameters except stress ratio C are constant, the reduction of the transverse compressive stress (i.e. the smaller $|C|$) will increase the critical buckling tensile stress $\sigma_{11,cr}$. As the tensile stress σ_{11} is dependent on strain ε and is barely affected by changing the geometries studied here (as shown in Figure 3-18(c)), the smaller stress ratio $|C|$ can delay the occurrence of wrinkling, which is consistent with the results shown in Figure 3-18(a). The advantage of the dogbone geometry is that it can reduce the transverse stress (i.e. $|C|$) by easing transverse constraints on the short edges of the gauge area, as a result of the extended parts of the dogbone geometry while the overall stress state stays in a uniaxial tension state. These observations show that the dogbone sample is better than the rectangular sample for preventing the occurrence of wrinkles in a uniaxial tensile test, and meanwhile, guaranteeing a uniaxial stress state in the gauge section of the thin film sample. Meanwhile, Eq. (3.7) also reveals the theoretical underpinning mechanism of the wrinkling delay caused by the increase of thickness, as shown in Figure 3-8.

On the other hand, it can be noted that the maximum transverse compressive stress $\sigma_{22_{min}}$ is reduced with increasing dogbone parameter β, as shown in Figure 3-18(b). To find out the mechanism behind this, the transverse compressive stress distribution for geometry with $\alpha = 0.4, \gamma = 1500$ and various β at strain $\varepsilon \sim 0.03$, is depicted in Figure 3-19(a). The distribution of the corresponding tensile stress (σ_{11}) on the short edges of gauge area with various β values is also shown in Figure 3-19(b). Furthermore, based on Figure 3-19, the transverse compressive strain of the centre (i.e. $\varepsilon_{22,C} = W_c/W - 1$), the transverse compressive strain of the edge of gauge area (i.e. $\varepsilon_{22,E} = W_E/W - 1$), and their difference (i.e. $\Delta\varepsilon_{22,E-C} = \varepsilon_{22,E} - \varepsilon_{22,C}$) of the dogbone geometries (with $\alpha = 0.4, \gamma = 1500$ and various β values where rectangular geometry can be regarded as the dogbone geometry with $\beta = 0$) at $\varepsilon \sim 0.03$ are also given in Table 3-5.

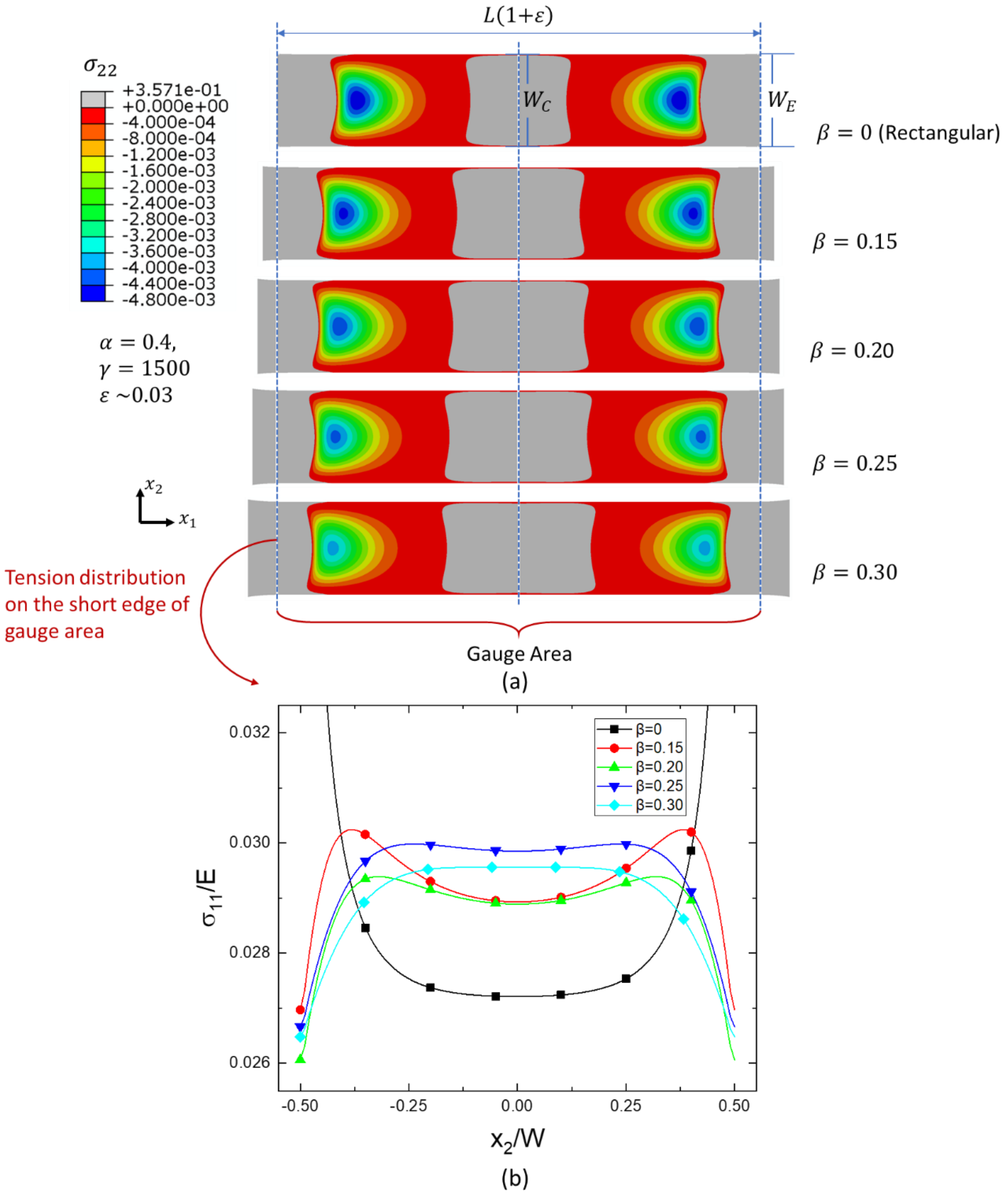

Figure 3-19 (a) The transverse compressive stress (σ_{22}) distribution at $\varepsilon = 0.03$ for both rectangular geometry (with $\gamma = 1500, \beta = 0$) and dogbone geometry (with $\alpha = 0.4, \gamma = 1500$ and various β values); (b) The tension stress in x_1 direction distributed on the short edge of gauge area. It should be noted that the grey region in (a) represents the non-compressive region.

Table 3-5 The compressive strains of the centre and gauge area edge, and their difference in the dogbone geometries (with $\alpha = 0.4, \gamma = 1500$ and various β values) at $\varepsilon \sim 0.03$.

β	$\varepsilon_{22,C}$	$\varepsilon_{22,E}$	$\Delta\varepsilon_{22,E-C}$
0	-0.0149	0	0.0149
0.15	-0.0146	-0.0098	0.0048
0.20	-0.0144	-0.0109	0.0035
0.25	-0.0147	-0.0120	0.0027
0.30	-0.0144	-0.0124	0.0020

Interestingly, with the increase of β, the localised lateral compression region spreads to the sides of the specimen, which reduces the magnitude of the maximum compressive stress ($\sigma_{22_{min}}$), as shown in Figure 3-19(a). In addition, Figure 3-19(b) shows that the distribution of the tensile stress on the short edges of gauge area becomes more uniform with the increase of β. By combining with Table 3-5, it is evident that the magnitude of $\sigma_{22_{min}}$ is reduced because the increase of β leads to a more stable stress state on the boundary of the gauge area, which allows more transversely compressive deformation on the short edges of the gauge area (no deformation when $\beta = 0$) without causing wrinkling. Moreover, $\lim_{\beta\to\infty} \sigma_{22_{min}} = 0$ can be obtained theoretically because the constraint condition on the short edge of the gauge area will become the same as that on the central area, which leads to $\Delta\varepsilon_{22,E-C} = 0$. In this case, the whole gauge area is under a pure uniaxial tension state, and the wrinkling will no longer occur.

3.4.5 Geometric defect effects

In a practical experiment, the geometric defect (or geometric imperfection) is inevitable, and therefore, its effects on CGB should be considered. Here, two kinds of geometric defects are studied, i.e. the defect introduced by sample cutting and the defect caused by the original manufacture of the thin film. The cutting defect is described by a small deflection represented by a half-sine-wave function $\delta_c(x_1) = m_c\, sin\big((x_1 - D) \times \pi/L\big)$ on two long parallel edges (i.e. $D < x_1 < L + D, x_2 = \pm W/2$), as shown in Figure 3-20. Two magnitudes of m_c, i.e. $\pm 0.001W$ and $\pm 0.01W$, are considered for different cutting precision, where the positive and negative values represent outward and inward deflections, respectively. The original manufacturing defect is described by a random thickness distribution $h(x_1, x_2) \in (h - \delta_m, h + \delta_m)$, which will be generated randomly and applied to the finite element model elements. The random thickness distribution is carried out using the 'element distribution' function when defining the shell thickness in Abaqus. The random thickness distribution model can be built by two main steps: (1) generating a random thickness matrix corresponding to the spatial coordinates of the separator model, i.e. $h(x_1, x_2) \in (h - \delta_m, h + \delta_m)$, with the help of the 'rand' function in Matlab; (2) importing the random thickness matrix $h(x_1, x_2)$ into Abaqus as an analytical field and using the 'element distribution' function when defining the shell thickness (details can be seen in 'Using a shell section integrated during the analysis to define the section behaviour' in Abaqus (2019)). The assumed thickness error δ_m is taken to be $0.001h$ and $0.01h$ with the consideration of manufacture precision. To improve the reliability of the random distribution effects, three random defects are generated for each given δ_m.

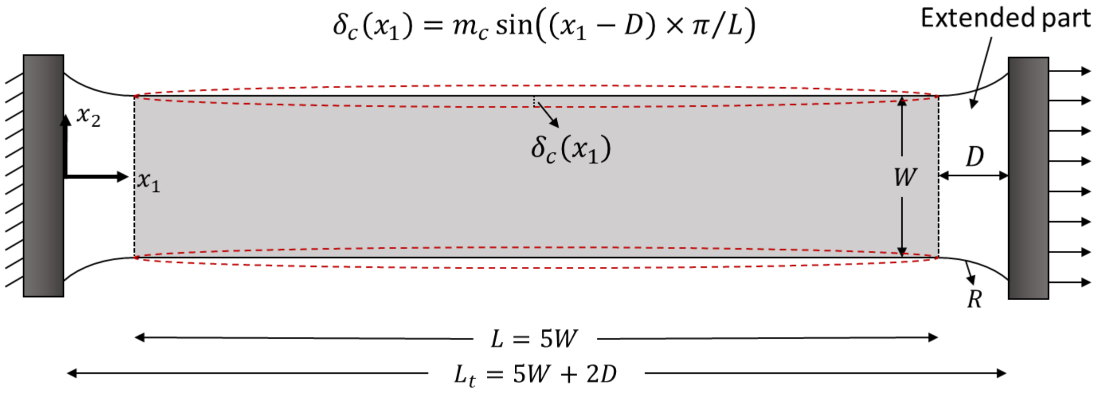

Figure 3-20 Cutting defects represented by half-sine-wave deflection ($\delta_c(x_1)$) along two long parallel edges in gauge area. Positive and negative values are associated with outward and inward deflections, respectively.

Based on the method introduced above for the description of two kinds of geometric defects, a CGB point $\alpha = 0.4, \beta = 0.305, \gamma = 1500$ is picked to investigate how the results will be affected by geometric defects. Firstly, the critical buckling strains, which is around 0.08 for the case without geometric defects, are evaluated for the influences brought by the geometric defects. The bifurcation diagrams of the dogbone geometry on this CGB point with two geometric defects modes are shown in Figure 3-21.

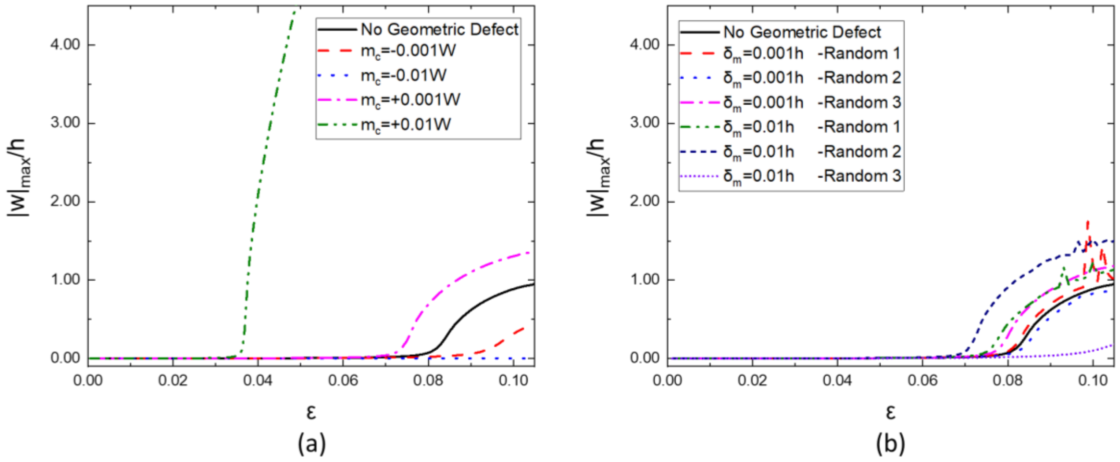

Figure 3-21 The bifurcation diagrams of dogbone geometry with $\alpha = 0.4, \beta = 0.305, \gamma = 1500$ under geometric defects caused by (a) cutting defect, and (b) original manufacturing defect.

As shown in Figure 3-21, the cutting defects can obviously influence the results (especially when $m_c = \pm 0.01W$). The outward deflection can diminish the wrinkling delay benefit brought by the dogbone geometry, whereas the inward deflection can enhance the wrinkling delay. The manufacturing defect of uneven thickness has less influence on the bifurcation diagrams compared to the cutting defect. In addition, due to the random distribution of the thickness with pre-set errors, the bifurcation points vary in a certain range around the bifurcation point ($\varepsilon \sim 0.08$) without geometric defects. The variation range depends on the magnitude of pre-set error, i.e. the smaller the pre-set error, the closer to the bifurcation point without geometric defects.

Based on the two kinds of geometric defects, their new CGB points are calculated. Then, the same method presented in Section 3.4.1, i.e. $\alpha = 0.4$ and $\gamma = 1500$ are fixed while β is varying to find the new CGBs for the various defects, is introduced. Table 3-6 shows the changes of the CGB from the origin CGB ($\alpha = 0.4, \beta = 0.305, \gamma = 1500$) caused by defects. Results shown in Table 3-6 support the conclusions made above based on Figure 3-21.

Table 3-6 The new CGB points due to the geometric defects compared to the origin CGB obtained from geometry without geometric defect.

Geometric defect modes	Defects parameter	New β			Relative errors to previous β
Sample cutting caused geometric defects	m_c				
	$+0.001W$	0.315			3.28%
	$-0.001W$	0.295			-3.28%
	$+0.01W$	0.440			44.26%
	$-0.01W$	0.200			-34.43%
Manufacturing caused geometric defects	δ_m (repeat three times)				
	$0.001h$	1	0.310		1.64%
		2	0.305		0
		3	0.310		1.64%
			Ave.	Stdev	
			0.308	0.0024	
	$0.01h$	1	0.315		3.28%
		2	0.320		4.92%
		3	0.295		-3.28%
			Ave.	Stdev	
			0.310	0.0108	

Ave. represents average and Stdev represents standard deviation.

The geometric defects discussed here only focus on two general types of defects due to cutting and manufacture to understand their influences on CGB. Further study is necessary to determine more accurate CGB if geometric defects could be quantified in actual experiments, but this is not within the scope of this research and will not be further investigated here.

3.5 Summary

In this chapter, we use a numerical method to investigate the wrinkling phenomenon which has been frequently observed in many previous studies on mechanical testing of separators. A method is proposed for the design of the dogbone thin film samples to delay or eliminate the wrinkling in uniaxial tensile tests. The new findings and contributions are

i) A critical geometric boundary (CGB) is introduced in geometric space to distinguish the wrinkling and non-wrinkling regions for uniaxial tensile tests.

ii) Based on the upper limit of the critical buckling strain defined in this study (non-wrinkling determined by no bifurcation when $\varepsilon < 0.08$), the rectangular sample with an aspect ratio (L/W) equals to 5 and thickness greater than $h = W/1200$ will not wrinkle in the uniaxial tensile test.

iii) Nested Intervals Method is used to find the typical CGB points in geometric parameter space, which can be used to guide the design of dogbone thin film samples for uniaxial tensile tests.

iv) For the relative thick thin film dogbone samples (with $W/h < 2000$), the wrinkling phenomenon is delayed until the critical strain $\varepsilon_{cr} \geq 0.08$ while for thinner dogbone samples (with $W/h > 2000$), the wrinkling can be eliminated before the critical strain reaches 0.08.

v) A function of CGB for all possible shapes of dogbone thin film samples with $W/h > 1200$ has been determined, and a 3D regime diagram is presented to define the geometric design space for thin film dogbone samples in uniaxial tensile test to prevent the occurrence of wrinkling.

vi) Lastly, by introducing geometric defects in FE models, the CGB is affected significantly by relatively large deflection in gauge area while the influence of the uneven thickness is small. In a practical application, only relatively large outward deflection could promote the occurrence of wrinkling in a uniaxial tensile test and influence the CGB. Therefore, the proposed method still has good reliability.

In conclusion, when designing a dogbone geometry for the isotropic thin film material, researchers just need to ensure the geometry-related non-dimensional parameters (α, β, γ) locates in Regime II as shown in Figure 3-17 or $F(\alpha, \beta, \gamma) > 0$ according to Eq. (3.6), no wrinkling will be shown during the uniaxial tensile test. The proposed methodology and the outcomes in the present chapter will be applicable to guide the design of isotropic separator samples in the uniaxial tensile test to improve the strain measurement accuracy (especially the transverse strain measurement), and meanwhile, allow the samples under uniaxial tensile stress state.

4 Mechanical Properties and Porosity Variations in Uniaxial Tensile Tests

4.1 Introduction

As introduced in Chapter 2, as a popular method to obtain the mechanical properties, the uniaxial tensile test has been widely conducted in the study of separators. In previous studies, engineering strains (or nominal strains) were either measured from the crosshead displacements (Cannarella et al. 2014, Sahraei et al. 2015, Xu et al. 2016, Zhang et al. 2017a) or using a digital image correlation (DIC) method (Luo et al. 2015, Zhang et al. 2016a, b, Kalnaus et al. 2017, Kalnaus et al. 2018a, Kalnaus et al. 2018b). DIC is a technique to measure the full-field displacement and strain by correlating the images of a tested specimen at different incremental deformation steps, which can produce a high-resolution deformation field on its surface (McCormick and Lord 2010). As a typical non-destructive testing method, DIC can avoid the errors caused by slipping and uneven deformation near the mechanical grips and provide more accurate measurements, which is particularly useful for the material tests of thin film specimens at a macroscopic level (Yan et al. 2018a). However, most of the uniaxial tensile tests of separators used DIC in 2D mode via a single camera (Zhang et al. 2016a, b, Kalnaus et al. 2017, Kalnaus et al. 2018b, Yan et al. 2018a), which may cause measurement errors if the camera is not perfectly perpendicular to the sample surface (Lava et al. 2011) or the sample has small out-of-plane displacements (Sutton et al. 2008). In addition, the selection of the virtual strain gauge (VSG) length area may influence the DIC measurement (Elmahdy and Verleysen 2018) due to the non-uniform strain distribution in the VSG length area (Kalnaus et al. 2017). Moreover, in most studies, strip-shaped samples were used according to ASTM D882, which, however, may sometimes cause wrinkling and can adversely affect the strain measurement accuracy (Nayyar et al. 2014, Zhang et al. 2016a, Zhu et al. 2018c). It is noted that the ‘strip-shaped’ used here is actually the ‘rectangular geometry’ indicated in Chapter 3, and the term ‘strip-shaped’ or ‘strip’ will continue to be used to describe the sample geometry in the following study. To overcome the weakness of the strip-shaped sample, we design a dogbone-shaped specimen based on the methodology proposed in the previous chapter (i.e. Chapter 3). By comparing the results of the specimens of two geometry, i.e. strip-shaped and dogbone-shaped, the proposed CGB method can also be validated.

In addition, the Poisson’s ratio is another important mechanical property for separator materials, but there are limited publications on their experimental measurements. The only publication that we can find about the research on Poisson’s ratio of separators is (Yan et al. 2018a). Yan et al. (2018a) found that the in-plane Poisson’s ratio of monolayer polypropylene (PP) separators varies with strain, and it only obeys the elastic symmetry relationship of an orthotropic material in a very small range of strain (up to 0.01 in (Yan et al. 2018a)). In constitutive models for separators, Poisson’s ratio values are usually set as a constant between 0.3 and 0.5 (Shi et al. 2011, Liu et al. 2016a).

Rather than only focusing on the mechanical properties of battery separators, the porosity of the separator is equally important. Excessive porosity can increase the ionic conductivity (Nunes-Pereira et al. 2013) but will adversely influence the overheat shutdown performance (Zhang 2007), which is important for the safety of LIBs. Furthermore, the non-uniform porosity distribution will also lead to an uneven distribution of the electric current, resulting in the lithium plating and lithium dendrites (Lee et al. 2014, Cannarella and Arnold 2015, Deimede and Elmasides 2015, Zhao et al. 2019). In most previous studies, the porosity of the separators was regarded as a constant value with uniform distribution. However, it has been shown that non-uniform stress and strain distributions can be generated in LIBs under complex external loading conditions (Greve and Fehrenbach 2012, Sahraei et al. 2012, Xu et al. 2015, Wang et al. 2019a), leading to non-uniform and varying porosity in separators (Cannarella and Arnold 2013, Lagadec et al. 2018c), which may affect separator’s electrochemical properties (e.g. tortuosity, resistance, etc.) and other physical properties (e.g. permeability) at both microscopic (Lagadec et al. 2018c) and macroscopic levels (Cannarella and Arnold 2013). Therefore, it is necessary to understand the relationship between porosity and strain state in a separator.

In this chapter, we conducted uniaxial tensile tests for four types of anisotropic commercial separators, i.e. two typical Celgard dry-processed separators and the Asahi Hipore wet-processed separators with two different thickness values, and one isotropic Asahi Hipore wet-processed separator. Based on the methodology proposed in the previous chapter (i.e. Chapter 3), we used specimens with two geometries, i.e. strip-shaped and dogbone-shaped, in the uniaxial tensile tests. During the experiment, the specimens with speckle pattern were recorded by 2 CCD cameras (i.e. cameras contain charge-coupled devices), and the full-field strains were measured by using the 3D DIC technique. The experimental strain results by selecting different sizes of VSG were also examined. In addition, the variation of the macroscopic Poisson's ratio caused by the change of pore structure is studied, and the relationship between the porosity and the tensile strain of the separators is determined. Finally, a model to describe the relationship between the separator's Poisson's ratio and porosity is proposed.

4.2 Materials

Commercial separators of monolayer polythene (PE) Asahi Kasei Hipore, monolayer PP Celgard 2500 and tri-layer (PP/PE/PP) Celgard 2325 were selected in this study with considering their wide usage (Deimede and Elmasides 2015) and different manufacturing methods. The Asahi Kasei Hipore samples are all made by the wet-processed method with two thicknesses of 16 µm (including anisotropic and isotropic behaviours) and 25 µm. Thus, Hipore-16 and Hipore-25 were used to represent the anisotropic ones with different thickness and Hipore-16-isotropic was used to represent the isotropic one, respectively. On the other hand, the Celgard samples are all made by the dry-process method with a thickness of 25 µm.

In order to find out which geometry of the thin film specimens can give reliable results, both strip-shaped and dogbone-shaped specimens were used in this study. According to the previous study (Nayyar et al. 2011), the rectangular thin film with the length-to-width aspect ratio greater than 3.7 can give a uniaxial stress state in a uniaxial tensile test, and meanwhile, meet the requirement of ASTM D882 standard. Therefore, the strip-shaped specimens were determined to be cut into 80 mm in length and 8mm in width by Swann Morton No 10A Surgical Scalpel Blade, and the grip separation was set to be 40 mm, as shown in Figure 4-1(a). The dogbone geometric parameters were determined by the proposed CGB method and pre-validated by FE simulation, as introduced in Chapter 3. However, there is still a gap between the theoretical results and the experimental results, which will be discussed in Chapter 6. The schematic of dogbone-shaped samples is shown in Figure 4-1(b). Figure 4-1(c) displays the specific cutting tool for dogbone-shaped samples and the dogbone-shaped sample that has been cut with this tool. To minimise the influences of the edge cutting and the localised compressive stress state near the clamped ends, the area of 25 mm × 6 mm in the centre is defined as the gauge area for both sample shapes to be investigated here. The printing paper was attached to the grip areas of specimens by super glue to prevent the specimens from tearing and slipping between the grips.

The microstructures of undeformed and deformed samples were taken using a Scanning Electron Microscope (Zeiss Sigma VP FEG SEM). A 10 nm thick layer of platinum was sputtered on the samples to avoid the charge build-up in SEM. Since it is difficult to carry out the in-situ tensile tests on separators (the electric beam can damage the new fibrils created without coating) (Zhu et al. 2018b), the deformed samples were imaged 4 days after the tensile test. It is noted that, after the samples were fully unloaded, they were all put into sample bags and still experienced a certain recovery within 48 hours due to the material's viscoelasticity, after which the recovery is hardly to be observed (only recovers within a certain tolerance of 1mm, measured by the ruler). It should be noted that the experiment of Hipore-16-isotropic separators was supplemented during the Covid-19 pandemic period, and due to the restriction of the labs, the SEM scanning of the deformed samples are not able to conduct.

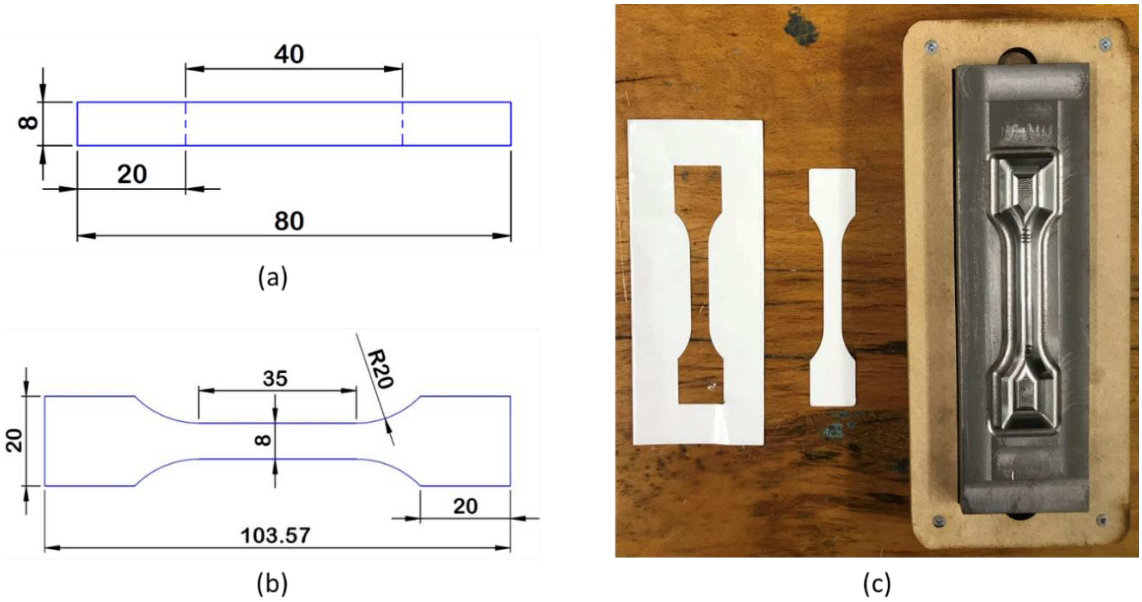

Figure 4-1 The schematic of (a) strip-shaped sample and (b) dogbone-shaped sample; (c) The dogbone cutting tool and a representative dogbone-shaped sample cut with this tool.

4.3 Methodology

4.3.1 3D DIC strain measurement

For the mechanical tests of such membrane materials, it is difficult to use an extensometer or a strain gauge to measure strain or displacement because the components are very thin and weak. Therefore, the non-contact measuring method is the best way to capture the deformation and strain distribution of these thin film materials.

DIC is an innovative non-contact optical technique that compares images of a tested specimen’s surface to generate full-field strain and displacement maps (McCormick and Lord 2010). Commonly, a speckle pattern (in this research, black speckle pattern was selected) is sprayed onto the surface of the tested specimen with high contrast backgrounds, i.e. black speckles, and white backgrounds. The pattern motion on the specimen caused by the applied load can be tracked and correlated to the reference image, and therefore, the displacement field can be calculated directly based on the calibration camera. In addition, the in-plane strain can be derived by using the engineering strain tensor (Eqs. (4.1)-(4.3)) based on the gradient of the displacement field captured by the DIC camera.

$$\varepsilon_{xx} = \frac{\partial u_{xx}}{\partial x} \tag{4.1}$$

$$\varepsilon_{yy} = \frac{\partial u_{yy}}{\partial y} \tag{4.2}$$

$$\varepsilon_{xy} = \varepsilon_{yx} = \frac{1}{2}\left(\frac{\partial u_{xx}}{\partial y} + \frac{\partial u_{yy}}{\partial x}\right) \tag{4.3}$$

where u_{xx}, u_{yy} is the displacement in x and y direction, respectively.

Based on the theory introduced above, an indispensable apparatus of the DIC system (the DIC kit used in this research was manufactured by LaVision) should be set up correctly, as shown in Figure 4-2(a). In front of the loading frame, two cameras were mounted horizontally on a tripod (calibrated by a spirit level as shown in Figure 4-2(b)) and to make sure the specimen was in the centre of the view. Two illumination lights were used to ensure the surface of the specimen is as bright as possible. By adjusting the cameras’ aperture and polarising filters (which are placed in front of the camera lens, as shown in Figure 4-2(b)), the oversaturation on the surface of the specimen can be avoided.

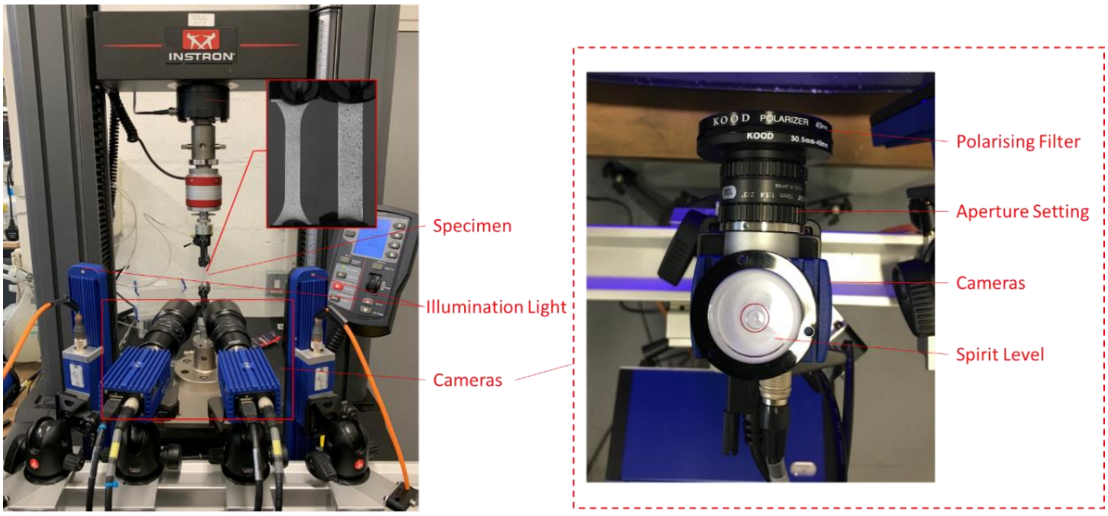

(a)

(b)

Figure 4-2 (a) The DIC setup with patterned sample mounted on the pneumatic grips, and (b) the detailed components in the camera adjustment. It should be noted that the lens in (b) is just for the explanation of the camera components, which was not used in this chapter.

In order to track the deformation during the test using 3D DIC technique, random speckle patterns on the specimens were created by spraying black paint on specimen surfaces (images of the amplified specimens in the red box in Figure 4-2(a)) using a 0.35 mm nozzle airbrush. Unlike 2D DIC, stereo calibration was required using a small etched calibration grid before carrying out the 3D DIC experiment. After the calibration, the specimens (i.e. both the strip-shaped and dogbone-shaped specimens) were mounted in the pneumatic grips suggested by ASTM D882 and loaded by an Instron loading frame with a 1000 N load cell.

All experiments were conducted at room temperature in the ambient atmosphere with three repeats for both MD and TD at a quasi-static nominal strain-rate of $\sim 10^{-3} s^{-1}$. During the tests, the image was taken every second, and the analogue outputs of load and displacement were used to synchronise the DIC and Instron loading machine. The calibration and image data were recorded by DaVis software via two Imager E-lite 5M CCD cameras (resolution of 2456 pixel × 2058 pixel). In order to obtain accurate results from DIC, all tests were stopped when the sample was damaged or the number of recording images reached 1000.

The longitudinal and transverse engineering strains of the specimens were all processed and computed by StrainMaster software, based on Eqs. (4.1)-(4.3). For each experiment, six different size VSGs, ranging from 25 mm × 6 mm down to 1 mm × 2 mm, were applied in DIC analysis to explore the effects of the VSG size. The DIC resolution uncertainty was estimated to be 0.005% strain based on the strain calculations from two recorded images of the sample in a still position under the same setting.

4.3.2 Initial porosity measurement

Porosity is defined as the ratio of the void volume to the total volume that includes the void volume and the matrix material volume of the separator. Electrolyte uptake method (Yu et al. 2018, Ding et al. 2020c, Xie et al. 2020), mercury intrusion porosimetry (MIP) (Arora and Zhang 2004), gas pycnometry (Palacio et al. 1999, Anovitz and Cole 2015), scanning electron microscope (SEM) (Lagadec et al. 2018c) and X-ray computed tomography (Finegan et al. 2016, Xu et al. 2020) were commonly used to determine the porosity of the samples. Material densities and porosities of the Celgard dry-processed separators can be obtained from available data (Peabody 2011, Finegan et al. 2016), while material densities and the porosities of the Hipore wet-processed separators measured by the non-destructive gas (i.e. helium was used here) pycnometry technique. Figure 4-3 shows the AccuPyc II 1340 gas pycnometer and the testing samples which were rolled into cylinders. The porosities of all samples were summarised and listed in Table 4-1. It is interesting to notice that the porosities in tri-layer separator samples are different in PP and PE layers since lower porosity PP layers are designed to have better mechanical integrity and PE layer with lower melting temperature is designed to shut down the transport pathway of ionic charge carriers when thermal runaway occurs.

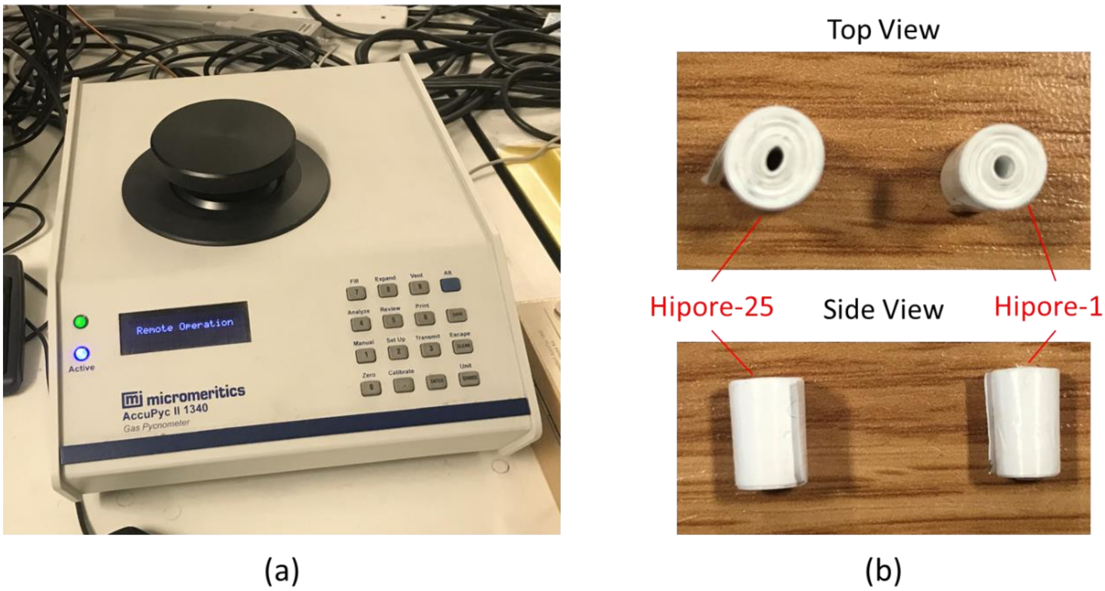

Figure 4-3 (a) AccuPyc II 1340 gas pycnometer; (b) two Hipore wet-processed separator samples for densities and porosities measuring.

Table 4-1 Characterisations of separator samples.

Sample	Composition	Density (g cm^{-3})		Initial porosity
		Avg	Stdev	
Celgard 2325	PP/PE/PP	0.91 (Peabody 2011)	-	41% (39% for PP layers, 44% for PE layer) (Finegan et al. 2016)
Celgard 2500	PP	0.91 (Peabody 2011)	-	53% (Finegan et al. 2016)
Hipore-16	PE	0.9927	0.0023	41.84%
Hipore-25	PE	0.9748	0.0013	40.79%
Hipore-16-isotropic	PE	0.9912	0.0019	43.35%

4.3.3 Relationship between porosity and strain under uniaxial tension

It has been shown that the Poisson’s ratios of the polymer matrix of the separators are relatively high (e.g. 0.42 in (Mark 2009)), which approaches the Poisson’s ratio value of

0.5 for incompressible isotropic materials. Therefore, the solid volume of the separator materials may be considered approximately as a constant during the test (Cannarella and Arnold 2013) based on the principle of mass conservation. Hence, the relationship between the current porosity Φ and the corresponding longitudinal engineering (nominal) strain ε_l of the deformed separator can be expressed as

$$\Phi(\varepsilon_l) = 1 - \frac{V_0(1 - \Phi_0)}{V(\varepsilon_l)} \tag{4.4}$$

where Φ_0 is the initial porosity, V_0 is the initial volume of the gauge area; $V(\varepsilon_l)$ is the current volume of the gauge area at longitudinal engineering strain ε_l. The current volume can be calculated by multiplying the measured length, width, and thickness before the occurrence of necking. According to (Zhang 2007), the thicknesses of all samples were measured before and immediately after tests by a micrometre with an accuracy of 1 µm. Interestingly, apart from the necking area of the tri-layer Celgard 2325 TD sample, no thickness variation was found in all samples, which means that the thickness can be regarded as a constant until the start of necking. The details of the measurement and phenomenon will be presented in Section 4.3.4. The in-situ length and width measurements were converted from the strain measured via 3D DIC, and Eq. (4.4) can be rewritten as

$$\Phi(\varepsilon_l) = 1 - \frac{L_0 W_0(1 - \Phi_0)}{L_0(1 + \varepsilon_l) W_0(1 + \varepsilon_t)} = 1 - \frac{1 - \Phi_0}{(1 + \varepsilon_l)(1 + \varepsilon_t)} \tag{4.5}$$

where ε_t is the measured transverse engineering strain, L_0 is the initial length and W_0 is the initial width of the gauge area. According to the definition of Poisson's ratio in the longitudinal direction, i.e. $v = -\varepsilon_t/\varepsilon_l$, the porosity can be finally expressed as

$$\Phi(\varepsilon_l) = 1 - \frac{1 - \Phi_0}{(1 + \varepsilon_l)(1 - v\varepsilon_l)} \tag{4.6}$$

It should be noted that the Poisson's ratio could be a variable function of the longitudinal engineering strain, i.e. $v = v(\varepsilon_l)$.

4.3.4 Details of thickness measurement (supplementary tests)

This section elaborates the supplementary thickness measurement, which is used to identify if the thickness is constant.

In order to eliminate the measurement errors caused by the speckle patterns on the surface and the curling at the edges, a supplementary uniaxial tensile test was carried out for the thickness measurement. The sample size here was determined to be a 160 mm × 25 mm strip, and the starting grip separation was set as 100 mm. All supplementary tests in this section were conducted following the method described in Section 4.3.1, but they were stopped when the crosshead displacement reached 100 mm. A digital micrometre with high precision of 1 µm was used by following the TAPPI T411 method. The measurement was stopped by the top ratchet when the contact force reaches 5-10 N to ensure the accuracy of the measurement. All samples were measured before and after the tensile test, and the measurements were repeated five times for each specimen. The measuring results are summarised in Table 4-2.

Table 4-2 The thickness values of separator samples.

Sample	Direction	Thickness (µm)	
		Before test	After test
Celgard 2325	MD	25±1	25±1
	TD		18±1 in the necking region and 25±1 in other regions
Celgard 2500	MD	25±1	25±1
	TD		25±1
Hipore-16	MD	16±1	16±1
	TD		16±1
Hipore-25	MD	25±1	25±2
	TD		25±2
Hipore-16-isotropic	MD	16±1	16±1
	TD		16±1

4.4 Results and discussion

4.4.1 DIC results

Figure 4-4 shows the uniaxial tensile engineering stress-strain curves for all samples, where the error bars are determined by standard deviation. The typical transverse strain vs. longitudinal strain curves are measured for all samples by applying a 25 mm × 6 mm VSG in the gauge area, as shown in Figure 4-5. As can be seen from both Figure 4-4 and

Figure 4-5, the dogbone samples generally have better repeatability than the strip ones, based on the error bars.

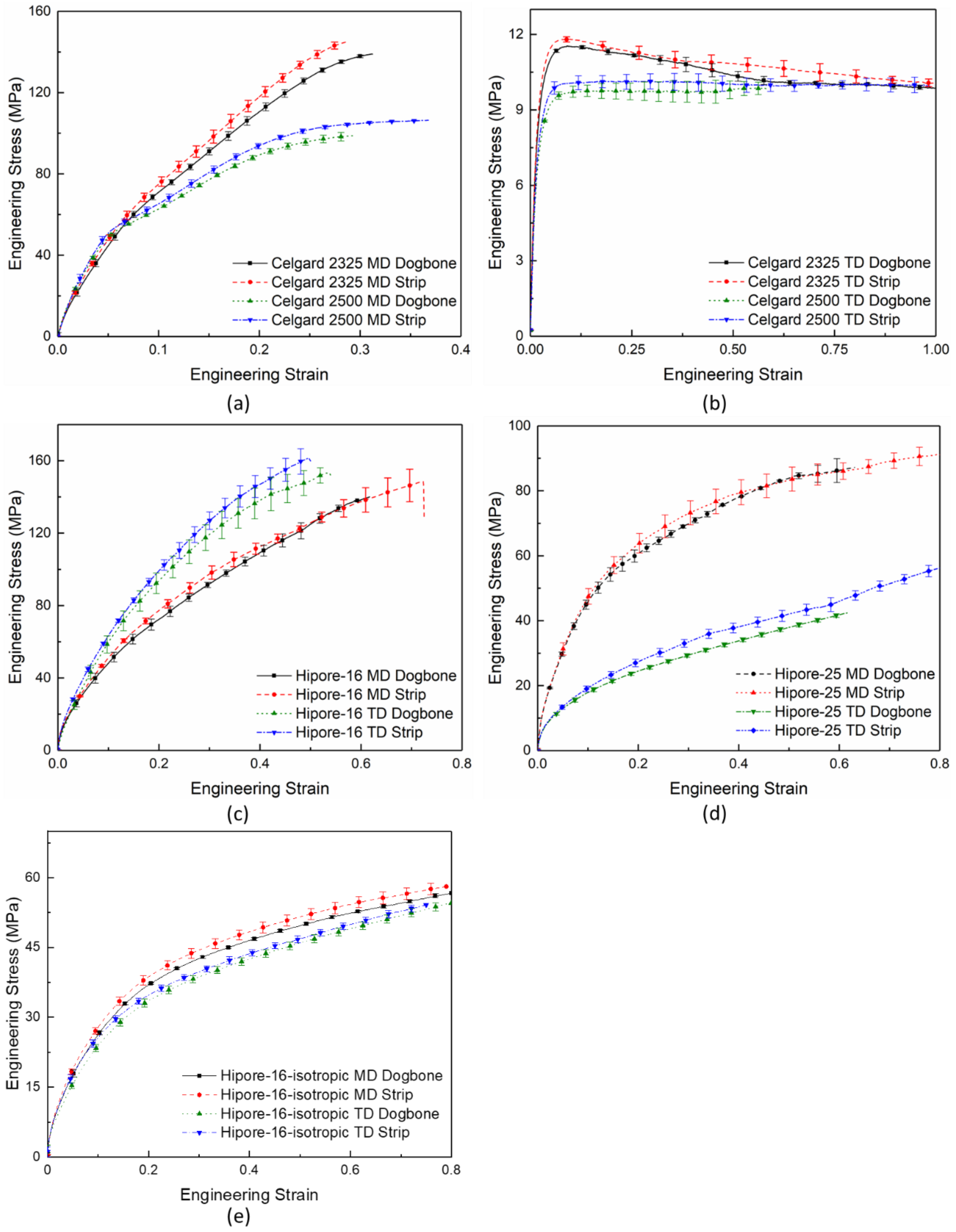

Figure 4-4 Engineering stress-strain curves of (a) Celgard dry-processed separators in MD, (b) Celgard dry-processed separators in TD, (c) Hipore-16, (d) Hipore-25 and (e) Hipore-16-isotropic.

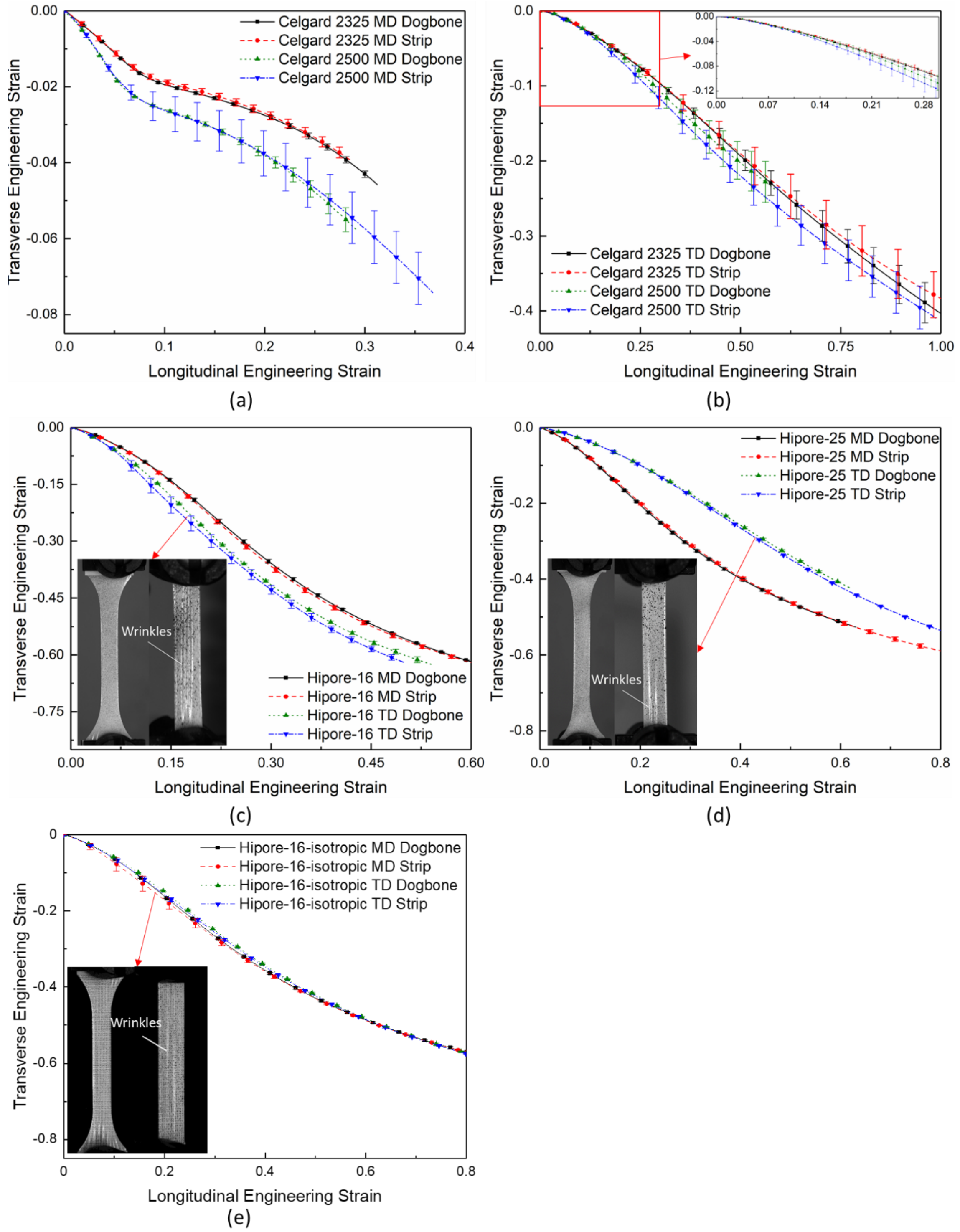

Figure 4-5 The transverse vs. longitudinal strain curves of (a) Celgard dry-processed separators in MD, (b) Celgard dry-processed separators in TD, (c) Hipore-16, (d) Hipore-25 and (e) Hipore-16-isotropic.

As shown in Figure 4-5(b), it can be noted that the results of the longitudinal strain vs. transverse strain curves for Celgard dry-processed in TD have relatively large standard deviations since the speckle patterns hidden in the wrinkle areas are not tracked effectively. According to the previous study (Zhu et al. 2018c), stretch-induced wrinkles are inevitable when a high anisotropic thin film is stretched in the low-stiffness direction, and this phenomenon can be observed in both dogbone- and strip-shaped Celgard samples here. This is because the wrinkle-free design method proposed in Chapter 3 is based on the assumption of isotropic material, the wrinkles that occurred in the Celgard samples who have high anisotropic property were not able to be eliminated.

However, for the Hipore wet-processed separators whose TD stiffness is similar to their MD stiffness, the same wrinkling phenomenon is observed in strip-shaped samples, but no wrinkle has been found in dogbone samples, as shown in Figure 4-5(c), (d) and (e), proving the wrinkle-free design method is successful for this kind of thin film material. As explained in Chapter 3, for the strip-shaped samples, the lateral contractions of the film caused by Poisson's effect are prevented by the clamped boundaries at two grip ends, which generate transverse compressive stress in the central area near the grips (Nayyar et al. 2011) and the thin film buckles to accommodate the in-plane strain incompatibility (Cerda et al. 2002). For the dogbone-shaped samples, the localised lateral compression region spreads to the sides of the specimen, and at the same time, the magnitude of the transverse compressive stress has been reduced to prevent the occurrence of wrinkling, as shown in Figure 3-19(a). It should be noted that even though the transverse compressive stress is negligible compared to the tensile stress, the produced wrinkles could adversely affect the DIC results (especially the transverse strain measurement).

To investigate the influence of VSG size and the strain distribution on the samples, a parametric study of VSG and the full-field strain observation have been carried out. Since Hipore-16-isotropic shows similar characteristics (except the fact that Hipore-16-isotropic is isotropic) to Hipore-16, the results of Hipore-16-isotropic will not be shown later in this chapter. Figure 4-6 presents the typical longitudinal strain vs. transverse strain curves obtained using different VSG sizes. The VSGs are applied to the centre of the gauge area for the specimens without apparent necking. For the specimens with noticeable necking, in order to find out the difference of the longitudinal strain vs. transverse strain relationships between the necking and other areas, the VSGs with the length of 1 mm are applied to the necking area while there is no change of the other VSG sizes in other areas. Figure 4-7 shows the longitudinal strain vs. transverse strain curves for other samples, where high consistency and similar feature (i.e. without wrinkling and structure rupture) as Celgard 2325 MD can be found.

As can be seen from Figure 4-6 and Figure 4-7, apart from the Celgard 2325 separators in TD, the results of other samples indicate that the relationships between longitudinal strain vs. transverse strain are almost independent of the VSG size, which means that Poisson's ratios of these samples can be determined reliably using the VSG sizes examined.

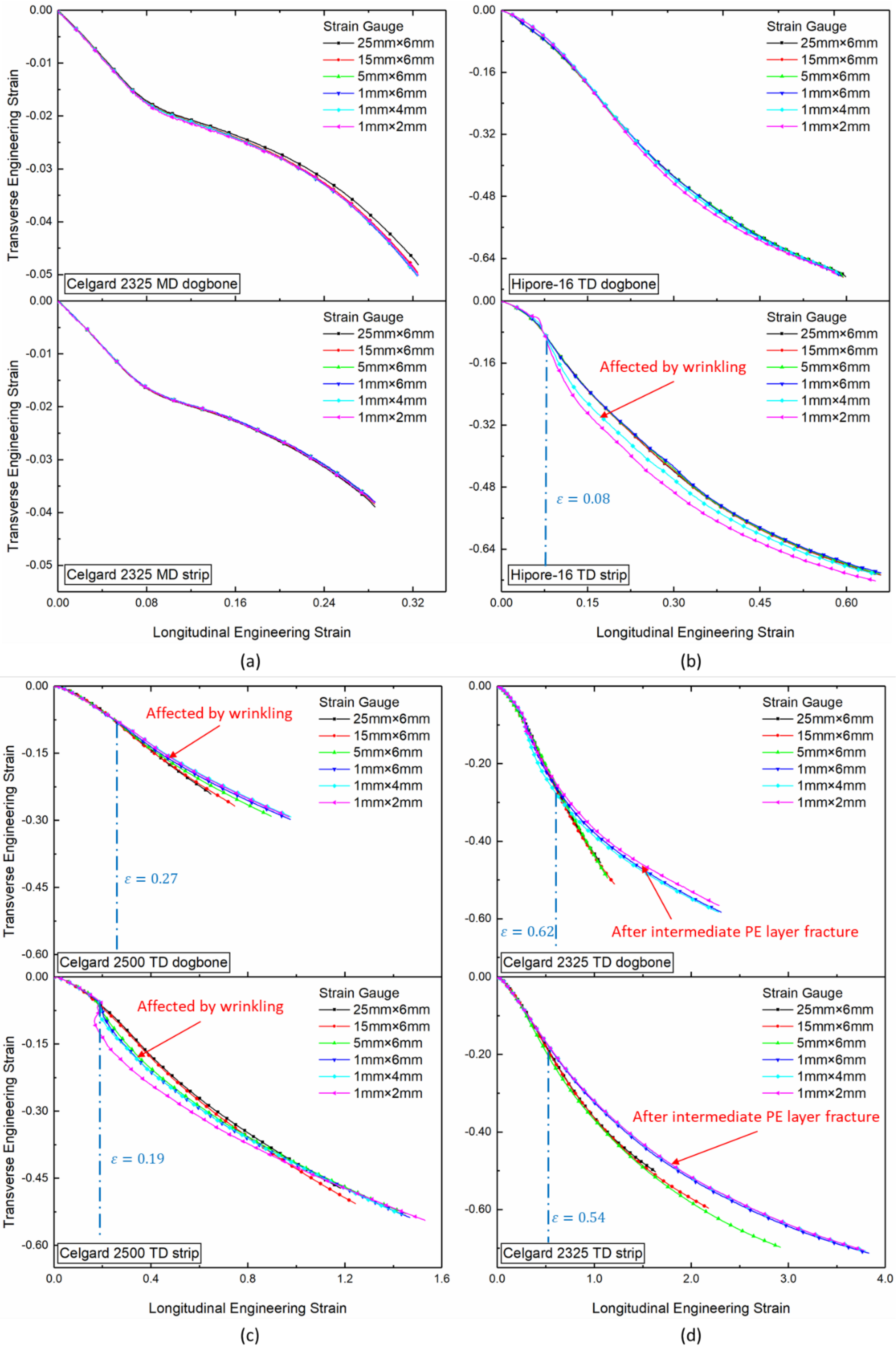

Figure 4-6 The transverse strain vs. longitudinal strain curves with different VSGs for (a) Celgard 2325 MD, (b) Hipore-16 TD, (c) Celgard 2500 TD, and (d) Celgard 2325 TD.

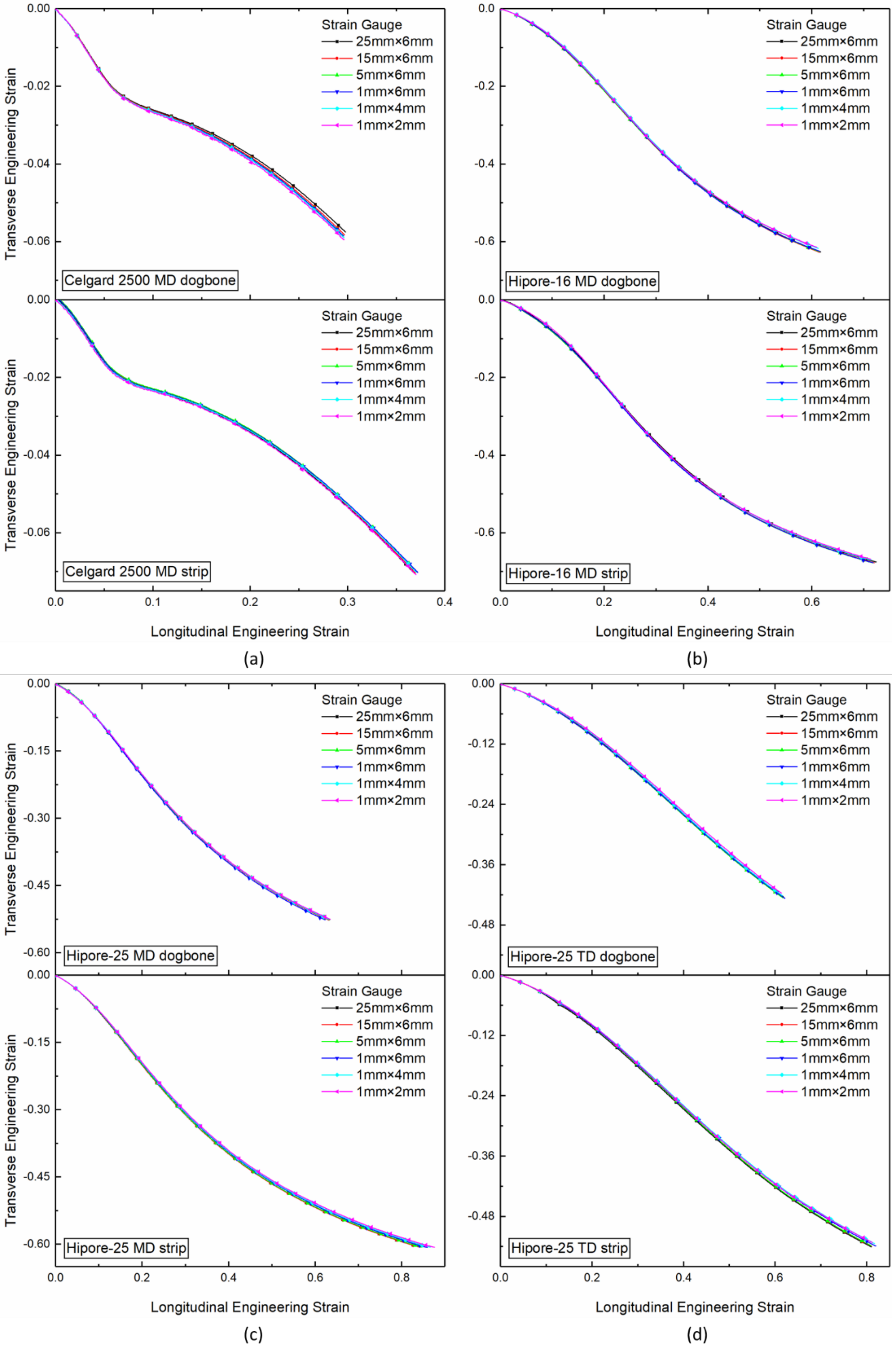

Figure 4-7 The transverse strain vs. longitudinal strain curves with different VSGs for (a) Celgard 2500 MD, (b) Hipore-16 MD, (c) Hipore-25 MD, and (d) Hipore-25 TD.

For the samples without necking (samples except for dry-processed separators in TD), uniform distribution of both axial and transverse strains can be observed from Figure 4-8(a) and (b), Figure 4-9 and Figure 4-10, which remains until failure or the end of tests, except the poor results caused by wrinkles in strip-shaped Hipore-16 TD (Figure 4-8(b)). The wrinkles cause measurement errors and result in the inconsistency of the curves starting from a longitudinal strain of 0.08, as shown in Figure 4-6(b).

For the samples with necking appearance, two different deformation mechanisms can be observed. For the Celgard 2500 in TD, even though the high localised strains generated in the necking area (Figure 4-8(c)) may cause the non-uniform distributions of longitudinal strain, it is observed from Figure 4-6(c) that the relationships between transverse and longitudinal strains are insensitive to the selection of the VSG size. However, similar to strip-shaped Hipore-16 TD (Figure 4-6(b)), inconsistent transverse strain vs. longitudinal strain curves caused by wrinkling are also observed after longitudinal strains of dogbone-shaped sample and strip-shaped sample reach 0.27 and 0.19, respectively. For the Celgard 2325 in TD, even though a similar necking phenomenon is found, Figure 4-8(d) shows that the local necking strains can reach a higher value of over 300% (this phenomenon has also been observed by Kalnaus et al. (2017)). In addition, curves of the relationship between the transverse and longitudinal strains start to be divided into two paths when the longitudinal strain reaches 0.62 in the dogbone-shaped sample and 0.54 in the strip-shaped sample, as shown in Figure 4-6(d), which is different from the phenomenon in strip-shaped Hipore-16 TD and Celgard 2500 TD. The curves for small VSGs with a length of 1mm applied on the necking regions become consistent and converge to one path, while the curves for other VSGs converge to another path. According to the SEM images of the necking cross-section area of the tri-layer Celgard 2325 separator before the test (Arora and Zhang 2004) and after the test (as shown in Figure 4-8(e) and (f), respectively), together with the observation of the 1/3 thickness reduction of the necking region (see Table 4-2), it suggests that the intermediate PE layer is fractured after the start of inconsistency. Therefore, the transverse strain vs. longitudinal strain curves, obtained from small VSG length after the occurrence of inconsistency, are the curves of the separator with only two PP layers instead of the original tri-layer one.

The underpinning causes for the influence of VSG size and the characteristics of the curves are summarised in Table 4-3.

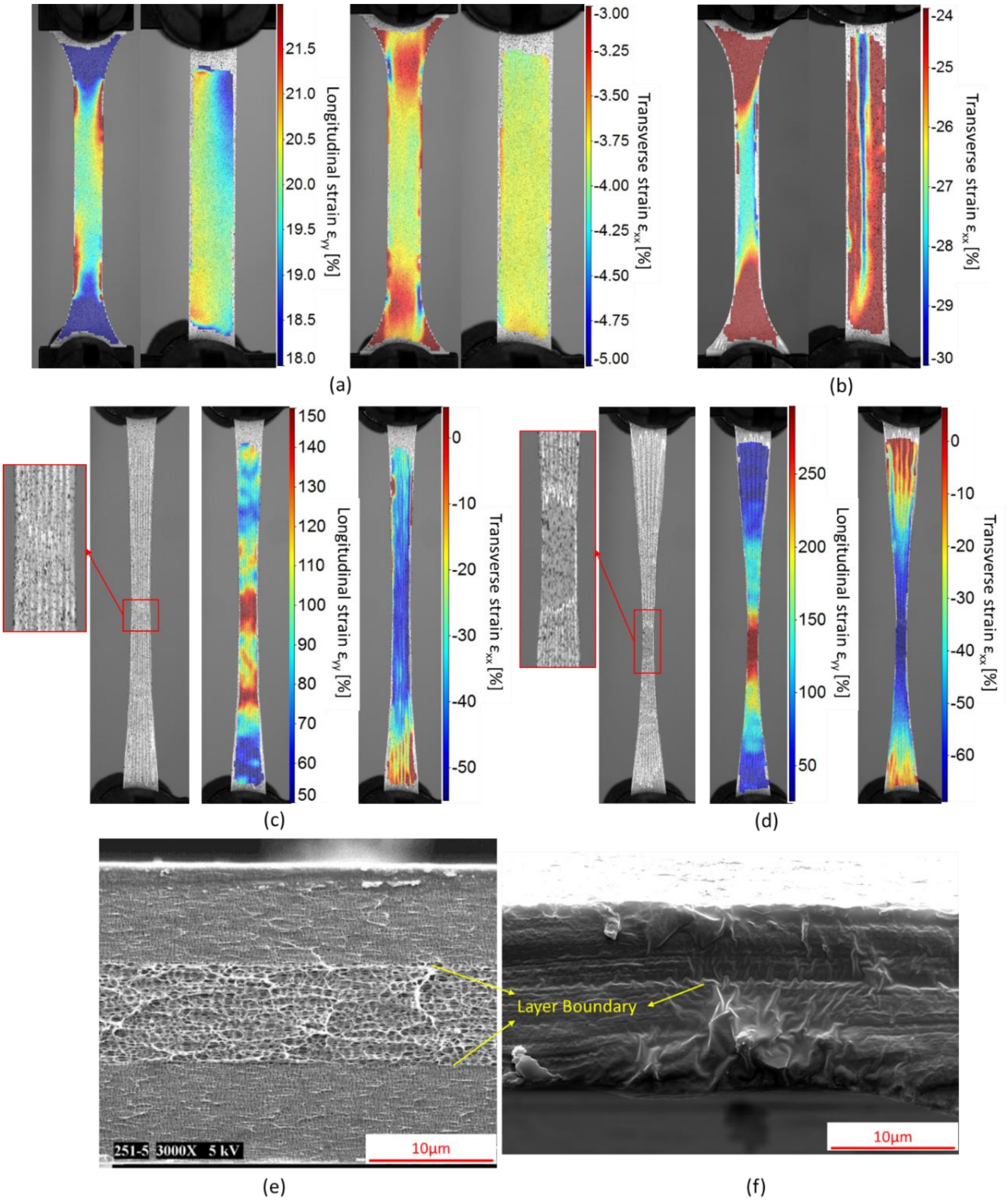

Figure 4-8 Strain distributions of (a) Celgard 2325 MD, (b) Hipore-16 TD at a longitudinal strain of 0.2; the original images and the strain distributions in (c) Celgard 2500 TD, and (d) Celgard 2325 TD at the grip movement of 36 mm; the SEM images of the necking cross-section areas of Celgard 2325 (e) before tests (Arora and Zhang 2004), and (f) after tests.

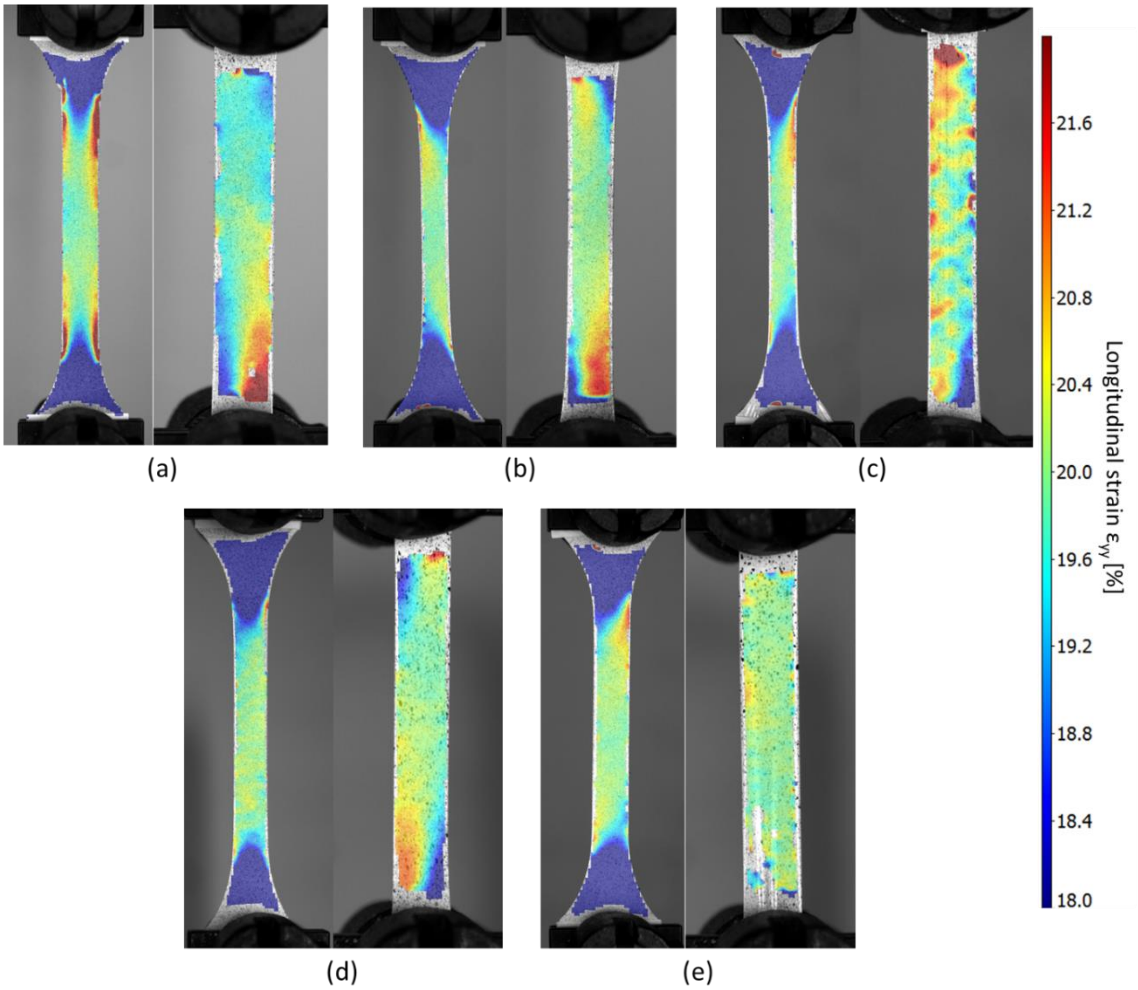

Figure 4-9 Full-field longitudinal strains of (a) Celgard 2500 MD, (b) Hipore-16 MD, (c) Hipore-16 TD, (d) Hipore-25 MD, and (e) Hipore-25 TD.

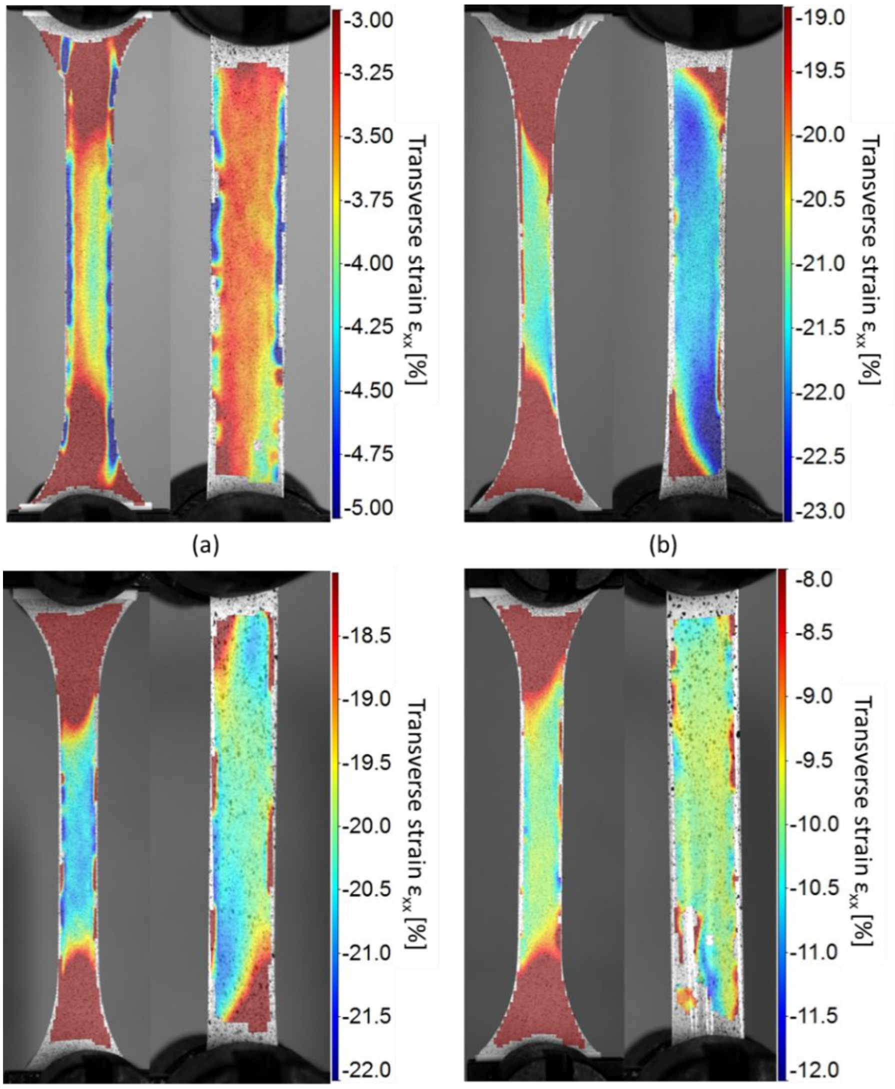

(a) (b) (c) (d)

Figure 4-10 Full-field transverse strains of (a) Celgard 2500 MD, (b) Hipore-16 MD, (c) Hipore-25 MD, and (d) Hipore-25 TD.

Table 4-3 Summary of the influence of VSG size and the underpinning causes.

Sample			Features of varying VSG curves	Causes
Celgard 2325	MD	Dogbone	Consistent	-
		Strip	Consistent	-
	TD	Dogbone	Curves for small VSG lengths converge to another path after a longitudinal strain of 0.62.	Middle PE layer rupture
		Strip	Curves for small VSG lengths converge to another path after a longitudinal strain of 0.54.	Middle PE layer rupture
Celgard 2500	MD	Dogbone	Consistent	-
		Strip	Consistent	-
	TD	Dogbone	Curves for small VSG lengths do not converge after a longitudinal strain of 0.27.	Wrinkling
		Strip	Curves for small VSG lengths do not converge after a longitudinal strain of 0.19.	Wrinkling
Hipore-16	MD	Dogbone	Consistent	-
		Strip	Consistent	-
	TD	Dogbone	Consistent	-
		Strip	Curves for small VSG lengths do not converge after longitudinal strain of 0.08.	Wrinkling
Hipore-25	MD	Dogbone	Consistent	-
		Strip	Consistent	-
	TD	Dogbone	Consistent	-
		Strip	Consistent	-

Based on the experimental results discussed in this section, the virtual live extensometer (i.e. the video extensometer), instead of DIC, is recommended for the uniaxial tensile test of the samples with uniform strain distributions (e.g. wet-processed separators, dry-processed separators in MD), which can monitor the strain results synchronously and save the post-processing time. On the other hand, DIC has a great advantage in analysing complex and non-uniform strain distributions in the sample.

4.4.2 Poisson's ratio

It should be noted that, due to the high porosity and microstructural characterisation of the samples, the Poisson's ratio calculated based on the transverse and longitudinal strains is actually a macroscopic value, instead of an intrinsic material property. In this section, the variations of Poisson's ratio are studied for strains between 0 and 0.5. The out-of-plane (i.e. through-thickness) Poisson's ratio is taken as 0 here because no thickness change is found in this range of strain, which has been discussed in Section 4.4.1. However, it seems that the in-plane Poisson's ratio is related to the complex meso-scale interactions of the pore structures, and therefore, a polynomial equation of the longitudinal strain with higher orders is selected, i.e.

$$v(\varepsilon_l) = \sum_{i=0}^{5} J_i(\varepsilon_l)^i \tag{4.7}$$

where ε_l is the longitudinal strain in the uniaxial stress state, and J_i are deformation constants obtained by fitting the experimental results. Poisson's ratio vs. strain curves are shown in Figure 4-11(a) and (b), and as a comparison, the transverse strain vs. longitudinal strain curves are also presented (Figure 4-11(c) and (d)). Constants J_i are summarised and listed in Table 4-4. The data obtained from dogbone samples with 25 mm × 6 mm VSG are used in this section.

Table 4-4 Polynomial parameters in Eq. (4.7).

Sample	Orientation	J_0	J_1	J_2	J_3	J_4	J_5
Celgard 2325	MD	0.174	2.744	-45.131	252.526	-611.701	553.140
	TD	0.088	1.632	-4.475	7.562	-6.671	2.265
Celgard 2500	MD	0.231	6.276	-115.174	750.556	-2135.757	2258.661
	TD	0.049	3.541	-23.205	85.843	-148.788	94.662
Hipore-16	MD	0.357	5.124	-7.655	-2.596	6.040	1.729
	TD	0.510	7.006	-17.730	18.002	-21.024	21.735
Hipore-25	MD	0.483	4.524	-6.977	-20.339	60.819	-42.666
	TD	0.225	2.146	-7.024	21.524	-35.688	21.557

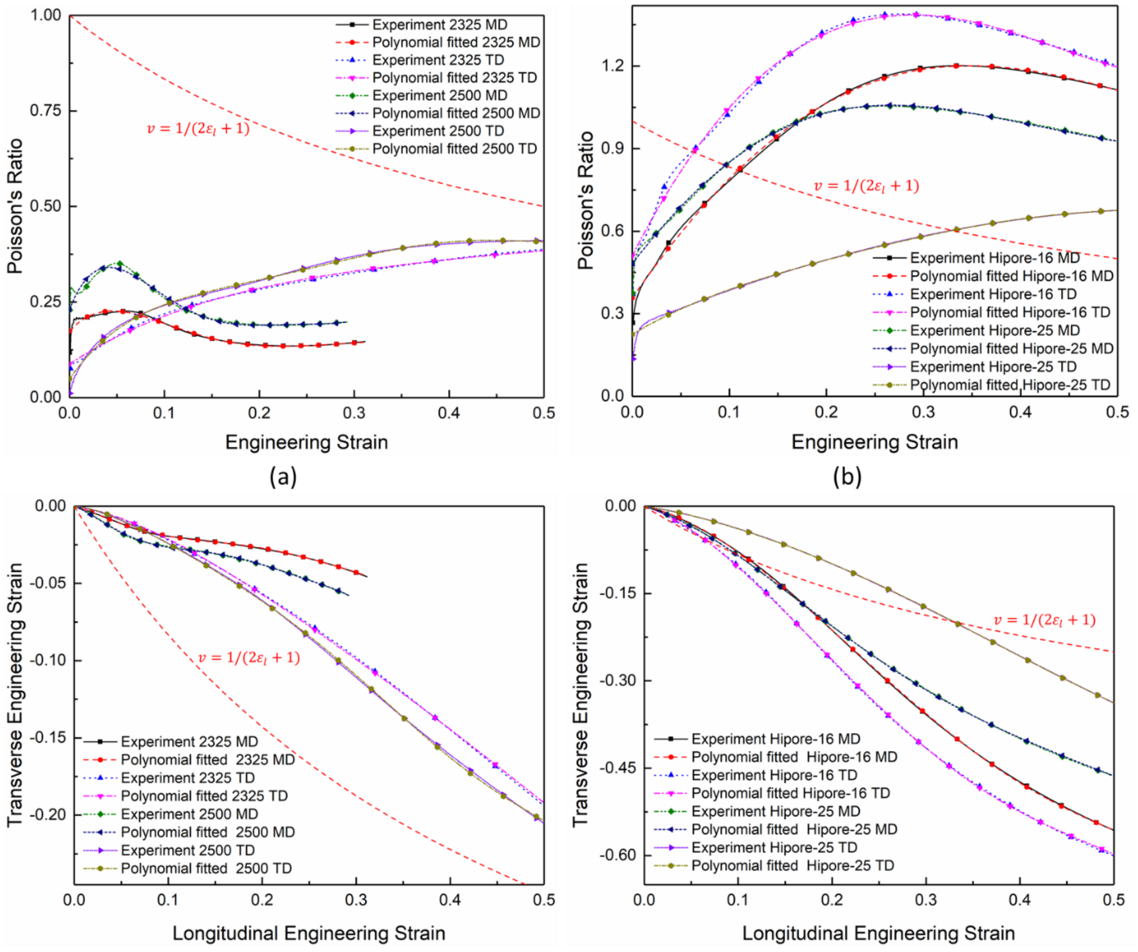

(a) (b)

(c) (d)

Figure 4-11 The Poisson's ratio vs. longitudinal strain curves for (a) Celgard dry-processed separators, and (b) Asahi Hipore wet-processed separators; the transverse strain vs. longitudinal strain curves for (c) Celgard dry-processed separators, and (d) Asahi Hipore wet-processed separators. (Note: Red dashed curves represent Poisson's ratio for constant volume).

As the volume can be calculated by

$$V = hLW = hL_0(1 + \varepsilon_l)W_0(1 - v\varepsilon_l) \tag{4.8}$$

where h is the thickness, which is approximately a constant in this case. Hence, the change of the volume is

$$dV = [1 - (2\varepsilon_l + 1)v]V_0 \tag{4.9}$$

and the in-plane Poisson's ratio for the zero-volume change (constant volume) can be obtained by

$$v = \frac{1}{2\varepsilon_l + 1} \tag{4.10}$$

which means the volume decreases under tension when the in-plane Poisson's ratio is greater than $1/(2\varepsilon_l + 1)$, and volume increase when the in-plane Poisson's ratio is less than $1/(2\varepsilon_l + 1)$. In order to indicate the volume variations of the samples, the red dashed curves of $v = 1/(2\varepsilon_l + 1)$ are illustrated in Figure 4-11, representing the constant volume. The experimental and polynomial fitted curves above the red dashed curves in Figure 4-11(a) and (b) represent volume decrease under tension, while those below the red dashed curves represent volume increase under tension. Figure 4-11(c) and (d) could be explained in a similar way.

It is shown that, for the Celgard dry-processed separators, the Poisson's ratios are fluctuated in MD and increased steadily in TD but remained less than 0.4. However, for the Asahi Hipore wet-processed separators, large Poisson's ratios can be observed (especially for the Hipore-16 TD, which can reach 1.4 at strain around 0.3), which means that the volume is decreased under tension. This unusual phenomenon can be attributed to the pore closure phenomenon under uniaxial stretching of the wet-processed separators, which will be discussed further in Section 4.4.3. When the pores collapse, the void volume reduces with the negligible changes of matrix material volume and leads to the total volume decrease, which causes the occurrence of a high Poisson's ratio. Therefore, even though the samples look like solid membranes, the invisible pore structures have strong influence on the transverse deformation and Poisson's ratio.

4.4.3 Porosity equation

Based on Eqs. (4.6) and (4.7), the variation of the porosity with longitudinal strain can be rewritten as:

$$\Phi(\varepsilon_l) = 1 - \frac{1 - \Phi_0}{(1 + \varepsilon_l)\left(1 - \varepsilon_l \sum_{i=0}^{5} J_i (\varepsilon_l)^i\right)} \tag{4.11}$$

where initial porosity Φ_0 and constants J_i are given in Table 4-1 and Table 4-4, respectively. The porosity vs. strain curves for all samples are presented in Figure 4-12.

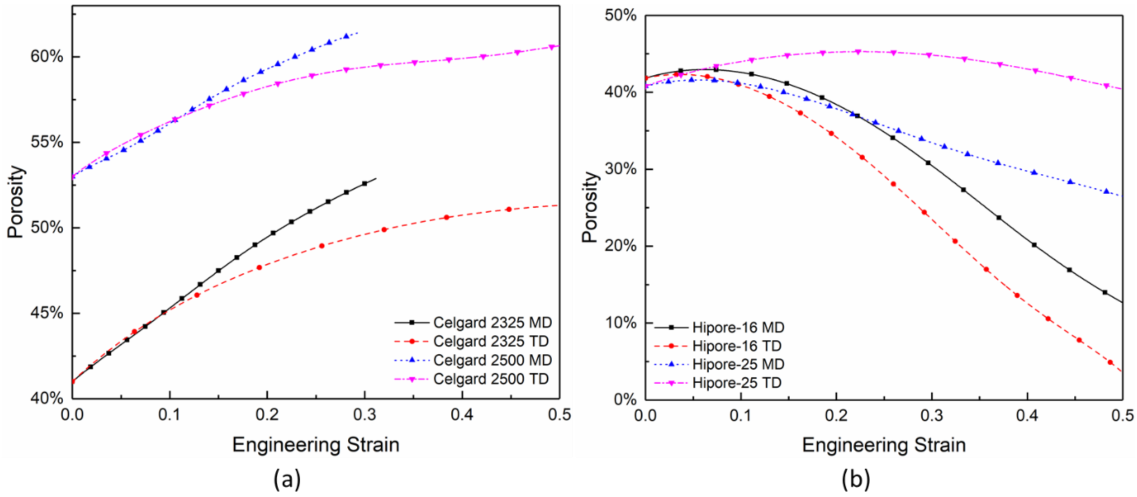

Figure 4-12 The porosity vs. strain curves of (a) Celgard dry-processed separators, and (b) Asahi Hipore wet-processed separators.

It can be clearly seen that the porosities of the Celgard dry-processed separators increase steadily with the longitudinal strains in both MD and TD. In the range of strain between 0 and 0.1, the porosities of all Celgard samples increase linearly with strain by around 5%. Then, the increase of porosity in MD is faster than that in TD. For the Asahi Hipore wet-processed separators, an opposite trend of porosity variation is observed compared to the dry-processed one. The porosities of all wet-processed samples increase slightly at the initial small strain, and then start to decrease with strain. Especially for the Hipore-16, the porosity is reduced significantly to less than 15% when the strain reaches 0.5. The difference in porosity variation between dry-processed and wet-processed separators is due to the different pore structures from different manufacturing processes, as shown in Figure 4-13.

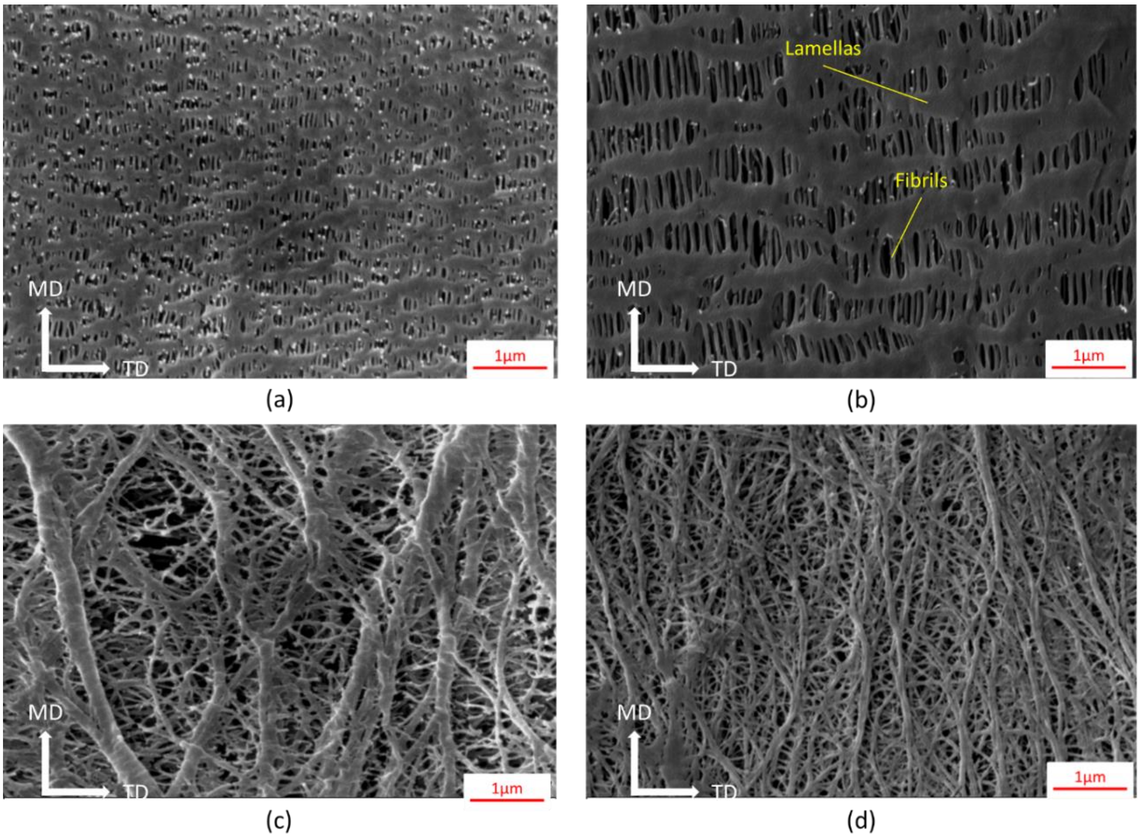

(a) (b) (c) (d)

Figure 4-13 SEM images of (a) Celgard 2325, (b) Celgard 2500, (c) Hipore-16 and (d) Hipore-25 before tensile test.

It can be clearly seen that the dry-processed separators have a split-like pore structure, which is mainly formed by the TD oriented lamellas and the MD oriented fibrils between lamellas (see Figure 4-13(a) and (b)), while the wet-processed separators have pores formed by unoriented fibrils of different sizes (see Figure 4-13(c) and (d)).

The phenomenon that the porosities of dry-processed separators increase with strains is supported by the interrupted in-situ tensile tests conducted by Zhu et al. (2018b). When a dry-processed separator is stretched in MD, the crazing of lamellas can cause the formation of new fibrils and new pores, and no change in pore size can be found. When it is loaded along with TD, no obvious new fibrils are developed, but the lamellas become thinner and the pore size is increased. Even the porous microstructures of a dry-processed separator are deformed in different ways when it is stretched in different directions, its porosities always increase as a result of increasing void volume with unchanged matrix material volume, which supports the porosity equation, i.e. Eq. (4.11), and the corresponding curves in Figure 4-12(a).

Figure 4-14 illustrates the microstructures of the deformed wet-processed separators after four days from the tensile tests (i.e. after the full recovery of the viscoelastic deformation). Although they are not the instantaneous microstructures of the sample at the end of the tensile test, it can be seen that the pore structures have changed, and the variation trends of their porosity are similar to the predicted results in Figure 4-12(b). When the Hipore-16 is stretched, the fibrils are forced to form lamellas caused by transverse shrinkage, as shown in Figure 4-14(a) and (b). Significant pore-closure can be found in this 16 µm thick wet-processed separator sample, especially for the one stretched in TD, which has a good agreement with the results in Figure 4-12(b). Compared to Hipore-16, Figure 4-14(c) and (d) show that Hipore-25 has a minor pore-closure characterisation under tensile loading. When Hipore-25 is stretched in MD, most of the pores are getting smaller and several bundles of thin lamellas are formed by the combination of fibrils, which is similar to the Hipore-16 stretched in MD. For the Hipore-25 stretched in TD, the pores are reshaped as a result of fibrils deformation, but no significant pore-closure can be found here, which also supports the trend shown in Figure 4-12(b).

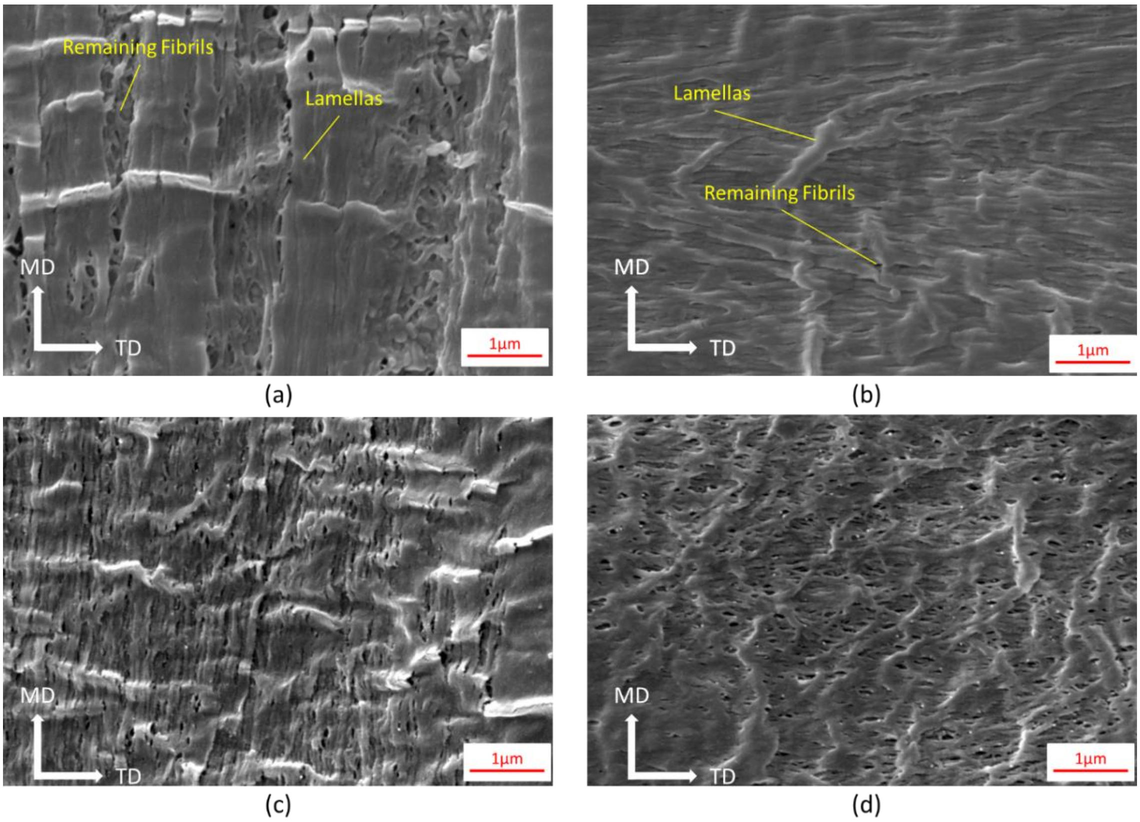

Figure 4-14 SEM images of after deformed samples: (a) Hipore-16 MD, (b) Hipore-16 TD, (c) Hipore-25 MD and (d) Hipore-25 TD.

Lastly, the mechanical safety of LIBs (or other liquid electrolyte batteries) is an important issue for current industrial applications such as EVs and other portable electronic products, and the separator is the most important factor to safety. Previously, studies of mechanical integrity were mostly focusing on the mechanical fracture of the separator on a macro-level when it suffered external loadings. However, when a LIB was deformed by an external loading (such as bending, crushing, etc.), deformations or strains were not distributed homogeneously. The local uneven porosity of the separators caused by inhomogeneous strain distribution can result in non-uniform distribution of the electric current, which should be considered in multiphysics modelling.

4.5 Summary

In this chapter, mechanical behaviours and porosity variations of four typical types of commercial separators were investigated by uniaxial tensile tests monitored by the 3D digital image correlation (DIC) technique. Traditional strip-shaped samples and wrinkle-free design guided dogbone-shaped samples were both tested for comparison. It is found that dogbone-shaped samples had better consistent results by avoiding the appearance of wrinkling in the wet-processed separators (even though two of them have slight anisotropy) compared to strip-shaped samples. However, as the wrinkle-free design method proposed in Chapter 3 is based on the assumption of isotropic material, its effectiveness for the dry-processed separators that are highly anisotropic is less than expected. Uniform strain distributions remain until the end of tests in both MD and TD of all wet-processed separators and in only MD of dry-processed separators, while localised high strains and apparent necking are observed in TD of dry-processed separators. Three typical types of transverse strain vs. longitudinal strain curves for different virtual strain gauge (VSG) sizes are observed. For the samples without structure ruptures and wrinkling, high consistent curves are found in the measurements. For these samples, it is also recommended to use a virtual live extensometer (i.e. video extensometer) in the uniaxial tensile test, because it can better monitor the strain results synchronously and save post-processing time. For the samples with severe wrinkling but without structure rupture, curves for small VSGs do not converge after a certain longitudinal strain. For the Celgard 2325 TD, as the intermediate PE layer rupture occurs in the necking region, the curves for small VSGs applied on necking converge to a different path compared to the curves for other VSGs.

In the range of strain between 0 and 0.5, the out-of-plane Poisson's ratio can be regarded as zero, and no thickness change can be found, while the in-plane Poisson's ratio varies with strain for all separators due to the meso-scale interactions of the pore structures. A polynomial function is used to describe the relationship between Poisson's ratio and longitudinal strain, and the coefficients are fitted by the DIC results. Distinct variations of Poisson's ratios are found in different samples, i.e. relatively small variations of Poisson's ratio (remained below 0.4) are found in dry-processed separators. In contrast, Poisson's ratios of wet-processed separators increase considerably and even exceed unity for the one with a thickness of 16 μm. The porosity variations associated with strains are calculated by the deformation based on the assumption of the constant volume of the matrix material. Different relationships between porosity and strain are found, in which the porosities of dry-processed separators increase with strain while the porosities of wet-processed separators decrease with strain. These characterisations also have a good agreement with the previous work (Zhu et al. 2018b) and SEM images of the microstructures of the samples, which demonstrates that the proposed porosity equation is reliable and can be used in both mechanical analyses and coupled mechanical-electrochemical (or multiphysics) analyses for batteries.

5 Hyper-Viscoelastic Constitutive Model for Isotropic Separators

5.1 Introduction

As introduced in Section 2.3, many analytical, numerical and experimental studies have been done for the elastic and elastic-plastic responses of various separators with different manufacturing processes (Zhang et al. 2016a, b, Yu et al. 2018, Ding et al. 2020a) under various environmental conditions (e.g. wet/dry (Cannarella et al. 2014, Xu et al. 2016, Xie et al. 2019), temperatures (Avdeev et al. 2013, Kalnaus et al. 2018b), charge-discharge cycles (Zhang et al. 2017c) and strain-rates (Cannarella et al. 2014, Xu et al. 2016, Kalnaus et al. 2017, Kalnaus et al. 2018b, Hao et al. 2020), as well as for separators when serving in batteries (Sahraei et al. 2015, Wang et al. 2019a, Yuan et al. 2019, Lee and Kim 2020, Yuan et al. 2020). However, the viscoelastic response commonly occurs in separators due to its inherent mechanical behaviour of viscosity. To investigate the viscoelastic properties of separators, creep tests using the dynamic mechanical analyser (DMA) were commonly used (Sheidaei et al. 2011, Xu et al. 2016, Yan et al. 2018a). Based on experimental results, both isotropic (Xu et al. 2016) and orthotropic (Yan et al. 2018a, Yan et al. 2020) viscoelastic models have been developed. However, these viscoelastic models are linear and usually limited by the small-strain condition up to 0.01 strain (Yan et al. 2018a, Yan et al. 2020), which have also been introduced in Section 2.4.

On the other hand, in most studies about the strain-rate effects of the separator (Cannarella et al. 2014, Kalnaus et al. 2017, Kalnaus et al. 2018b, Hao et al. 2020), the investigated nominal strain-rates range from $10^{-6}\ s^{-1}$ up to $2 \times 10^{-1}\ s^{-1}$, in which viscoelasticity dominates the stress response of the separators. Therefore, the increase of the stress response with strain-rate found in the previous studies should be attributed to the viscoelastic effect. In the present study, the strain-rate effect will not be used to avoid confusion.

From Chapter 4, it can be known that the separator can experience a large deformation and the accompanied viscoelastic behaviour, which means that a constitutive model that can address these issues is necessary. Therefore, the hyper-viscoelastic (HVE) model has been reviewed in Section 2.5.

In this chapter, we will introduce the ‘two-step method’ (Grujicic et al. 2009, Briody et al. 2012, Wei and Olatunbosun 2016) and the numerical ‘stress solution method’ (Goh et al. 2004, Fazekas and Goda 2018, 2019), propose an ‘inverse stress solution method’ and compare these three methods to demonstrate the advantages of the inverse stress solution method. A series of tension-relaxation tests were applied to a commercial wet-processed isotropic separator under four different loading nominal strain-rates. Firstly, the theory of the HVE model is introduced, which is composed of a hyperelastic model (including Neo-Hookean model, Mooney-Rivlin model, and Marlow model) (see Section 5.4.1) and a finite-strain viscoelastic model (see Section 5.4.2). Then, the parameter calibration methods, i.e. the ‘two-step method’ and the ‘stress solution method’, will be elaborated based on the principle of the HVE model. Finally, a new ‘inverse stress solution method’ will be proposed. Based on the three methods, HVE material models are calibrated by the same set of experimental data. The HVE models determined by three methods are established in FE software Abaqus and compared with the experimental results.

5.2 Experimental Method

5.2.1 Material

In this chapter, the isotropic commercial wet-processed separator of monolayer polythene (PE) with 16 µm thickness manufactured by Asahi Kasei, which is Hipore-16-isotropic in Chapter 4, is selected to be studied. The microstructure of the separator captured by scanning electron microscope (SEM) can be seen from Figure 5-1(a). The nominal stress-strain curves and longitudinal-transverse strain curves were tested by uniaxial tensile test and measured by 3D DIC by following the methods introduced in Chapter 4, as shown in Figure 5-1(b) and (c) (or Figure 4-4(e) and Figure 4-5(e)), respectively. It can be seen from these figures that the sample has a high isotropic characteristic because an equally biaxial stretching method was applied in the stretching step during the manufacturing of the wet-processed separator. Moreover, no evident linear elastic regime can be observed in Figure 5-1(b), and Figure 5-1(c) shows its

Poisson's ratio is close to $v = 0.5$ (i.e. material is almost incompressible). The details of the studied separator sample in this chapter are shown in Table 5-1.

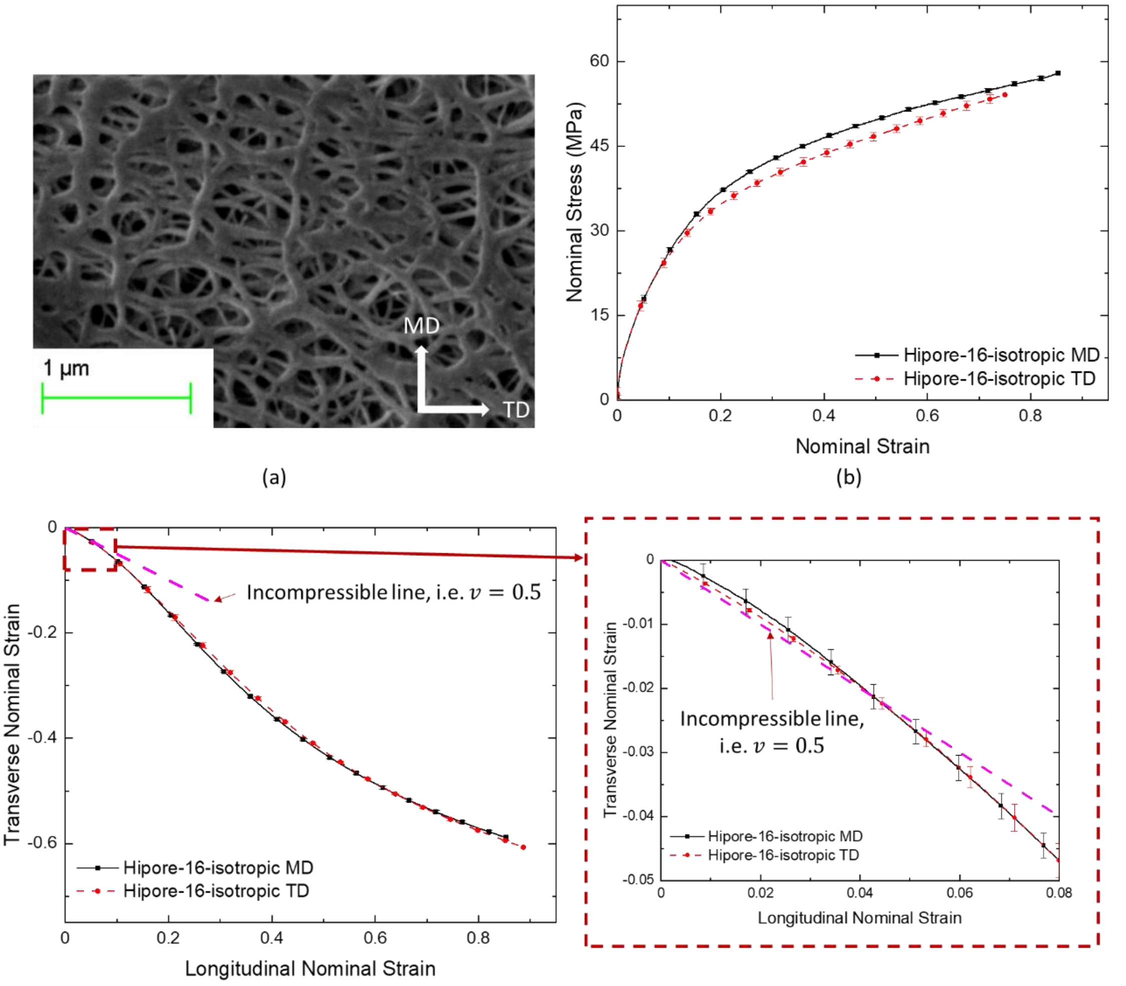

(a) (b)

(c)

Figure 5-1 (a) SEM characterisation images of Asahi Kasei wet-processed separator; (b) Nominal stress-strain curves; (c) transverse-longitudinal strain curves of samples tested separately along MD and TD, measured by 3D DIC according to the methodology introduced in Chapter 4, where high isotropy and no evident linear elastic regime were observed.

Table 5-1 The details of the studied wet-processed separator.

Manufacturer	Composition	Thickness	Porosity	Gurley	Puncture Strength [a]	Tensile Strength
Asahi Kasei	PE	16 μm	43.35%	177 sec	700 g/mil	>1500 kg/cm^2

[a] Puncture strength (g/mil) means a gram-force per 0.025 mm thickness, which means 700 g/mil ≈ 274 N/mm (Baldwin et al. 2010).

5.2.2 Sample preparation and experimental setup

As a virtual live extensometer will be used in this study, two black dots will be marked on the sample to be traced (details see the last paragraph of this section). To reduce the effects caused by the black dots, the size of the sample should be increased. However, due to the Covid-19 pandemic, the manufacturing of the dogbone cutter (similar to Figure 4-1(c)) will be difficult. As can be seen in Figure 4-9, the wrinkling phenomenon only has an insignificant influence on the strain measurement in longitudinal direction (x_1 direction shown in Figure 3-1). Therefore, to simplify the experimental preparation, strip-shaped samples (instead of dogbone-shaped samples) were determined to be used in this chapter without the loss of measurement accuracy because only the nominal strain in the longitudinal direction is required in the following analysis. It is also advantageous to use a strip-shaped sample, instead of using a dogbone-shaped sample, to study the material viscoelasticity because the nominal strain for the relaxation stage is controlled by the crossheads, between which a uniform sample should be used. According to ASTM D882, in order to maintain a uniaxial stress state during the test, the samples were cut into 145 mm in length and 16 mm in width by Swann Morton No 10A Surgical Scalpel Blade, and the grip separation (gauge length) was set to be 80 mm, as shown in Figure 5-2(a). Besides, super glue was used to attach the printing paper to the clamping areas of specimens, to prevent the specimens from tearing and slipping between the grips.

In the uniaxial tensile test, specimens were mounted in a pair of pneumatic grips (i.e. air-actuated grips) according to the recommendations in ASTM D882, and then loaded by an Instron loading machine with a 1000 N load cell. The setup of the experiment is shown in Figure 5-2(b). As the wet-processed separator investigated here is regarded as an isotropic material, the loading direction will be carried out on MD of the samples. All experiments were conducted at room temperature (i.e. 22±2 ºC, which is an important condition of the experiment) with at least four repeats.

In the experiments introduced in this section, a virtual live extensometer has been used as a function implemented in DaVis 10 software (manufactured by LaVision). Based on the prior DIC measurement results and the outcome from Chapter 4, the wet-processed separator has uniform deformation (i.e. homogeneity of strain distribution) during the uniaxial tensile test. Hence, a virtual live extensometer can be used effectively and precisely to replace the 3D DIC technique for the measurement of nominal strain. In order to trace the accurate nominal strain during the uniaxial tensile test in real-time, two black dots were marked permanently in the centre area of the specimen by a marker pen with a 50 mm separation as the gauge length, then framed and traced by a virtual extensometer in the field of camera view, as shown in Figure 5-2(b). The nominal strain reading was synchronously written to the data recording of the loading machine via analogue input with a sampling frequency of 50 Hz.

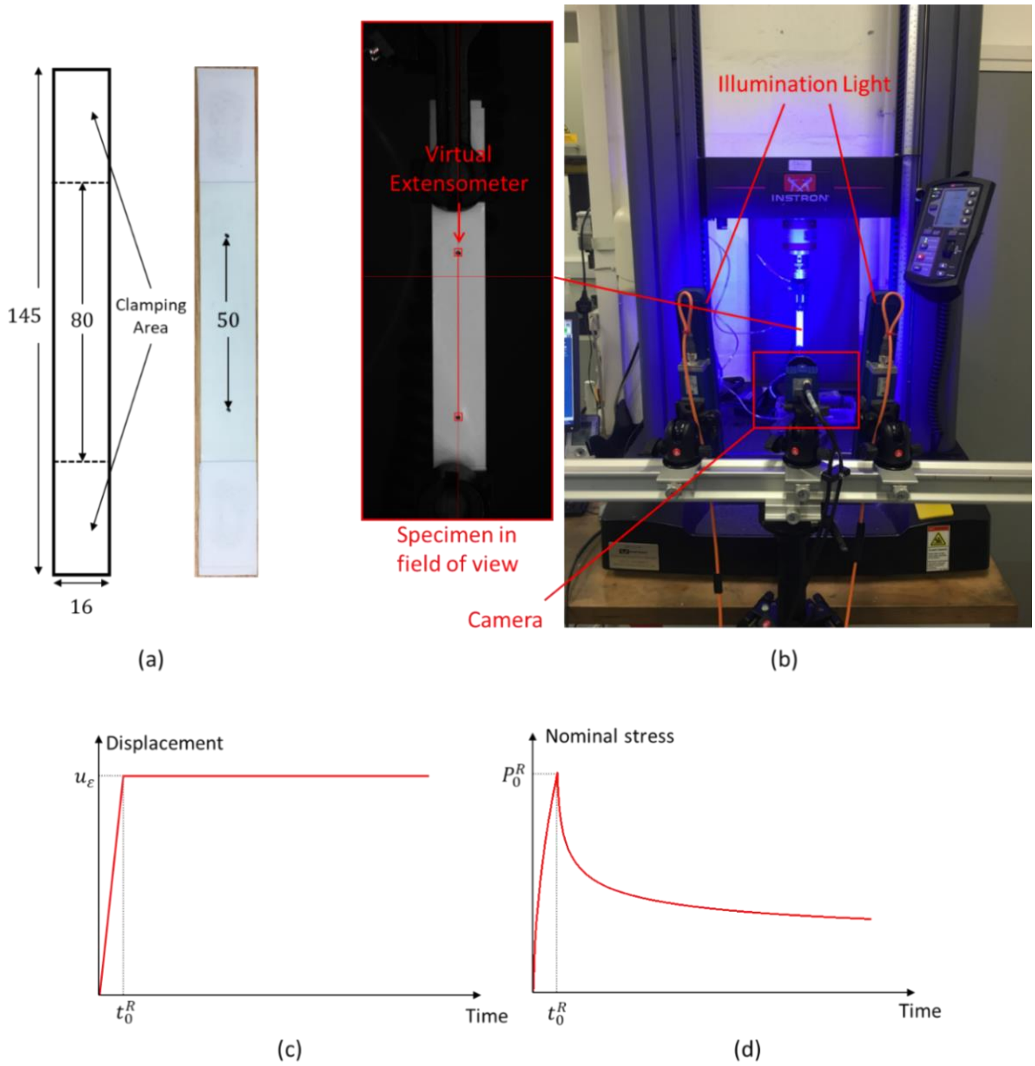

Figure 5-2 (a) The schematic of specimens used in uniaxial tensile test; (b) the experimental setup of uniaxial tensile tests measured by a virtual live extensometer; (c) the representative curves of crosshead displacement vs. time; (d) nominal stress vs. time in the experiment.

5.2.3 Tension-relaxation test

To determine the time-dependent mechanical behaviours of this wet-processed isotropic separator, a tension-relaxation test was designed according to ASTM E328-13. The tension-relaxation test can be divided into two stages, i.e. the uniaxial tensile loading stage and the stress relaxation stage. In the tensile loading stage (or ramp-loading stage), a ramp-loading is applied by the moving grip controlled by displacement (i.e. displacement-controlled constraint) at a constant speed (or loading nominal strain-rate) to generate stress response until a given nominal strain (ε_R) (obtained from virtual extensometer) is reached. It should be noted that the nominal strain measured by the live virtual extensometer keeps as a constant when the crosshead is stopped to move. In the stress relaxation stage, the displacement constraint at the end of the ramp-loading stage remains constant (i.e. the movement of the crosshead is stopped) to keep a given constant nominal strain for a long period, during which the stress relaxation is recorded. The schematics of the crosshead motion and the typical nominal stress recorded in the tension-relaxation test can be seen in Figure 5-2(c) and (d), respectively. P_0^R, u_ε and t_0^R represent the initial nominal stress, the displacement constraint corresponding to the given nominal strain and the time at the beginning of the relaxation stage, respectively.

In the first stage (i.e. ramp-loading stage), various loading speeds, i.e. 0.008 mm/s, 0.08 mm/s, 0.8 mm/s and 8 mm/s, were set, which correspond to the loading nominal strain-rates of $10^{-4}\ s^{-1}$, $10^{-3}\ s^{-1}$, $10^{-2}\ s^{-1}$ and $10^{-1}\ s^{-1}$, respectively. It should be noted that the loading nominal strain-rates presented above are calculated based on the relative movement of the crossheads, which are also close to the value calculated by the measurement of the virtual live extensometer. Besides, the given nominal strains (ε_R) used in the stress relaxation stage were set as 0.05, 0.1 and 0.15, respectively. For all relaxation stages under different loading conditions, a sufficiently long relaxation time of 2500 s was set to obtain the complete relaxation processes.

5.3 Experimental results

Based on the experimental setup introduced above, the experimental results of the uniaxial tension-relaxation test with various loading nominal strain-rates and different strain-controlled relaxations (ε_R) are presented in Figure 5-3.

It is shown in Figure 5-3 that the experimental results at four different loading nominal strain-rates have good consistency, i.e. the loading response in the ramp-loading stage increases with strain-rate. It should be noted that, in the case of $10^{-1}\ s^{-1}$ in Figure 5-3(a), the nominal stress experienced a sudden drop between the first stage (loading at constant strain-rate) and the second stage (relaxation at constant strain) in the experiment. The underlying reason for this phenomenon is that the moving crosshead cannot be stopped immediately at the prescribed relaxation strain when it is loaded at a relatively high loading nominal strain-rate of $10^{-1}\ s^{-1}$, leading to a small overshot around the maximum stress, as shown in Figure 5-4. In addition, it should be noted that due to the same reason (i.e. the moving crosshead cannot be stopped immediately at the prescribed relaxation strain), the actual constrained strain ($\varepsilon_R = 0.058, 0.116, 0.159$) at the stress-relaxation stage is slightly higher than the prescribed strain (i.e. $\varepsilon_R = 0.05, 0.10, 0.15$) in the case of this loading nominal strain-rate, as shown in Figure 5-3(a).

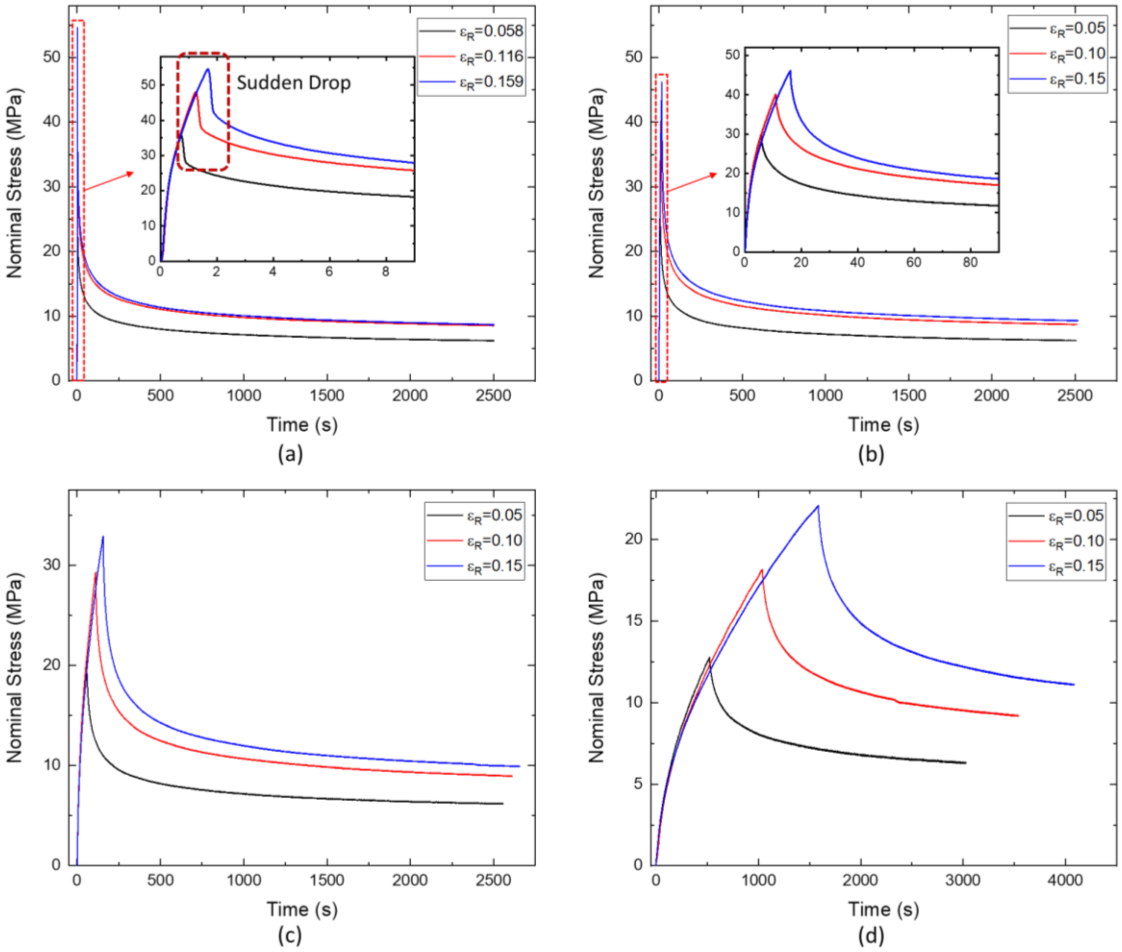

Figure 5-3 The nominal stress-time curves with various initial relaxation strains under loading nominal strain-rate of (a) $10^{-1}\ s^{-1}$, (b) $10^{-2}\ s^{-1}$, (c) $10^{-3}\ s^{-1}$, and (d) $10^{-4}\ s^{-1}$.

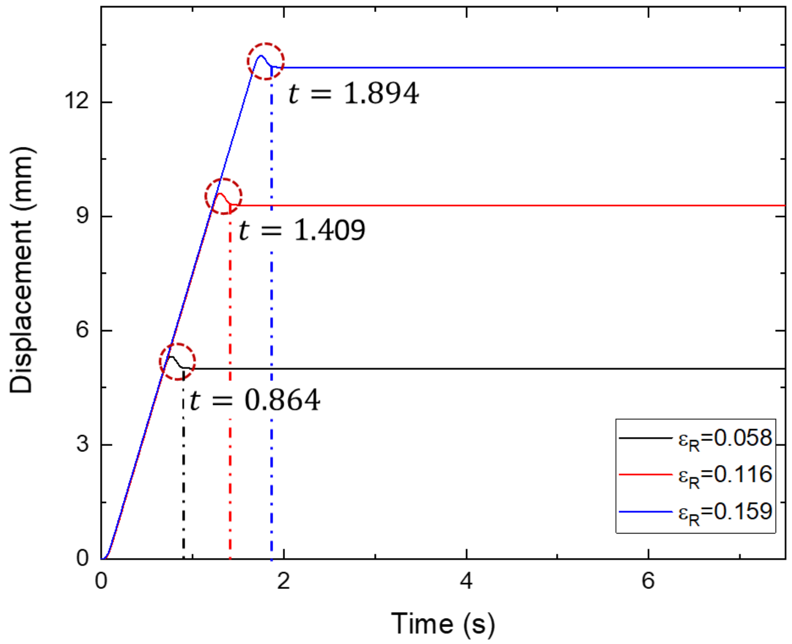

Figure 5-4 The curves of the crosshead movement vs. time of the tension-relaxation test at loading nominal strain-rate of $10^{-1}\ s^{-1}$.

Figure 5-5 shows the nominal stress-strain curves at various loading nominal strain-rates (with error bars determined by the standard deviation). On the other hand, Figure 5-6 and Figure 5-7 show the variations of the uniaxial nominal stresses (P) with time for $\varepsilon_R = 0.05, 0.10, 0.15$ at different loading nominal strain-rates.

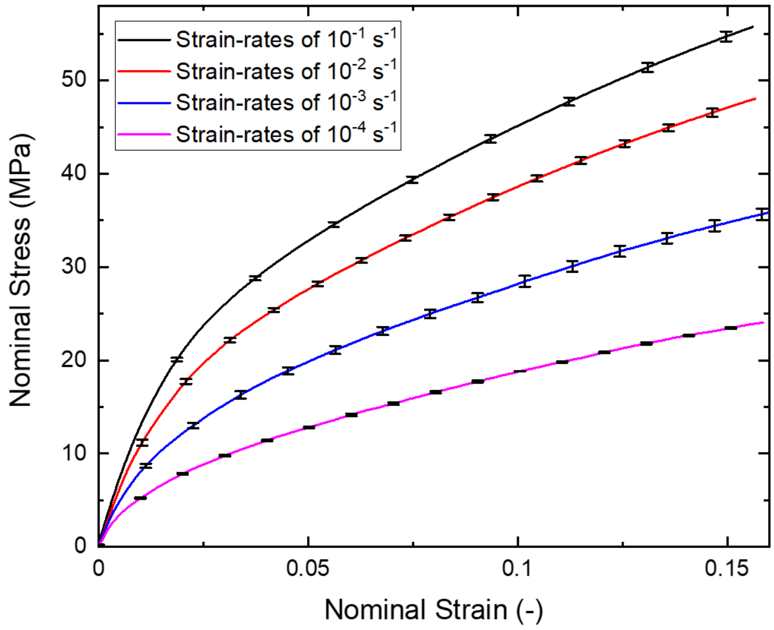

Figure 5-5 The nominal stress vs. nominal strain curves at various loading nominal strain-rates.

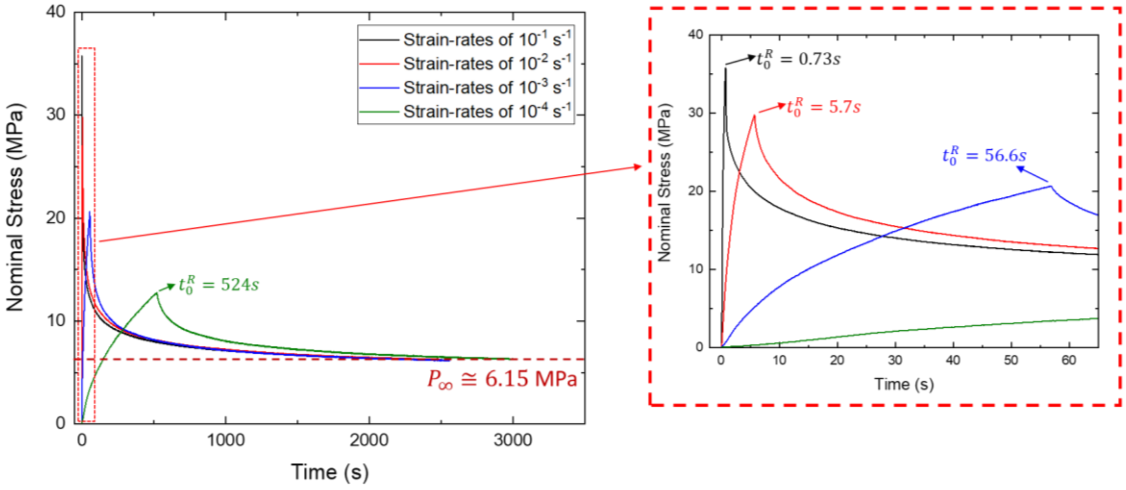

Figure 5-6 The nominal stress vs. time with $\varepsilon_R = 0.05$ at various loading nominal strain-rates.

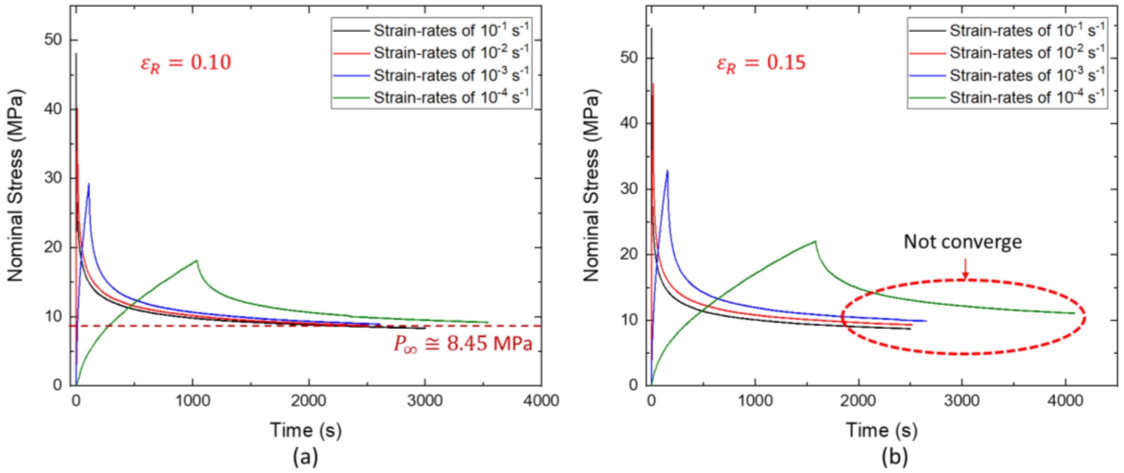

Figure 5-7 The nominal stress vs. time with (a) $\varepsilon_R = 0.10$ and (b) $\varepsilon_R = 0.15$ at various loading nominal strain-rates.

As can be seen in Figure 5-5, it is evident that the nominal stress increases with the strain-rate, which was also observed in previous studies (Cannarella et al. 2014, Kalnaus et al. 2017, Kalnaus et al. 2018b, Hao et al. 2020). In their studies, this phenomenon was regarded as a strain-rate effect, and for the variation of Young's modulus under different nominal strain-rates (range from $10^{-6}\ s^{-1}$ up to $2 \times 10^{-1}\ s^{-1}$), effective moduli (defined as a function of nominal strain-rate) was used to describe them, i.e. Eq. (2.7). However, in classical solid mechanics (Johnson 1983, Jones 2011), strain-rate effect is normally relevant to the yield stress instead of Young's modulus. In addition, as can be seen in Figure 5-6, the long-term nominal stress P_∞ is eventually converged to a same value around $P_\infty \cong 6.15$ MPa with the increase of time. Similar phenomenon was also observed from experiments for $\varepsilon_R = 0.10$, as shown in Figure 5-7(a). This phenomenon indicates that the material response can be interpreted as viscoelastic response (modulus is varying with time) without the involvement of permanent deformation (i.e. no yield stress in this case). Furthermore, the modulus shows a high nonlinearity with the deformation in Figure 5-6, indicating that the modulus should be nonlinear and varying with deformation, which is contrary to previous studies (they consider modulus is a constant under single strain-rate) (Cannarella et al. 2014, Kalnaus et al. 2017, Kalnaus et al. 2018b, Hao et al. 2020). Hence, in this study, the viscoelastic effects are more suitable to describe the material behaviour of separator compared to the strain-rate effects mentioned in previous studies (Cannarella et al. 2014, Kalnaus et al. 2017, Kalnaus et al.

2018b, Hao et al. 2020), and the effective modulus should be related to the stress relaxation time instead of strain-rate.

On the other hand, the long-term nominal stress is unable to converge at different loading nominal strain-rate when $\varepsilon_R = 0.15$, which implies that the separators were yielded or damaged when $\varepsilon_R = 0.15$. Material yield or damage occurs at different strains when $\varepsilon > \varepsilon_y$ where $0.10 < \varepsilon_y < 0.15$ is the yielding strain, depending on nominal strain-rate, which belongs to visco-elastoplastic regime where the strain-rate effect is usually referred to its effect on the plastic deformation, which is outside the scope of this research and will not be further investigated here. Therefore, the viscoelastic effects are investigated in the strain range of $0 < \varepsilon < 0.10$ in this study.

Based on the experimental observation (i.e. existence of nonlinear elastic regime, various stress-strain relationships in ramp-loading stage and distinct viscoelastic behaviour in stress-relaxation stage), a nonlinear hyper-viscoelastic (HVE) model is considered here for the isotropic homogeneous wet-processed separator.

5.4 Theory of hyper-viscoelastic (HVE) constitutive model

In this section, the framework of the hyper-viscoelastic (HVE) constitutive model used in Abaqus (Abaqus 2019) is elaborated. It should be noted that the symbol in bold (e.g. $\boldsymbol{\sigma}$) represents a tensor.

5.4.1 Incompressible hyperelastic models under uniaxial tension

According to the previous studies (Cannarella and Arnold 2013), the separator materials have a relatively high Poisson's ratio (approaches to 0.5). Meanwhile, Figure 5-1(c) also shows that the separator used in this study has the characteristics close to incompressible materials (i.e. $v = 0.5$). Therefore, the separator can be assumed as an incompressible material here. In the development of the incompressible hyperelastic constitutive model, the mechanical behaviour is usually described by the relationship between the strain energy potential (or strain energy density) W_e and the invariants of strain tensor ($I_{1,2,3}$). In most of previous research, Neo-Hookean (NH) model (Nayyar et al. 2014, Fazekas and Goda 2019) and Mooney-Rivlin (MR) model (Goh et al. 2004, Grujicic et al. 2009, Fazekas and Goda 2018, A. López-Campos et al. 2019, Fazekas and Goda 2019) are two most common hyperelastic models used in the relevant studies. These two hyperelastic models can be expressed as (Mooney 1940, Rivlin 1948)

$$W_e^{NH} = C_{10}(I_1 - 3) \tag{5.1}$$

$$W_e^{MR} = C_{10}(I_1 - 3) + C_{01}(I_2 - 3) \tag{5.2}$$

where the strain energy potential W_e is the strain energy stored per unit of reference volume (i.e. the original volume); C_{10} and C_{01} are the material parameters (MR model becomes NH model when $C_{01} = 0$); I_1 and I_2 are the first and second invariant of strain tensor, given by (Mooney 1940, Rivlin 1948)

$$I_1 = {\lambda_1}^2 + {\lambda_2}^2 + {\lambda_3}^2 \tag{5.3}$$

$$I_2 = {\lambda_1}^{-2} + {\lambda_2}^{-2} + {\lambda_3}^{-2} \tag{5.4}$$

where λ_i is the principle stretch ratio in ith direction, which is related to the nominal strain ε via $\lambda_i = 1 + \varepsilon_i$, $(i = 1,2,3)$.

Besides NH and MR models, Marlow's hyperelastic model (Marlow 2003) is also common in hyperelastic material studies (Ghoreishy 2012, Ghoreishy et al. 2014). It allows the use of only uniaxial test data to calibrate the model parameters, which is also available in Abaqus (2019). However, unlike other hyperelastic models, Marlow model is determined directly from the experimental nominal stress-strain data, which can be described by (Marlow 2003)

$$W_e^{Marlow} = W_e^{Marlow}(I_1) \tag{5.5}$$

Therefore, in Marlow model, there are $2M$ parameters where M is the sampling number of (stress, strain) points in a material test.

In the case of uniaxial tensile loading, the deformation gradient **F**, expressed in the principal stretch ratio, can be written as

$$\mathbf{F} = \begin{bmatrix} \lambda_1 & 0 & 0 \\ 0 & \lambda_2 & 0 \\ 0 & 0 & \lambda_3 \end{bmatrix} \tag{5.6}$$

where $\lambda_1 = \lambda$ denotes the principle stretch ratio in the direction of uniaxial loading, and λ_2 and λ_3 indicate the stretch ratios in the other two transverse directions. As the material is assumed to be incompressible and isotropic, the total volume change at a point (i.e. the determinant of deformation gradient **F**) is zero, or $\det \mathbf{F} = 1$, which leads to $\lambda_1\lambda_2\lambda_3 = 1$. Therefore, $\lambda_2 = \lambda_3 = 1/\sqrt{\lambda}$, and Eq. (5.6) can be written as

$$\mathbf{F} = \begin{bmatrix} \lambda & 0 & 0 \\ 0 & 1/\sqrt{\lambda} & 0 \\ 0 & 0 & 1/\sqrt{\lambda} \end{bmatrix} \tag{5.7}$$

and Eqs. (5.3) and (5.4) become

$$I_1 = {\lambda_1}^2 + {\lambda_2}^2 + {\lambda_3}^2 = \lambda^2 + \frac{2}{\lambda} \tag{5.8}$$

$$I_2 = {\lambda_1}^{-2} + {\lambda_2}^{-2} + {\lambda_3}^{-2} = \frac{1}{\lambda^2} + 2\lambda \tag{5.9}$$

As the strain energy potential W_e is determined by the principal stretches $(\lambda_1, \lambda_2, \lambda_3)$, the uniaxial instantaneous Cauchy stress σ_0 and nominal stress (i.e. the first Piola-Kirchhoff stress) P_0 can be determined by $\lambda \cdot \partial W_e/\partial\lambda$ and $\partial W_e/\partial\lambda$, respectively. The stress solutions of the three hyperelastic models can be expressed as

$$\sigma_0^{NH} = \lambda \frac{\partial W_e^{NH}}{\partial \lambda} = 2C_{10}\left(\lambda^2 - \frac{1}{\lambda}\right) \tag{5.10}$$

$$\sigma_0^{MR} = \lambda \frac{\partial W_e^{MR}}{\partial \lambda} = 2(C_{10}\lambda + C_{01})\left(\lambda - \frac{1}{\lambda^2}\right) \tag{5.11}$$

$$\sigma_0^{Marlow} = \lambda \frac{\partial W_e^{Marlow}}{\partial \lambda} \tag{5.12}$$

$$P_0^{NH} = \frac{\partial W_e^{NH}}{\partial \lambda} = 2C_{10}\left(\lambda - \frac{1}{\lambda^2}\right) \tag{5.13}$$

$$P_0^{MR} = \frac{\partial W_e^{MR}}{\partial \lambda} = 2(C_{10}\lambda + C_{01})\left(1 - \frac{1}{\lambda^3}\right) \tag{5.14}$$

$$P_0^{Marlow} = \frac{\partial W_e^{Marlow}}{\partial \lambda} \tag{5.15}$$

5.4.2 Finite-strain viscoelasticity

To characterise both nonlinear elastic behaviour and viscoelastic behaviour under finite-strain regime, the hyper-viscoelastic (HVE) model in Abaqus material library (i.e. a combination of the hyperelastic model and a time-domain finite-strain viscoelastic model) is used to describe the behaviour of the separator in FE modelling in this research. It should be noted that the pure hyperelastic model, which is a time-independent model as introduced in Section 5.4.1, is usually determined by converting the nominal stress-strain relations into strain energy potential forms $W_e\left(I_{1,2,3}\right)$ (Abaqus 2019). However, in the HVE model, the experimentally-measured stress response to the applied strain is a 'time-dependent' viscoelastic stress response $\boldsymbol{\sigma}(\mathbf{F},t)$, consisting of the 'time-independent' (i.e. 'instantaneous') stress response (i.e. elastic or hyperelastic response) $\boldsymbol{\sigma}_0(\mathbf{F})$ and the 'time-dependent' viscoelastic relaxation response. It should be noted that in the HVE model defined in (Abaqus 2019), Kirchhoff stress tensor is used. However, in the case of an incompressible material, the instantaneous Kirchhoff stress tensor is the same as the instantaneous Cauchy stress tensor (Holzapfel 2002), and therefore, Cauchy stress tensor $\boldsymbol{\sigma}$ is used here. The constitutive equations and derivation equations in this section refer to (Holzapfel 2002, Fazekas and Goda 2018, Abaqus 2019, Fazekas and Goda 2019)

To clarify the relationship between $\boldsymbol{\sigma}_0(\mathbf{F})$ and $\boldsymbol{\sigma}(\mathbf{F},t)$, we firstly decompose the Cauchy stress tensor ($\boldsymbol{\sigma}_0$ and $\boldsymbol{\sigma}$) as the summation of the deviatoric part and hydrostatic part

$$\boldsymbol{\sigma}_0(\mathbf{F}) = \boldsymbol{\sigma}_0^D(\mathbf{F}) + \boldsymbol{\sigma}_0^H(\mathbf{F}) \tag{5.16}$$

$$\boldsymbol{\sigma}(\mathbf{F},t) = \boldsymbol{\sigma}^D(\mathbf{F},t) + \boldsymbol{\sigma}^H(\mathbf{F},t) \tag{5.17}$$

where superscript D and H represent the deviatoric and hydrostatic parts, respectively; subscript 0 denotes the instantaneous stress response. In practice, the deformation (or strain) is applied as a function of time t, and therefore, the deformation history ($\mathbf{F}(t)$) can be used to replace $\mathbf{F}$ in Eq. (5.16), i.e.

$$\boldsymbol{\sigma}_0\left(\mathbf{F}(t)\right) = \boldsymbol{\sigma}_0^D\left(\mathbf{F}(t)\right) + \boldsymbol{\sigma}_0^H\left(\mathbf{F}(t)\right) \tag{5.18}$$

On the other hand, the hyper-viscoelastic stress $\boldsymbol{\sigma}(\mathbf{F},t)$, which is the actually measured stress, can therefore be expressed as a function of single variable of time, i.e. $\boldsymbol{\sigma}(t)$, i.e.

$$\boldsymbol{\sigma}(t) = \boldsymbol{\sigma}^D(t) + \boldsymbol{\sigma}^H(t) \tag{5.19}$$

Therefore, the relationship between the 'time-dependent' viscoelastic stress response $\boldsymbol{\sigma}(t)$ and the instantaneous stress response $\boldsymbol{\sigma}_0\left(\mathbf{F}(t)\right)$ can be written in the following form according to (Abaqus 2019)

$$
\begin{aligned}
\boldsymbol{\sigma}(t) &= \boldsymbol{\sigma}^D(t) + \boldsymbol{\sigma}^H(t) \\
&= \left(\boldsymbol{\sigma}_0^D\big(\mathbf{F}(t)\big) + \int_0^t \frac{\dot{G}(s)}{G_0} \boldsymbol{\sigma}_0^D\big(\mathbf{F}(t-s)\big) ds\right) \\
&\quad + \left(\boldsymbol{\sigma}_0^H\big(\mathbf{F}(t)\big) + \int_0^t \frac{\dot{K}(s)}{K_0} \boldsymbol{\sigma}_0^H\big(\mathbf{F}(t-s)\big) ds\right)
\end{aligned}
\tag{5.20}
$$

where s is the reduced time, $\dot{G}(s) = dG(s)/ds$, and $\dot{K}(s) = dK(s)/ds$. $G(t)$ and $K(t)$ are the time-dependent shear and bulk moduli, respectively; G_0 and K_0 are the instantaneous shear and bulk moduli, respectively. The term 'instantaneous' can be regarded as when the time approaches to 0, e.g. $G_0 = \lim\limits_{t\to 0} G(t)$ is the instantaneous shear modulus and $\boldsymbol{\sigma}_0\big(\mathbf{F}(t)\big) = \boldsymbol{\sigma}_0^D\big(\mathbf{F}(t)\big) + \boldsymbol{\sigma}_0^H\big(\mathbf{F}(t)\big) = \lim\limits_{t\to 0} \boldsymbol{\sigma}(\mathbf{F}, t)$ is the instantaneous Cauchy stress. Theoretically, increasing the loading speed applied to the sample (or reducing the loading time) in a test can reduce the time-dependent viscoelastic influence (i.e. $\lim\limits_{t\to 0}\left[\int_0^t \big(\dot{G}(s)/G_0\big) \cdot \boldsymbol{\sigma}_0^D\big(\mathbf{F}(t-s)\big) ds + \int_0^t \big(\dot{K}(s)/K_0\big) \cdot \boldsymbol{\sigma}_0^H\big(\mathbf{F}(t-s)\big) ds\right] = 0$) on the experimental determination of $\boldsymbol{\sigma}_0(\mathbf{F})$. However, the inevitable inertial effect may cause the overshooting of the machine-controlled displacement (see Figure 5-4), and thus, a sudden drop of the measured 'instantaneous' stress (see Figure 5-3(a)). Therefore, it is impossible to obtain accurate instantaneous stress-strain data directly from a single ramp-loading tensile test. Hence, it is necessary to develop an experimental procedure with an associated calibration method to determine material parameters in HVE model (including hyperelastic parameters and viscoelastic parameters) from the experimental data.

Firstly, in the case of incompressible materials, the HVE behaviour of the material is assumed to be incompressible during relaxation, i.e. the relaxation bulk modulus $K(t)$ is a constant or $\dot{K}(t) = 0$. Therefore, in Eq. (5.20), $\int_0^t \dot{K}(s)/K_0 \cdot \boldsymbol{\sigma}_0^H\big(\mathbf{F}(t-s)\big) ds = 0$, which means that the hydrostatic part remains the same as its instantaneous counterpart, i.e. $\boldsymbol{\sigma}^H(t) = \boldsymbol{\sigma}_0^H\big(\mathbf{F}(t)\big)$.

For the time-dependent relaxation shear modulus $G(t)$, the generalised Maxwell model (Figure 5-8), which is a linear viscoelastic model and has been used in small-strain viscoelasticity theory, will be used in the finite-strain HVE model. The time-dependent relaxation shear modulus $G(t)$ can be expressed in a Prony series form, i.e.

$$G(t) = G_\infty + \sum_{i=1}^{N} G_i e^{-t/\tau_i^R} \tag{5.21}$$

where G_∞ is the long-term (equilibrium) modulus defined as $G_\infty = G(t \to \infty)$, N is the number of viscoelastic branches (i.e. Prony terms), G_i , $\tau_i^R = \eta_i/G_i$ and η_i are respectively the shear modulus, the retardation time and the coefficient of viscosity for the i th Maxwell branch. Figure 5-8 illustrates the graphical representation of the generalised Maxwell model used here. It should be noted that G_i in Figure 5-8 do not necessarily represent linear springs when they are parts of the HVE model.

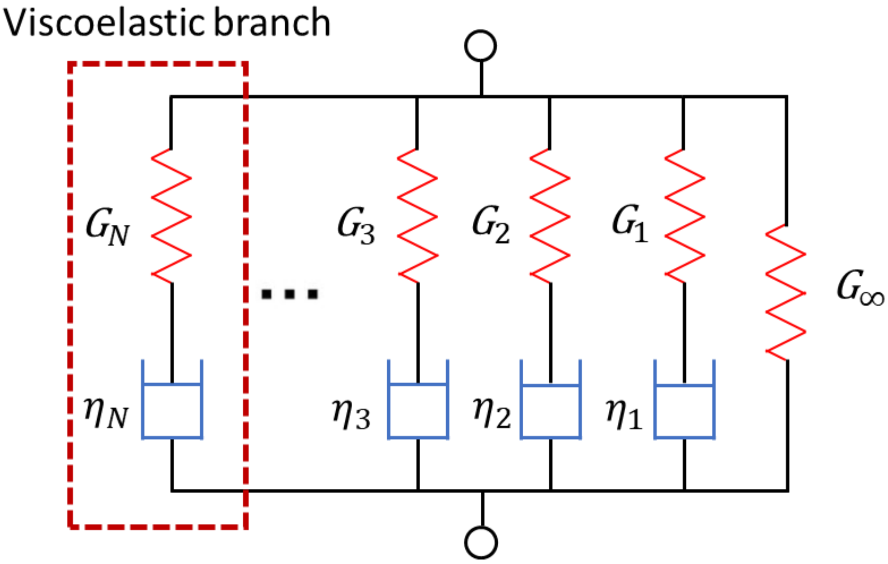

Figure 5-8 The generalised Maxwell model.

Let $g_i = G_i/G_0$ and $g_\infty = G_\infty/G_0$ with the instantaneous shear modulus G_0 being defined as,

$$G_0 = G(t = 0) = G_\infty + \sum_{i=1}^{N} G_i \tag{5.22}$$

Eq. (5.21) can be transformed into

$$G(t) = G_0 \left(g_\infty + \sum_{i=1}^{N} g_i e^{-t/\tau_i^R} \right) \tag{5.23}$$

with the following relationship

$$g_{\infty} = 1 - \sum_{i=1}^{N} g_i \tag{5.24}$$

Hence, by normalising Eq. (5.23) using G_0 and substituting g_{∞} in Eq. (5.24) to Eq. (5.23), the Prony series can be expressed as

$$g(t) = \frac{G(t)}{G_0} = 1 - \sum_{i=1}^{N} g_i \left(1 - e^{-t/\tau_i^R}\right) \tag{5.25}$$

where $g(t)$ is the normalised relaxation modulus corresponding to time, which links the 'time-dependent' stress to the 'instantaneous' stress in Eq. (5.20), and g_i are dimensionless relaxation parameters for each Maxwell branch. It is evident from Eq. (5.25) that $\lim_{t \to 0} g(t) = 1$.

However, the viscoelastic model in the Prony series form introduced above is established based on the small strain theory, in which the reference configuration can be approximate to the current configuration. To extend it to a finite-strain formulation, it is necessary to map the stress in the configuration at time $(t - s)$ (i.e. the reference configuration) into the configuration at time (t) (i.e. the current configuration), because the Cauchy stress is based on the current configuration, which is different from the reference configuration in the case of finite-strain deformation. To overcome this, Simo (1987) introduced a push-forward operator $\mathbf{F}_t^{-1}(t - s)$ based on the definition of relative deformation gradient, $\mathbf{F}_t(t - s) = \mathbf{F}(t - s)\mathbf{F}^{-1}(t)$, where $\mathbf{F}_t(t - s)$ means deformation gradient at time $(t - s)$ measured relative to the one at time (t). Hence, based on the viscoelastic model in the Prony series form in Eq. (5.23) and using the deviatoric-split hereditary integral formulation (i.e. Eq. (5.20)) in the reference configuration (i.e. using $\mathbf{F}_t(t - s)$ to connect reference and current configurations) for materials under finite-strain, the viscoelastic influenced deviatoric stress $\boldsymbol{\sigma}^D(t)$ in Eq. (5.20) can be expressed in the current configuration (Abaqus 2019)

$$\begin{aligned} \boldsymbol{\sigma}^D(t) &= \boldsymbol{\sigma}_0^D\big(\mathbf{F}(t)\big) \\ &\quad - dev\left[\sum_{i=1}^{N} \frac{g_i}{\tau_i^R} \int_0^t \mathbf{F}_t^{-1}(t - s)\boldsymbol{\sigma}_0^D\big(\mathbf{F}(t - s)\big)\mathbf{F}_t^{-T}(t - s)\, e^{-s/\tau_i^R}\, ds\right] \end{aligned} \tag{5.26}$$

where $dev[\cdot] \equiv (\cdot) - \frac{1}{3} \cdot \mathrm{tr}(\cdot)\mathbf{I}$ is to calculate the deviatoric part of the corresponding stress tensor. Then, the total time-dependent Cauchy stress response $\boldsymbol{\sigma}(t)$ can be obtained as

$$\begin{aligned}\boldsymbol{\sigma}(t) &= \boldsymbol{\sigma}^{D}(t) + \boldsymbol{\sigma}^{H}(t)\\ &= \boldsymbol{\sigma}_0^{D}\big(\mathbf{F}(t)\big)\\ &\quad -dev\left[\sum_{i=1}^{N}\frac{g_i}{\tau_i^R}\int_0^t \mathbf{F}_t^{-1}(t-s)\boldsymbol{\sigma}_0^{D}\big(\mathbf{F}(t-s)\big)\mathbf{F}_t^{-T}(t-s)\, e^{-\frac{s}{\tau_i^R}}\, ds\right]\\ &\quad +\boldsymbol{\sigma}_0^{H}\big(\mathbf{F}(t)\big)\end{aligned} \tag{5.27}$$

For the specific case of uniaxial tension state, the instantaneous Cauchy stress tensor $\boldsymbol{\sigma}_0\big(\mathbf{F}(t)\big)$ becomes

$$\boldsymbol{\sigma}_0\big(\mathbf{F}(t)\big) = \begin{bmatrix}\sigma_0\big(\lambda(t)\big) & 0 & 0\\ 0 & 0 & 0\\ 0 & 0 & 0\end{bmatrix} \tag{5.28}$$

where $\sigma_0\big(\lambda(t)\big)$ (without bold) is the instantaneous uniaxial Cauchy stress. The deformation gradient $\mathbf{F}(t)$ is replaced by uniaxial stretch $\lambda(t)$. Therefore, the instantaneous deviatoric Cauchy stress tensor $\boldsymbol{\sigma}_0^{D}\big(\mathbf{F}(t)\big)$ can be obtained as

$$\boldsymbol{\sigma}_0^{D}\big(\mathbf{F}(t)\big) = \boldsymbol{\sigma}_0\big(\mathbf{F}(t)\big) - \frac{\operatorname{tr}\boldsymbol{\sigma}_0\big(\mathbf{F}(t)\big)}{3}\mathbf{I} = \sigma_0\big(\lambda(t)\big)\begin{bmatrix}\frac{2}{3} & 0 & 0\\ 0 & -\frac{1}{3} & 0\\ 0 & 0 & -\frac{1}{3}\end{bmatrix} \tag{5.29}$$

and the instantaneous hydrostatic Cauchy stress tensor $\boldsymbol{\sigma}_0^{H}\big(\mathbf{F}(t)\big)$ can be obtained as

$$\boldsymbol{\sigma}_0^{H}\big(\mathbf{F}\,(t)\big) = \frac{\operatorname{tr}\boldsymbol{\sigma}_0\big(\mathbf{F}(t)\big)}{3}\mathbf{I} = \frac{\sigma_0\big(\lambda(t)\big)}{3}\mathbf{I} = \boldsymbol{\sigma}^{H}(t) = \frac{\operatorname{tr}\boldsymbol{\sigma}(t)}{3}\mathbf{I} = \frac{\sigma(t)}{3}\mathbf{I} \tag{5.30}$$

Also, the relative deformation gradient can be written as

$$\mathbf{F}_t(t-s) = \mathbf{F}(t-s)\mathbf{F}^{-1}(t) = \begin{bmatrix}\frac{\lambda(t-s)}{\lambda(t)} & 0 & 0\\ 0 & \sqrt{\frac{\lambda(t)}{\lambda(t-s)}} & 0\\ 0 & 0 & \sqrt{\frac{\lambda(t)}{\lambda(t-s)}}\end{bmatrix} \tag{5.31}$$

Based on Eqs. (5.27)-(5.31), the uniaxial constitutive relation can be expressed as

$$\boldsymbol{\sigma}(t) = \sigma_0\big(\lambda(t)\big)\begin{bmatrix} \frac{2}{3} & 0 & 0 \\ 0 & -\frac{1}{3} & 0 \\ 0 & 0 & -\frac{1}{3} \end{bmatrix} - \sum_{i=1}^{N} \frac{g_i}{\tau_i^R} \int_0^t \frac{2\lambda^3(t) + \lambda^3(t-s)}{\lambda(t)\lambda^2(t-s)} \sigma_0\big(\lambda(t-s)\big) e^{-\frac{s}{\tau_i^R}} ds \cdot \begin{bmatrix} \frac{2}{9} & 0 & 0 \\ 0 & -\frac{1}{9} & 0 \\ 0 & 0 & -\frac{1}{9} \end{bmatrix} + \frac{\sigma(t)}{3}\mathbf{I} \tag{5.32}$$

For a given loading scheme (e.g. the displacement-controlled loading at constant nominal strain-rate in this study), $\sigma_0\big(\lambda(t)\big)$ can be expressed as $\sigma_0(t)$. Therefore, the time-dependent uniaxial Cauchy stress $\sigma(t)$ (i.e. $\sigma_{11}(t)$ in the index notation expression of tensor $\boldsymbol{\sigma}(t)$) can be known as

$$\sigma(t) = \sigma_0(t) - \frac{1}{3}\sum_{i=1}^{N} \frac{g_i}{\tau_i^R} \int_0^t \frac{2\lambda^3(t) + \lambda^3(t-s)}{\lambda(t)\lambda^2(t-s)} \sigma_0(t-s) e^{-s/\tau_i^R} ds \tag{5.33}$$

where $\sigma_0(t)$ can be determined by Eqs. (5.10)-(5.12). Then, Eq. (5.33) can be rewritten in incremental form, i.e. (Fazekas and Goda 2018, 2019)

$$\sigma(t+\Delta t) = \sigma_0(t+\Delta t) - \sum_{i=1}^{N}\big(A_i(t+\Delta t) + B_i(t+\Delta t)\big) \tag{5.34}$$

where

$$A_i(t+\Delta t) = \frac{2}{3} g_i \left[\frac{\lambda^2(t+\Delta t)}{\lambda^2(t)}\sigma_0(t)\beta_i + \sigma_0(t+\Delta t)\alpha_i\right] + \frac{\lambda^2(t+\Delta t)}{\lambda^2(t)} A_i(t)\gamma_i$$

$$B_i(t+\Delta t) = \frac{1}{3} g_i \left[\frac{\lambda(t)}{\lambda(t+\Delta t)}\sigma_0(t)\beta_i + \sigma_0(t+\Delta t)\alpha_i\right] + \frac{\lambda(t)}{\lambda(t+\Delta t)} B_i(t)\gamma_i \tag{5.35}$$

with $\gamma_i = e^{-\Delta t/\tau_i^R}$, $\alpha_i = 1 - (1-\gamma_i)\tau_i^R/\Delta t$ and $\beta_i = (1-\gamma_i)\tau_i^R/\Delta t - \gamma_i$.

As mentioned above, the hyperelastic model parameters are determined by nominal stress-strain data (i.e. Eqs. (5.13)-(5.15)), and therefore, Eqs. (5.34) and (5.35) should be transformed to first Piola-Kirchhoff stress (i.e. nominal stress) forms. The first P-K stress tensor $\mathbf{P}(t)$ has following relationship to the Cauchy stress tensor $\boldsymbol{\sigma}(t)$ (Holzapfel 2002)

$$\mathbf{P}(t) = J(t)\boldsymbol{\sigma}(t)\mathbf{F}^{-\mathrm{T}} \tag{5.36}$$

where $J(t) = \det \mathbf{F}(t) = dV/dV_0 = 1$ is a constant for incompressibility here. Based on Eq. (5.36), it can be known that the nominal uniaxial stress $P(t)$ (i.e. $P_{11}(t)$ in the index notation expression of tensor $\mathbf{P}(t)$) can be obtained by $P(t) = \sigma(t)/\lambda(t)$. Therefore, after being divided by $\lambda(t+\Delta t)$ on both sides of Eq. (5.34), we can have

$$P(t+\Delta t) = P_0(t+\Delta t) - \sum_{i=1}^{N}\left(\bar{A}_i(t+\Delta t) + \bar{B}_i(t+\Delta t)\right) \tag{5.37}$$

where

$$\bar{A}_i(t+\Delta t) = \frac{2}{3}g_i\left[\frac{\lambda(t+\Delta t)}{\lambda(t)}P_0(t)\beta_i + P_0(t+\Delta t)\alpha_i\right] + \frac{\lambda(t+\Delta t)}{\lambda(t)}\bar{A}_i(t)\gamma_i$$

$$\bar{B}_i(t+\Delta t) = \frac{1}{3}g_i\left[\frac{\lambda^2(t)}{\lambda^2(t+\Delta t)}P_0(t)\beta_i + P_0(t+\Delta t)\alpha_i\right] + \frac{\lambda^2(t)}{\lambda^2(t+\Delta t)}\bar{B}_i(t)\gamma_i \tag{5.38}$$

where α_i, β_i and γ_i have the same definitions as those in Eq. (5.35). In Eqs. (5.37) and (5.38), P_0 is the instantaneous nominal stress in hyperelastic model (see Eqs. (5.13)-(5.15)), which can correspond to the nominal strain via stretch history $\lambda(t)$; P is the time-dependent nominal stress corresponding to stretch history $\lambda(t)$ with considering the viscoelastic effect.

5.5 Parametrical calibration of the material parameters in HVE model

In this section, the previous methods (i.e. the two-step method and the numerical stress solution method) and the proposed inverse stress solution method are described and incorporated in the framework of the HVE theory introduced in Section 5.4. As discussed in Section 5.3, the present experiments cannot guarantee the pure viscoelastic deformation when $\varepsilon > 0.10$ (i.e. plastic deformation or damage may be involved when $\varepsilon > 0.10$). Therefore, the present study limits the nominal strain range to $0 \le \varepsilon \le 0.10$ to ensure that the separator only has viscoelastic response.

5.5.1 Two-step method

In most previous research, the two-step method is widely used (Grujicic et al. 2009, Briody et al. 2012, Wei and Olatunbosun 2016, Shanahan et al. 2017, Jridi et al. 2019). The main idea of this method is to determine the hyperelastic parameters and viscoelastic parameters separately. Specifically, the hyperelastic parameters are determined by a relative short-term uniaxial tensile test. For example, Shanahan et al. (2017) used a loading nominal strain-rate of $1.67 \times 10^{-3}\ s^{-1}$ (around 24 seconds to strain of 0.4), and Fazekas and Goda (2018) used a loading nominal strain-rate of $2.7 \times 10^{-1}\ s^{-1}$ (around 7.4 seconds to strain of 2.0) obtained from (Bódai and Goda 2011). For the viscoelastic parameters, according to ASTM E328-13, a reasonably rapid stress-application rate (usually controlled by the crosshead speed or strain-rate without causing impact or vibration effects) should be applied to generate an equivalent instantaneous stress for the subsequent stress-relaxation stage. Therefore, a proper tension-relaxation test can satisfy the parametrical calibration for the two-step method, i.e. (i) the nominal stress-strain relation in the ramp-loading stage is used to determine the hyperelastic model, i.e. Eqs. (5.13)-(5.15); (ii) the stress-time relation obtained in the stress-relaxation stage is used to determine the Prony series parameters of viscoelasticity, i.e. Eq. (5.25). It should be noted that, in previous studies (Shanahan et al. 2017, Fazekas and Goda 2018) and the ASTM E328-13, no specific instruction about the short-term or rapid stress-application rate is suggested in ASTM E328-13. For example, Shanahan et al. (2017) and Fazekas and Goda (2018) used two distinct-different loading strain-rates, and ASTM E328-13 gives an ambiguous statement of 'The stress-application rate in either case should be reasonably rapid, but without impact or vibration, so that any relaxation during the stress-application period will be small' for user's interpretation.

As mentioned above, various loading nominal strain-rates were adopted to determine the hyperelastic parameters (instantaneous elastic properties) in previous studies (i.e. Shanahan et al. (2017) and Fazekas and Goda (2018)). Therefore, we selected two sets of relative short-term ramp-loading data, obtained at loading nominal strain-rates of $10^{-1}\ s^{-1}$ and $10^{-2}\ s^{-1}$, to determine the hyperelastic properties and assess their influence on the results. Furthermore, three hyperelastic constitutive models, i.e. NH, MR and Marlow models, are used. Figure 5-9 shows the comparison of the nominal stress-strain curves of the experimental data (i.e. Marlow model) and two fitted hyperelastic models (i.e. NH and MR models, fitted by Abaqus material evaluation function) at loading nominal strain-rates of $10^{-1}\ s^{-1}$ and $10^{-2}\ s^{-1}$. As shown in Figure 5-9, the parameters determined by fitting NH and MR hyperelastic models to the experimental data are not able to accurately describe the experimental stress-strain data of the material. Even though there are other hyperelastic models with high-order parameters that can better fit the data, e.g. third-order Ogden model and fourth-order reduced polynomial model, these models may cause difficulties of convergence in the numerical simulation based on FE software.

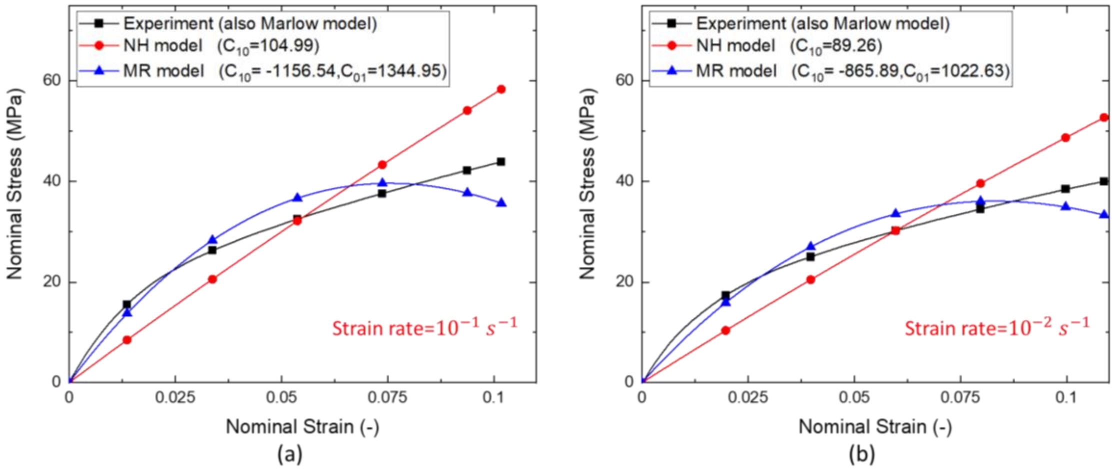

Figure 5-9 The comparison of nominal stress-strain curves of experimental (Marlow model) and NH and MR hyperelastic models at loading nominal strain-rates of (a) $10^{-1}\ s^{-1}$ and (b) $10^{-2}\ s^{-1}$, respectively.

On the other hand, according to the standard (i.e. ASTM E328-13), the Prony series parameters (i.e. Eq. (5.25)) can be determined by the stress-relaxation stage in the tension-relaxation experiment. The relaxation time is described by t^R, and $t^R = t - t_0^R$ is set to start when the relaxation begins at $t = t_0^R$ (see Figure 5-2(c) and (d)). By knowing $G(t^R) = E(t^R)/2(1+v)$ and $\sigma^R(t^R) = E(t^R)\varepsilon_R$, where $E(t^R)$ is the effective Young's modulus varying with time and $v \sim 0.5$ is the Poisson's ratio for an incompressible material, Eq. (5.25) can be written in the following form, i.e.

$$g(t^R) = \frac{G(t^R)}{G_0} = \frac{E(t^R)}{E_0} = \frac{\sigma^R(t^R)}{\sigma_0^R} = \frac{P^R(t^R)}{P_0^R} = 1 - \sum_{i=1}^{N} g_i \left(1 - e^{-t^R/\tau_i^R}\right) \qquad (5.39)$$

where E_0 is the instantaneous Young's modulus equals to $3G_0$; the last equation is used to determine the normalised relaxation modulus in Prony series. In Eq. (5.39), the index R represents the quantities obtained in the relaxation process, i.e. $P^R(t^R)$ is the nominal stress varying with time during the relaxation process and P_0^R is the nominal stress at the beginning of the stress-relaxation. Prony term number N is set to 5 in this study as it is the minimum number that can give the required convergence in the studied case.

According to ASTM E328-13, as the stress at the beginning of the stress-relaxation stage is regarded as an instantaneous stress for the determination of Prony series, the time duration of the ramp-loading stage should be short. Here, the stress-relaxation curves for $\varepsilon_R = 0.05$ (i.e. relaxation start when $\lambda = 1.05$) associated with loading nominal strain-rates of $10^{-1}\ s^{-1}$ and $10^{-2}\ s^{-1}$ are used to fit the Prony series parameters because they have the shortest loading time before the stress-relaxation stage in the experiments under each nominal strain-rate. However, the test with a loading nominal strain-rate of $10^{-1}\ s^{-1}$ had an obvious overshooting problem for the initial relaxation stress, as can be seen from Figure 5-3(a) and Figure 5-4. In this case, we consider the stress-relaxation starts at $t = 0.864$, which is the time that the constrained strain becomes a constant (i.e. $\varepsilon_R = 0.058$), as shown in Figure 5-4. It should be noted that this is still theoretically inaccurate as this stress response (i.e. P_0^R) has already been affected by viscoelastic stress-relaxation during the ramp-loading stage. Such effect is not considered in the two-step method.

The curves of the normalised modulus (g) vs. relaxation time (t^R) during the stress-relaxation stage in the case of loading nominal strain-rates of $10^{-1}\ s^{-1}$ and $10^{-2}\ s^{-1}$ that used to determine the Prony series fitting curves and the corresponding parameters can be seen in Figure 5-10.

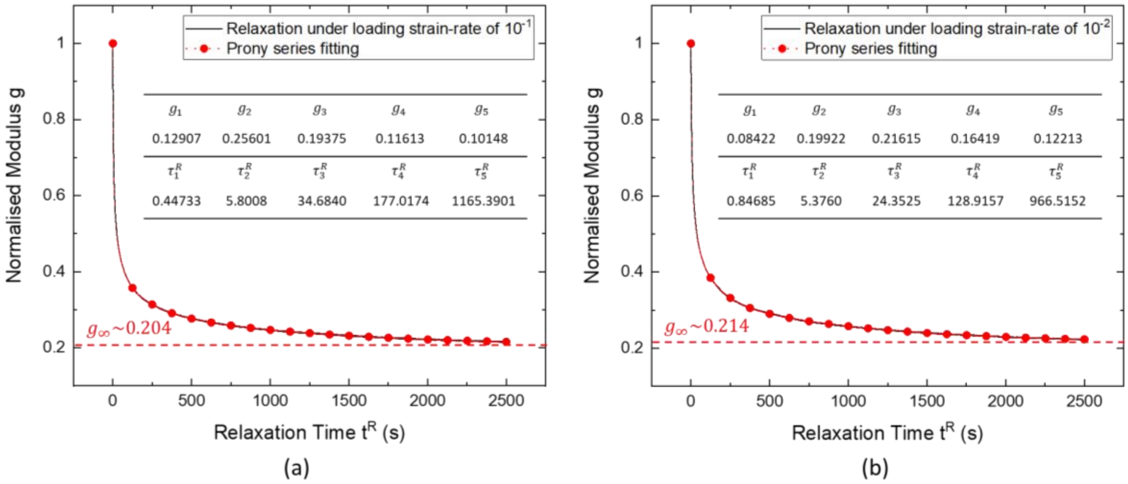

(a)

(b)

Figure 5-10 Parametrical calibration of the Prony series parameters and the fitted curves of normalised modulus vs. relaxation time for $\varepsilon_R = 0.05$ at loading nominal strain-rates of (a) $10^{-1}\ s^{-1}$, and (b) $10^{-2}\ s^{-1}$.

In summary, the parameters of HVE models determined using the two-step method are presented in Table 5-2 and Table 5-3. In this two-step method, the same parameters of Prony series for the viscoelastic model are applied to all HVE models obtained under the same loading nominal strain-rate. The HVE model determined by different methods is named meaningfully by ‘parametrical calibration method’-‘hyperelastic model’-HVE. Also, as two sets of data obtained from different loading nominal strain-rates were used to separately determine two groups of HVE model using the two-step (TS) method, we use TS1 to represent the HVE model determined by data with loading nominal strain-rate of $10^{-1}\ s^{-1}$ and TS2 to represent the HVE model determined by data with loading nominal strain-rate of $10^{-2}\ s^{-1}$. For example, ‘TS1-NH-HVE’ means the HVE model based on the Neo-Hookean (NH) hyperelastic model determined by two-step (TS) method using the first data set with loading nominal strain-rate of $10^{-1}\ s^{-1}$. This naming rule will also be used in other parametrical calibration methods.

The HVE models defined in Table 5-2 and Table 5-3 will be compared with other HVE models and experimental results in Section 5.6.

Table 5-2 The parameters of HVE models determined by the two-step method under the loading nominal strain-rate of $10^{-1}\ s^{-1}$.

HVE parameters	TS1-NH-HVE	TS1-MR-HVE	TS1-Marlow-HVE[a]
C_{10} (MPa)	104.99	-1156.54	-
C_{01} (MPa)	-	1344.95	-
g_1 (-)	0.12907	0.12907	0.12907
g_2 (-)	0.25601	0.25601	0.25601
g_3 (-)	0.19375	0.19375	0.19375
g_4 (-)	0.11613	0.11613	0.11613
g_5 (-)	0.10148	0.10148	0.10148
τ_1^R (s)	0.44733	0.44733	0.44733
τ_2^R (s)	5.8008	5.8008	5.8008
τ_3^R (s)	34.6840	34.6840	34.6840
τ_4^R (s)	177.0174	177.0174	177.0174
τ_5^R (s)	1165.3901	1165.3901	1165.3901

[a] The hyperelastic model of the TS1-Marlow-HVE model is the Marlow model determined by directly inputting the nominal stress-strain data obtained from ramp-loading stage at loading nominal strain-rate of $10^{-1}\ s^{-1}$ (see Figure 5-9(a)).

Table 5-3 The parameters of HVE models determined by the two-step method under the loading nominal strain-rate of $10^{-2}\ s^{-1}$.

HVE parameters	TS2-NH-HVE	TS2-MR-HVE	TS2-Marlow-HVE[a]
C_{10} (MPa)	89.26	-865.89	-
C_{01} (MPa)	-	1022.63	-
g_1 (-)	0.08422	0.08422	0.08422
g_2 (-)	0.19922	0.19922	0.19922
g_3 (-)	0.21615	0.21615	0.21615
g_4 (-)	0.16419	0.16419	0.16419
g_5 (-)	0.12213	0.12213	0.12213
τ_1^R (s)	0.84685	0.84685	0.84685
τ_2^R (s)	5.37601	5.37601	5.37601
τ_3^R (s)	24.3525	24.3525	24.3525
τ_4^R (s)	128.9157	128.9157	128.9157
τ_5^R (s)	966.5152	966.5152	966.5152

[a] The hyperelastic model of the TS2-Marlow-HVE model is the Marlow model determined by directly inputting the nominal stress-strain data obtained from the ramp-loading stage at a loading nominal strain-rate of $10^{-2}\ s^{-1}$ (see Figure 5-9(b)).

5.5.2 Stress solution method

The stress solution method was first proposed by Goh et al. (2004) based on the numerical algorithm in FEA (Sunderland et al. 2001) for calculating the time-dependent stress (i.e. Eq. (5.33)), which was developed by Fazekas and Goda (2018) to an iterative model (i.e. Eqs. (5.37) and (5.38)). The main procedure of this method is to

(i) assume a hyperelastic constitutive model, e.g. Neo-Hookean model, Mooney-Rivlin model, etc.;

(ii) give initial values to the undetermined parameters in HVE (both hyperelastic parameters and Prony series parameters), and pre-calculate the instantaneous stress response associated with the deformation history $\lambda(t)$ using Eqs. (5.10)-(5.12) in Cauchy stress form $\sigma_0(t)$ and Eqs. (5.13)-(5.15) in nominal stress form $P_0(t)$;

(iii) use Eq. (5.33) or the corresponding iterative forms (i.e. Eqs. (5.34) or (5.37)) to calculate the time-dependent stress response $\sigma(t)$ or $P(t)$;

(iv) optimise the HVE parameters by minimising the error between the calculated and experimentally-measured time-dependent stress responses.

Specifically, in the case of the uniaxial tensile test, it can be assumed that there is no loading at the starting point when $t = 0$, which indicates that the initial conditions are $P_0(0) = P(0) = \bar{A}_i(0) = \bar{B}_i(0) = 0$ and $\lambda(0) = \varepsilon(0) + 1 = 1$. Then, by substituting Eqs. (5.13) or (5.14) into Eqs. (5.37) and (5.38), the time-dependent nominal stress $P(t)$ associated with a known deformation history $\lambda(t)$ can be calculated. It should be noted that as the time-dependent nominal stress is calculated from the deformation history (which is a step-by-step ramp-loading), the loading nominal strain-rate is not necessarily to be strictly a constant. Therefore, Eq. (5.37) becomes an equation with multiple parameters for both $P_0(t)$ and $g(t)$ to be fitted (i.e. C_{10}, C_{01}, g_i are the unknown parameters to be fitted). Since the calculations start from $t = 0$, stress-solution method considers the stress-relaxation during loading stage, which is fundamentally different from the two-step method. In this sense, the stress-solution method is more accurate than the two-step method, and the former could be used to validate the latter.

Now, there are two sets of data, i.e. the experimental data contain measured nominal stresses $P_j^{Meas}(t)$ associated with the measured stretches $\lambda_j^{Meas}(t)$ at the jth data point, and the calculated nominal stresses $P_j^{Cal}(t)$ corresponding to the measured stretches $\lambda_j^{Meas}(t)$ at the jth data point based on Eq. (5.37). In order to calibrate the undetermined parameters (i.e. C_{10}, C_{01}, g_i), following error function (RMSD, root-mean-square deviation) is defined first

$$\mathrm{RMSD} = \sqrt{\frac{1}{M}\sum_{j=1}^{M}\left(P_j^{Meas}(t) - P_j^{Cal}(t)\right)^2} \tag{5.40}$$

where M is the number of data point used in the minimisation of the error function. In this study, the generalised reduced gradient (GRG) nonlinear algorithm (Lasdon et al. 1978) is used to calibrate the undetermined parameters until the RMSD reaches its minimum, which can be expressed in a mathematical form as

$$\begin{cases} \text{argmin RMSD} = \begin{cases} \{C_{10}, g_i, \tau_i^R\} & \text{for NH model based HVE model} \\ \{C_{10}, C_{01}, g_i, \tau_i^R\} & \text{for MR model based HVE model} \end{cases} \\ s.t. \begin{cases} \sum_{i=1}^{N} g_i < 1 \\ g_i > 0 \\ \tau_i^R > 0 \end{cases} \end{cases} \tag{5.41}$$

where the formulas after '$s.t.$' are the constraints when minimising the RMSD. As the algorithm needs an initial value for each parameter to start, the parametric values shown in Table 5-2 are used. The Prony term number N is also set to be 5 here. It should be noted that since the GRG nonlinear algorithm is a local optimisation method rather than a global optimisation method, if the initial values are arbitrarily determined, then the expected results might not be achieved.

In most previous studies (Nayyar et al. 2014, Fazekas and Goda 2019, Shojaeiarani et al. 2019), the HVE models can only be validated with different loading nominal strain-rates only at the loading stage, and the data used in the calibration is the (stress, strain, time) data sets obtained from the ramp-loading stage. In some studies (Goh et al. 2004, Fazekas and Goda 2018, Shojaeiarani et al. 2019), the data in the stress-relaxation stage was considered and validated by the numerical simulation, but it is only limited to the case with single loading nominal strain-rate. To find out whether this method can effectively predict the behaviour at the stress-relaxation stage, we separately establish two main groups of HVE models, i.e. (i) the HVE models calibrated by stress solution method only using the (stress, strain, time) data sets obtained from the ramp-loading stage ($0 \le t \le t(\varepsilon = 0.10)$) at all four loading nominal strain-rates; and (ii) the HVE models calibrated by stress solution method using the data in both ramp-loading stage and stress-relaxations stage (i.e. the entire consecutive tension-relaxation experiment data) at four loading nominal strain-rates.

After the calibration based on the stress solution method introduced above, the optimised HVE parameters based on NH model and MR model are shown in Table 5-4. Here, SS1-NH-HVE and SS1-MR-HVE were used to represent the HVE models based on Neo-Hookean (NH) model (i.e. Eq. (5.1)) and Mooney-Rivlin (MR) model (i.e. Eq. (5.2)) as the hyperelastic part, whose parameters are calibrated by stress solution (SS) method using the experimental data only at ramp-loading stage ($0 \le t \le t(\varepsilon = 0.10)$). Similarly, SS2-NH-HVE and SS2-MR-HVE were used to represent the HVE models calibrated by the experimental data obtained from both ramp-loading stage and stress-relaxation stage. The predicted nominal stress-strain relationships from the hyperelastic models obtained by both cases (i.e. only ramp-loading data, ramp-loading, and stress-relaxation data) are compared with experimental data for loading nominal strain-rate of $10^{-1}\ s^{-1}$ in Figure 5-11.

Table 5-4 The parameters of HVE models determined by the optimisation of Eqs. (5.40) and (5.41).

HVE parameters	SS1-NH-HVE	SS1-MR-HVE	SS2-NH-HVE	SS2-MR-HVE
C_{10} (MPa)	103.11	-747.64	233.94	-683.89
C_{01} (MPa)	-	993.98	-	896.46
g_1 (-)	0.3691	0.4653	0.5963	0.3688
g_2 (-)	0.1976	0.1668	0.08147	0.1726
g_3 (-)	0.03258	0.1866	0.1690	0.07649
g_4 (-)	0.3647	-	0.08393	0.1490
g_5 (-)	-	-	-	0.1150
τ_1^R (s)	3.7361	0.07751	0.06694	0.1051
τ_2^R (s)	50.4356	8.0470	4.2751	7.3901
τ_3^R (s)	593.0148	130.3204	58.6886	103.7288
τ_4^R (s)	1369.5198	-	591.3045	90.9405
τ_5^R (s)	-	-	-	896.4617

'-' For g_i and τ_i^R means that the optimisation result of g_i is approximately zero, and therefore, this and higher terms are not considered.

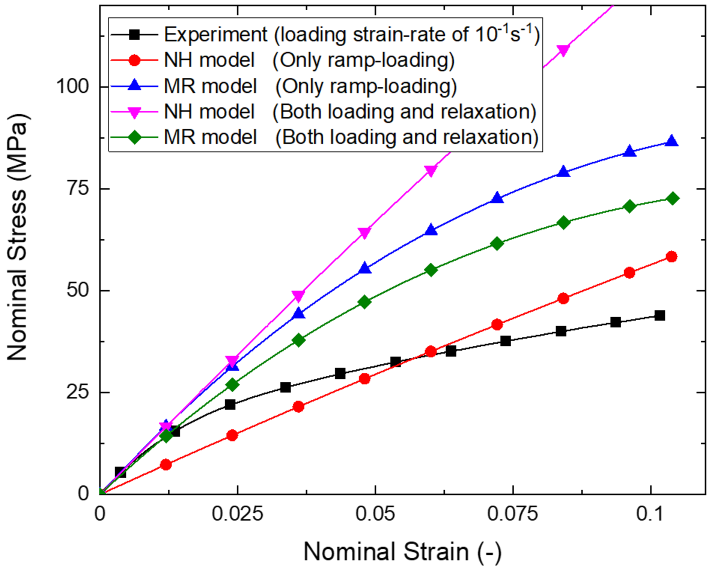

Figure 5-11 Comparisons of the nominal stress-strain curve of the experiment at loading nominal strain-rate of $10^{-1}\ s^{-1}$ with the hyperelastic model predictions from the stress solution method using different experimental data.

As can be seen from Figure 5-11, the hyperelastic models obtained under various situations (i.e. hyperelastic forms, with/without relaxation data during calibration) have noticeable differences. Among these four hyperelastic models, three of them have stress-strain relations that have large deviations from the experimental data obtained at the loading nominal strain-rate of $10^{-1}\ s^{-1}$, which are unacceptable. By observing Table 5-4, it can be known that when the GRG algorithm optimises the HVE parameters, the hyperelastic parameters and the Prony series parameters will influence each other to reach a local best result. As a result, once one kind of the parameters (hyperelastic or Prony series) has been over adjusted, another kind of the parameters will also be over adjusted to achieve the desired results. For example, as shown in the SS2-NH-HVE model in Table 5-4, as one of the retardation time τ_1^R has been adjusted too small (i.e. 0.06694), which has the most significant influence on viscoelastic response ($g_1 = 0.5963$), the stress response of the HVE model will drop significantly in a very short time. As a result, the stress response of the corresponding NH model will be optimised to a higher value to counteract the overlarge viscoelastic influence.

The HVE models defined in Table 5-4 will be compared with other HVE models and experimental results in Section 5.6.

5.5.3 Inverse stress solution method

Even the stress solution method can successfully optimise the HVE model and give a good prediction of the stress response in the past studies (Goh et al. 2004, Fazekas and Goda 2018, 2019), this method has only been used to develop HVE models with parameterised hyperelastic models (e.g. NH-HVE and MR-HVE in Section 5.5.2). In Section 5.4.2, Eqs. (5.37) and (5.38) are used to calculate the time-dependent nominal stress corresponding to the stretch history $\lambda(t)$, where the instantaneous nominal stress is calculated based on the parameterised hyperelastic models. However, if the instantaneous nominal stress-strain relations cannot be accurately expressed by the parameterised hyperelastic models, their corresponding HVE models based on the stress solution method cannot give satisfactory predictions. Therefore, the Marlow model (based on discrete nominal stress-strain input) is considered here as the hyperelastic model in the HVE model, which cannot be used in the previously proposed stress solution method. In addition, the previously proposed stress solution method has two significant limitations, i.e. i) too many parameters need to be fitted (both hyperelastic and Prony series parameters) simultaneously, which increases the risk of local optimisation, as discussed at the end of Section 5.5.2; ii) the stability condition (e.g. Drucker stability conditions) is difficult to be satisfied in FE modelling, which will be presented and discussed later in Section 5.6.3.

To address the limitations above-mentioned, an inverse stress solution method is proposed in this study. This method does not minimise the difference between the calculated time-dependent nominal stress and the experimental time-dependent nominal stress, but minimise the difference of the instantaneous nominal stresses calculated under different ramp-loading nominal strain-rates. According to the theoretical framework of the HVE constitutive model (as introduced in Section 5.4), the hyperelastic behaviour is assumed to be an intrinsic property of a material (as shown in Figure 5-12), and therefore, the instantaneous nominal stress-strain relations should be the same even under different loading nominal strain-rates. In addition, as the constraints (i.e. nominal strain in this study) keep constant during the stress-relaxation stage, the instantaneous nominal stress response should not change in this stage, as shown in Figure 5-12(b).

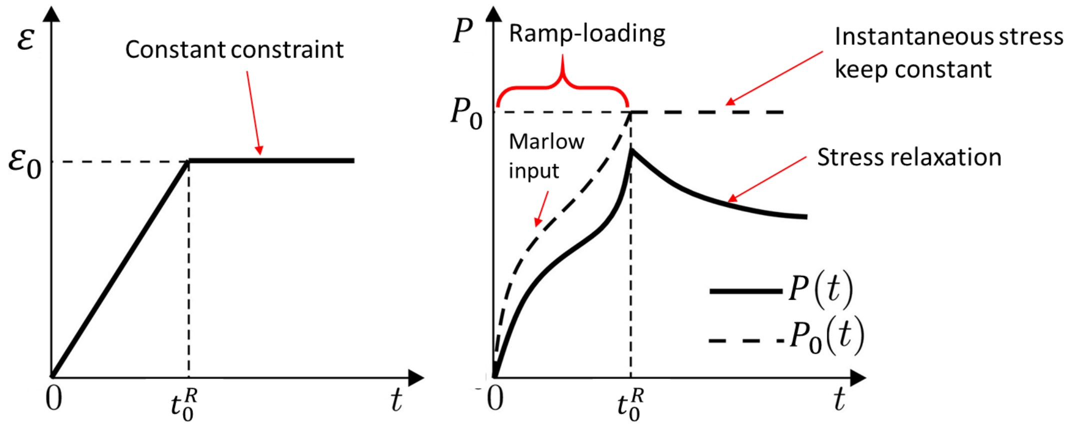

(a) (b)

Figure 5-12 The schematic of (a) The deformation (strain) history, and (b) the comparison between the instantaneous stress and the time-dependent measured stress with time in the tension-relaxation experiment.

Specifically, the first step of this method is to obtain the expression of the instantaneous nominal stress. Regarding $P_0(t+\Delta t)$ as a dependent variable, Eqs. (5.37) and (5.38) are transformed into

$$P_0(t+\Delta t)=\frac{P(t+\Delta t)+\sum_{i=1}^{N}\left[\bar{\bar{A}}_i(t)\frac{\lambda(t+\Delta t)}{\lambda(t)}+\bar{\bar{B}}_i(t)\frac{\lambda^2(t)}{\lambda^2(t+\Delta t)}\right]}{1-\sum_{i=1}^{N}\alpha_i g_i} \tag{5.42}$$

where

$$\bar{\bar{A}}_i(t)=\bar{A}_i(t)\gamma_i+\frac{2}{3}P_0(t)\beta_i g_i$$

$$\bar{\bar{B}}_i(t)=\bar{B}_i(t)\gamma_i+\frac{1}{3}P_0(t)\beta_i g_i \tag{5.43}$$

where α_i, β_i and γ_i have the same definitions as those in Eq. (5.35), and $\bar{A}_i(t)$ and $\bar{B}_i(t)$ have the same definitions as those in Eq. (5.38). In Eq. (5.42), $P(t+\Delta t)$ is the experimentally-measured nominal stress corresponding to the stretch history $\lambda(t)$; while in Eq. (5.43), $P_0(t)$ is the calculated instantaneous nominal stress at the last time step. Therefore, by using the same initial conditions that $P_0(0)=P(0)=\bar{A}_i(0)=\bar{B}_i(0)=0$ and $\lambda(0)=\varepsilon(0)+1=1$, $P_0(t)$ (or $P_0(\lambda)$) can be determined using Eq. (5.42) and the knowing loading history $P(t)$ and deformation history $\lambda(t)$ from the experiment if (g_i, τ_i^R) are given. It can be noticed that no hyperelastic model parameter is required in this method, which resolves the problem that two kinds of parameters will influence each other in the optimisation.

The second step is to minimise the instantaneous nominal stress-strain relations between different sets of data. As the stretch histories $\lambda(t)$ in different experiments are different, and every point of the nominal strain should correspond to a unique time-independent nominal stress, we need to unify the experimental data points based on the stretch λ. In this study, we equally divide the stretch history in the range of $1 \leq \lambda \leq 1.10$ (i.e. $0 \leq \varepsilon \leq 0.10$) into 1000 data points, and use linear interpolation to determine the experimentally-measured time and nominal stress corresponding to each stretch point λ_j. Then, as the instantaneous nominal stress-strain relation is unique for the material, the standard deviation of the nominal stress-strain relations obtained under various loading conditions should be close to 0. The average of the standard deviation can be expressed as

$$\mathrm{AVESTD} = \frac{1}{M_1}\sum_{j=1}^{M_1}\sqrt{\frac{1}{M_2}\sum_{q=1}^{M_2}\left(P_{0_{q,j}} - \mu_j\right)^2} \tag{5.44}$$

where M_1 is the total number of the data point of λ for each data set in the ramp-loading stage; M_2 is the number of the data set used for calibration; μ_j is mean of the calculated P_0 in each data set on the jth data point of λ where $\mu_j = \left(P_{0_{1,j}} + P_{0_{2,j}} + \cdots + P_{0_{M_2,j}}\right) / M_2$; $P_{0_{q,j}}$ is the calculated P_0 in the qth data set on the jth data point of λ. As we divide the stretch history in the ramp-loading stage into 1000 data points, M_1 is set to be 1000 in this study. In addition, four ramp-loading data sets correspond to the loading nominal strain-rates of $10^{-4}\,s^{-1}$, $10^{-3}\,s^{-1}$, $10^{-2}\,s^{-1}$ and $10^{-1}\,s^{-1}$ are used in this study, and therefore, $M_2 = 4$. Then, similar to the method used in Section 5.5.2, the GRG nonlinear algorithm is used to calibrate the undetermined parameters (g_i, τ_i^R) by minimising the AVESTD in Eq. (5.44), which can be expressed in a mathematical form as

$$\begin{cases} \mathrm{argmin\ AVESTD} = \{g_i, \tau_i^R\} \\ s.t. \begin{cases} \sum_{i=1}^{N} g_i < 1 \\ g_i > 0 \\ \tau_i^R > 0 \end{cases} \end{cases} \tag{5.45}$$

Furthermore, if the data in the relaxation stage is also used in the calibration, another constraint that $P_0(t+\Delta t)$ should be a constant when $t > t_0^R$ needs to be considered, as shown in Figure 5-12(b), which means that $P_0(\lambda > 1+\varepsilon_R) = P_0(\lambda = 1+\varepsilon_R)$ should be satisfied for all four loading nominal strain-rates. Therefore, to satisfy this constraint, the following error function can be defined for the relaxation stage data

$$\mathrm{RMSD}^R = \sqrt{\frac{1}{M_3}\sum_{j=1}^{M_3}\left(P_{0_j} - \mu_{M_1}\right)^2} \tag{5.46}$$

where $M_3 = 1000$ is the total number of data points in the relaxation stage at different loading nominal strain-rates; $\mu_{M_1} = \frac{1}{M_2}\sum_{q=1}^{M_2} P_{0_{q,M_1}}$, where $M_1 = 1000$, is the mean of the calculated P_0 in each data set at the beginning of the stress-relaxation (or at the end of ramp-loading). Hence, the undetermined parameters can be calibrated with considering both ramp-loading data and stress-relaxation data by

$$\begin{cases} \operatorname{argmin}\ (\mathrm{AVESTD} + \mathrm{RMSD}^R) = \{g_i, \tau_i^R\} \\ s.t. \begin{cases} \sum_{i=1}^{N} g_i < 1 \\ g_i > 0 \\ \tau_i^R > 0 \end{cases} \end{cases} \tag{5.47}$$

Similarly, GRG nonlinear algorithm can also be used to optimise the parameters.

The last step is to average the instantaneous nominal stress at each stretch (strain) point among the M_2 (4 in this study) sets of experimental data, and the instantaneous nominal stress-strain data after averaging is the one to determine the corresponding Marlow model, as shown in Figure 5-12(b).

Similar to the stress solution method, we separately established two HVE models based on the proposed inverse stress solution method, i.e. ISS1-Marlow-HVE and ISS2-Marlow-HVE. The former model (ISS1-Marlow-HVE) is calibrated by using the (stress, strain, time) data sets obtained only from the ramp-loading stage ($0 \le t \le t(\varepsilon = 0.10)$) at all four loading nominal strain-rates via the proposed inverse stress solution (ISS) method (i.e. Eq. (5.45)). The latter model (ISS2-Marlow-HVE) is calibrated using the (stress, strain, time) data sets obtained from both ramp-loading and stress-relaxation stages at all four loading nominal strain-rates via Eq. (5.47).

The calibrated Prony series parameters can be seen in Table 5-5, based on which Marlow model used for the hyperelastic part of the ISS1-Marlow-HVE model can be determined by Eq. (5.42), which is shown by the red curve in Figure 5-13; the one for the ISS2-Marlow-HVE can also be determined by the same way, as shown by the blue curve in Figure 5-13.

Table 5-5 The parameters of ISS-Marlow-HVE models determined by the proposed inverse stress solution method.

HVE parameters	ISS1-Marlow-HVE model	ISS2-Marlow-HVE model
Hyperelastic model	Marlow model determined by red curve shown in Figure 5-13.	Marlow model determined by blue curve shown in Figure 5-13.
g_1 (-)	0.13306	0.02123
g_2 (-)	0.20399	0.50345
g_3 (-)	0.10587	0.08012
g_4 (-)	0.24506	0.19505
g_5 (-)	-	-
τ_1^R (s)	0.30596	24.44652
τ_2^R (s)	8.03538	51.32463
τ_3^R (s)	75.77047	550.34974
τ_4^R (s)	75.76945	525.09290
τ_5^R (s)	-	-

'-' for g_i and τ_i^R means that the optimisation result of g_i is approximately zero.

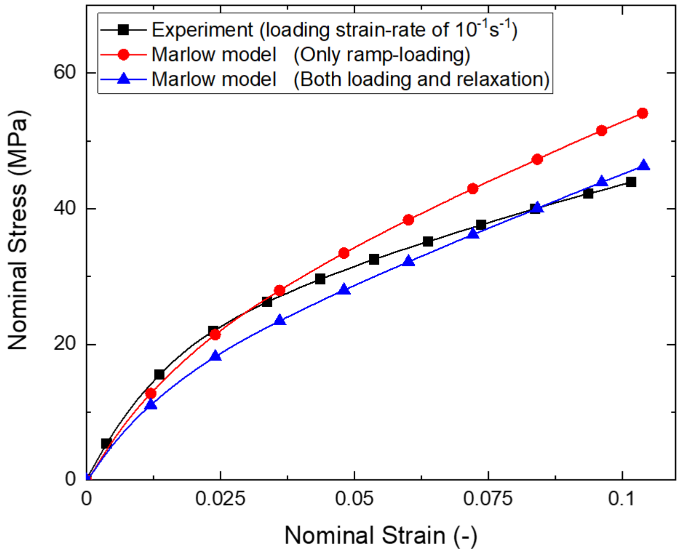

Figure 5-13 The nominal stress-strain curves of experiment (loading nominal strain-rate of $10^{-1}\ s^{-1}$) and the Marlow hyperelastic models determined by the inverse stress solution method.

In contrast to the instantaneous stress-strain relations (i.e. hyperelastic models) obtained by the previous stress solution method (see Figure 5-11), the stress-strain relations of these two Marlow models seems more reasonable, which are close to the experimental data obtained at the highest loading nominal strain-rate of $10^{-1}\ s^{-1}$ (i.e. the stress-relaxation has the smallest influence on the measured stress-strain curve). This phenomenon also demonstrates the advantage of the proposed inverse stress-solution that the involvement of only one kind of parameters (i.e. only Prony series but no hyperelastic parameters) in the optimisation can prevent the over-optimisation of the HVE model parameters.

5.6 Comparison and discussion

In this section, the time-dependent stress responses of three HVE models under various loading nominal strain-rates are firstly calculated based on Eqs. (5.37) and (5.38), and compared with the experimental results obtained at corresponding loading nominal strain-rates. Then, the commercial FE software Abaqus was used for the numerical simulation. The numerical results were validated by experimental load-time results of the tension-relaxation test, which include the uniaxial tensile ramp-loading stage ($0 < \varepsilon < 0.10$) at all four loading nominal strain-rates and the following stress-relaxation stage (i.e. $\varepsilon =$

0.10 lasts for 2500s). The parameters of HVE models, including the hyperelastic parameter and the viscoelastic Prony series parameters, which have already been presented in Section 5.5, were used in equation calculations and FEM simulations.

5.6.1 Comparison of model predictions and experimental results

According to Eqs. (5.37) and (5.38), once the HVE parameters are determined, the time-dependent nominal stress response can be predicted with the given deformation history $\lambda(t)$ (or strain history $\varepsilon(t)$). In the determination of parameters in various HVE models, the experimental data from the only ramp-loading stage and from the whole ramp-loading-relaxation stage at various loading nominal strain-rates were used separately to calculate the time-dependent nominal stress responses.

Figure 5-14 to Figure 5-17 show the comparison between the experimentally-measured nominal stress response and the calculated time-dependent nominal stress responses (varying with time) at different loading nominal strain-rates, where all calculated responses are computed via Eqs. (5.37) and (5.38) based on HVE models given in Section 5.5. To better show the efficiency of different methods, the HVE models are divided into three groups, i.e. (a) HVE models obtained by the two-step method, (b) HVE models determined by the stress solution method and the inverse stress solution method without involving the stress-relaxation data, and (c) HVE models determined by the stress solution method and the inverse stress solution method involving all data (including continuous ramp-loading data and stress-relaxation data). On the other hand, in order to show the performance of each HVE model more intuitively, the R-squared values (R^2), i.e. coefficient of determination, between the experimental results and the model predicted results are calculated and summarised for all cases in Table 5-6 and Table 5-7. Table 5-6 shows the R^2 only in the ramp-loading stage, i.e. $t < t_0^R$ in Figure 5-14 to Figure 5-17. R^2 is a good indicator to evaluate the accuracy of an HVE model, which has been used in many previous studies. Table 5-7 shows the R^2 during the entire experiment (including both ramp-loading stage and stress-relaxation stage). Furthermore, the best R^2 results at each loading nominal strain-rate and the best two overall R^2 results were highlighted in yellow in both Table 5-6 and Table 5-7. In comparison, the worst R^2 results at each loading nominal strain-rate and the worst two overall R^2 results were highlighted in green.

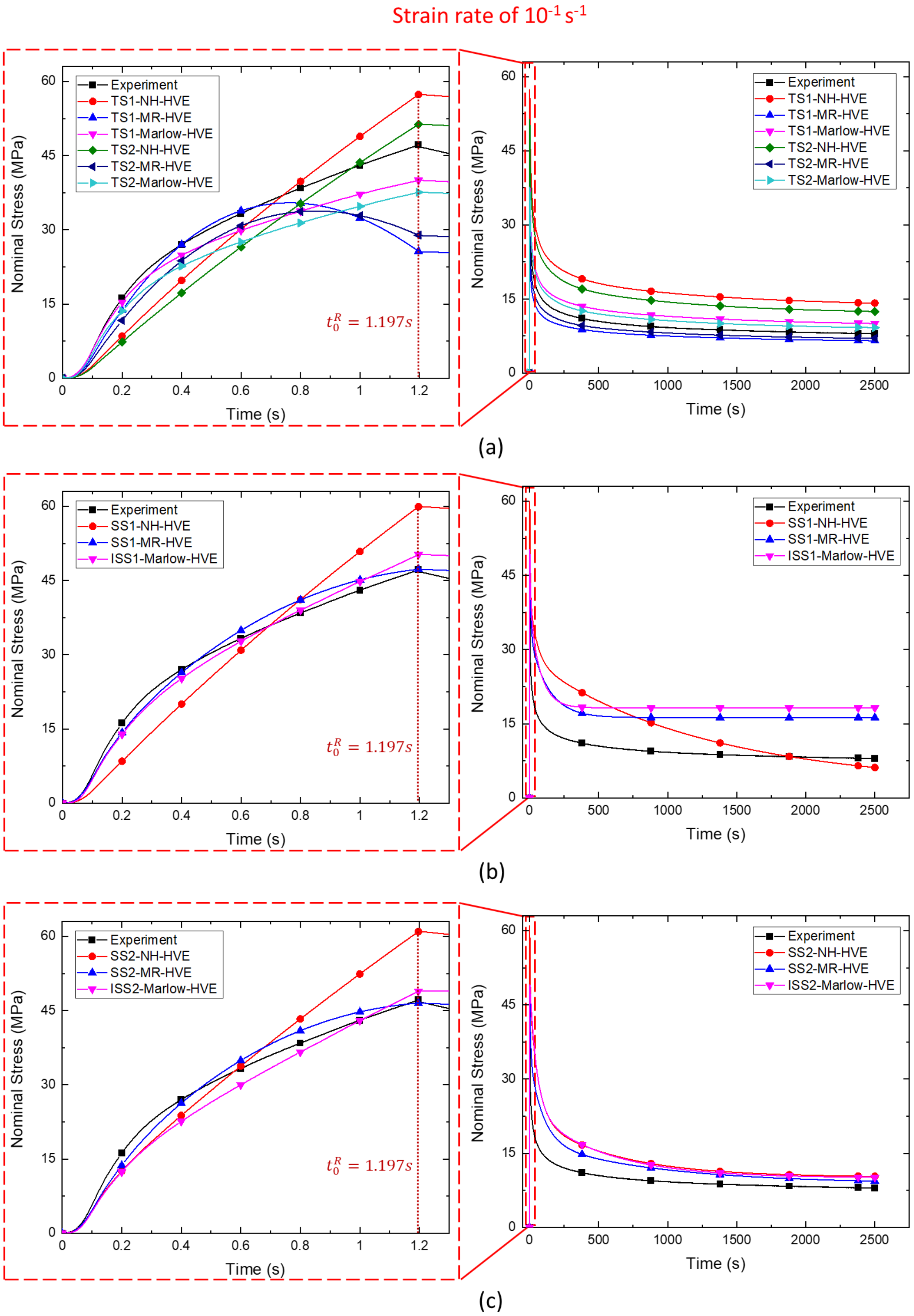

Figure 5-14 The time-dependent nominal stress vs. time curves of HVE models obtained by (a) two-step method, (b) (inverse) stress solution methods without stress-relaxation data, and (c) (inverse) stress solution methods with stress-relaxation data, at loading nominal strain-rate of $10^{-1}\ s^{-1}$.

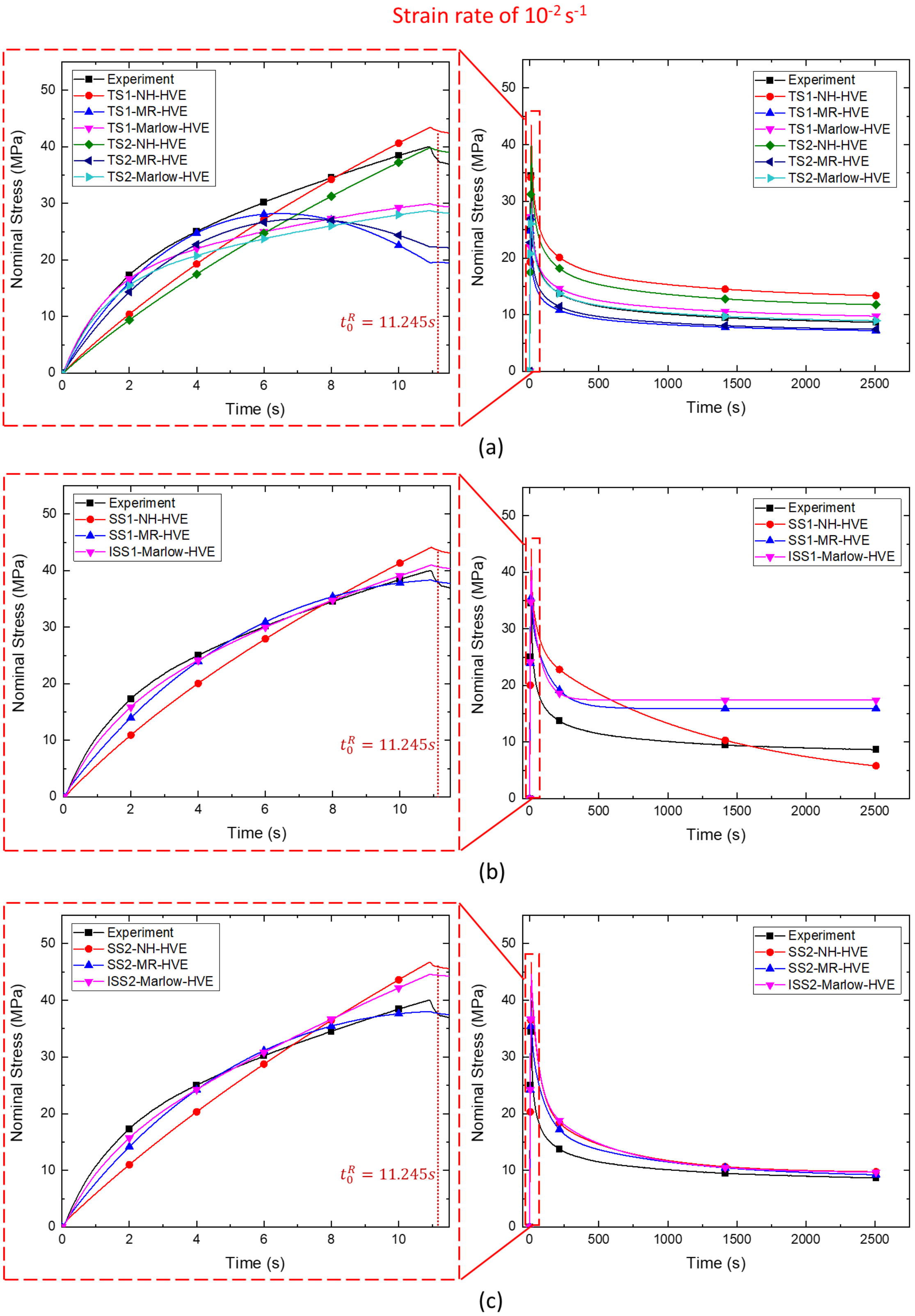

Figure 5-15 The time-dependent nominal stress vs. time curves of HVE models obtained by (a) two-step method, (b) (inverse) stress solution methods without stress-relaxation data, and (c) (inverse) stress solution methods with stress-relaxation data, at loading nominal strain-rate of $10^{-2}\ s^{-1}$.

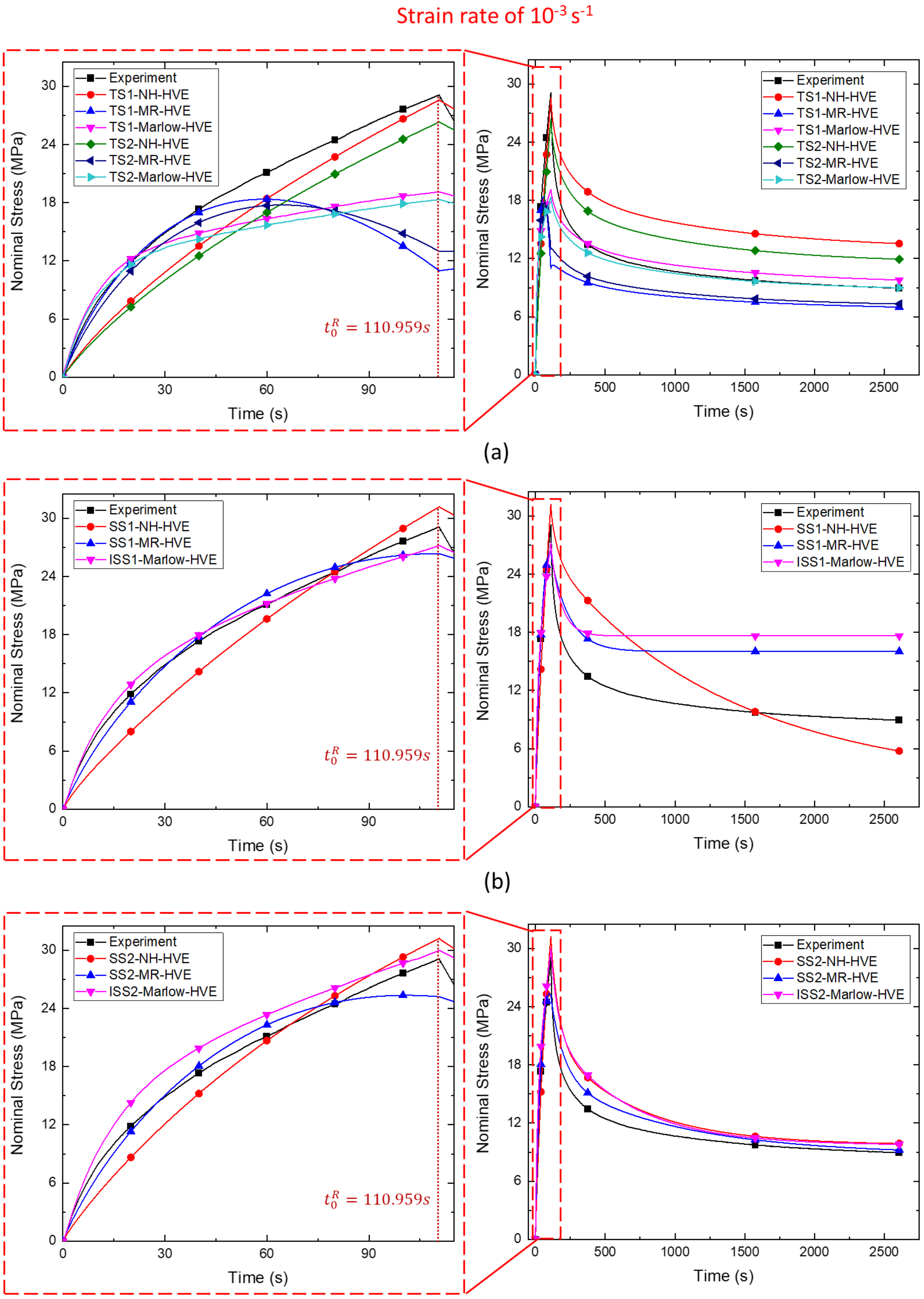

(a)

(b)

(c)

Figure 5-16 The time-dependent nominal stress vs. time curves of HVE models obtained by (a) two-step method, (b) (inverse) stress solution method without stress-relaxation data, and (c) (inverse) stress solution method with stress-relaxation data, at loading nominal strain-rate of $10^{-3}\ s^{-1}$.

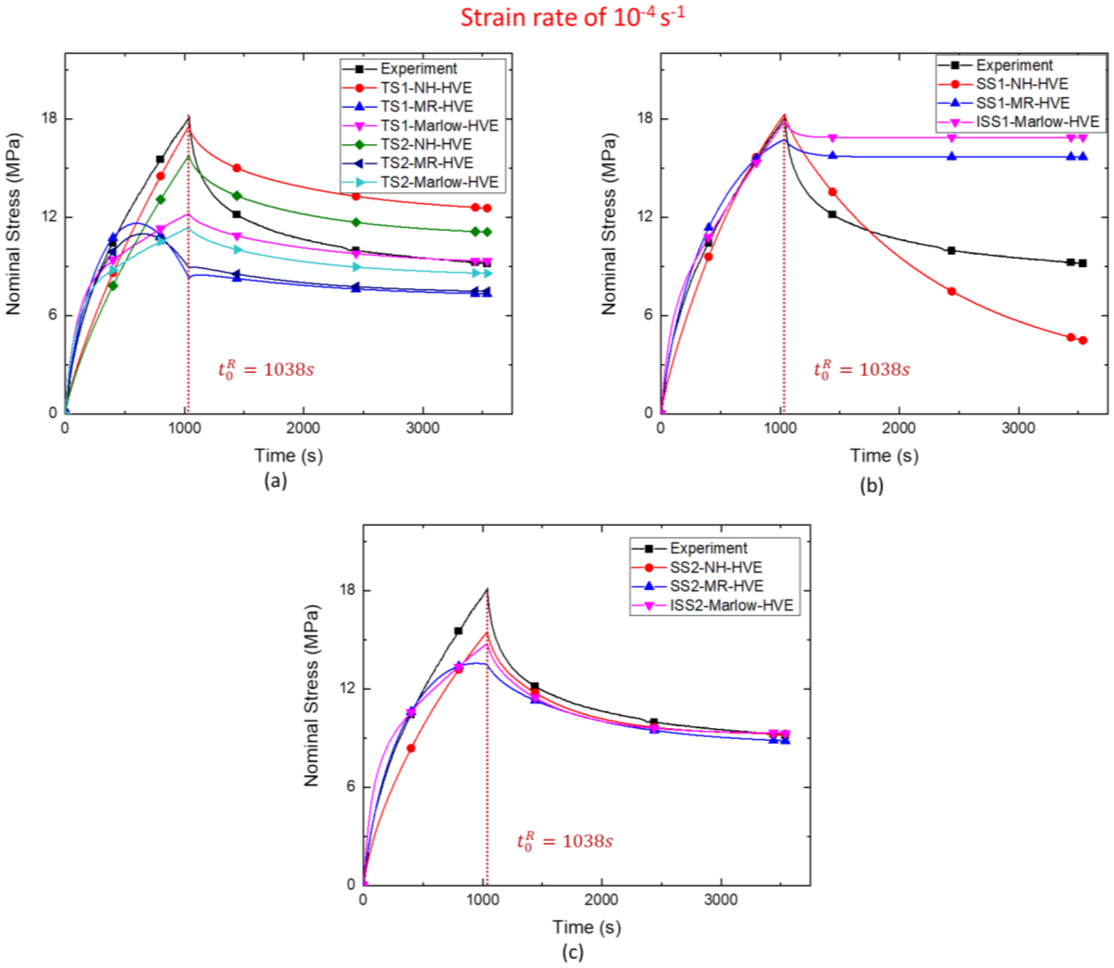

Figure 5-17 The time-dependent nominal stress vs. time curves of HVE models obtained by (a) two-step method, (b) (inverse) stress solution methods without stress-relaxation data, and (c) (inverse) stress solution methods with stress-relaxation data, at loading nominal strain-rate of $10^{-4}\ s^{-1}$.

Table 5-6 The reliability of HVE models at only ramp-loading stage under various loading nominal strain-rates.

Material models	R^2 under different loading nominal strain-rates				Mean of R^2	Standard deviation of R^2
	$10^{-1}\ s^{-1}$	$10^{-2}\ s^{-1}$	$10^{-3}\ s^{-1}$	$10^{-4}\ s^{-1}$		
TS1-NH-HVE	0.812	0.824	0.851	0.898	0.8462	0.0329
TS1-MR-HVE	0.692	0.332	0.001	0.332	0.3393	0.2444
TS1-Marlow-HVE	0.908	0.675	0.437	0.560	0.6450	0.1735
TS2-NH-HVE	0.783	0.714	0.706	0.730	0.7332	0.0303
TS2-MR-HVE	0.710	0.421	0.127	0.333	0.3981	0.2095
TS2-Marlow-HVE	0.792	0.547	0.312	0.388	0.5097	0.1839
SS1-NH-HVE	0.762	0.848	0.895	0.970	0.8688	0.0753
SS1-MR-HVE	0.983	0.973	0.981	0.981	0.9796	0.0038
ISS1-Marlow-HVE	0.985	0.992	0.984	0.986	0.9867	0.0032
SS2-NH-HVE	0.789	0.812	0.930	0.796	0.8319	0.0572
SS2-MR-HVE	0.983	0.975	0.967	0.856	0.9454	0.0518
ISS2-Marlow-HVE	0.955	0.949	0.928	0.859	0.9227	0.0381

Table 5-7 The reliability of HVE models at both stages under various loading nominal strain-rates.

Material models	R^2 under different loading nominal strain-rates				Mean of R^2	Standard deviation of R^2
	$10^{-1}\ s^{-1}$	$10^{-2}\ s^{-1}$	$10^{-3}\ s^{-1}$	$10^{-4}\ s^{-1}$		
TS1-NH-HVE	0.532	0.826	0.698	0.526	0.6455	0.1249
TS1-MR-HVE	0.864	0.678	0.295	-0.011	0.4563	0.3391
TS1-Marlow-HVE	0.929	0.848	0.646	0.557	0.7452	0.1497
TS2-NH-HVE	0.704	0.827	0.733	0.663	0.7318	0.0605
TS2-MR-HVE	0.889	0.725	0.399	0.045	0.5144	0.3236
TS2-Marlow-HVE	0.916	0.793	0.570	0.334	0.6532	0.2220
SS1-NH-HVE	0.616	0.857	0.787	0.667	0.7315	0.0952
SS1-MR-HVE	0.565	0.858	0.695	-0.102	0.5038	0.3651
ISS1-Marlow-HVE	0.345	0.811	0.536	-0.621	0.2677	0.5392
SS2-NH-HVE	0.752	0.884	0.924	0.811	0.8430	0.0662
SS2-MR-HVE	0.914	0.974	0.971	0.840	0.9247	0.0544
ISS2-Marlow-HVE	0.813	0.944	0.925	0.858	0.8853	0.0524

Firstly, as can be seen from Figure 5-14(a) to Figure 5-17(a) and the R^2 in Table 5-6 and Table 5-7, the HVE models obtained by two-step method have relative unsatisfied results in both ramp-loading stage and stress-relaxation stage, especially in the case of lower loading nominal strain-rates ($10^{-3}\ s^{-1}$ and $10^{-4}\ s^{-1}$). This is because the viscoelastic parameters are only determined by one set of the high nominal strain-rate test. If there are measurement or machine errors at the beginning of the stress-relaxation stage, the error will continue to accumulate with time. For the case of high loading nominal strain-rates (e.g. $10^{-1}\ s^{-1}$), the viscoelastic effect in ramp-loading stage is insignificant due to the short loading period, and therefore, the predictive results in this case are relatively better (especially at the beginning of the ramp-loading stage). However, in the case of low loading nominal strain-rates (e.g. $10^{-4}\ s^{-1}$), the accumulating errors with time will be amplified, resulting in increasingly inaccurate predictive results. It should be noted that the differences between the models determined by the experimental data of loading nominal strain-rates of $10^{-1}\ s^{-1}$ and $10^{-2}\ s^{-1}$ (i.e. model names start with 'TS1' and 'TS2', respectively) are not significant. On the other hand, all MR based HVE models obtained by the two-step method have the most unsatisfied results and experience a stress drop before the stress-relaxation stage. This phenomenon indicates that the MR based constitutive models do not satisfy the Drucker stability conditions (Romanov 2001), i.e. $d\sigma : d\varepsilon > 0$, which may cause an error in FE simulations. It should be noted that even though TS1-Marlow-HVE has the best R^2 results for both stages among all the models at loading nominal strain-rate of $10^{-1}\ s^{-1}$ (see Table 5-6), the predicted nominal stress value at the beginning of the relaxation stage still has a distinct difference from the experimentally-measured value (see Figure 5-14(a)).

Secondly, in contrast to the HVE models determined by the traditional two-step method, the previously proposed stress-solution method and the presently proposed inverse stress solution method show better performance. However, as can be seen from Figure 5-14(b) to Figure 5-17(b), if the HVE parameters are calibrated only with the experimental data in the ramp-loading stage, the prediction in the stress-relaxation stage will not be accurate, although the prediction in the ramp-loading stage is better than the models calibrated by data of both stages (Table 5-6). This is because the ramp-loading data usually covers only a relatively short-term period (see t_0^R in Figure 5-14 to Figure 5-17) compared to the stress-relaxation period (2500s), which leads to the situation that the largest retardation time τ_1^R in the HVE model is calibrated with only ramp-loading data in a short time period, which is insufficient to represent the relaxation state in long-term period, e.g. the largest τ_1^R is around 76s in ISS1-Marlow-HVE model but the full process of the tension-relaxation test can be as long as around 3000s.

Lastly, as can be seen from Figure 5-14(c) to Figure 5-17(c), compared to the other nine HVE models, all three HVE models calibrated by the experimental data in both stages based on the stress solution or inverse stress solution method (i.e. HVE names start with 'SS2' or 'ISS2') have better R^2 results. For the equation-based calculation, the MR hyperelastic model based SS2-MR-HVE model gives the best overall R^2 results. However, the equation-based calculations only have had preliminary assessments here, as some other factors that may cause the convergence error in the FE simulations have not been considered here.

5.6.2 FE model

In order to evaluate the actual performance of the HVE models in the application of FEM, an FE analysis (FEA) is conducted. The FE model (Figure 5-18(a)) was established with the same geometry of the testing sample gauge area introduced in Figure 5-2(a), i.e. a rectangle with 80 mm length and 16 mm width. The mesh size was determined as 1.6 mm (i.e. 1/10 of the width) based on mesh convergence analysis. The 4-node quadrilateral shell element with reduced integration (S4R) was applied to meet the requirement of finite-strain deformation. The quasi-static step is specifically used to analyse the time-dependent material response, where the inertial effects can be neglected (it is similar to the common ‘static’ step, but can consider time-dependent effects such as creep or relaxation). In the first step (ramp-loading stage), one end of the sample was fixed, and the other end moved in x_1-direction under displacement-control while the other five degrees of freedom at two ends were constrained, as shown in Figure 5-18. The time-step T_L (i.e. t_0^R in Figure 5-14 to Figure 5-17) and the boundary condition (displacement U_1 or U_{ua}) in this step were determined separately according to the tension loading process at different loading nominal strain-rates (i.e. $\dot{\varepsilon} \sim (U_1(mm)/80mm)/T_L$) up to the nominal strain of 0.10, as listed in Table 5-8. In the second step, the boundary condition was fixed (i.e. U_{ua} remains unchanged) and the time-step T_H was set as 2500s. The boundary condition and the step-time set in the FE simulation are illustrated in Figure 5-18(b). To better trace the simulation evolution, the automatic increment was selected with the maximum time increment set as $0.01T_L$ and $0.01T_H$ for each step, respectively. The maximum number of increments is set to be 10000 for each step.

Table 5-8 Details of boundary condition and time-step used in FE simulations of the uniaxial tension loading stage, representing separators loaded at various loading nominal strain-rates.

Case of loading nominal strain-rate (s^{-1})	U_1 or U_{ua} (mm)	Loading step time period T_L (s)	Holding constraint step time period T_H (s)
10^{-1}	9.102	1.197	2500
10^{-2}	8.703	11.245	2500
10^{-3}	8.856	110.959	2500
10^{-4}	8.305	1038	2500

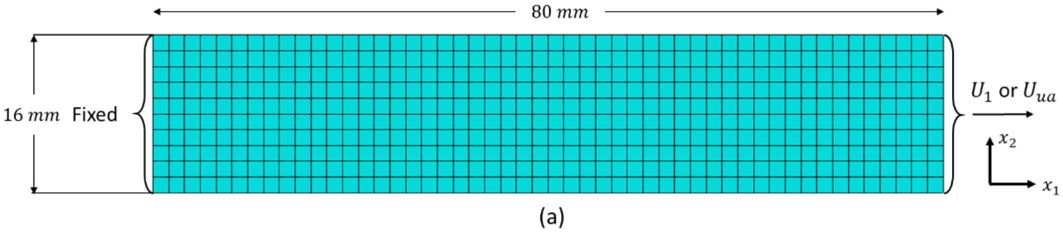

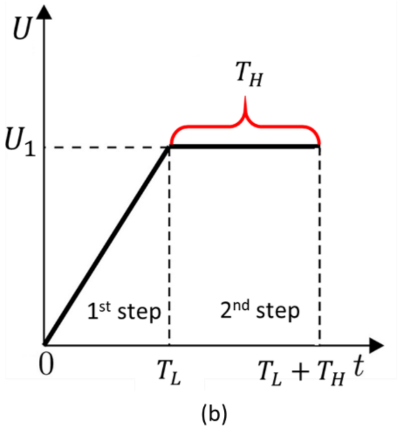

Figure 5-18 (a) FE model geometry with mesh and boundary condition; (b) the illustration of the boundary condition and the time-step set in the FE simulation.

The HVE material model in Abaqus is a combination of the hyperelastic model and viscoelastic model. In this study, HVE models based on three hyperelastic models (i.e. NH model, MR model and Marlow model) and a time-domain viscoelastic model (based on Prony series form) are established via three methods presented in Section 5.5. Figure 5-19 shows the illustration of the materials card setting for the HVE model used in Abaqus. The parameters used in HVE models determined by three methods are listed in Table 5-2, Table 5-3, Table 5-4 and Table 5-5, respectively.

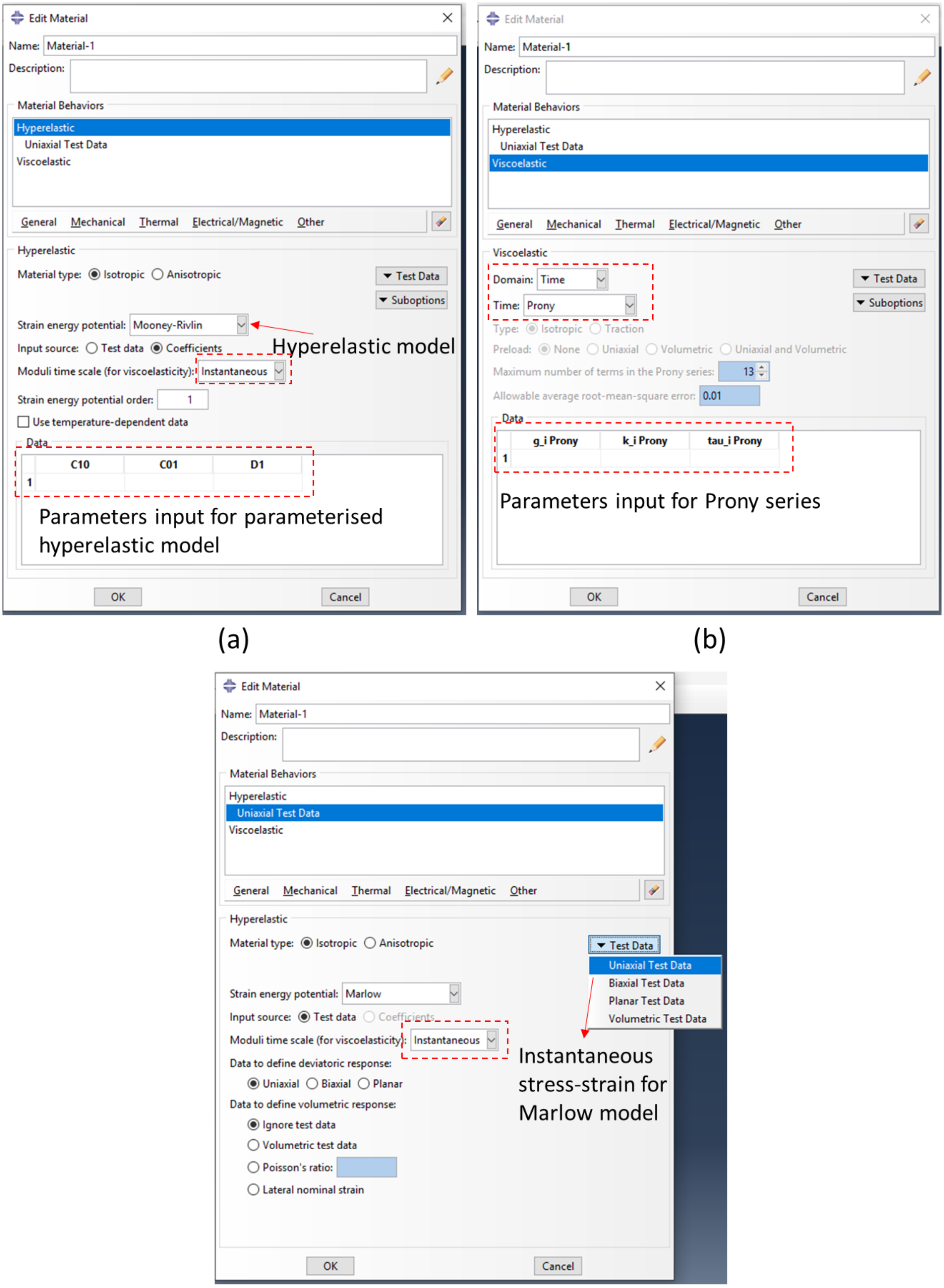

(a)

Name: Material-1
Material Behaviors: Hyperelastic; Uniaxial Test Data; Viscoelastic
Hyperelastic
Material type: ● Isotropic ○ Anisotropic
Strain energy potential: Mooney-Rivlin
Input source: ○ Test data ● Coefficients
Moduli time scale (for viscoelasticity): Instantaneous
Strain energy potential order: 1
☐ Use temperature-dependent data

	C10	C01	D1
1			

Hyperelastic model

Parameters input for parameterised hyperelastic model

(b)

Name: Material-1
Material Behaviors: Hyperelastic; Uniaxial Test Data; Viscoelastic
Viscoelastic
Domain: Time
Time: Prony
Type: ● Isotropic ○ Traction
Preload: ● None ○ Uniaxial ○ Volumetric ○ Uniaxial and Volumetric
Maximum number of terms in the Prony series: 13
Allowable average root-mean-square error: 0.01

	g_i Prony	k_i Prony	tau_i Prony
1			

Parameters input for Prony series

(c)

Name: Material-1
Material Behaviors: Hyperelastic; Uniaxial Test Data; Viscoelastic
Hyperelastic
Material type: ● Isotropic ○ Anisotropic
Test Data: Uniaxial Test Data; Biaxial Test Data; Planar Test Data; Volumetric Test Data
Strain energy potential: Marlow
Input source: ● Test data ○ Coefficients
Moduli time scale (for viscoelasticity): Instantaneous
Data to define deviatoric response: ● Uniaxial ○ Biaxial ○ Planar
Data to define volumetric response:
● Ignore test data
○ Volumetric test data
○ Poisson's ratio:
○ Lateral nominal strain

Instantaneous stress-strain for Marlow model

Figure 5-19 The material card setting for HVE model of (a) parameterised hyperelastic model (e.g. NH model and MR model), (b) time-domain viscoelastic model with Prony series form, and (c) test data input Marlow hyperelastic model.

5.6.3 Comparison of numerical and experimental results

In order to validate the efficiency of the HVE model, the outputs of the total reaction force on the moving edge against time from FE simulations were used to compare with the corresponding experimental results obtained from the tension-relaxation tests at different loading nominal strain-rates, as shown in Figure 5-20 to Figure 5-23.

From Figure 5-20 to Figure 5-23, it can be observed that some of the HVE models cannot continue the numerical simulation due to the errors that occurred in the simulation process. To figure out the reason for the computing errors of these HVE models, the error messages were checked in the message files provided by Abaqus and summarised in Table 5-9. Except for these problematic HVE models, other HVE models can be successfully run in the FE simulations. It is found that these HVE models have similar predictive performance to the results presented in Section 5.6.1.

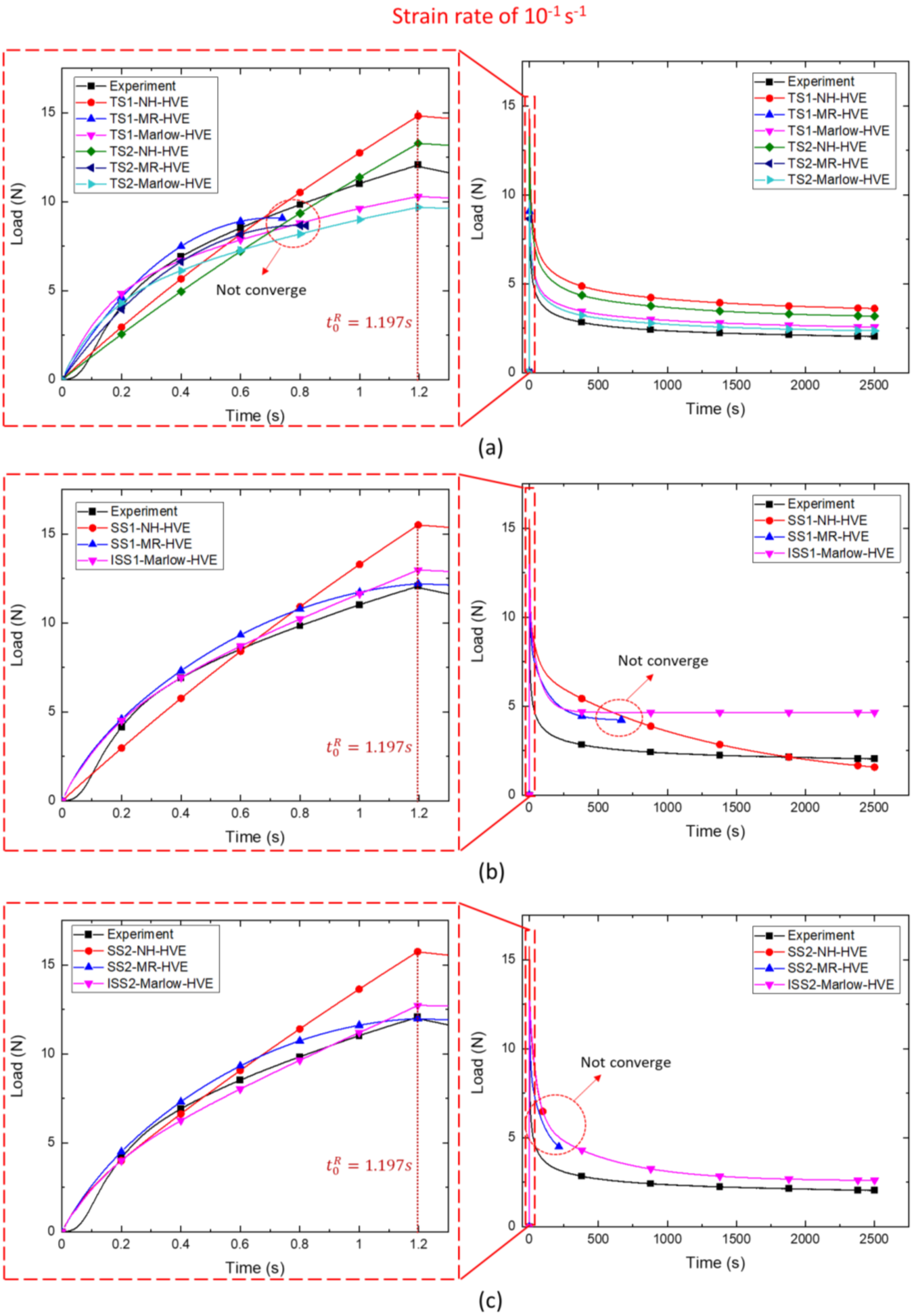

Figure 5-20 The force-time curves obtain from experiments and FE simulations based on (a) two-step method, (b) (inverse) stress solution methods without stress-relaxation data, and (c) (inverse) stress solution methods with stress-relaxation data, at loading nominal strain-rate of $10^{-1}\ s^{-1}$.

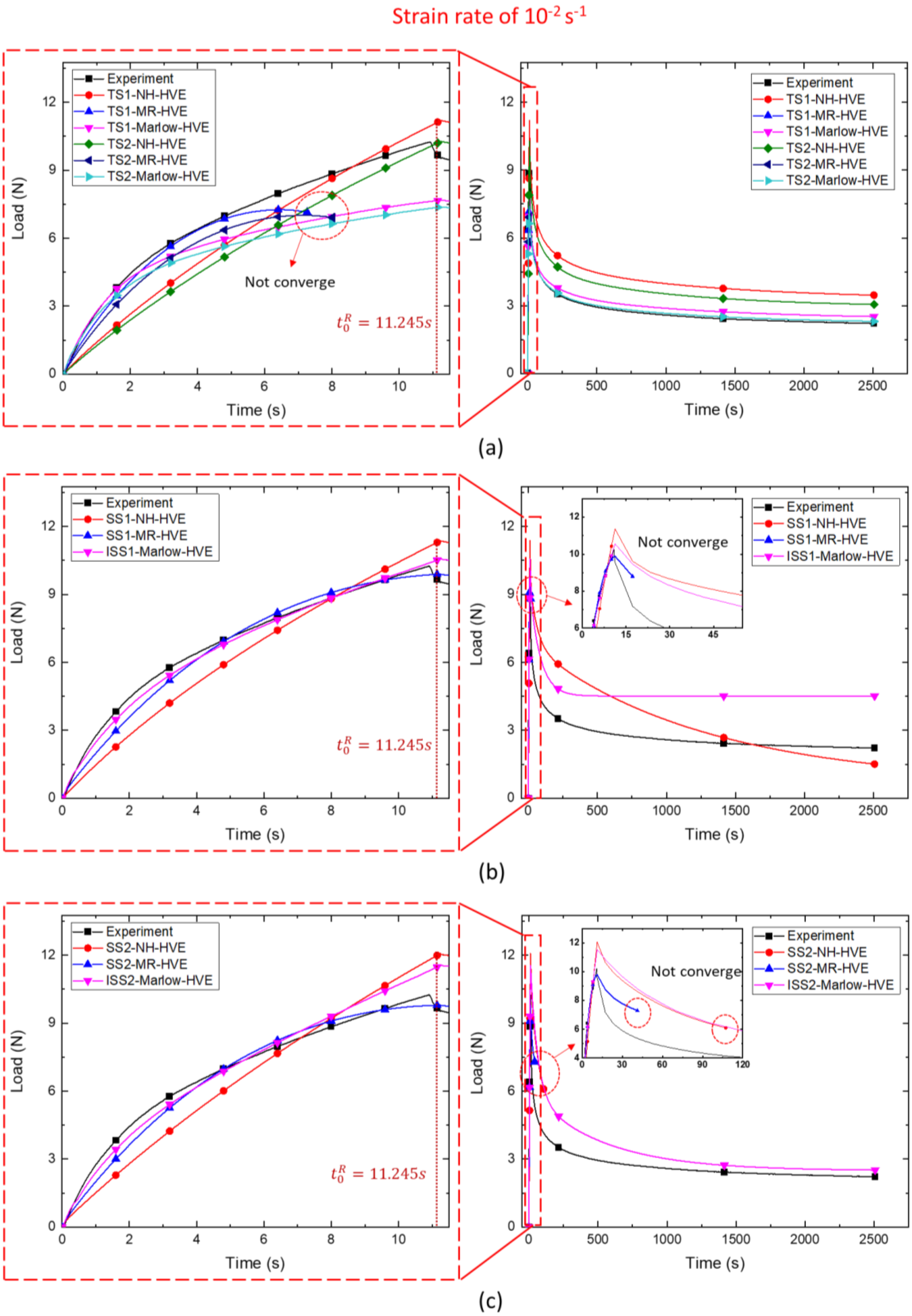

Figure 5-21 The force-time curves obtain from experiments and FE simulations based on (a) two-step method, (b) (inverse) stress solution methods without stress-relaxation data, and (c) (inverse) stress solution methods with stress-relaxation data, at loading nominal strain-rate of $10^{-2}\ s^{-1}$.

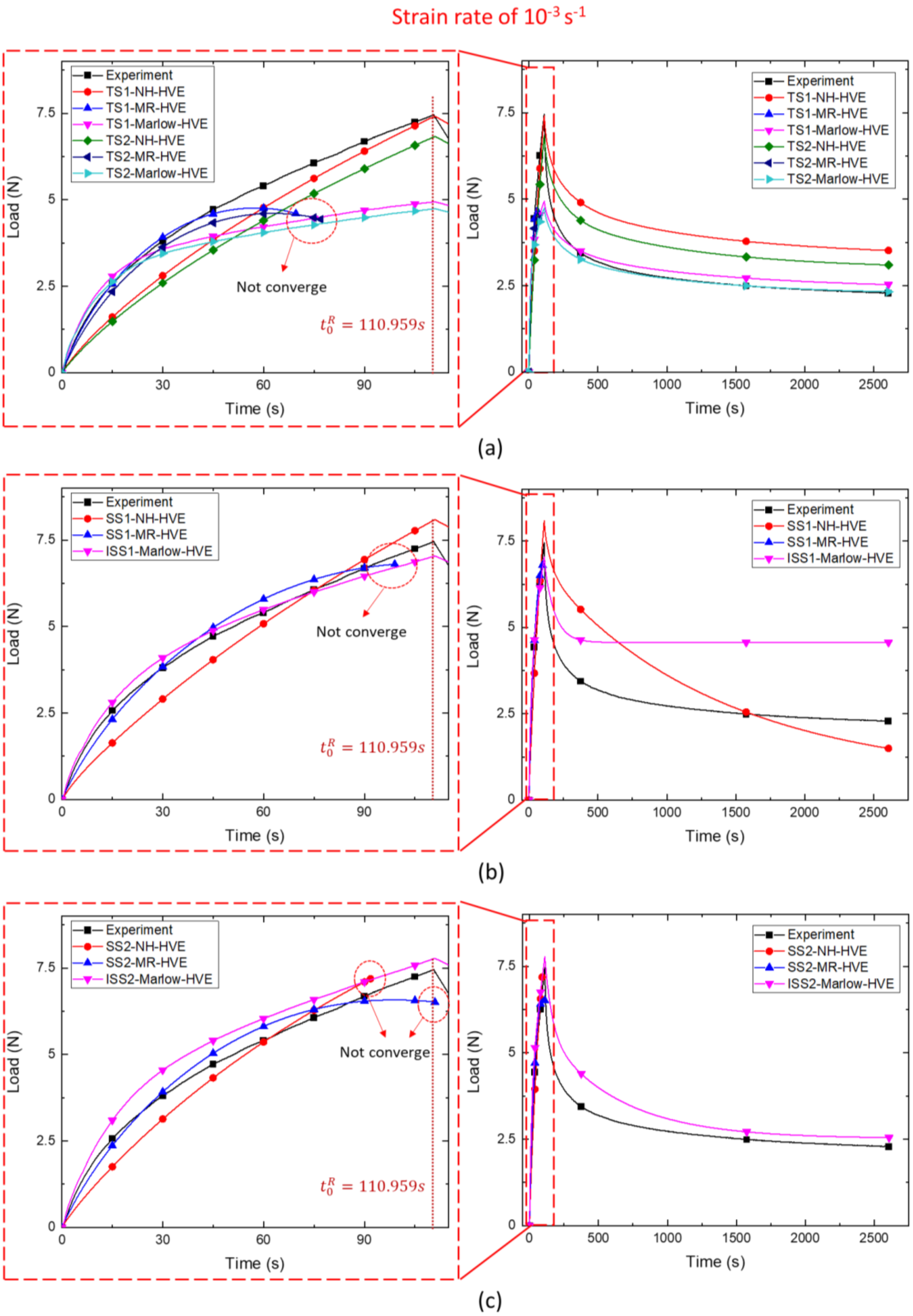

Figure 5-22 The force-time curves obtain from experiments and FE simulations based on (a) two-step method, (b) (inverse) stress solution methods without stress-relaxation data, and (c) (inverse) stress solution methods with stress-relaxation data, at loading nominal strain-rate of $10^{-3}\ s^{-1}$.

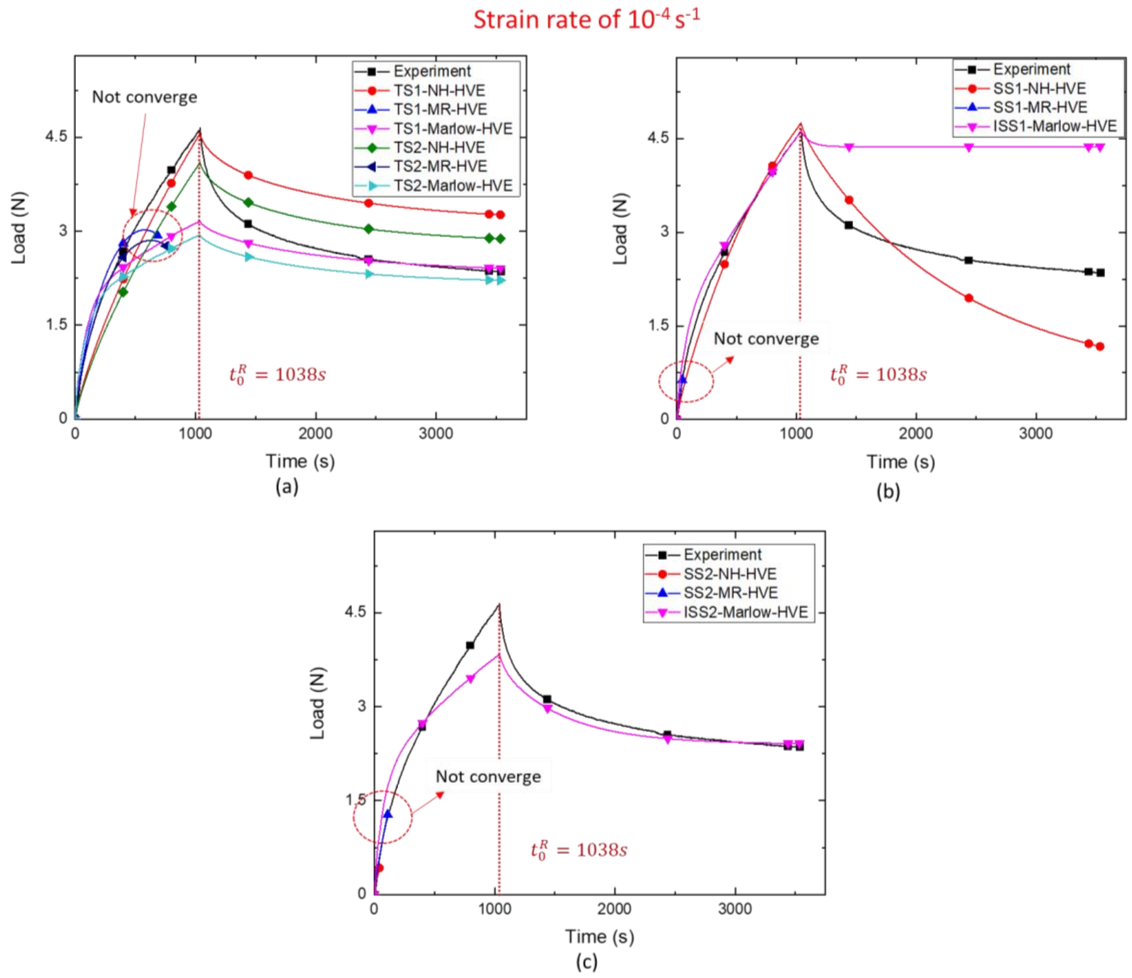

Figure 5-23 The force-time curves obtain from experiments and FE simulations based on (a) two-step method, (b) (inverse) stress solution methods without stress-relaxation data, and (c) (inverse) stress solution methods with stress-relaxation data, at loading nominal strain-rate of $10^{-4}\ s^{-1}$.

Table 5-9 The error problems of HVE models in FE simulation.

Material models	Error happens?	If error happens, at which stage it happens		Reason
TS1-NH-HVE	No	-		-
TS1-MR-HVE	Yes	All in ramp-loading stage		Not satisfy Drucker stability condition
TS1-Marlow-HVE	No	-		-
TS2-NH-HVE	No	-		-
TS2-MR-HVE	Yes	All in ramp-loading stage		Not satisfy Drucker stability condition
TS2-Marlow-HVE	No	-		-
SS1-NH-HVE	No	-		-
SS1-MR-HVE	Yes	Stress-relaxation 10^{-1} s^{-1}, 10^{-2} s^{-1}	Ramp-loading 10^{-3} s^{-1}, 10^{-4} s^{-1}	Force and moment equilibrium cannot be achieved within tolerance
ISS1-Marlow-HVE	No	-		-
SS2-NH-HVE	Yes	Stress-relaxation 10^{-1} s^{-1}, 10^{-2} s^{-1}	Ramp-loading 10^{-3} s^{-1}, 10^{-4} s^{-1}	Force and moment equilibrium cannot be achieved within tolerance
SS2-MR-HVE	Yes	Stress-relaxation 10^{-1} s^{-1}, 10^{-2} s^{-1}	Ramp-loading 10^{-3} s^{-1}, 10^{-4} s^{-1}	Not satisfy Drucker stability conditions (10^{-3} s^{-1}); Force and moment equilibrium cannot be achieved within tolerance (10^{-1} s^{-1}, 10^{-2} s^{-1}, 10^{-4} s^{-1}).
ISS2-Marlow-HVE	No	-		-

By running the FE simulation of each HVE model, it can be seen that even though the MR based HVE model determined by the stress-solution method (i.e. SS2-MR-HVE) has the best performance in all equation-based calculations (see Table 5-7), this model has a convergence problem in actual FE simulations. Not only SS2-MR-HVE but also all other

HVE models based on MR hyperelastic model have convergence problems in FE analysis, as shown in Table 5-9. According to the message files, there are two kinds of error cause the convergence problem in the computing, i.e. (1) not satisfying Drucker stability condition after a certain strain (i.e. the stress will not increase monotonously with strain without considering time factors), and (2) force and moment equilibrium cannot be achieved within tolerance. For the first kind of error, it is caused by the MR hyperelastic model, which was predicted in Section 5.6.1. The second kind of error is more complicated, as no explicit reason can be known from the computing result files or message files. As stated in the or message files, it is speculated that 'force and moment equilibrium cannot be achieved within tolerance' is caused by high nonlinearly in the equilibrium equations as a result of the combination of hyperelastic model and viscoelastic model, which are both nonlinear models. This problem may be able to be solved by an explicit solver, but it can take a long time to compute (as the duration of the stress-relaxation stage is very long).

On the other hand, among all HVE models, the ones that use Marlow model as their hyperelastic part have the most stable performance in FE analysis. Moreover, according to Table 5-6, Table 5-7, Figure 5-14 to Figure 5-17 and Figure 5-20 to Figure 5-23, it can be seen that the HVE model determined by the proposed inverse stress solution method (i.e. ISS2-Marlow-HVE) has the best performance among all HVE models. Therefore, compared to HVE models determined by other methods, the proposed ISS2-Marlow-HVE can effectively predict the material behaviour within the strain up to 0.10 at various loading nominal strain-rates from $10^{-1}\ s^{-1}$ down to $10^{-4}\ s^{-1}$, in both ramp-loading and stress-relaxation stages.

Overall, the proposed inverse stress solution method could be used for the parametrical calibration of HVE models for isotropic separators or even other incompressible materials with similar characteristics (i.e. viscoelasticity, large nonlinear elastic regime) deformed in the elastic regime. It should be noted that the proposed method is limited to the materials with viscoelastic behaviour only related to time (i.e. $g(t)$). For the materials with viscoelastic behaviour related to both time and deformation (i.e. $g(t, \varepsilon)$), e.g. (A. López-Campos et al. 2019), the proposed method needs to be further developed.

5.7 Summary

In this chapter, a comprehensive analytical-experimental-numerical method is proposed to study the commercial wet-processed isotropic separators. A hyper-viscoelastic (HVE) model is presented to overcome the limitation of small strain for the validity of the current viscoelastic model. Uniaxial tension-relaxation tests, including the tension ramp-loading and stress-relaxation stages, are performed at four loading nominal strain-rates and measured by a live virtual extensometer. Based on experimental observations and further analytical and numerical studies, important findings are summarised below.

i) Due to the uncontrollable machine factors, it is impossible to stop the moving crosshead at high loading nominal strain-rate ($10^{-1}\,s^{-1}$ in this study) immediately at the prescribed relaxation strain, leading to an overshot around the beginning of relaxation.

ii) No matter which loading nominal strain-rate is applied to the separators, the nominal stresses finally converge to a same value for a prescribed nominal strain $\varepsilon < 0.10$ after experiencing a sufficiently long time, i.e. the long-term nominal stresses are the same after the separators experience different loading nominal strain-rates.

iii) Particularly, the long-term nominal stress P_∞ eventually converge to a same value in experiments at different loading nominal strain-rates for $\varepsilon_R = 0.05$ and 0.10 but not for $\varepsilon_R = 0.15$. This phenomenon implies that the separators were yielded or damaged when $\varepsilon > 0.10$, and therefore, $0 < \varepsilon < 0.10$ can be regarded as the elastic regime in this study.

Based on the experimental observation and the framework of the HVE model, three parametrical calibration methods (i.e. two-step method, stress solution method and the proposed inverse stress solution method) are used to establish various HVE material models, which are validated by the FE simulation. Furthermore, by comparing the numerical results of HVE models determined by various calibration methods with the experimental results, following important findings can be drawn:

a) The two-step method has the least reliable overall performance among the three parametrical calibration methods as it only uses experimental data under a single loading rate.

b) The previous stress solution method requires the optimisation of both hyperelastic parameters and Prony series parameters at the same time. In contrast, the proposed inverse stress solution method only optimises the Prony series parameters, which avoids the misplacement of errors from one set of parameters to the other set of parameters.

c) If data in the stress-relaxation stage is not considered in the parametrical calibration, the HVE models determined by the (inverse) stress solution methods can accurately predict the ramp-loading stage, but not the stress-relaxation stage due to the lack of material data on its long-term viscoelastic behaviour.

d) Even though the HVE model based on Mooney-Rivlin (MR) hyperelastic model, which is determined by the previous stress solution method, has the best predictive performance and has been validated by the numerical equation, this hyperelastic model is prone to violating the Drucker stability condition, causing numerical instability in FE simulation. In contrast, Marlow model has no such problem.

e) Compared to other parametrical calibration methods, the HVE model determined by the proposed inverse stress solution method (i.e. ISS2-Marlow-HVE) demonstrates the best predictive results at various loading nominal strain-rates within the strain up to 0.1, in both ramp-loading and stress-relaxation stages.

Consequently, the proposed analytical-experimental-numerical method enables the researchers to investigate the separators in both long-term and short-term deformations in the applications of batteries due to large deformations caused by mechanical abuses. Moreover, the proposed method can also be extended to other similar materials with large nonlinear elastic regimes and viscoelastic sensitive characteristics (e.g. polymer, rubber).

6 Discussion

In this chapter, the author discusses the intrinsic connections among various parts of the work presented in previous chapters, as well as their limitations. The potential applications of this PhD research to the study of the safety issues of liquid electrolyte batteries are also discussed.

6.1 The CGB method proposed in uniaxial tensile test of separators

As shown in the pilot study in the present research and previous studies of mechanical test of separators (Zhang et al. 2016a, Zhu et al. 2018c, Hao et al. 2020), thin-film-structure separators can be easily wrinkled during the uniaxial tensile test, which is the most common and important experimental method to determine the mechanical property of a material. It has been warned by some researchers (e.g. Zhu et al. 2018c) that wrinkling may cause inaccurate strain measurement. Because strain (or deformation) is a key mechanical factor that bridges the whole study of the PhD project, i.e. the porosity variation $\Phi(\varepsilon_l)$ in Chapter 4 and the time-dependent stress response $\sigma\big(\lambda(t)\big)$ or $P\big(\lambda(t)\big)$ in Chapter 5, it is necessary to guarantee the accuracy of strain measurement. In Chapter 3, a wrinkle-free design (i.e. CGB method) method was proposed based on FE method to avoid the occurrence of wrinkling in the uniaxial tensile test of thin film materials. By comparing the experimental results of test samples with and without wrinkling, it can inform the conditions when a wrinkle-free design is required or the wrinkling effect can be ignored so that acceptable experimental design and procedure can be determined. For example, in Chapter 4, wrinkle-free design is necessary as the determination of porosity variation (i.e. Eq. (4.5)) requires the measurement of both longitudinal and transverse strains. However, in Chapter 5, wrinkling can be ignored as it has only limited influence on uniaxial stress response calculation. This will be further discussed in Section 6.2.

On the other hand, it should be noted that there is a slight difference between the theoretical results in Chapter 3 and the experimental results observed in Chapter 4. In Chapter 3, it has been concluded that when the geometry of the thin film satisfies

$F(\alpha,\beta,\gamma) = \beta - 0.043 \cdot (\gamma - 1200)^{0.30} \cdot \alpha^{-(3.769 \cdot \gamma^{-0.3421})} > 0$, i.e. Eq. (3.6), the wrinkling phenomenon can be avoided in the uniaxial tensile test. Therefore, when $\gamma < 1200$, as a sufficient but simpler condition, no wrinkling phenomenon should happen. However, in Chapter 4, even though the non-dimensional geometric factor γ of the strip-shaped wet-processed separator is only 500, which is less than 1200, the wrinkling phenomenon can still be observed. Based on the observation in the real experiment and the author's knowledge, this unexpected phenomenon could be attributed to the following factors:

1) Manufacturing defect or imperfection

As discussed in Section 3.4.5, the geometric defect or geometric imperfection, e.g. cutting defect or uneven thickness, can have an adverse effect on the result of the proposed CGB method as the stiffness of the structure is changed. These geometric defects tend to occur in the manufacturing process (e.g. uneven thickness) or the sample preparation (e.g. non-parallel long edges in gauge area). For example, a speckle pattern was sprayed on the surface of separators, which may cause a change in the stiffness of the thin film structure, even though it would not affect the in-plane deformation behaviour (Yan et al. 2018a).

2) Not ideal boundary condition

In the real experiment, the ideal two-end-clamped boundary condition presented in Figure 3-1 is impossible to be perfectly replicated. In some tests, the wrinkles have already been observed for the strip-shaped specimens when the pneumatic grips are closed. In the author's opinion, it is highly likely that the rough surfaces inside the grips (it has to be rough enough to enhance the friction) cause lateral contraction to the separator sample when the grip is closed, because lateral contraction is the main reason for the occurrence of wrinkling, as presented in Chapter 3. For example, the occurrence of wrinkling near the grips was observed in the dogbone-shaped specimen of Hipore-16-isotropic, as shown in Figure 4-5(e), while no wrinkle can be seen in the gauge area.

3) Material model of the separator

In Chapter 3, the material model of the studied thin film material is assumed to be a typical linear elastic solid material model. In contrast, in Chapter 5, it can be seen that a hyper-viscoelastic model is more suitable for the separator in terms of the stress-strain response. Moreover, the porous microstructure characteristics, e.g. porosity variation, may also affect the stiffness of the thin film structure while the CGB method was studied based on a solid material. Therefore, the selection of the material model may also affect the results, which needs more investigation in the future.

Therefore, there is a difference between the theoretical CGB results based on the assumption of perfectly elastic material under ideal uniaxial loading conditions and the actual experimental results, due mainly to the three potential factors presented above. Among these three potential factors, the second factor (i.e. not ideal boundary condition) has the most significant impact on the appearance of this difference, as it directly generates the in-plane transverse compressive stress.

In order to achieve the wrinkle-free design suitable for practical applications, i.e. uniaxial tensile tests in this project, two methods may be able to help, i.e. to improve the experimental preparation to reduce the adverse effect caused by the above-mentioned factors, or to correct the CGB boundary to achieve a more conservative result.

For the former method, Nayyar (2013) designed a pair of special clamps for the thin film sample and only made a speckle pattern in the centre area, as shown in Figure 6-1. However, this method needs many trials, which is impractical due to the limited access to the laboratory during the Covid-19 pandemic. Meanwhile, the application of the speckle pattern in the centre alone cannot give a global strain distribution result, which is important in the study introduced in Chapter 4.

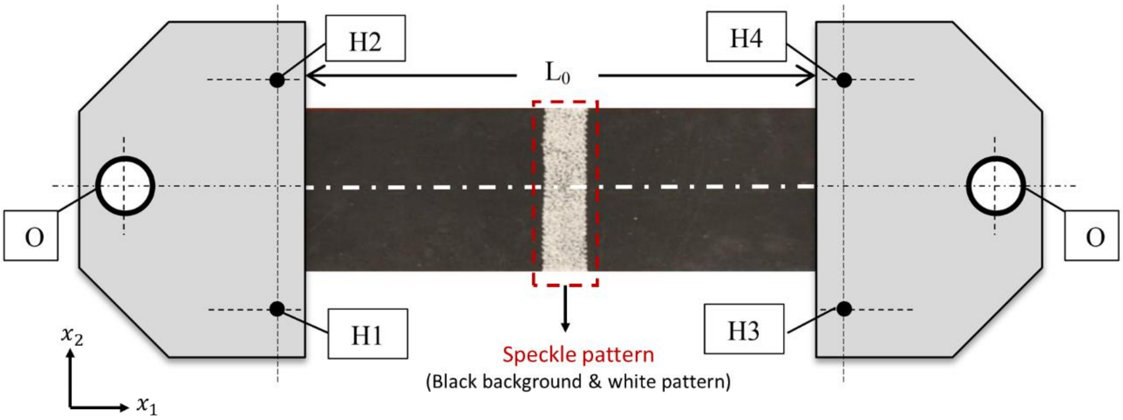

Figure 6-1 The thin film sample, with speckle pattern only in the centre area, clamped by a pair of special clamps (Adapted from Nayyar 2013). H1-H4 are the holes for bolts to secure the clamps tightly, and grips are used to hold the clamps in the Instron machine by passing a pin through hole ‘O’ in the clamps and the grips.

Therefore, in order to improve the accuracy of the study, the second method is adopted. According to the observation in the pilot study, a 'safety factor' η is introduced to Eq. (3.6) to consider the above uncertainties, and therefore, Eq. (3.6) becomes

$$F(\alpha,\beta,\gamma) = \beta - 0.043 \cdot (\eta \cdot \gamma - 1200)^{0.30} \cdot \alpha^{-\left(3.769 \cdot (\eta \cdot \gamma)^{-0.3421}\right)} = 0 \tag{6.1}$$

where other parameters can be referred to Chapter 3. Therefore, in order to avoid the wrinkling, $\eta = 4$ is determined based on the observation results of strip-shaped separators in Chapter 4, and $\alpha = 0.4, \beta = 1.785, \gamma = 500$ can be obtained according to Figure 4-1. In this case, $F(\alpha,\beta,\gamma) = 1.37 > 0$ can be calculated based on the modified CGB function, i.e. Eq. (6.1), which satisfies the wrinkle-free design condition. It should be noted that the 'safety factor' is only given to guarantee the wrinkle-free design.

On the other hand, even though the wrinkle-free design method is based on the assumption of isotropic materials, the proposed wrinkle-free design method is also applicable to the separators with slight anisotropic, e.g. wet-processed separators studied in Chapter 4. Moreover, the wrinkle-free design method considering different material models (e.g. dry-processed separators with high anisotropic behaviour, hyper-viscoelastic behaviour) needs a further comprehensive study in the future.

6.2 Selection of thin film sample shape and strain measurement method

As discussed in Section 6.1, by comparing the measurement results of experiments with and without wrinkling, we can distinguish the measurements that are affected by wrinkling from those that are not. In previous research (Zhu et al. 2018c), it has been proved that wrinkling can have an adverse influence on strain measurement in transverse direction (x_2 direction in Figure 3-1), which is also observed in Chapter 4, i.e. Figure 4-8(b). In contrast, the strain measurement in longitudinal direction (i.e. x_1 direction in Figure 3-1) shows consistency in experiments with and without wrinkling phenomenon, as shown in Figure 4-8(a) and Figure 4-9, indicating that wrinkle-free design is less important if only longitudinal results are required.

In Chapter 4, the variations of Poisson's ratio and porosity require accurate strain measurement in transverse direction, according to Eqs. (4.5) and (4.6). In this case, the adverse effect on transverse strain measurement caused by wrinkling should be avoided, and therefore, a wrinkle-free design for the thin film separator sample is necessary for this study.

On the other hand, in Chapter 5, the study of the material constitutive model was reduced to a 1D problem (i.e. uniaxial loading condition), and only longitudinal strain is required in this study. According to the consistency shown in the experiments with and without wrinkling, the strip-shaped separator was decided to be used to simplify the sample preparation. Furthermore, it is also advantageous to use a strip-shaped sample instead of a dogbone-shaped sample to study the material viscoelasticity, as the nominal strain for the stress relaxation stage is controlled by the crossheads, between which a uniform sample should be used.

For the strain measurement method, if necking occurs during the experiment, e.g. Figure 4-8(c) and (d), DIC is required to obtain a full-field strain map. Otherwise, a virtual live extensometer is a better choice as it can monitor the strain variation lively (note: post-processing is required in DIC analysis), and no speckle pattern (which may change the mechanical behaviour of such thin film structure) is required. It should be noted that most devices can only apply one virtual live extensometer simultaneously, which means if other strain measurements in addition to longitudinal strain measurement are required, DIC should still be used.

In summary, a guideline of the selection of sample shape and strain measurement method can be seen in Figure 6-2.

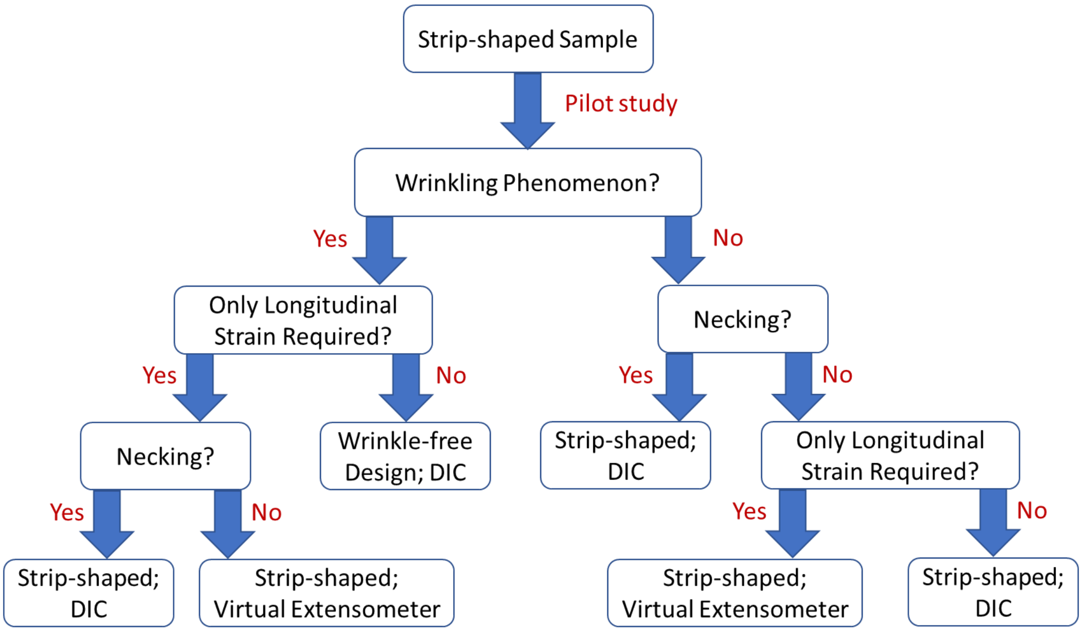

Figure 6-2 A guideline diagram of the selection of sample shape and strain measurement method.

6.3 The relative benefits of two-step method and proposed inverse stress solution method

In Chapter 5, the hyper-viscoelastic model (i.e. HVE model) was used to study the short- and long-term mechanical behaviour of separators. Based on the methodology of the experiment (Section 5.2) and the theory (Section 5.4), two traditional (i.e. two-step method and stress solution method) and the presently proposed (i.e. inverse stress solution method) parametrical calibration methods were assessed for their performances. As can be seen from Figure 5-14 to Figure 5-17 (or from Figure 5-20 to Figure 5-23), the proposed inverse stress solution has the best overall reliability in the simulation, especially at the ramp-loading stage. However, on the other hand, it is interesting to observe that even though the overall predictive results by the two-step method are not satisfactory, the Marlow-model-based HVE models (i.e. TS1-Marlow-HVE and TS2-Marlow-HVE) show a good convergence to the experimental results in the stress-relaxation stage, indicating that if the long-term stress-relaxation result is required, this method may give good predictive results. Therefore, in the real application, it would be better to use a hybrid model in simulation, i.e. using HVE model calibrated by inverse stress solution method for the case of ramp-loading and short-term duration, and using Marlow-based-HVE model calibrated by two-step method for the case of long-term stress relaxation. For example, when an electric vehicle suffers from a collision, the batteries will experience two stages, i.e. a short-term deformation caused by the external force and a long-term force state subjected to the external permanent deformation. If a study is trying to figure out what happens to the battery or the battery separator in a short period after the collision, the Marlow-model-based HVE model calibrated by the inverse stress solution method should be used. In contrast, if a state of battery or battery separator after a long period since the collision is required, the Marlow-based-HVE model calibrated by two-step method is more suitable to use.

6.4 Further comments on the Neo-Hookean model and Mooney-Rivlin model used in HVE model

In Chapter 5, three hyperelastic models, i.e. Neo-Hookean (NH) model, Mooney-Rivlin (MR) model and Marlow model, were selected to be studied. In the FE numerical simulation (Section 5.6.3), it is found that only Marlow-model-based HVE models are not suffering from a convergence problem. For the NH-model-based HVE models, only SS2-NH-HVE has a convergence problem, while all MR-model-based HVE models have been interrupted in the simulation due to the convergence problem. It is necessary to understand the difference between these two models, and the reasons why these two models have a convergence problem.

NH model is the earliest proposed and also simplest hyperelastic model, which is similar to Hooke’s law (Boulanger and Hayes 2001). NH model assumes that the material has an initial linear range, e.g. NH models in Figure 5-9 and Figure 5-11, and is not able to give accurate prediction at large strains (Kim et al. 2012a). Unlike NH model, MR model is a phenomenological model based on stored-energy function, which was first proposed by Mooney (1940) and then expressed in terms of invariants by Rivlin (1948). Compared to NH model, MR model is available to relative complicated mechanical behaviours (Mihai et al. 2015) but less stable at large strain conditions (Kim et al. 2012a, Shojaeiarani et al. 2019). For example, Shojaeiarani et al. (2019) found out that the maximum stable strain can only be around 0.05-0.1 for MR model in the case of uniaxial tension, which is similar to the situation in this research (instability occurs before target strain). The reason for this phenomenon is that this two-parameter fitted strain energy function model tends to cause a stress drop after a certain strain, which violates the Drucker stability conditions, i.e. $d\sigma : d\varepsilon > 0$. Therefore, NH model has better stability while MR model has better accuracy in the simulation.

6.5 The PhD work and findings used in multiphysics study

This PhD research aims to establish a more accurate material model of separators that can be used in both mechanical and multiphysics simulations of batteries. For the multiphysics simulation, a principle diagram for mechanical-electrochemical-thermal effects can be seen in Figure 6-3 (Shi et al. 2011, Cannarella and Arnold 2013, Fu et al. 2013, Wu et al. 2014).

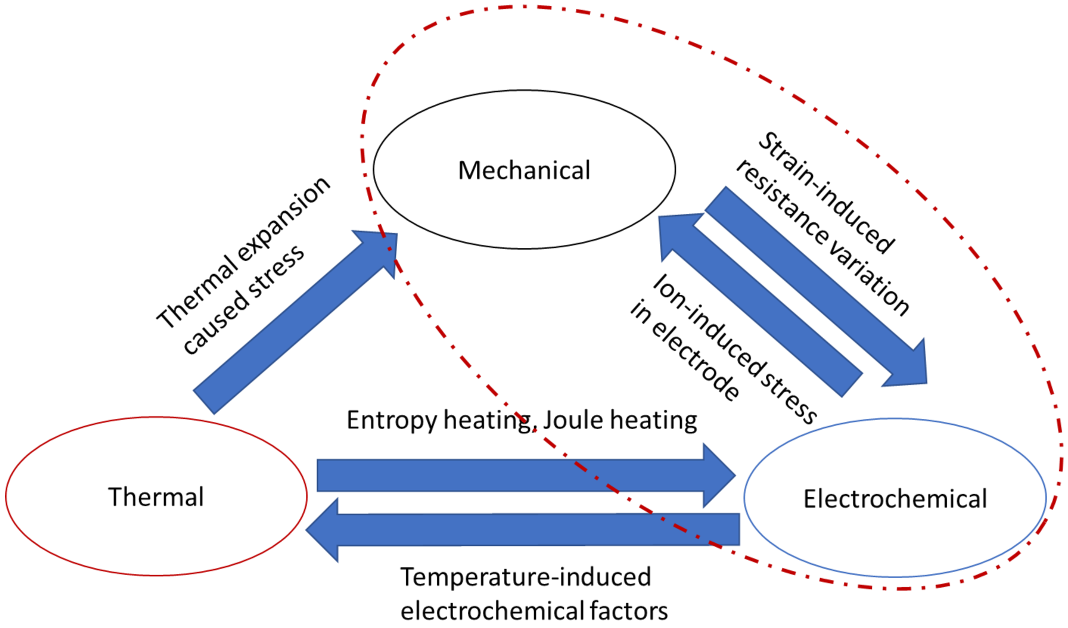

Figure 6-3 The principle diagram for coupled mechanical-electrochemical-thermal effects.

As shown in Figure 6-3, the multiphysics modelling of the battery is a complicated problem, as there are tens of factors that will influence each other during the application. Therefore, the battery model is usually simplified to a simple homogeneous material by only considering several representative factors. Especially for the mechanical model, the strain-induced factors (e.g. porosity) that can significantly influence the electrochemical behaviours (Cannarella and Arnold 2013, Yuan et al. 2020) are usually not considered in the multiphysics simulations. This PhD project provides a deeper insight into the strain-induced porosity variation, which can be extended to bridge the variation of electrochemical factors such as tortuosity and electrical resistance in the battery. In addition, the HVE model proposed in Chapter 5 can also provide a more accurate stress response in both short- and long-term duration. These two models are both important in coupled mechanical-electrochemical modelling, and all these factors can be expressed by strain as a variable.

7 Conclusions and Future Works

7.1 Conclusions

Although the separator is not involved in electrochemical reactions when batteries are in use, it is the most important component in terms of the safety inside the liquid electrolyte batteries, and therefore, it is important to fully understand its mechanical behaviours. After a careful literature review on the studies of mechanical properties of separators, limitations of the previous research are identified, e.g. wrinkling caused measurement error, mesoscale characteristics related to macroscale deformation, viscoelastic behaviour in large deformation, etc. Aiming at these limitations, a comprehensive analytical-experimental-numerical study has been done in this research to improve the test method, explore the mesoscale features and establish a more applicable material model with the proposed parametrical calibration method. Based on the investigation results shown in Chapter 3 to Chapter 5, the primary contributions are outlined in the following three parts.

1) **The method to improve the experimental measurement accuracy.**
   In this part, the wrinkling phenomenon, which usually happens in mechanical tensile tests and could adversely affect the measurement accuracy in the transverse directions, was studied in Chapter 3. It was found that the geometry of the thin film sample plays a critical role in the wrinkling behaviour. The influence of geometry on the wrinkling was studied based on FEM, and a critical geometric boundary (CGB) was proposed to distinguish the wrinkling and non-wrinkling regions for uniaxial tensile tests. Based on the Nested Intervals Method, a function of CGB for all possible shapes of dogbone thin film samples has been determined to prevent the occurrence of wrinkling. Furthermore, the underpinning mechanism was also analysed and discussed, and its applications were validated in Chapter 4.
2) **The general tensile mechanical properties of separators and the connection between macroscale deformation and mesoscale characteristics.**
   In this part, with the help of the 3D DIC technique, the real-time macroscale deformation status can be obtained under the uniaxial tensile test. Based on the

analysis of the strain distribution and the engineering strain obtained under different virtual strain gauge (VSG) sizes, it can be seen that the strains are distributed homogeneously for the wet-processed separators and the dry-processed separators (before the occurrence of necking). The strain analysis also demonstrated the occurrence of wrinkling, which may adversely influence the measurement accuracy in transverse direction. The dogbone geometry proposed in Chapter 3 can effectively solve the wrinkling problem. On the other hand, based on the assumption of the incompressible matrix material, the porosity with macroscale deformation can be analytically calculated. It was found that the porosities of dry-processed separators increase with strain while the porosities of wet-processed separators decrease with strain, which was also validated by the mesoscale characterisation observed by the scanning electron microscope (SEM).

3) **The proposed hyper-viscoelastic constitutive model and the corresponding parametrical calibration method for finite strain deformation.**

   In this part, to address the issue that the traditional viscoelastic model can only apply to small strain deformation, a hyper-viscoelastic (HVE) constitutive model is studied. According to previous studies and the analysis from Chapter 4, the homogeneous distribution of strain can be found in wet-processed separators, which allows the live virtual extensometer to measure the engineering strain in longitudinal direction in real-time. By conducting the isotropic wet-processed separator in a designed tension-relaxation experiment with various nominal strain-rates, it is found that the traditional two-step method has an intrinsic problem to determine the model parameters, which is also demonstrated by the comparison between FE simulations based on two-step method and corresponding experimental results. For the stress solution method, which is another traditional parametrical calibration method, it is found that two kinds of parameters (i.e. hyperelastic parameters and viscoelastic parameters) can influence each other during the optimisation process. It is also found that the HVE models obtained by the traditional stress solution method seem challenging to satisfy the numerical convergence in FE simulations. On the other hand, the proposed inverse stress solution method not only reduces the number of required parameters in calibration (only viscoelastic parameters required), but also is applicable to FE simulations without causing convergence problems. The final comparison between FE simulation results and experimental results shows that the proposed inverse stress solution method is a hybrid analytical-experimental-numerical method, which can effectively calibrate the HVE model and accurately describe the viscoelastic properties of the isotropic separators in finite-strain under various loading nominal strain-rates.

In addition, it should be noted that the CGB method that can prevent wrinkling in the material test (i.e. uniaxial tensile test) proposed in Chapter 3 is not only applicable to the separators investigated in this research, but also applicable to other materials with thin film structure, e.g. Kapton film, etc. Meanwhile, the parametrical calibration method for hyper-viscoelastic (HVE) models using tension-relaxation tests and the proposed inverse stress solution method can be generally applied to materials with characteristics of large deformation and viscoelasticity.

7.2 Future works

In this thesis, the new findings collectively provide some new insights into the mechanical properties of separators used in liquid electrolyte rechargeable batteries from experimental and theoretical aspects. These new findings on CGB, porosity formula and HVE model improve the experimental design, bridge macroscale-mesoscale characteristics, and develop a more accurate viscoelastic model under finite-strain condition. However, some limitations are still not been addressed, and the following aspects are worthy of further investigation

i) The CGB proposed in this research is actually an upper boundary, while for the materials with a smaller Poisson’s ratio, the CGB should be smaller. Therefore, it is recommended to involve Poisson’s ratio as an independent factor to improve the CGB formulation as it currently only considers geometry-related non-dimensional parameters. In addition, factors like manufacturing imperfection, not ideal boundary conditions and material constitutive model, which were discussed in Section 6.1, are also worthy of being studied in the future.

ii) As the porosity is changed with the deformation of the separators, the tortuosity is also changed at the same time. The tortuosity, which is an important factor in ionic exchange during the daily use of batteries, is also an important factor of the deformed separators to indicate the safety condition instead of using mechanical damage as an indicator. The latter (mechanical damage) was usually used to determine the short-circuit inside the batteries under mechanical abuse.

iii) Even though the proposed HVE model in this research can accurately predict the mechanical properties with considering viscoelasticity and large deformation, it is limited to the materials with viscoelastic behaviour only influenced by the time factor. Nevertheless, for materials whose viscoelastic behaviour is affected not only by time but also by other factors (e.g. deformation, temperature), the proposed HVE model needs to be further developed.

iv) The proposed inverse stress solution method in this thesis adopted the generalised reduced gradient (GRG) nonlinear algorithm as the optimisation/calibration method. However, the solution obtained by the GRG algorithm is highly dependent on the initial conditions, and it is difficult to gain the global optimum solution when the problem becomes complicated (e.g. high nonlinearity, massive undetermined parameters), i.e. the optimum solution is likely to be a local optimum solution near the initial conditions given by researchers. It means that if the given initial conditions are far from the optimal point, the correctness of the optimised results can be significantly affected. In the future, therefore, it will be better to find a suitable global optimisation method, which can efficiently and effectively find the global optimum results instead of the GRG algorithm used in the present study.

v) In this study, only elasticity behaviour is considered in numerical simulation and constitutive model theory. However, in some of the experimental results in Chapters 4 and 5, it can be found that the plasticity could happen if the deformation is larger than the elastic limit. Therefore, whether in the wrinkling analysis or the establishment of the hyper-viscoelastic model, plastic and damage behaviours are important issues worthy of further study.

Bibliography

A. López-Campos, J., Segade, A., R. Fernández, J., Casarejos, E. and A. Vilán, J. (2019) Behavior characterization of visco-hyperelastic models for rubber-like materials using genetic algorithms. *Applied Mathematical Modelling, 66*, pp. 241-255.

Abaqus (2019) Version 2019 Documentation. in *Dassault Systemes Simulia Corporation*.

Anovitz, L. M. and Cole, D. R. (2015) Characterization and analysis of porosity and pore structures. *Reviews in Mineralogy & Geochemistry, 80*(1), pp. 61-164.

Arora, P. and Zhang, Z. J. (2004) Battery separators. *Chemical Reviews, 104*(10), pp. 4419-62.

Avdeev, I., Martinsen, M. and Francis, A. (2013) Rate- and Temperature-Dependent Material Behavior of a Multilayer Polymer Battery Separator. *Journal of Materials Engineering and Performance, 23*(1), pp. 315-325.

Baldwin, R. S., Bennett, W. R., Wong, E. K., Lewton, M. and Harris, M. K. (2010) Battery separator characterization and evaluation procedures for NASA's advanced lithium-ion batteries. *Nasa/Tm, 216099*.

Basu, S. and Debnath, A. K. (2019) Chapter 5 - Special Instrument. in Basu, S. and Debnath, A. K., (eds.) *Power Plant Instrumentation and Control Handbook (Second Edition),*Boston: Academic Press. pp. 321-415.

Bódai, G. and Goda, T. (2011) A new, tensile test-based parameter identification method for large-strain generalized maxwell-model. *Acta Polytechnica Hungarica, 8*(5), pp. 89-108.

Boresi, A. P. (2003) *Advanced mechanics of materials,* 6th ed. / Arthur P. Boresi, Richard J. Schmidt. ed., New York ;: J. Wiley.

Bosnjak, N., Nadimpalli, S., Okumura, D. and Chester, S. A. (2020) Experiments and modeling of the viscoelastic behavior of polymeric gels. *Journal of the Mechanics and Physics of Solids, 137*, pp. 103829.

Boulanger, P. and Hayes, M. (2001) Finite-Amplitude Waves in Mooney-Rivlin and Hadamard Materials. in,Vienna: Springer Vienna. pp. 131-167.

Briody, C., Duignan, B., Jerrams, S. and Tiernan, J. (2012) The implementation of a visco-hyperelastic numerical material model for simulating the behaviour of polymer foam materials. *Computational Materials Science, 64*, pp. 47-51.

Cai, W., Wang, H., Maleki, H., Howard, J. and Lara-Curzio, E. (2011) Experimental simulation of internal short circuit in Li-ion and Li-ion-polymer cells. *Journal of Power Sources, 196*(18), pp. 7779-7783.

Cannarella, J. and Arnold, C. B. (2013) Ion transport restriction in mechanically strained separator membranes. *Journal of Power Sources, 226*, pp. 149-155.

Cannarella, J. and Arnold, C. B. (2015) The effects of defects on localized plating in lithium-ion batteries. *Journal of the Electrochemical Society, 162*(7), pp. A1365-A1373.

Cannarella, J., Liu, X. Y., Leng, C. Z., Sinko, P. D., Gor, G. Y. and Arnold, C. B. (2014) Mechanical Properties of a Battery Separator under Compression and Tension. *Journal of the Electrochemical Society, 161*(11), pp. F3117-F3122.

Cao, Y. and Hutchinson, J. W. (2012) From wrinkles to creases in elastomers: the instability and imperfection-sensitivity of wrinkling. *Proceedings of the Royal Society A: Mathematical, Physical and Engineering Sciences, 468*(2137), pp. 94-115.

CCM (2017) *CCM: China's wet process separator market will boom in 2017*, Available: http://www.cnchemicals.com/Press/89035-CCM:%20China%E2%80%99s%20wet%20process%20separator%20market%20will%20boom%20in%202017.html [Accessed 04 Sept 2020].

Cerda, E. and Mahadevan, L. (2003) Geometry and physics of wrinkling. *Physical Review Letters, 90*(7), pp. 074302.

Cerda, E., Ravi-Chandar, K. and Mahadevan, L. (2002) Wrinkling of an elastic sheet under tension. *Nature, 419*(6907), pp. 579.

Chen, J. C., Yan, Y. D., Sun, T., Qi, Y. and Li, X. D. (2014) Deformation and fracture behaviors of microporous polymer separators for lithium ion batteries. *RSC Advances, 4*(29), pp. 14904-14914.

Chung, Y. S., Yoo, S. H. and Kim, C. K. (2009) Enhancement of Meltdown Temperature of the Polyethylene Lithium-Ion Battery Separator via Surface Coating with Polymers Having High Thermal Resistance. *Industrial & Engineering Chemistry Research, 48*(9), pp. 4346-4351.

Coman, C. D. (2007) On the applicability of tension field theory to a wrinkling instability problem. *Acta Mechanica, 190*(1-4), pp. 57-72.

Dai, X., Yuan, T., Zu, Z., Shao, X., Li, L., Cheng, X., Zhou, J., Yang, F. and He, X. (2020) Experimental study of wrinkling behavior of membrane structures via visual method. *Thin-Walled Structures, 149*, pp. 106537.

Deimede, V. and Elmasides, C. (2015) Separators for lithium-ion batteries: A review on the production processes and recent developments. *Energy Technology, 3*(5), pp. 453-468.

DeMeuse, M. T. (2021) Chapter 9 - Future developments in battery separators. in DeMeuse, M. T., (ed.) *Polymer-Based Separators for Lithium-Ion Batteries*: Elsevier. pp. 159-172.

Ding, L., Xu, R., Pu, L., Yang, F., Wu, T. and Xiang, M. (2019a) Pore formation and evolution mechanism during biaxial stretching of β-iPP used for lithium-ion batteries separator. *Materials & Design, 179*, pp. 107880.

Ding, L., Zhang, C., Wu, T., Yang, F., Cao, Y. and Xiang, M. (2020a) The compression behavior, microstructure evolution and properties variation of three kinds of commercial battery separators under compression load. *Journal of Power Sources, 451*.

Ding, L., Zhang, C., Wu, T., Yang, F., Lan, F., Cao, Y. and Xiang, M. (2020b) Effect of temperature on compression behavior of polypropylene separator used for Lithium-ion battery. *Journal of Power Sources, 466*, pp. 228300.

Ding, L., Zhang, D., Wu, T., Yang, F., Lan, F., Cao, Y. and Xiang, M. (2020c) The Influence of Multiple Stimulations on the Unusual Delamination Phenomenon of a Li-Ion Battery Separator Prepared by a Wet Process. *Industrial & Engineering Chemistry Research, 59*(10), pp. 4568-4579.

Ding, X., Zhao, Y., Yan, D. and Zhang, K. (2019b) Controllable Propagation of Bending Waves in Wrinkled Films. *Journal of Applied Mechanics, 86*(6), pp. 061005.

Djian, D., Alloin, F., Martinet, S., Lignier, H. and Sanchez, J. Y. (2007) Lithium-ion batteries with high charge rate capacity: Influence of the porous separator. *Journal of Power Sources, 172*(1), pp. 416-421.

Doyle, M., Fuller, T. F. and Newman, J. (1993) Modeling of galvanostatic charge and discharge of the lithium/polymer/insertion cell. *Journal of the Electrochemical Society, 140*(6), pp. 1526-1533.

Eisensteine, P. A. (2017) *Tesla Under Fire After Explosive Crash*, Available: https://www.nbcnews.com/business/autos/tesla-under-fire-after-explosive-crash-n722541 [Accessed 08.01 2018].

Elmahdy, A. and Verleysen, P. (2018) The use of 2D and 3D high-speed digital image correlation in full field strain measurements of composite materials subjected to high strain rates. in *ICEM 2018,*Brussels, Belgium pp. 538.

Faghfouri, S. and Rammerstorfer, F. G. (2020) Mode transitions in buckling and post-buckling of stretched-twisted strips. *International Journal of Non-Linear Mechanics, 127,* pp. 103609.

Fazekas, B. and Goda, T. J. (2018) Determination of the hyper-viscoelastic model parameters of open-cell polymer foams and rubber-like materials with high accuracy. *Materials & Design, 156,* pp. 596-608.

Fazekas, B. and Goda, T. J. (2019) Closed-form and numerical stress solution-based parameter identification for incompressible hyper-viscoelastic solids subjected to various loading modes. *International Journal of Mechanical Sciences, 151,* pp. 650-660.

Ferry, J. D. (1980) *Viscoelastic properties of polymers,* 3rd ed. ed., New York: Wiley.

Finegan, D. P., Cooper, S. J., Tjaden, B., Taiwo, O. O., Gelb, J., Hinds, G., Brett, D. J. L. and Shearing, P. R. (2016) Characterising the structural properties of polymer separators for lithium-ion batteries in 3D using phase contrast X-ray microscopy. *Journal of Power Sources, 333,* pp. 184-192.

Flores-Johnson, E. A., Li, Q. M. and Mines, R. A. W. (2008) Degradation of Elastic Modulus of Progressively Crushable Foams in Uniaxial Compression. *Journal of Cellular Plastics, 44*(5), pp. 415-434.

Friedl, N., Rammerstorfer, F. G. and Fischer, F. D. (2000) Buckling of stretched strips. *Computers & Structures, 78*(1-3), pp. 185-190.

Fu, C., Wang, T., Xu, F., Huo, Y. and Potier-Ferry, M. (2019) A modeling and resolution framework for wrinkling in hyperelastic sheets at finite membrane strain. *Journal of the Mechanics and Physics of Solids, 124,* pp. 446-470.

Fu, R., Xiao, M. and Choe, S.-Y. (2013) Modeling, validation and analysis of mechanical stress generation and dimension changes of a pouch type high power Li-ion battery. Journal of Power Sources, 224, pp. 211-224.

Fuller, T. F., Doyle, M. and Newman, J. (1994) Simulation and optimization of the dual lithium ion insertion cell. *Journal of the Electrochemical Society, 141*(1), pp. 1-10.

Ghoreishy, M. H. R. (2012) Determination of the parameters of the Prony series in hyper-viscoelastic material models using the finite element method. *Materials & Design, 35,* pp. 791-797.

Ghoreishy, M. H. R., Firouzbakht, M. and Naderi, G. (2014) Parameter determination and experimental verification of Bergström–Boyce hysteresis model for rubber compounds reinforced by carbon black blends. *Materials & Design*, *53*, pp. 457-465.

Gilaki, M. and Avdeev, I. (2016) Impact modeling of cylindrical lithium-ion battery cells: a heterogeneous approach. *Journal of Power Sources*, *328*, pp. 443-451.

Goh, S. M., Charalambides, M. N. and Williams, J. G. (2004) Determination of the Constitutive Constants of Non-Linear Viscoelastic Materials. *Mechanics of Time-Dependent Materials, 8*(3), pp. 255-268.

Gor, G. Y., Cannarella, J., Prévost, J. H. and Arnold, C. B. (2014) A Model for the Behavior of Battery Separators in Compression at Different Strain/Charge Rates. *Journal of the Electrochemical Society, 161*(11), pp. F3065-F3071.

Greve, L. and Fehrenbach, C. (2012) Mechanical testing and macro-mechanical finite element simulation of the deformation, fracture, and short circuit initiation of cylindrical Lithium ion battery cells. *Journal of Power Sources, 214*, pp. 377-385.

Grujicic, M., Pandurangan, B., Arakere, G., Bell, W. C., He, T. and Xie, X. (2009) Seat-cushion and soft-tissue material modeling and a finite element investigation of the seating comfort for passenger-vehicle occupants. *Materials & Design, 30*(10), pp. 4273-4285.

Hao, W. Q., Xie, J. M., Zhang, X., Wang, P. and Wang, F. H. (2020) Strain rate effect and micro-buckling behavior of anisotropy macromolecular separator for lithium-ion battery. *Express Polymer Letters, 14*(3), pp. 206-219.

Healey, T. J., Li, Q. and Cheng, R. B. (2013) Wrinkling behavior of highly stretched rectangular elastic films via parametric global bifurcation. *Journal of Nonlinear Science, 23*(5), pp. 777-805.

Hirayama, M. and Takahashi, H. (2016) Wrinkle detection device and wrinkle detection method. in: Google Patents.

Holzapfel, G. A. (2002) Nonlinear solid mechanics: a continuum approach for engineering science. *Meccanica, 37*(4), pp. 489-490.

Howard, W. F. and Spotnitz, R. M. (2007) Theoretical evaluation of high-energy lithium metal phosphate cathode materials in Li-ion batteries. *Journal of Power Sources, 165*(2), pp. 887-891.

Hu, D. Y., Meng, K. P., Jiang, H. L., Xu, J. and Liu, R. R. (2015) Strain rate dependent constitutive behavior investigation of AerMet 100 steel. *Materials & Design, 87*, pp. 759-772.

Huang, Q., Hu, H., Yu, K., Potier-Ferry, M., Belouettar, S. and Damil, N. (2015) Macroscopic simulation of membrane wrinkling for various loading cases. *International Journal of Solids and Structures, 64-65*, pp. 246-258.

Huang, Q., Yang, J., Huang, W., Giunta, G., Belouettar, S. and Hu, H. (2020) The boundary effects on stretch-induced membrane wrinkling. *Thin-Walled Structures, 154*, pp. 106838.

Ihm, D., Noh, J. and Kim, J. (2002) Effect of polymer blending and drawing conditions on properties of polyethylene separator prepared for Li-ion secondary battery. *Journal of Power Sources, 109*(2), pp. 388-393.

Iwasa, T. (2017) Approximate estimation of wrinkle wavelength and maximum amplitude using a tension-field solution. *International Journal of Solids and Structures, 121*, pp. 201-211.

Iwasa, T. (2018) Experimental verification on wrinkling behavior given by wrinkling analysis using the tension field theory. *International Journal of Solids and Structures, 136-137*, pp. 1-12.

Jacques, N. and Potier-Ferry, M. (2005) On mode localisation in tensile plate buckling. *Comptes Rendus Mécanique, 333*(11), pp. 804-809.

Johnson, A. R., Quigley, C. J. and Mead, J. L. (1994) Large Strain Viscoelastic Constitutive Models for Rubber, Part I: Formulations. *Rubber Chemistry and Technology, 67*(5), pp. 904-917.

Johnson, G. R. (1983) A constitutive model and data for materials subjected to large strains, high strain rates, and high temperatures. *Proc. 7th Inf. Sympo. Ballistics*, pp. 541-547.

Johnson, M. B. and Wilkes, G. L. (2001) Microporous membranes of polyoxymethylene from a melt-extrusion process: (I) effects of resin variables and extrusion conditions. *Journal of Applied Polymer Science, 81*(12), pp. 2944-2963.

Johnson, M. B. and Wilkes, G. L. (2002a) Microporous membranes of isotactic poly(4-methyl-1-pentene) from a melt-extrusion process. I. Effects of resin variables and extrusion conditions. *Journal of Applied Polymer Science, 83*(10), pp. 2095-2113.

Johnson, M. B. and Wilkes, G. L. (2002b) Microporous membranes of polyoxymethylene from a melt-extrusion process: (II) Effects of thermal annealing and stretching on porosity. *Journal of Applied Polymer Science, 84*(9), pp. 1762-1780.

Jones, N. (2011) *Structural Impact*, 2 ed., Cambridge: Cambridge University Press.

Jridi, N., Arfaoui, M., Hamdi, A., Salvia, M., Bareille, O., Ichchou, M. and Ben Abdallah, J. (2019) Separable finite viscoelasticity: integral-based models vs. experiments. *Mechanics of Time-Dependent Materials, 23*(3), pp. 295-325.

Kalnaus, S., Kumar, A., Wang, Y., Li, J., Simunovic, S., Turner, J. A. and Gorney, P. (2018a) Strain distribution and failure mode of polymer separators for Li-ion batteries under biaxial loading. *Journal of Power Sources, 378*, pp. 139-145.

Kalnaus, S., Wang, Y., Li, J., Kumar, A. and Turner, J. A. (2018b) Temperature and strain rate dependent behavior of polymer separator for Li-ion batteries. *Extreme Mechanics Letters, 20*, pp. 73-80.

Kalnaus, S., Wang, Y. and Turner, J. A. (2017) Mechanical behavior and failure mechanisms of Li-ion battery separators. *Journal of Power Sources, 348*, pp. 255-263.

Khalil, S., Belaasilia, Y., Hamdaoui, A., Braikat, B., Jamal, M., Damil, N. and Azari, Z. (2019) ANM analysis of a wrinkled elastic thin membrane. *Comptes Rendus Mécanique, 347*(10), pp. 701-709.

Kim, B., Lee, S. B., Lee, J., Cho, S., Park, H., Yeom, S. and Park, S. H. (2012a) A comparison among Neo-Hookean model, Mooney-Rivlin model, and Ogden model for chloroprene rubber. *International Journal of Precision Engineering and Manufacturing, 13*(5), pp. 759-764.

Kim, T. Y., Puntel, E. and Fried, E. (2012b) Numerical study of the wrinkling of a stretched thin sheet. *International Journal of Solids and Structures, 49*(5), pp. 771-782.

Kossa, A. and Berezvai, S. (2016) Visco-hyperelastic Characterization of Polymeric Foam Materials. *Materials Today: Proceedings, 3*(4), pp. 1003-1008.

Kramer, D., Freunberger, S. A., Flückiger, R., Schneider, I. A., Wokaun, A., Büchi, F. N. and Scherer, G. G. (2008) Electrochemical diffusimetry of fuel cell gas diffusion layers. *Journal of Electroanalytical Chemistry, 612*(1), pp. 63-77.

Kudrolli, A. and Chopin, J. (2018) Tension-dependent transverse buckles and wrinkles in twisted elastic sheets. *Proceedings of the Royal Society A: Mathematical, Physical and Engineering Sciences, 474*(2214), pp. 20180062.

Lagadec, M. F., Ebner, M., Zahn, R. and Wood, V. J. J. o. T. E. S. (2016) Communication—technique for visualization and quantification of lithium-ion battery separator microstructure. *Journal of the Electrochemical Society, 163*(6), pp. A992-A994.

Lagadec, M. F., Zahn, R., Müller, S. and Wood, V. (2018a) Topological and network analysis of lithium ion battery components: the importance of pore space connectivity for cell operation. *Energy & Environmental Science, 11*(11), pp. 3194-3200.

Lagadec, M. F., Zahn, R. and Wood, V. (2018b) Characterization and performance evaluation of lithium-ion battery separators. *Nature Energy, 4*(1), pp. 16-25.

Lagadec, M. F., Zahn, R. and Wood, V. (2018c) Designing polyolefin separators to minimize the impact of local compressive stresses on lithium ion battery performance. *Journal of the Electrochemical Society, 165*(9), pp. A1829-A1836.

Lai, X., Jin, C., Yi, W., Han, X., Feng, X., Zheng, Y. and Ouyang, M. (2021) Mechanism, modeling, detection, and prevention of the internal short circuit in lithium-ion batteries: Recent advances and perspectives. *Energy Storage Materials, 35*, pp. 470-499.

Landesfeind, J., Hattendorff, J., Ehrl, A., Wall, W. A. and Gasteiger, H. A. (2016) Tortuosity determination of battery electrodes and separators by impedance spectroscopy. *Journal of the Electrochemical Society, 163*(7), pp. A1373-A1387.

Lasdon, L. S., Waren, A. D., Jain, A. and Ratner, M. (1978) Design and Testing of a Generalized Reduced Gradient Code for Nonlinear Programming. *ACM Transactions on Mathematical Software, 4*(1), pp. 34-50.

Lava, P., Coppieters, S., Wang, Y., Van Houtte, P. and Debruyne, D. (2011) Error estimation in measuring strain fields with DIC on planar sheet metal specimens with a non-perpendicular camera alignment. *Optics and Lasers in Engineering, 49*(1), pp. 57-65.

Lecieux, Y. and Bouzidi, R. (2010) Experimental analysis on membrane wrinkling under biaxial load – Comparison with bifurcation analysis. *International Journal of Solids and Structures, 47*(18-19), pp. 2459-2475.

Lee, D.-C. and Kim, C.-W. (2020) Detailed Layered Nonlinear Finite Element Analysis for Lithium-Ion Battery Cells to Predict Internal Short Circuits Due to Separator Fractures under Hemisphere Indentation. *Journal of the Electrochemical Society, 167*(12), pp. 120511.

Lee, H., Yanilmaz, M., Toprakci, O., Fu, K. and Zhang, X. W. (2014) A review of recent developments in membrane separators for rechargeable lithium-ion batteries. *Energy & Environmental Science, 7*(12), pp. 3857-3886.

Li, B., Liu, R., Cong, Q., Guo, H. and Lin, Q. (2021) Stress Superposition Method and free vibration of corner tensioned rectangular thin membranes. *Thin-Walled Structures, 159*, pp. 107201.

Li, Q. and Healey, T. J. (2016) Stability boundaries for wrinkling in highly stretched elastic sheets. *Journal of the Mechanics and Physics of Solids, 97*, pp. 260-274.

Li, Q. M., Magkiriadis, I. and Harrigan, J. J. (2006) Compressive Strain at the Onset of Densification of Cellular Solids. *Journal of Cellular Plastics, 42*(5), pp. 371-392.

Li, Z., Huang, J., Yann Liaw, B., Metzler, V. and Zhang, J. (2014) A review of lithium deposition in lithium-ion and lithium metal secondary batteries. *Journal of Power Sources, 254*, pp. 168-182.

Lin, C. C. and Mote Jr, C. D. (1996) The wrinkling of rectangular webs under nonlinearly distributed edge loading. *Journal of Applied Mechanics, 63*(3), pp. 655-659.

Liu, B., Yin, S. and Xu, J. (2016a) Integrated computation model of lithium-ion battery subject to nail penetration. *Applied Energy, 183*, pp. 278-289.

Liu, F., Xu, F. and Fu, C. (2019) Orientable wrinkles in stretched orthotropic films. *Extreme Mechanics Letters, 33*, pp. 100579.

Liu, Q., Du, C., Shen, B., Zuo, P., Cheng, X., Ma, Y., Yin, G. and Gao, Y. (2016b) Understanding undesirable anode lithium plating issues in lithium-ion batteries. *RSC Advances, 6*(91), pp. 88683-88700.

Love, C. T. (2011) Thermomechanical analysis and durability of commercial micro-porous polymer Li-ion battery separators. *Journal of Power Sources, 196*(5), pp. 2905-2912.

Luo, H., Jiang, X., Xia, Y. and Zhou, Q. (2015) Fracture mode analysis of lithium-ion battery under mechanical loading. In Paper Presented to the International Mechanical Engineering Congress and Exposition, Houston, Texas, USA.

Luo, W., Cheng, S., Wu, M., Zhang, X., Yang, D. and Rui, X. (2021) A review of advanced separators for rechargeable batteries. *Journal of Power Sources, 509*, pp. 230372.

Luo, Y., Niu, Y., Li, M. and Kang, Z. (2017a) A multi-material topology optimization approach for wrinkle-free design of cable-suspended membrane structures. *Computational Mechanics, 59*(6), pp. 967-980.

Luo, Y., Xing, J., Kang, Z., Zhan, J. and Li, M. (2020) Uncertainty of membrane wrinkling behaviors considering initial thickness imperfections. *International Journal of Solids and Structures, 191-192*, pp. 264-277.

Luo, Y., Xing, J., Niu, Y., Li, M. and Kang, Z. (2017b) Wrinkle-free design of thin membrane structures using stress-based topology optimization. *Journal of the Mechanics and Physics of Solids, 102*, pp. 277-293.

Mansfield, E. H. (1969) Tension field theory, a new approach which shows its duality with inextensional theory. in *Applied Mechanics*: Springer. pp. 305-320.

Mansfield, E. H. (1970) Load transfer via a wrinkled membrane. *Proceedings of the Royal Society of London. A. Mathematical and Physical Sciences, 316*(1525), pp. 269-289.

Mansfield, E. H. (1981) Gravity-induced wrinkle lines in vertical membranes. *Proceedings of the Royal Society of London. A. Mathematical and Physical Sciences, 375*(1762), pp. 307-325.

Mark, J. E. (2009) *Polymer Data Handbook (2nd Edition),* Oxford University Press.

Markets, R. a. (2018) *China Lithium Battery Separator Market, 2018-2022: Market Size Grew from CNY 1.3 Billion in 2013 to CNY 4.25 Billion in 2017*, Available: https://www.prnewswire.com/news-releases/china-lithium-battery-separator-market-2018-2022-market-size-grew-from-cny-1-3-billion-in-2013-to-cny-4-25-billion-in-2017--300697624.html [Accessed 04/09 2020].

Marlow, R. S. (2003) A general first-invariant hyperelastic constitutive model. *Constitutive Models for Rubber*, pp. 157-160.

Martins, A. D., Silvestre, N. and Bebiano, R. (2020) A new modal theory for wrinkling analysis of stretched membranes. *International Journal of Mechanical Sciences, 175*, pp. 105519.

Matyka, M., Khalili, A. and Koza, Z. (2008) Tortuosity-porosity relation in porous media flow. *Physical Review E, 78*(2), pp. 026306.

McCormick, N. and Lord, J. (2010) Digital Image Correlation. *Materials Today, 13*(12), pp. 52-54.

Mihai, L. A., Chin, L., Janmey, P. A. and Goriely, A. (2015) A comparison of hyperelastic constitutive models applicable to brain and fat tissues. *Journal of the Royal Society Interface, 12*(110), pp. 20150486.

Mooney, M. (1940) A Theory of Large Elastic Deformation. *Journal of Applied Physics, 11*(9), pp. 582-592.

Nayyar, V. (2010) *Stretch-induced compressive stress and wrinkling in elastic thin sheets*. Unpublished Master of Science in Engineering, University of Texas at Austin.

Nayyar, V. (2013) *Stretch-induced wrinkling of thin sheets*. Unpublished Doctor of Philosophy, The University of Texas at Austin.

Nayyar, V., Ravi-Chandar, K. and Huang, R. (2011) Stretch-induced stress patterns and wrinkles in hyperelastic thin sheets. *International Journal of Solids and Structures, 48*(25-26), pp. 3471-3483.

Nayyar, V., Ravi-Chandar, K. and Huang, R. (2014) Stretch-induced wrinkling of polyethylene thin sheets: Experiments and modeling. *International Journal of Solids and Structures, 51*(9), pp. 1847-1858.

Nicholson, D. W. and Nelson, N. W. (1990) Finite-Element Analysis in Design with Rubber. *Rubber Chemistry and Technology, 63*(3), pp. 368-406.

Nomura, K. and Kataoka, T. (2018) Device and method for producing separator roll. in: Google Patents.

Nunes-Pereira, J., Costa, C. M., Leones, R., Silva, M. M. and Lanceros-Méndez, S. (2013) Li-ion battery separator membranes based on poly(vinylidene fluoride-trifluoroethylene)/carbon nanotube composites. *Solid State Ionics, 249-250*, pp. 63-71.

Ogden, R. W. (1986) Recent Advances in the Phenomenological Theory of Rubber Elasticity. *Rubber Chemistry and Technology, 59*(3), pp. 361-383.

Orendorff, C. J. (2012) The Role of Separators in Lithium-Ion Cell Safety. *Interface magazine, 21*(2), pp. 61-65.

Palacio, L., Pradanos, P., Calvo, J. I. and Hernandez, A. (1999) Porosity measurements by a gas penetration method and other techniques applied to membrane characterization. *Thin Solid Films, 348*(1-2), pp. 22-29.

Pan, B. and Tian, L. (2016) Advanced video extensometer for non-contact, real-time, high-accuracy strain measurement. *Optics Express, 24*(17), pp. 19082-19093.

Panaitescu, A., Xin, M., Davidovitch, B., Chopin, J. and Kudrolli, A. (2019) Birth and decay of tensional wrinkles in hyperelastic sheets. *Physical Review E, 100*(5-1), pp. 053003.

Patel, K. K., Paulsen, J. M. and Desilvestro, J. (2003) Numerical simulation of porous networks in relation to battery electrodes and separators. *Journal of Power Sources, 122*(2), pp. 144-152.

Peabody, C. and Arnold, C. B. (2011) The role of mechanically induced separator creep in lithium-ion battery capacity fade. *Journal of Power Sources, 196*(19), pp. 8147-8153.

Peabody, C. A. (2011) *Characterization of Mechanical Stress Effects on Lithium-ion Battery Materials,* Princeton University.

Pulidindi, K. and Pandey, H. (2021) *Battery Separators Market Size By Product (Polypropylene, Polyethylene, Ceramic, Nylon), By Battery (Lithium-ion, Lead Acid), By End-user (Automotive, Consumer Electronics, Industrial, Power Storage,), Industry Analysis Report, Regional Outlook, Growth Potential, Price Trends, Competitive Market Share & Forecast, 2021 – 2027,* Available: https://www.gminsights.com/industry-analysis/battery-separator-market#:~:text=Polyethylene%20battery%20separator%20to%20dominate%20the%20market%20during%20the%20forecast%20period&text=Polyethylene%20(PE)%20separators%20held%20a,of%20over%2017%25%20through%202027. [Accessed 27.03 2021].

Puntel, E., Deseri, L. and Fried, E. (2011) Wrinkling of a Stretched Thin Sheet. *Journal of Elasticity, 105*(1-2), pp. 137-170.

Ramadass, P., Fang, W. and Zhang, Z. (2014) Study of internal short in a Li-ion cell I. Test method development using infra-red imaging technique. *Journal of Power Sources, 248,* pp. 769-776.

Rivlin, R. S. (1948) Large elastic deformations of isotropic materials IV. further developments of the general theory. *Philosophical Transactions of the Royal Society of London. Series A, Mathematical and Physical Sciences, 241*(835), pp. 379-397.

Romanov, K. I. (2001) The drucker stability of a material. *Journal of Applied Mathematics and Mechanics, 65*(1), pp. 155-162.

Roth, E. P., Doughty, D. H. and Pile, D. L. (2007) Effects of separator breakdown on abuse response of 18650 Li-ion cells. *Journal of Power Sources, 174*(2), pp. 579-583.

Ruiz, V., Pfrang, A., Kriston, A., Omar, N., Van den Bossche, P. and Boon-Brett, L. (2018) A review of international abuse testing standards and regulations for lithium ion batteries in electric and hybrid electric vehicles. *Renewable and Sustainable Energy Reviews, 81,* pp. 1427-1452.

SAE, S. (2009) J2464: Electric and hybrid electric vehicle rechargeable energy storage system safety and abuse testing. in: Pennsylvania, USA: SAE.

Sahraei, E., Campbell, J. and Wierzbicki, T. (2012) Modeling and short circuit detection of 18650 Li-ion cells under mechanical abuse conditions. *Journal of Power Sources, 220,* pp. 360-372.

Sahraei, E., Kahn, M., Meier, J. and Wierzbicki, T. (2015) Modelling of cracks developed in lithium-ion cells under mechanical loading. *RSC Advances, 5*(98), pp. 80369-80380.

Sahraei, E., Meier, J. and Wierzbicki, T. (2014) Characterizing and modeling mechanical properties and onset of short circuit for three types of lithium-ion pouch cells. *Journal of Power Sources, 247,* pp. 503-516.

Santhanagopalan, S., Ramadass, P. and Zhang, J. (2009) Analysis of internal short-circuit in a lithium ion cell. *Journal of Power Sources, 194*(1), pp. 550-557.

Sarkar, A., Shrotriya, P. and Chandra, A. (2019) Modeling of separator failure in lithium-ion pouch cells under compression. *Journal of Power Sources, 435*, pp. 226756.

Shanahan, C., Tofail, S. A. M. and Tiernan, P. (2017) Viscoelastic braided stent: Finite element modelling and validation of crimping behaviour. *Materials & Design, 121*, pp. 143-153.

Sheidaei, A., Xiao, X. R., Huang, X. S. and Hitt, J. (2011) Mechanical behavior of a battery separator in electrolyte solutions. *Journal of Power Sources, 196*(20), pp. 8728-8734.

Shi, D. H., Xiao, X. R., Huang, X. S. and Kia, H. (2011) Modeling stresses in the separator of a pouch lithium-ion cell. *Journal of Power Sources, 196*(19), pp. 8129-8139.

Shojaeiarani, J., Hosseini-Farid, M. and Bajwa, D. (2019) Modeling and experimental verification of nonlinear behavior of cellulose nanocrystals reinforced poly(lactic acid) composites. *Mechanics of Materials, 135*, pp. 77-87.

Simo, J. C. (1987) On a fully three-dimensional finite-strain viscoelastic damage model: Formulation and computational aspects. *Computer Methods in Applied Mechanics and Engineering, 60*(2), pp. 153-173.

Sipos, A. A. and Fehér, E. (2016) Disappearance of stretch-induced wrinkles of thin sheets: A study of orthotropic films. *International Journal of Solids and Structures, 97-98*, pp. 275-283.

Spotnitz, R. and Franklin, J. (2003) Abuse behavior of high-power, lithium-ion cells. *Journal of Power Sources, 113*(1), pp. 81-100.

Steigmann, D. J. (2008) Two-dimensional models for the combined bending and stretching of plates and shells based on three-dimensional linear elasticity. *International Journal of Engineering Science, 46*(7), pp. 654-676.

Sun, Y. and Li, Q. M. (2015) Effect of entrapped gas on the dynamic compressive behaviour of cellular solids. *International Journal of Solids and Structures, 63*, pp. 50-67.

Sunderland, P., Yu, W. and Månson, J.-A. (2001) A thermoviscoelastic analysis of process-induced internal stresses in thermoplastic matrix composites. *Polymer Composites, 22*(5), pp. 579-592.

Sutton, M. A., Yan, J. H., Tiwari, V., Schreier, H. W. and Orteu, J. J. (2008) The effect of out-of-plane motion on 2D and 3D digital image correlation measurements. *Optics and Lasers in Engineering, 46*(10), pp. 746-757.

Tessler, A., Sleight, D. W. and Wang, J. T. (2005) Effective Modeling and Nonlinear Shell Analysis of Thin Membranes Exhibiting Structural Wrinkling. *Journal of Spacecraft and Rockets, 42*(2), pp. 287-298.

Timoshenko, S. P. and Gere, J. M. (2009) *Theory of elastic stability,* Courier Corporation.

Tjaden, B., Brett, D. J. L. and Shearing, P. R. (2016) Tortuosity in electrochemical devices: a review of calculation approaches. *International Materials Reviews, 63*(2), pp. 47-67.

Tye, F. L. (1983) Tortuosity. *Journal of Power Sources, 9*(2), pp. 89-100.

Von Kármán, T. (1967) *The wind and beyond : Theodore von Kármán, pioneer in aviation and pathfinder in space,* (1st ed.). ed., Boston: Little, Brown.

Wagner, H. (1931) *Flat Sheet Metal Girders with Very Thin Metal Web, Part I - General Theories and Assumptions (NACA Technical Memorandum 604),* National Advisory Committee for Aeronautics/NASA.

Wang, C. G., Du, X. W., Tan, H. F. and He, X. D. (2009) A new computational method for wrinkling analysis of gossamer space structures. *International Journal of Solids and Structures, 46*(6), pp. 1516-1526.

Wang, H., Lara-Curzio, E., Rule, E. T. and Winchester, C. S. (2017) Mechanical abuse simulation and thermal runaway risks of large-format Li-ion batteries. *Journal of Power Sources, 342,* pp. 913-920.

Wang, H., Simunovic, S., Maleki, H., Howard, J. N. and Hallmark, J. A. (2016) Internal configuration of prismatic lithium-ion cells at the onset of mechanically induced short circuit. *Journal of Power Sources, 306,* pp. 424-430.

Wang, L., Yin, S. and Xu, J. (2019a) A detailed computational model for cylindrical lithium-ion batteries under mechanical loading: From cell deformation to short-circuit onset. *Journal of Power Sources, 413,* pp. 284-292.

Wang, Q., Ping, P., Zhao, X., Chu, G., Sun, J. and Chen, C. (2012) Thermal runaway caused fire and explosion of lithium ion battery. *Journal of Power Sources, 208,* pp. 210-224.

Wang, T., Fu, C., Xu, F., Huo, Y. and Potier-Ferry, M. (2019b) On the wrinkling and restabilization of highly stretched sheets. *International Journal of Engineering Science, 136,* pp. 1-16.

Wang, X., Law, S.-S., Yang, Q. and Yang, N. (2018) Numerical study on the dynamic properties of wrinkled membranes. *International Journal of Solids and Structures, 143,* pp. 125-143.

Wang, X., Yin, L. and Yang, Q. (2019c) Numerical analysis of the wrinkling behavior of thin membranes. *Archive of Applied Mechanics, 89*(11), pp. 2361-2380.

Ward, I. M. and Sweeney, J. (2004) *An introduction to the mechanical properties of solid polymers,* 2nd ed. ed., New York: Wiley.

Wei, C. and Olatunbosun, O. A. (2016) The effects of tyre material and structure properties on relaxation length using finite element method. *Materials & Design, 102,* pp. 14-20.

Weighall, M. J. (1991) Recent advances in polyethylene separator technology. *Journal of Power Sources, 34*(3), pp. 257-268.

Wiedenmann, D., Keller, L., Holzer, L., Stojadinović, J., Münch, B., Suarez, L., Fumey, B., Hagendorfer, H., Brönnimann, R., Modregger, P., Gorbar, M., Vogt, U. F., Züttel, A., Mantia, F. L., Wepf, R. and Grobéty, B. (2013) Three-dimensional pore structure and ion conductivity of porous ceramic diaphragms. *AIChE Journal, 59*(5), pp. 1446-1457.

Wong, Y. W. and Pellegrino, S. (2006a) Wrinkled Membranes Part I: Experiments. *Journal of Mechanics of Materials and Structures, 1*(1), pp. 3-25.

Wong, Y. W. and Pellegrino, S. (2006b) Wrinkled Membranes Part II: Analytical Models. *Journal of Mechanics of Materials and Structures, 1*(1), pp. 27-61.

Wong, Y. W. and Pellegrino, S. (2006c) Wrinkled Membranes Part III: Numerical Simulations. *Journal of Mechanics of Materials and Structures, 1*(1), pp. 63-95.

Wu, W., Xiao, X. R., Huang, X. S. and Yan, S. T. (2014) A multiphysics model for the in situ stress analysis of the separator in a lithium-ion battery cell. *Computational Materials Science, 83,* pp. 127-136.

Wu, Y. P., Rahm, E. and Holze, R. (2003) Carbon anode materials for lithium ion batteries. *Journal of Power Sources, 114*(2), pp. 228-236.

Xie, W., Dang, Y., Wu, L., Liu, W., Tang, A. and Luo, Y. (2020) Experimental and molecular simulating study on promoting electrolyte-immersed mechanical properties of cellulose/lignin separator for lithium-ion battery. *Polymer Testing, 90.*

Xie, W., Liu, W., Dang, Y., Tang, A., Deng, T. and Qiu, W. (2019) Investigation on electrolyte-immersed properties of lithium-ion battery cellulose separator through multi-scale method. *Journal of Power Sources, 417,* pp. 150-158.

Xiong, R., Ma, S., Li, H., Sun, F. and Li, J. (2020a) Toward a Safer Battery Management System: A Critical Review on Diagnosis and Prognosis of Battery Short Circuit. *iScience, 23*(4), pp. 101010.

Xiong, R., Sun, W., Yu, Q. and Sun, F. (2020b) Research progress, challenges and prospects of fault diagnosis on battery system of electric vehicles. *Applied Energy, 279*, pp. 115855.

Xu, H., Usseglio-Viretta, F., Kench, S., Cooper, S. J. and Finegan, D. P. (2020) Microstructure reconstruction of battery polymer separators by fusing 2D and 3D image data for transport property analysis. *Journal of Power Sources, 480.*

Xu, H., Zhu, M., Marcicki, J. and Yang, X. G. (2017) Mechanical modeling of battery separator based on microstructure image analysis and stochastic characterization. *Journal of Power Sources, 345*, pp. 137-145.

Xu, J., Liu, B., Wang, L. and Shang, S. (2015) Dynamic mechanical integrity of cylindrical lithium-ion battery cell upon crushing. *Engineering Failure Analysis, 53*, pp. 97-110.

Xu, J., Wang, L., Guan, J. and Yin, S. (2016) Coupled effect of strain rate and solvent on dynamic mechanical behaviors of separators in lithium ion batteries. *Materials & Design, 95*, pp. 319-328.

Yan, D., Zhang, K., Peng, F. and Hu, G. (2014) Tailoring the wrinkle pattern of a microstructured membrane. *Applied Physics Letters, 105*(7), pp. 071905.

Yan, S., Deng, J., Bae, C., He, Y., Asta, A. and Xiao, X. R. (2018a) In-plane orthotropic property characterization of a polymeric battery separator. *Polymer Testing, 72*, pp. 46-54.

Yan, S., Deng, J., Bae, C., Kalnaus, S. and xiao, x. (2020) Orthotropic Viscoelastic Modeling of Polymeric Battery Separator. *Journal of the Electrochemical Society, 167*(9).

Yan, S., Huang, X. and Xiao, X. (2018b) Measurement of the through thickness compression of a battery separator. *Journal of Power Sources, 382*, pp. 13-21.

Yang, Y., Fu, C. and Xu, F. (2020) A finite strain model predicts oblique wrinkles in stretched anisotropic films. *International Journal of Engineering Science, 155*, pp. 103354.

Yeoh, O. H. (1993) Some Forms of the Strain Energy Function for Rubber. *Rubber Chemistry and Technology, 66*(5), pp. 754-771.

Yu, Y., Xiong, B., Zeng, F. X., Xu, R., Yang, F., Kang, J., Xiang, M., Li, L., Sheng, X. and Hao, Z. (2018) Influences of compression on the mechanical behavior and electrochemical performances of separators for lithium ion batteries. *Industrial & Engineering Chemistry Research, 57*(50), pp. 17142-17151.

Yuan, C., Gao, X., Wong, H. K., Feng, B. and Xu, J. (2019) A Multiphysics Computational Framework for Cylindrical Battery Behavior upon Mechanical Loading Based on LS-DYNA. *Journal of the Electrochemical Society, 166*(6), pp. A1160-A1169.

Yuan, C., Wang, L., Yin, S. and Xu, J. (2020) Generalized separator failure criteria for internal short circuit of lithium-ion battery. *Journal of Power Sources, 467*, pp. 228360.

Zhang, C., Xu, J., Cao, L., Wu, Z. and Santhanagopalan, S. (2017a) Constitutive behavior and progressive mechanical failure of electrodes in lithium-ion batteries. *Journal of Power Sources, 357*, pp. 126-137.

Zhang, S. S. (2007) A review on the separators of liquid electrolyte Li-ion batteries. *Journal of Power Sources, 164*(1), pp. 351-364.

Zhang, X., Rumierz, G. P., Humiston, K. F., Haire, C. E., Fields, T. S., Braswell, M. A. and Proctor, R. A. (2017b) Biaxially oriented porous membranes, composites, and methods of manufacture and use. in Publication, U. S. P. A., (ed.) *United States Patent Application Publication*: Celgard LLC.

Zhang, X., Sahraei, E. and Wang, K. (2016a) Deformation and failure characteristics of four types of lithium-ion battery separators. *Journal of Power Sources, 327*, pp. 693-701.

Zhang, X., Sahraei, E. and Wang, K. (2016b) Li-ion battery separators, mechanical integrity and failure mechanisms leading to soft and hard internal shorts. *Sci Rep, 6*, pp. 32578.

Zhang, X., Zhu, J. and Sahraei, E. (2017c) Degradation of battery separators under charge–discharge cycles. *RSC Advances, 7*(88), pp. 56099-56107.

Zhao, Y., Spingler, F. B., Patel, Y., Offer, G. J. and Jossen, A. (2019) Localized swelling inhomogeneity detection in lithium ion cells using multi-dimensional laser scanning. *Journal of the Electrochemical Society, 166*(2), pp. A27-A34.

Zheng, L. (2009) *Wrinkling of dielectric elastomer membranes*. Unpublished Doctor of Philosophy , California Institute of Technology.

Zhu, J., Wierzbicki, T. and Li, W. (2018a) A review of safety-focused mechanical modeling of commercial lithium-ion batteries. *Journal of Power Sources, 378*, pp. 153-168.

Zhu, J., Zhang, X., Luo, H. and Sahraei, E. (2018b) Investigation of the deformation mechanisms of lithium-ion battery components using in-situ micro tests. *Applied Energy, 224*, pp. 251-266.

Zhu, J., Zhang, X. and Wierzbicki, T. (2018c) Stretch-induced wrinkling of highly orthotropic thin films. *International Journal of Solids and Structures, 139-140*, pp. 238-249.

Zhu, X., Wang, H., Wang, X., Gao, Y., Allu, S., Cakmak, E. and Wang, Z. (2020) Internal short circuit and failure mechanisms of lithium-ion pouch cells under mechanical indentation abuse conditions: An experimental study. *Journal of Power Sources, 455*.

Zinth, V., von Lüders, C., Hofmann, M., Hattendorff, J., Buchberger, I., Erhard, S., Rebelo-Kornmeier, J., Jossen, A. and Gilles, R. (2014) Lithium plating in lithium-ion batteries at sub-ambient temperatures investigated by in situ neutron diffraction. *Journal of Power Sources, 271*, pp. 152-159.